Universidade de Aveiro
2017
Departamento de Engenharia de Materiais e Cerâmica

Monika Małgorzata Tomczyk

Desenho de materiais funcionais 2D para futuras aplicações em microeletrónica

Designing 2D functional materials for future microelectronics applications

Universidade de Aveiro

2017

Departamento de Engenharia de Materiais e Cerâmica

Monika Małgorzata Tomczyk

Desenho de materiais funcionais 2D para futuras aplicações em microeletrónica

Designing 2D functional materials for future microelectronics applications

Tese apresentada à Universidade de Aveiro para cumprimento dos requisitos necessários à obtenção do grau de Doutor em Ciência e Engenharia de Materiais, realizada sob a orientação científica da Doutora Paula M. L. S. Vilarinho, Professora Associada do Departamento de Engenharia de Materiais e Cerâmica da Universidade de Aveiro.

Thesis presented to the University of Aveiro in fulfillment of the requirements for the awarding of the degree of Doctor in Materials Science and Engineering under the scientific guidance of Professor Paula M. L. S. Vilarinho, Associate Professor of the Department of Materials and Ceramic Engineering of the University of Aveiro.

Apoio financeiro da FCT e do FSE no âmbito do III Quadro Comunitário de Apoio.

o júri / the jury

presidente

Prof. Doutora Ana Isabel Couto Neto da Silva Miranda

professora catedrática da Universidade de Aveiro

vogais / examiners committee

Prof. Doutora Maria de Jesus Matos Gomes

professora catedrática, Escola de Ciências, Universidade do Minho

Prof. Doutor Abílio de Jesus Monteiro Almeida

professor associado com agregação, Faculdade de Ciências, Universidade do Porto

Prof. Doutor Luís Manuel Cadillon Martins Costa

professor associado com agregação, Universidade de Aveiro

Prof. Doutora Isabel Maria das Mercês Ferreira

professora associada, Faculdade de Ciências e Tecnologia, Universidade Nova de Lisboa

Prof. Doutora Paula Maria Lousada Silveirinha Vilarinho

professora associada, Universidade de Aveiro (orientadora)

agradecimentos / acknowledgements

The majority of experimental work was performed at the Department of Materials and Ceramic Engineering, part of the associated laboratory – CICECO (Centre for Research in Ceramics and Composite Materials), and I am mostly grateful to my supervisor Prof. Paula M. Vilarinho for giving me the opportunity to do PhD under her supervision. Her constant encouragement, guidance and excellent mentorship over the past four years helped me to develop, organize, write and present good scientific communications, ending up with this thesis.

Part of the work was carried out in The Instituto de Ciencia de Materiales de Madrid (ICMM), Consejo Superior de Investigaciones Cientificas (CSIC) in Madrid (Spain) in the group of Electroceramics for Information Technologies. I would like to thank Prof. M. Lourdes Calzada, Dr. Ricardo Jiménez and Dr. Iñigo Bretos for for sharing their extensive knowledge on low temperature thin films preparation and electrical characterization.

I would like to thank Prof. Ian M. Reaney from Department of Engineering Materials, University of Sheffield for consultations about the microstructure of the investigated thin films via TEM.

I would like to thank Dr. Daniel G. Stroppa from International Iberian Nanotechnology Laboratory for his kind help on TEM sample preparation by FIB and HRTEM studies.

I would also like to thank all the lab members for their help over the years.

Then, plenty of others have had impact on the work, and I want to thank all of them.

I acknowledge FCT, the Portuguese Foundation for Science and Technology, for financial support, under the grant SFRH/BD/80123/2011.

palavras-chave

Eletrocerâmicas, Filmes finos, Ferroelétricos sem chumbo, $BiFeO_3$, $(Na_{0.5}Bi_{0.5})TiO_3$, deposição de soluções químicas, Eletrónica flexível, Silício, poliimida, método de precursores de soles difásicos (SDSG), método de foto-deposição de solução química (FDSQ)

resumo

Devido à redução de dimensões e ao aumento da velocidade de processamento de dados nos dispositivos microeletrónicos baseados em semicondutores convencionais, estão a ser exploradas abordagens inovadoras envolvendo novos materiais tais como óxidos funcionais. Com o rápido desenvolvimento da indústria eletrónica existe uma maior necessidade de elevado desempenho, de elevada fiabilidade, e de componentes eletrónicos miniaturizados integrados em vários dispositivos. A fim de tornar os dispositivos amplamente acessíveis e de fácil utilização, requisitos adicionais devem ser considerados: o tamanho e peso desejados, o custo reduzido, o baixo consumo de energia e a portabilidade. Materiais funcionais de baixa dimensionalidade são muito promissores para cumprir essas exigências. Em particular, os ferroeléctricos de filmes finos bidimensionais (2D) têm recebido grande atenção devido à sua crescente utilização em memórias não voláteis, detectores piroelétricos, transdutores piezoeléctricos miniaturizados e dispositivos sintonizáveis de micro-ondas. A temperatura de cristalização é um parâmetro chave na preparação de ferroelétricos 2D. Muitos filmes finos ferroelétricos são cristalizados a temperaturas >600 °C. Esses valores estão acima da temperatura que certos elementos do dispositivo funcional podem suportar. Recentemente, este facto tornou-se ainda mais importante, devido às promissoras aplicações que podem ser consideradas caso os ferroeléctricos 2D sejam compatíveis com substratos poliméricos flexíveis de baixo custo e de baixo ponto de fusão. A compatibilidade de filmes finos ferróicos com estes últimos tipos de substratos é muito difícil, mas se conseguida pode ampliar acentuadamente a gama de aplicações para os mais recentes requisitos de eletrónica flexível e microeletrónica, onde dispositivos leves e baratos são exigidos.

Neste trabalho, é implementada uma combinação da modificação da química de precursores e assistência por luz UV, com promoção simultânea da cristalização pela introdução de sementes nanocristalinas na solução precursora, para a fabricação de filmes finos ferróicos sem chumbo - Método de Precursores Fotossensíveis Semeados. Neste contexto, o principal objetivo deste trabalho foi fabricar filmes finos sem chumbo $BiFeO_3$ (BFO) e $Na_{0.5}Bi_{0.5}TiO_3$ (NBT) a baixas temperaturas (~300 °C) com uma resposta ferroelétrica competitiva. Além disso, a investigação do efeito do elétrodo-base sobre as propriedades dielétricas e ferroelétricas de filmes finos de BFO foi levada a cabo, e a comparação entre o comportamento de condensadores de BFO com base em IrO_2, $LaNiO_3$ (LNO) e Pt foi estabelecida. Adicionalmente, os efeitos dos vários eléctrodos sobre a microestrutura de filmes finos ferroeléctricos de BFO foram estudados por microscopia eletrónica de transmissão (TEM) de alta resolução.

Primeiramente, filmes finos finos de perovesquite BFO e NBT foram preparados sobre substratos de silício revestidos com Pt, por deposição de solução química. Os filmes finos de BFO foram preparados a temperaturas na gama de 400-500 °C, a partir de soluções de precursores estequiométricas e com excesso de

Bi. Os filmes de BFO cristalinos foram obtidos a 400 °C, o limite inferior de temperatura. Os filmes preparadas com excesso de Bi possuem curvas de histerese ferroelétrica mais definidas do que aqueles sem qualquer excesso, para filmes com espessuras ~150 nm. Uma vez que as densidades de corrente de fuga nos filmes finos diminuem com a diminuição da temperatura de processamento, a polarização de filmes finos de BFO preparados com excesso Bi e recozidos a 400 e 450 °C pode ser efetivamente comutada à temperatura ambiente. Obtiveram-se valores de polarização remanescente de P_r ~10 e ~60 μC/cm^2 com campos coercivos de E_C ~ 205 e 235 kV/cm para os filmes finos preparados a 400 e 450 °C, respectivamente. Os filmes finos de NBT foram preparados a temperaturas entre 400 e 650 °C. As propriedades estruturais e ferroelétricas dos filmes foram examinadas. A constante dieléctrica observada e as perdas dieléctricas a 100 kHz são 616 e 0,032, respectivamente, enquanto que a polarização remanescente observada e o campo coercivo são P_r ~ 24 μC/cm^2 e E_C ~ 215 kV/cm, respectivamente para o filme de NBT recozido a 650 °C. O recozimento térmico, em atmosfera de oxigénio após cada camada de revestimento, é eficaz na promoção da cristalização do filme na fase de perovesquite romboédrica a uma baixa temperatura de 400 °C. No entanto, obteve-se um ciclo P-E quase linear para os filmes NBT cristalizados a 400 °C devido à sua incipiente cristalinidade.

Os filmes finos de BFO foram depositados numa gama de elétrodos para determinar o seu papel no controlo da formação de fases e da microestrutura. A cristalização em elétrodos de óxido seguiu a sequência: amorfa → $Bi_2O_2(CO_3)$ → perovesquite, enquanto que nos elétrodos de Pt cristalizaram diretamente a partir da fase amorfa. Os elétrodos de IrO_2 promoveram a formação da fase de perovesquite à temperatura mais baixa e o LNO induziu adicionalmente o crescimento epitaxial local. O LNO tem a estrutura de perovesquite com o parâmetro de rede a = 0.384 nm, compatível com o de BFO, a = 0.396 nm, e assim a epitaxia é mais provável. Todas as composições exibiram precipitados inteiramente coerentes ricos em Fe dentro do interior de grão da matriz de perovesquite, enquanto que a incoerente segunda fase de $Bi_2Fe_4O_9$ foi também observada nos limites de grão de BFO crescido em eléctrodos de Pt. Esta última pode ser observada por difração de raios X, bem como TEM, mas os precipitados coerentes foram observados apenas por TEM, principalmente evidenciados pelo seu contraste Z em imagens de campo escuro anular. Estes dados têm consequências acentuadas permitindo alargar a utilização de filmes de BFO sob campo aplicado, a aplicações como atuadores, sensores e aplicações de memória.

Em seguida, os filmes finos de BFO foram depositados em substratos de Si com elétrodos distintos, como Pt, LNO e IrO_2, para investigar o efeito do elétrodo-base sobre o crescimento e as propriedades elétricas do BFO. Todas os filmes de BFO são compostos por grãos colunares cujo tamanho é dependente do elétrodo-base. Não se observou textura para filmes de 320 nm de espessura fabricados em Pt orientado (111). Os filmes sobre eléctrodos de óxido, em particular sobre LNO são altamente orientados no plano (012). A grande polarização remanescente em BFO/Pt e BFO/IrO_2 é atribuída à alta contribuição de corrente de fuga. Os filmes BFO de 400 nm de espessura em LNO possuem uma baixa densidade de corrente de fuga ~4×10^{-6} A/cm^2, uma grande polarização remanescente de 50 μC/cm^2 e um pequeno campo coercitivo de 180 kV/cm à temperatura ambiente. Demonstramos que as camadas de LNO aumentam a cristalinidade e a orientação de filmes finos BFO, o que se reflete nas suas propriedades funcionais. Este estudo mostra que, além da simples necessidade de filmes monofásicos, os elétrodos de óxido de metal têm um impacto relevante no desenvolvimento de filmes finos BFO de alta qualidade fabricados por métodos químicos de deposição de solução. Estes resultados têm uma implicação grande para a fabricação de dispositivos BFO baseados em filmes finos.

Finalmente, provamos que é possível fabricar diretamente filmes finos de BFO sem chumbo em substratos flexíveis de poliamida com funcionalidades ferroelétricas e magnéticas (multiferroicidade) à temperatura ambiente. O nosso método inovador, baseado em soluções de Precursores Fotossensíveis e nanosementes cristalinas, foi usado com sucesso para diminuir a temperatura de cristalização de filmes finos de BFO até uma temperatura tão baixa quanto 300 °C, a mais baixa temperatura reportada até agora para a preparação de filmes finos multiferróicos de BFO. Apesar deste excepcionalmente baixo nível

térmico, obtém-se uma polarização remanescente P_r de 2.8 μC/cm^2 para os filmes *semeados + UV*, com um campo coercitivo E_C de 300 kV/cm. A estratégia de síntese baseada na utilização de precursores fotossensíveis sementados pode ser transferida para qualquer outra família de óxidos metálicos funcionais.

keywords

Electroceramics, Thin films, Lead-free ferroelectric, $BiFeO_3$, $Na_{0.5}Bi_{0.5}TiO_3$, chemical solution deposition, flexible electronics, Si, polyimide, seeded precursor solution method, photochemical solution deposition method

abstract

With the dimensions reduction and data processing speeds increasing of conventional semiconductor based microelectronic devices, innovative approaches involving new materials such as functional oxides are being explored. With the rapid development of the electronics industry there is a need for high performance, high reliability and miniaturized electronic components integrated into various devices. In order to make the devices user friendly and widely accessible, additional requirements should be considered: the desired size and weight, low cost, low power consumption, and portability in addition to high levels of functionality. Low dimensional functional materials hold great promises to fulfil those requirements. In particular, two-dimensional (2D) thin film ferroelectrics have received wide attention because of their growing use as non-volatile memories, pyroelectric detectors, miniaturized piezoelectric transducers and tunable microwave devices. Crystallization temperature is a key parameter in preparation of 2D-ferroelectrics. Many ferroelectric thin films are crystallized at temperatures >600 °C. This is above the temperature that certain elements of the functional device can withstand. Recently it became even more important due to promising applications that can be envisaged if 2D-ferroelectrics will be compatible with low cost, low melting temperature flexible polymeric substrates. The compatibility of ferroic thin films with those last types of substrates can markedly widen the range of applications towards the most recent requirements of flexible electronics and microelectronics, where lightweight and cheap devices are demanded.

In this work, a combination of the modification of precursor chemistry and the assistance of UV-light, with simultaneous promotion of crystallization by introducing nanocrystalline seeds in the precursor solution, is implemented to fabricate lead-free ferroic thin films - Seeded Photosensitive Precursor Method. Within this context, the main objective of this work was to fabricate lead-free $BiFeO_3$ (BFO) and $Na_{0.5}Bi_{0.5}TiO_3$ (NBT) thin films with a competitive ferroelectric response at low temperatures. Moreover, investigations of the effect of the bottom electrode on the dielectric and ferroelectric properties of BFO thin films was conducted and the comparison between the behavior of IrO_2, $LaNiO_3$ (LNO) and Pt based BFO capacitors established. Additionally, the effects of these various bottom electrodes on the microstructure of $BiFeO_3$ ferroelectric films was studied by high-resolution TEM.

Firstly, BFO and NBT perovskite thin films were prepared on Pt-coated silicon substrates by chemical solution deposition. BFO was prepared at temperatures in the range 400-500 °C, and from stoichiometric and Bi excess precursor solutions. Crystalline BFO films were obtained at the lowest temperature limit of 400 °C. The films prepared with Bi excess possess more defined ferroelectric hysteresis loops than those without any excess; for films with thicknesses ~150 nm. As the leakage current densities in the films decrease with decreasing the processing temperature, polarization of BFO films prepared with Bi excess

and annealed at 400 and 450 °C can be effectively switched at room temperature. Remanent polarization values of P_r ~ 10 and ~60 μC/cm^2 with coercive fields of E_C ~ 205 and 235 kV/cm were obtained for the films prepared at 400 and 450 °C, respectively. NBT thin films were prepared at temperatures from 400 to 650 °C. Structural and ferroelectric properties of the films were examined. The observed dielectric constant and dielectric losses at 100 kHz are 616 and 0.032, respectively, while the observed remanent polarization and coercive field are P_r ~ 24 μC/cm^2 and E_C ~ 215 kV/cm, respectively for the NBT film annealed at 650 °C. Thermal annealing in an oxygen atmosphere after each layer of coating is effective in promoting crystallization of the film into rhombohedral perovskite phase at a low temperature of 400 °C. However, almost linear, *P-E* loop was obtained for those NBT films crystallized at 400 °C due to incipient crystallinity.

BFO thin films were grown on a range of electrodes to determine their role in controlling phase formation and microstructure. The crystallization on oxide electrodes followed the sequence: amorphous → $Bi_2O_2(CO_3)$ → perovskite, while those on Pt crystallized directly from the amorphous phase. IrO_2 electrodes promoted perovskite phase formation at the lowest temperature and $LaNiO_3$ additionally induced local epitaxial growth. LNO has the perovskite structure with lattice parameter a = 0.384 nm, compatible with that of BFO, a = 0.396 nm and thus epitaxy is more likely. It was observed for the first time that all compositions exhibited fully coherent Fe-rich precipitates within the grain interior of the perovskite matrix, whereas incoherent $Bi_2Fe_4O_9$ second phase was also observed at the grain boundaries of BFO grown on Pt electrodes. The latter could be observed by X-ray diffraction as well as transmission electron microscopy (TEM) but coherent precipitates were only observed by TEM, principally evidenced by their Z contrast in annular dark field images. These data have pronounced consequences for the extended use of BFO films under applied field for actuator, sensor and memory applications.

Then, BFO thin films were deposited on Si-based substrates with distinct electrodes, such as Pt, LNO, and IrO_2, in order to investigate the effect of bottom electrode on the growth and electrical properties of BFO. All BFO films are composed of columnar grains which size is dependent on the bottom electrode. No texture was observed for 320 nm thick films fabricated on (111) oriented Pt. Films on oxide electrodes, in particular on LNO are highly (012) oriented. The large remanent polarization in BFO/Pt and BFO/IrO_2 is attributed to the high leakage current contribution. 400 nm thick BFO films on LNO possess a low leakage current density ~4×10^{-6} A/cm^2, a large remanent polarization of 50 μC/cm^2 and a small coercive field of 180 kV/cm at room temperature. We demonstrate that LNO layers enhance the crystallinity and orientation of BFO thin films, which is reflected in their functional properties. This study shows that besides the simple need of monophasic films metal oxide electrodes have a relevant impact on the development of high quality BFO thin films fabricated by chemical solution deposition methods. These results have a broad implication for the fabrication of BFO thin film based devices.

Finally, we prove that it is possible to directly fabricate lead-free BFO thin films on flexible polyamide substrates with ferroelectric and magnetic functionalites (multiferroicity) at room temperature. Our own proprietary novel solution-based Seeded Photosensitive Precursor Method was successfully used to decrease the crystallization temperature of BFO thin films down to a temperature as low as 300 °C, the lowest reported up to now for the preparation of multiferroic BFO thin films. Despite this exceptionally low thermal budget a remanent polarization P_r of 2.8 μC/cm^2 is obtained for the *seeded + UV* films, with a coercive field E_C of 300 kV/cm. The synthesis strategy based on the use of seeded photosensitive precursors can be transferred to any family of functional metal oxide.

Table of contents

List of Figures

List of Tables

List of Symbols

$\Delta_r G°_m$	Gibbs free energy of the equilibrium reaction
a	lattice parameter
A	absorbance
Å	angstrom, unit of length
c	lattice parameter
C_p	capacitance of the parallel circuit
d, d_n, d_ψ	space between the planes (lattice spacing)
d_{31}	piezoelectric transverse coefficient
d_{33}	piezoelectric coefficient in the z-direction
d_n	
d_ψ	lattice spacing for each ψ
$\mathrm{d}E/\mathrm{d}H$	magnetoelectric coefficient
E	electric field
E_C	coercive electric field
f	frequency
I	current
I, I_0	transmitted/incident radiation
J	current density
k_{31}, k_{33}	electromechanical coupling coefficients
n	refractive index
v	Poisson's ratio
P	polarization
P_r	remanent polarization
P_s	spontaneous polarization
R_p	resistance of the parallel circuit
S	area
t	time
t	film thickness
T	transmittance
$tan\delta$	dielectric loss
T_C	Curie temperature
T_d	temperature of depolarization

T_m	melting temperature
T_N	Neel temperature
V	voltage
Z	atomic number
α	thermal expansion coefficient
σ	residual stress
γ	pyroelectric coefficient
ε_r	dielectric constant
ε_0	dielectric constant of vacuum, $\varepsilon_0 = 8.854 \times 10^{-12}$ F·m^{-1}
θ, ω	incident angle
λ	wavelength

List of Abbreviations

2D	two-dimensional
ABO_3	perovskite structure
AC	alternating current
AcOH	acetic acid, $C_2H_4O_2$
ADF	annular dark-field
AFE	antiferroelectric state
AFM	antiferromagnetic
AFM	atomic force microscopy
BET	Brunauer–Emmett–Teller
BF	bright field
BFO	bismuth ferrite, $BiFeO_3$
BiOAc	bismuth acetate, $Bi(CH_3COO)_3$
BLNF	La and Nb co-doped $BiFeO_3$
BSE	backscattered electrons
BST	barium strontium titanate, $(Ba, Sr)TiO_3$
BT	barium titanate, $BaTiO_3$
CMOS	complementary metal oxide semiconductor
CSD	chemical solution deposition
CVD	chemical vapour deposition
DC	direct current
DF	dark field
DTA	differential thermal analysis
EBSD	diffracted backscattered electrons
EDS	energy-dispersive X-ray spectrometry
EELS	electron energy-loss spectrometry
e.g.	for example (Latin *exemplī grātiā*)
et al.	and others (Latin *et alii*)
etc.	and other things (Latin *etceteros*)
EtOH	ethanol, C_2H_6O
FE	ferroelectric
$Fe(acac)_3$	iron(III) acetylacetonate, $Fe(C_5H_7O_2)_3$
FeRAMs	ferroelectric random access memories

FIB	focus ion milling
FM	ferromagnetic
FTIR	Fourier transformed infrared
Hacac	acetylacetone, $C_5H_8O_2$
HAADF	high-angle annular dark-field
GI-XRD	grazing incidence X-ray diffraction
IC	integrated circuit
i.e.	it is (Latin *id est*)
ITRS	International Technology Roadmap for Semiconductors
JCPDS	Joint Committee on Powder Diffraction Standards
IR	infrared
KNN	potassium sodium niobate, $(K, Na)NbO_3$
LDFZ	laser-diode-heated floating zone
LNO	lanthanum nickelate, $LaNiO_3$
LPCVD	low-pressure chemical vapour deposition
MEMS	microelectromechanical systems
MERAM	magnetoelectric random access memory
MOCVD	metalorganic chemical vapour deposition
MOD	metalorganic decomposition
MPB	morphotropic phase boundary
NaOAc	sodium acetate, CH_3COONa
NBT	sodium bismuth titanate, $Na_{0.5}Bi_{0.5}TiO_3$
P-E	polarization-electric field
pc	pseudo-cubic
PCSD	photo chemical solution deposition
PFM	piezoresponse force microscopy
PLD	pulsed laser deposition
PT	lead titanate, $PbTiO_3$
PVA	poly(vinyl alcohol)
PVD	physical vapour deposition
PZT	lead zirconate titanate, $PbZr_{1-x}Ti_xO_3$
RF	radio frequency
RoHS	Restriction of Hazardous Substances (Directive 2002/95/EC)
RT	room temperature
RTA	rapid thermal annealing

SAD	selected area diffraction
SBT	strontium bismuth tantalate, $SrBi_2Ta_2O_9$
SDSG	seeded diphasic sol gel
SEM	scanning electron microscopy
SPM	scanning probe microscopy
SPS	spark plasma sintering
SRO	strontium ruthenate, $SrRuO_3$
STEM	scanning transmission electron microscopy
t-OBu	tert-butoxide, $(CH_3)_3CO$
TEM	transmission electron microscopy
TF	thin film
TG	thermogravimetric analysis
Ti(OiPr)$_4$	titanium tetra-isopropoxide, $C_{12}H_{28}O_4Ti$
TMR	tunnel magnetoresistance
UV	ultraviolet
WEEE	Waste of electrical and electronic equipment (Directive 2012/19/EU)
VSM	vibrating sample magnetometer
XPS	X-ray photoelectron spectroscopy
XRD	X-ray diffraction

Chapter 1. INTRODUCTION

1.1. Motivation

With the dimension's reduction and speeds increasing of conventional semiconductor based microelectronic devices, scientific community and the technology sector are facing difficulties in keeping pace with the newer device demands of the modern times. Innovative approaches involving new materials such as functional oxides are being explored to challenge this problem. With this rapid development of the electronics industry there is a need for high performance, high reliability and miniaturized electronic components integrated into various devices. In order to make the devices user friendly and widely accessible, additional requirements should be considered: the desired size and weight, low cost, low power consumption, and portability [1]. Low dimensional ferroelectric materials hold great promises to fulfil those requirements. In particular, two-dimensional (2D) thin film ferroelectrics have received wide attention because of their growing use as non-volatile memories, pyroelectric detectors, miniaturized piezoelectric transducers and tunable microwave devices [2]. Utilization of novel materials and structures in real microelectronics applications requires integration of ferroelectric thin films on silicon with the conventional platform, such as CMOS (Complementary Metal-Oxide Semiconductor) technology. Among the many methods available for processing of ferroelectric thin films chemical solution deposition (CSD) is possibly the one with the lowest capital cost, while offering high versatility for creation of a wide range of compositions, microstructures and ultimately properties. Therefore, CSD is one of the most frequently used preparation methods for the fabrication of 2D-ferroelectrics. Crystallization temperature is a key parameter in preparation of 2D-ferroelectrics. Many ferroelectric thin films are crystallized at temperatures >600 °C. This is above the temperature that certain elements of the functional device can withstand. Recently it became even more important due to promising applications that can be envisaged if 2D-ferroelectrics will be compatible with low cost, low melting temperature flexible and rigid metallic and polymeric substrates.

For several years, low temperature synthesis of ferroelectric-films has been attempted with modifications at the "precursor/green state film level" and at the "post depositions level". Within the first, use of seed-layers and of excess of volatile components or combination of both is widely reported [3-6]. Control of solution chemistry to increase

homogeneity at the molecular level and thus, reactivity of precursors, has been used for the preparation of ferroelectric-films at low-temperatures as well [7]. Depending on the composition 2D ferroelectrics have been reported at around 500 °C, but the main drawback are the very poor properties, if any.

Concerning modifications at the "post deposition processing level" the most widely used strategy involves rapid thermal annealing (RTA). While RTA of lead-based perovskite films can both minimize the formation of the intermediate phases and greatly reduce thermal budget needed for crystallization, required process temperatures are still too high for some applications [8]. In the meantime other alternative methods such as laser-assisted crystallization [8] or laser lift-off [9], are being used for 2D-ferroelectrics.

Worthwhile to mention are attempts associated with the use of diphasic precursor sols (SDSG) process, developed by Paula Vilarinho research group, that allowed the preparation of lead zirconate titanate ($Pb(Zr, Ti)O_3$, PZT) films at 410 °C/30 h and 550 °C/30 min with very reasonable dielectric response [10-13]. In this methodology perovskite nanometric particles are dispersed in precursor solution and act as seeds to promote nucleation of the perovskite phase at low temperatures. Crystallization kinetics is enhanced and the activation energy for the perovskite formation is reduced, microstructure improved and better dielectric response obtained. Another important approach is the use of Photo-Chemical-Solution Deposition (PCSD), developed by Lourdes Calzada research group, based on the use of sol-gel precursors sensitive to ultraviolet (UV) light [14] and on the use of UV radiation sources of high intensity [15] to catalyze precursors chemical reactions towards oxide crystallization. The combination of nucleation of crystalline phase at low-temperatures, by modification of the precursors chemistry, with simultaneous promotion of the crystallization, by introducing nanocrystalline nucleus, was recently used for fabrication of PZT thin films at low synthesis-temperature with optimized dielectric response [16].

The development of less hazardous compounds is considered a crucial challenge nowadays, especially in the electronic industry, where legislations enforce alternative non-hazardous materials [17]. Therefore, in the case of ferroelectrics, relaxor-ferroelectrics and piezoelectrics, strong efforts are directed on looking for lead free alternatives for the commercially used PZT. Bismuth-based perovskites, such as those based on the multiferroic bismuth ferrite, $BiFeO_3$ (BFO), or the relaxor-ferroelectric sodium bismuth titanate,

$(Na_{0.5}Bi_{0.5})TiO_3$ (NBT), are shown as promising candidates in this area [18, 19]. Limitations for these compounds are related to the high annealing temperatures necessary for the crystallization of these perovskite phases and volatilization of high-vapour pressure elements such as Bi at the temperatures required for the film fabrication.

Bismuth ferrite has undoubtedly been studied more extensively than any other multiferroic being hailed the most promising lead free single phase multiferroic candidate for devices, due to its multiferroic nature above room temperature [20]. However, dielectric losses, leakage current and tendency to fatigue of BFO are the main hurdles to overcome for any kind of electronic applications [20]. The majority of these devices are fabricated such that the ferroic is deposited on a bottom electrode, typically using $Pt/TiO_2/SiO_2/Si$ substrates to provide an electrical contact for input and output data. Naturally, the performance of the device is strongly dependent on the quality of the interface between the ferroic and electrode/substrate heterostructure. Degradation in performance is commonly attributed to interfacial effects that induce internal stresses, modify the local defect chemistry and create non-optimized crystallographic orientations [21]. In principle, these limitations may be minimized if a suitable interlayer is introduced between the film and the Pt electrode. Moreover, oxide electrodes, such as $SrRuO_3$, IrO_2, RuO_2 and $LaNiO_3$ (LNO) used instead of Pt improve performance since they prevent undesired compositional modification and impede charge interdiffusion processes [22]. However, up to now, very few reports have been available on the dielectric and ferroelectric behavior of chemical solution deposited BFO thin films on LNO and IrO_2 electrodes [23-27] and no research focusing on the comparative study of oxide electrodes and Pt has been conducted.

Therefore, the main aim of this PhD work is to fabricate functional lead free piezoelectric and ferroelectric BFO and NBT thin films with optimized ferroelectric properties, at low temperatures (<450 °C) by a modified CSD method, to be compatible with the silicon based technology and principally with flexible substrates, such as polymeric, with technological added value to be used in future generation of microelectronic devices. The reduction of the synthesis temperature will be attained by a process that results from the combination of two unique synthesis processes, SDSG with PCSD, the so-called Seeded Photosensitive Precursor Method.

Growth of a technologically important and lead free multifunctional material, BFO is chosen to demonstrate the versatility of this method to grow complex oxide thin films directly on flexible substrates at temperature as low as 300 °C. The evaluation of the ferroelectric and piezoelectric properties of these low-temperature BFO films will be presented.

Moreover, investigation of the effect of the bottom electrode on the dielectric and ferroelectric properties of BFO thin films will be conducted. The comparison between the behavior of IrO_2, LNO and Pt based BFO capacitors will be established. Additionally, the effects of these various bottom electrodes on the microstructure of BFO ferroelectric films will be studied by high-resolution TEM and annular dark field (ADF) scanning transmission electron microscopy (STEM) in order to establish the microstructure-processing parameters relationship is principal to yield high quality BFO thin films.

The main objective of this PhD work is presented in Figure 1-1.

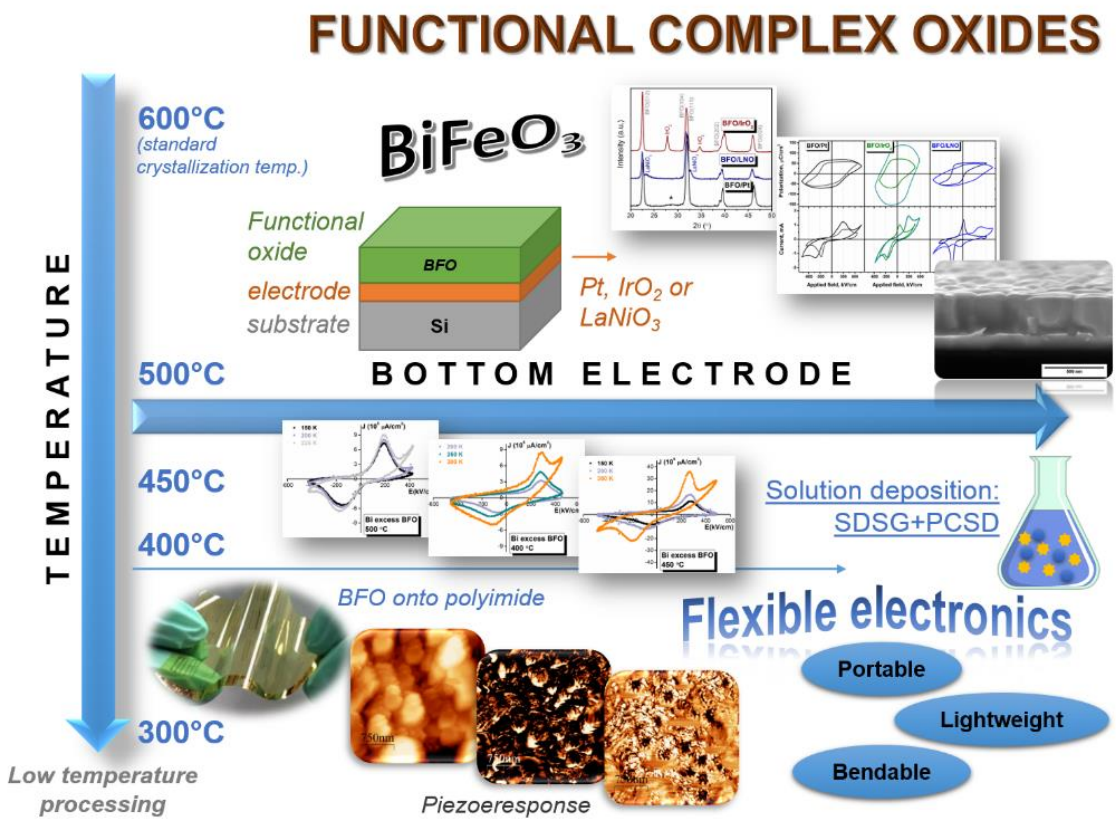

Figure 1-1. Schematic showing the motivation of the work.

1.2. Organization of the thesis

The thesis is organized as follows:

The present chapter (Chapter 1) describes the motivation and the objective of the work.

Chapter 2 provides the state of the art of the materials under investigation in the thesis. The importance of functional materials, with particular incidence on complex oxides with perovskite-like structure, ABO_3, is presented. The chapter includes a detailed review of structural, physical and chemical features of lead free ferroics as BFO and NBT, with published works on solution processed thin films. Different strategies to decrease the crystallization temperature of ferroelectric thin films are reviewed.

Chapter 3 presents the experimental methods used and implemented in the thesis: processing procedures and characterization techniques.

Chapter 4 is fully devoted to the disclosure and discussion of the achieved results. Within this chapter, five subsections correspond to the following topics: 4.1 – NBT thin films by CSD annealed at different temperatures, 4.2 – BFO thin films preparation by chemical solution deposition towards finding temperature limit of crystallization, 4.3 and 4.4 – comparative study of BFO thin films on distinct bottom electrodes: their microstructure and electrical performance, and 4.5 – strategy towards low temperature processing of BFO on flexible substrates.

And finally, chapter 5 summarizes the main observation and results obtained during the realization of this work, and draws main conclusions, highlighting the main contribution of our work.

Chapter 2. STATE OF THE ART

Abstract: The purpose of this chapter is to provide the background in which the current work was developed by presenting a review on the state of the art of the most significant aspects related with the thesis subject. Within this context it starts by emphasising the importance of functional oxides in microelectronics. Basic concepts and physical principles of relevant properties of functional materials are introduced with special focused on ferroelectricity and ferroelectric thin films preparation and applications. Some integration issues into devices are presented and the need for low temperature processing of ferroelectric thin films is highlighted. A detailed review on multiferroic $BiFeO_3$ (BFO) and ferroelectric $Na_{0.5}Bi_{0.5}TiO_3$ (NBT) is subsequently presented. The literature review covers the available information on the processing, properties and application of these compounds. The chapter further includes details on the major synthesis approaches, used to decrease the crystallization temperature of ferroelectric thin films.

2.1. Introduction to functional materials: properties and applications

Functional materials are defined as materials that possess particular properties and perform specific functions [28]. The physical and chemical properties are sensitive to a change in the environment such as temperature, pressure, electric field, magnetic field, optical wavelength, adsorbed gas molecules and the pH value. The functional materials utilize the native properties and functions of their own to achieve an intelligent action [29]. Examples include semiconductors ferroelectrics, piezoelectrics, magnetic materials, ionic conductors, *etc*. Functional materials are found in all classes of materials: ceramics, metals, polymers and organic molecules [28].

Functional ceramic materials consist of a huge group of inorganic compounds, and mainly include piezoelectric, dielectric, ferroelectric, semiconductor, superconducting, magnetic, and currently the very attractive group of multiferroic materials that shows simultaneous ferroelectric order with ferromagnetic ordering. The functional ceramic materials can be classified as [30]:

- *Electrical/magnetic* (for example *electroceramics* as their primary function is related to the electrical properties), to be used as insulators, semiconductors, conductors and magnets for capacitors, memories, data and information storage, energy conversion, *etc*.;
- *Optical*, to be used as components for lenses, lasers, fibers due to their good transparency to light with distinct wavelength;
- *Chemical*, to be used as catalysts, sensors;
- *Biological*, to be used as bioceramics, mostly for implants, and as nanomaterials in drug delivery systems.

The listed above groups with their respective examples are shown in Figure 2-2.

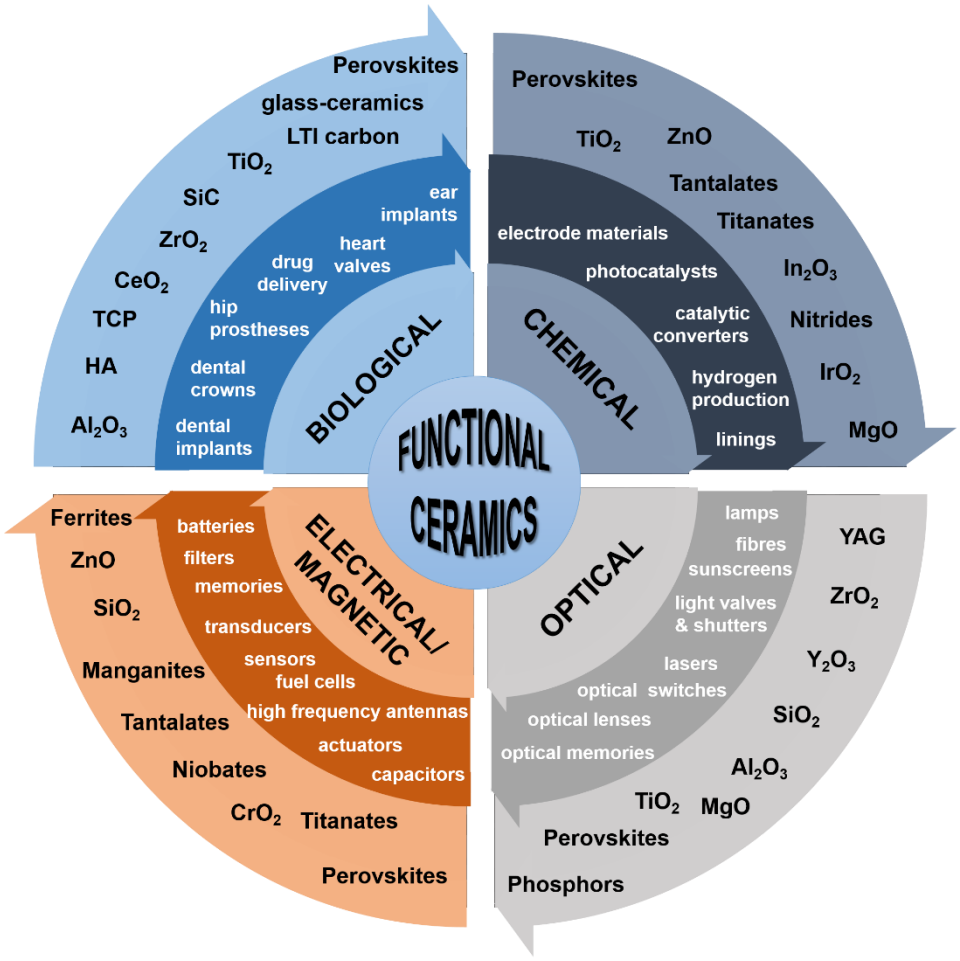

Figure 2-2. Spectrum of functional ceramic materials applications. Adopted from [30].

The dominant compositions among functional ceramic materials are oxides that offer a variety of chemical, physical, structural and microstructural features [31]. ABO_3 perovskite and perovskite related compounds are one of the dominant families of functional oxide ceramics. This is a large family of compounds having crystal structures related to the mineral perovskite $CaTiO_3$. In the ideal form the crystal structure of a cubic ABO_3 perovskite is described as a corner sharing $[BO_6]$ octahedra with the A cation occupying the 12-fold coordination site formed in the middle of the cube of eight such octahedral (Figure 2-3). The interest in perovskite – type compounds arises from the large variety of properties they exhibit and also and very importantly from the flexibility to accommodate almost all of the elements of the periodic table in the structure what permits designing materials performance adequate to applications; this constitutes a unique relevant added value of this family of

materials [32]. Perovskite materials due to their intriguing and unusual physical properties have been extensively studied for both practical applications and theoretical modelling, and many discoveries from high-temperature superconductors to the organic-inorganic semiconductors for high-efficiency photovoltaics lead to many revolutionary discoveries for new device concepts [33]. Perovskite-type ferroelectrics are indeed of great interest and show a very wide range of useful functional properties [34].

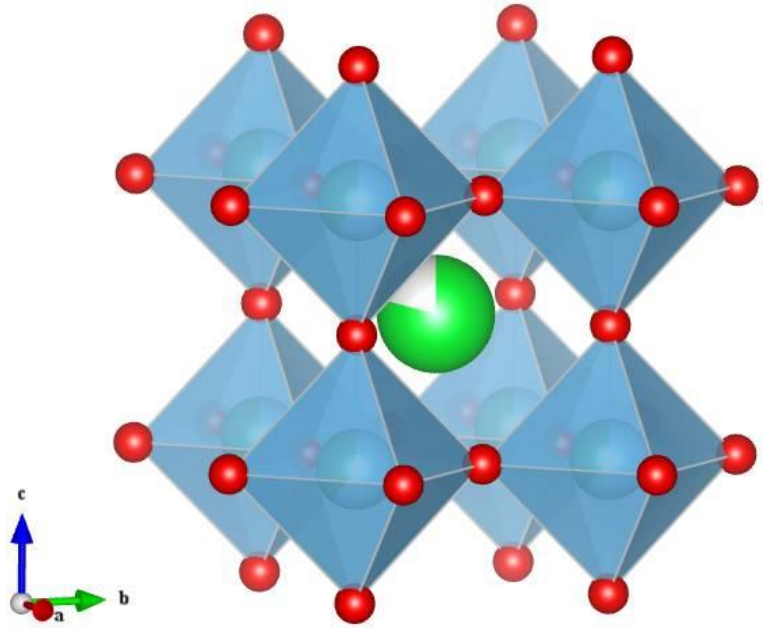

Figure 2-3. Perovskite structure with chemical formula ABO_3. The red spheres are oxygen atoms, the blue spheres are B-atoms (a smaller metal cation, such as Ti^{4+}), and the green spheres are the A-atoms (a larger metal cation, such as Ca^{2+}).

A ferroelectric perovskite has a permanent spontaneous polarisation P_S that can be switched in direction by the application of an external electric field. Ferroelectricity is a symmetry based phenomena. Low symmetry of a crystal, in particular a non-centrosymmetric crystal symmetry, is essential for the occurrence of ferroelectricity. From the 32 classes of symmetry, 11 point groups possess a centre of symmetry hence, they are nonpolar and 21 possess a non-centrosymmetric structure, hence they are polar or piezoelectric. Form these 21 non centrosymmetric 20 point groups materials show piezoelectric effect. Ten of these 20 classes possess a unique axis of symmetry (are polar) and an electric polarisation exists within the structure in the absence of an applied field. The

electric polarisation in these polar materials changes with temperature, making them pyroelectric. Ferroelectrics are a subgroup of pyroelectrics [35].

Ferroelectrics are dielectrics that exhibit spontaneous polarization below the ferroelectric Curie temperature (T_C), and the polarization direction can be changed by an applied electric field. At temperatures above T_C, the crystals are nonpolar (centrosymmetric crystal structure), and no longer ferroelectric and behave like normal dielectrics [36]. The dielectric constants of ferroelectric materials are extremely high, especially near the Curie temperature. A ferroelectric crystal consists of domains; *i.e.*, regions with uniform spontaneous polarization. The formation of ferroelectric domains is to minimize the electrostatic energy of depolarizing fields and the elastic energy that is associated with mechanical constraints to which the ferroelectric material is subjected as it is cooled through T_C temperature. The boundary of two neighbouring domains is called a domain wall. In the absence of an electrical field, the domains are randomly oriented, which result in near complete compensation of the spontaneous polarization. When an external electric field is applied, domains become oriented along the field and the polarization of the material becomes different from zero. The switching of domain orientation proceeds through domain-wall motion [37].

The most prominent feature of a ferroelectric material is the reversibility of the polarization, which results in a hysteresis loop in the dependence of polarization P on electric field E. The polarization increases linearly with the applied electric field, and when the field strength is increased the domains start to align with the direction of the applied field, giving rise to a rapid non-linear increase in the polarization up to P_S. When the external field is removed, many of the domains are still aligned, hence the material shows a remanent polarization, P_r. When the electric field with opposite direction is applied, the domain reorients accordingly, and the external field needed to reduce the polarization to zero is called the coercive field, E_C. Therefore, the (P-E) hysteresis loop is characterized by Ps, P_r, and E_C. Saturation polarization is the maximum polarization that can be reached, remanent polarization is the polarization present when no electric field is applied, and coercive field is a value of electric filed that is required to bring the polarization to zero [28].

Ferroelectric materials also exhibit piezoelectricity and pyroelectricity. Piezoelectricity is the ability to develop an electrical charge proportional to a mechanical stress or vice versa.

The polarization generated from a mechanical stress is called the direct or generator effect, while the converse or motor effect is associated with the mechanical deformation derived from an applied electric field. The relationships between the strain X, stress σ, electric field strength E, electric polarisation P in a piezoelectric material are [28]:

$$P = d \times \sigma \quad (1)$$

(direct effect)

$$X = d \times E \quad (2)$$

(converse effect)

where, d is a piezoelectric constant.

In a pyroelectric materials the change in temperature produces a change in spontaneous polarisation [28]. All ferroelectrics belong to pyroelectric and piezoelectric classes, but not vice versa [35]. Figure 2-4 illustrates the basis of piezoelectricity, pyroelectricity and ferroelectricity, as well as the classification of material groups based on the symmetry point group.

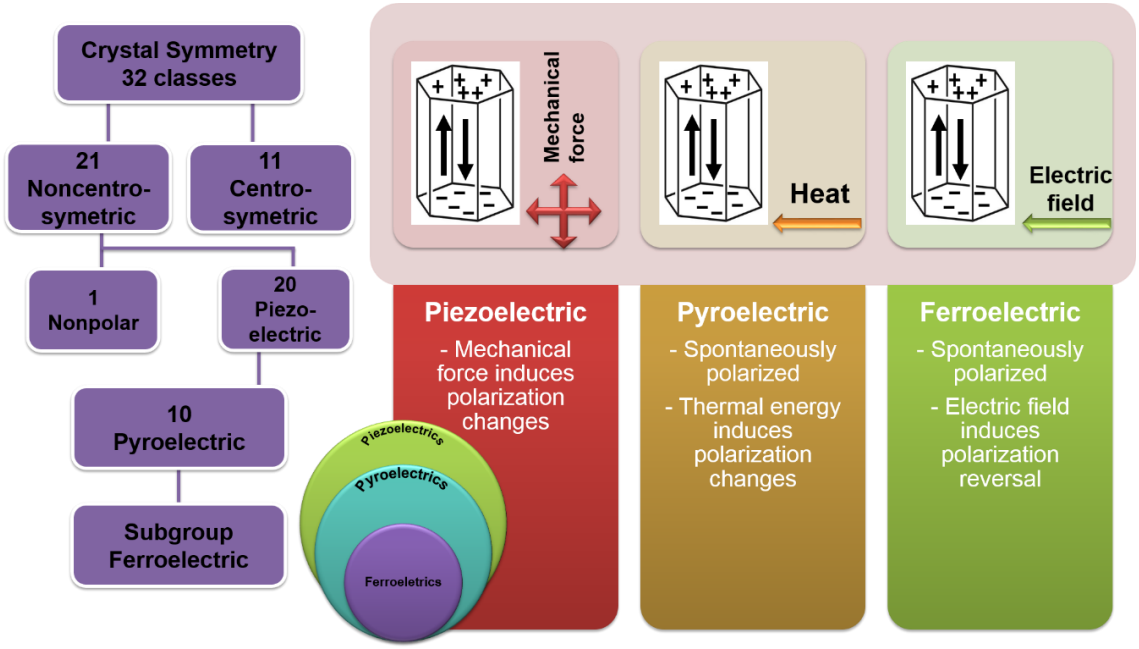

Figure 2-4. Schematic representation of piezoelectricity, pyroelectricity and ferroelectricity based on crystal symmetry and their origin. Scheme also shows that all ferroelectric materials are pyroelectric and piezoelectric but not vice versa [35].

Because of their high dielectric constant, large polarization, and piezoelectric properties, ferroelectric materials have a wide range of applications, as presented in Figure 2-5. The high dielectric constant of ferroelectrics has been utilized to produce capacitors with tunable capacitance. Pyroelectricity has been utilized for ultrasensitive infrared detectors. On the other hand, piezoelectricity has made materials applicable to high performance actuators, vibration sensors, and other devices. Among the many attractive physical properties of ferroelectric oxides, the reversible spontaneous electric polarization has attracted attention, as a medium for non-volatile data storage devices [38].

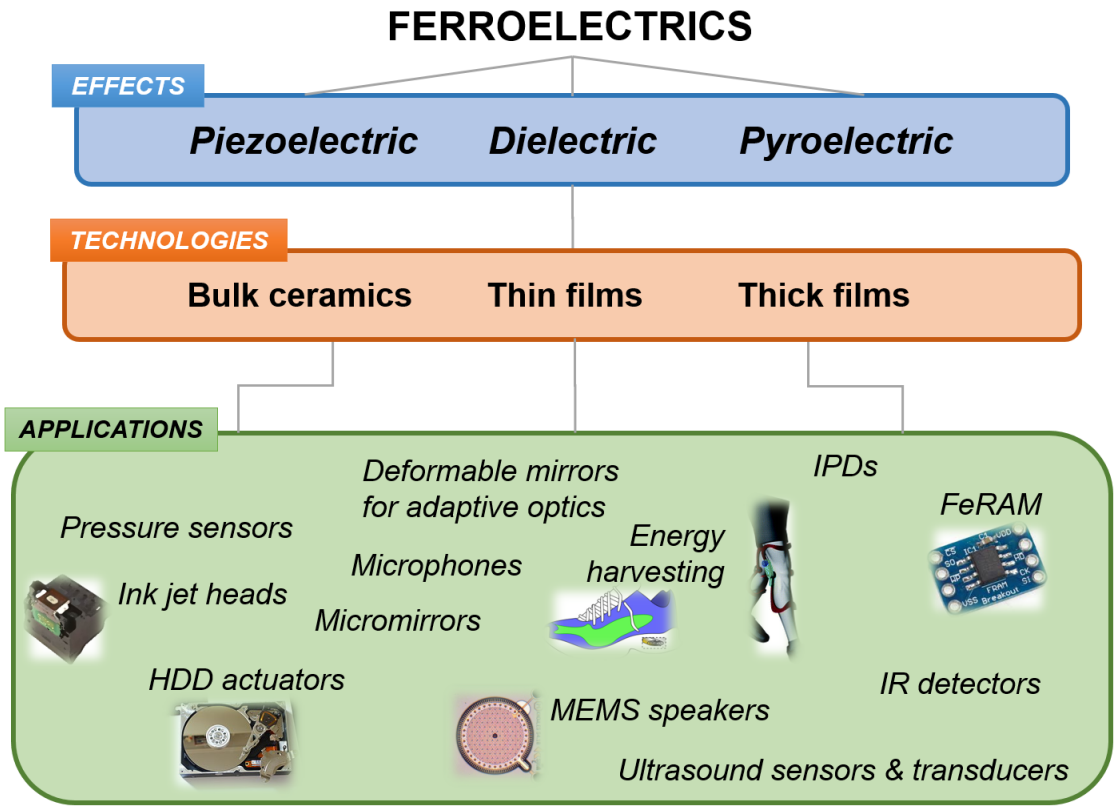

Figure 2-5. Some of the examples of applications of ferroelectric materials due to their piezoelectric, dielectric and pyroelectric properties [38]. (Thin Film PZT for Semiconductor Application Trends & Technology 2013 Report by Yole Developpement). IPD – Integrated Passives Devices, HDD – Hard Disk Drive, MEMS - MicroElectroMechanical System, FeRAM - Ferroelectric Random Access Memory, IR – Infrared.

Trend towards miniaturisation of electronic devices has been the driving force for the reduction of the size of the ferroelectric material. Especially in the form of thin films, ferroelectrics promise cost effective devices with an important functionality, high performance and a low energy consumption. Typical device examples include thin films for non-volatile ferroelectric random access memories (FeRAM), microactuators, microwave phase shifters, infrared sensors and ferroelectric memristors. Very recent review on thin film ferroelectric materials and their applications discusses several exciting possibilities for the development of new devices, including those in electronic, thermal and photovoltaic applications, and transduction sensors and actuators [39]. Currently the fabrication of those devices involves the integration of the ferroelectric thin film with the Complementary Metal Oxide Semiconductor (CMOS) Integrated Circuit (IC). Therefore, the technologies for fabricating ferroelectric films on silicon have developed rapidly during last years. Figure 2-6 summarizes the most important thin films deposition techniques.

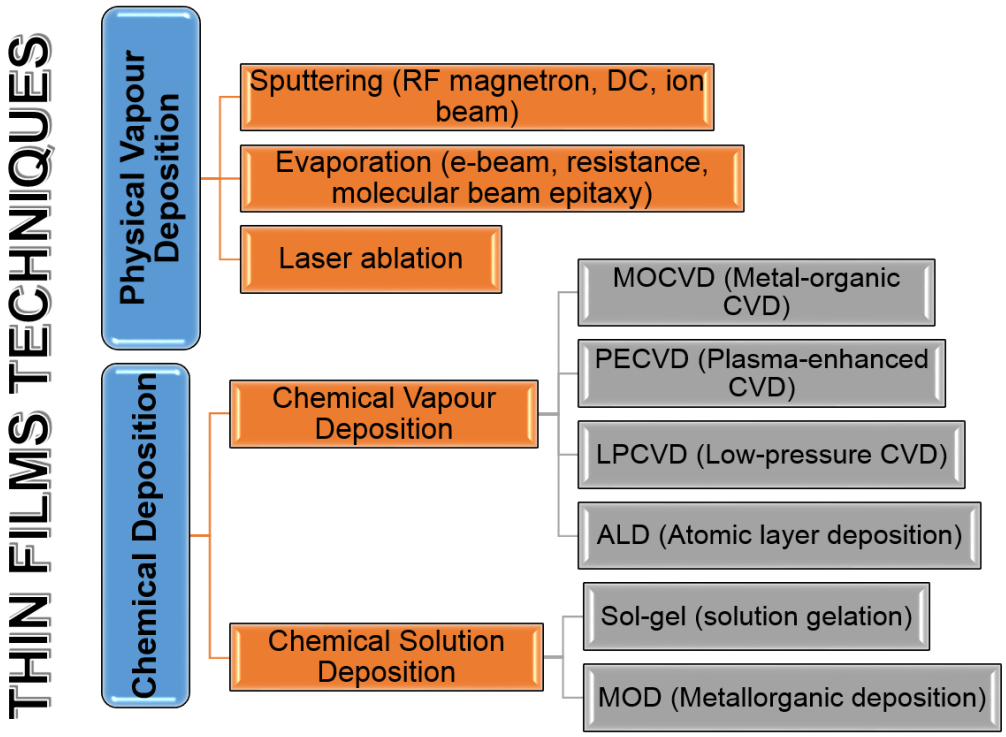

Figure 2-6. Thin film deposition techniques. Adapted from Haertling [40].

Film fabrication techniques can be divided into two general classes: physical vapour deposition (PVD) techniques and chemical deposition techniques, this including chemical vapour deposition (CVD) and chemical solution deposition (CSD).

In the former, atoms from a source are transferred in a continuous and controlled manner under a vacuum atmosphere (>10^{-5} Torr) to the substrate, in which the nucleation and growth of the film occurs atomistically. Depending on how the particles (atoms or ions) are removed from the target, the following PVD techniques are considered: Radio frequency (RF) sputtering, ion beam sputtering, electron beam evaporation and laser ablation, among others. The former allows for careful control of film thickness and orientation, and compatibility with the semiconductor integrated circuit processing. The difficulty in controlling the stoichiometry of multicomponent films, the slow rates of deposition (normally around 1 Å/s), the need for high-temperature post-deposition crystallization annealing and the high cost related with equipment acquisition and maintenance are the main disadvantages of these methods [41].

Chemical methods allow higher deposition rates, good stoichiometry control, and the production of large area defect- free films when compared with the previous ones. CVD is very attractive for industrial manufacturing of conformal functional films. However, the expensive equipment, limited availability and toxicity of sources of precursors for functional materials restrict the use of this technology. On the other hand, CSD methods, especially sol-gel, have been increasingly used for the preparation of films of functional materials. CSD techniques do not require vacuum ambience, are cheaper and faster, allow for a good stoichiometry control and production of large area defect-free films with good properties, although the texture degree of the film is inferior to that of films prepared by PVD. Wet processes include sol-gel, metallorganic decomposition (MOD), electrochemical reaction and hydrothermal routes [42-46].

2.2. Lead free ferroelectrics

Nowadays, among a number of perovskite systems, there is a demand to explore novel compounds, or engineer already existing compositions, in order for example to prevent the use of lead based systems, typified by $Pb(Zr, Ti)O_3$ [47]. $Pb(Zr_{1-x}Ti_x)O_3$ based compositions lying near the morphotropic phase boundary (MPB, $PbZr_{0.52}Ti_{0.48}O_3$) have been the leader materials for modern sensors, actuators and transducers applications due to their superior dielectric, piezoelectric and electromechanical coupling coefficients.

On the downside PZT contains more than 60 %wt of the element lead. International efforts in drastically reducing the use of toxic substances from everyday applications are increasing. The EU passed the Waste Electrical and Electronic Equipment (WEEE) and Restriction of the use of certain Hazardous Substances in electrical and electronic equipment (RoHS) in 2003. The RoHS directive took effect in 2006 and it restricts the use of six hazardous materials, what includes lead, in the manufacture of various types of electronic and electrical equipment. Currently, an exemption is made for piezoelectrics, because known lead free piezoceramics are not yet good enough to replace lead containing materials.

It is, therefore, desirable and of the utmost importance to find alternatives to the currently market-dominating lead containing piezoelectrics and ferroelectrics in all current or future applications. Perovskite-type ferroelectrics as $BaTiO_3$ (BT), NBT, $K_{0.5}Na_{0.5}NbO_3$ (KNN), $KNbO_3$, BFO, among others, are well-known lead-free piezoelectric/ferroelectric materials [48]. Figure 2-7 compares the remanent polarization and Curie temperature for compositions among these families. It is obvious when contrasting the ferroelectric properties of those compositions, BFO stands clearly out holding the largest remanent polarization (60 $\mu C/cm^2$) values and high Curie temperature (~830 °C) among the lead free compositions. The Curie temperature plays an important role from the industrial point of view since it limits applications of ferroelectric materials above T_C. Above the T_C, the ferroelectric material loses the P_S and the ferroelectric state. Thus, the working temperature of devices made of ferroelectric materials is limited by the T_C. This by itself clearly demonstrates the attractiveness from the application point of view in this material. In addition and adding value to its performance, as said before, BFO exhibits multiferroism what indeed justifies the high interest from both the academic and industrial community in

this material. Indeed BFO is a multiferroic material with multifunctional properties such as conductive domain walls, a strain-driven MPB, a bandgap (~2.7 eV) in the visible range, large birefringence (0.25-0.3), a strong photovoltaic effect and sizeable linear electro-optic coefficients [49].

Figure 2-7 also reveals that among the lead free materials families NBT possesses relatively high T_C, together with relative high P_r. NBT ceramics exhibit good ferroelectric (P_r = 38 μC/cm^2 and Ec = 75 kV/cm) and piezoelectric properties (d_{33} = 102 pC/N) [50].

Therefore, BFO and NBT were selected to be studied in this work.

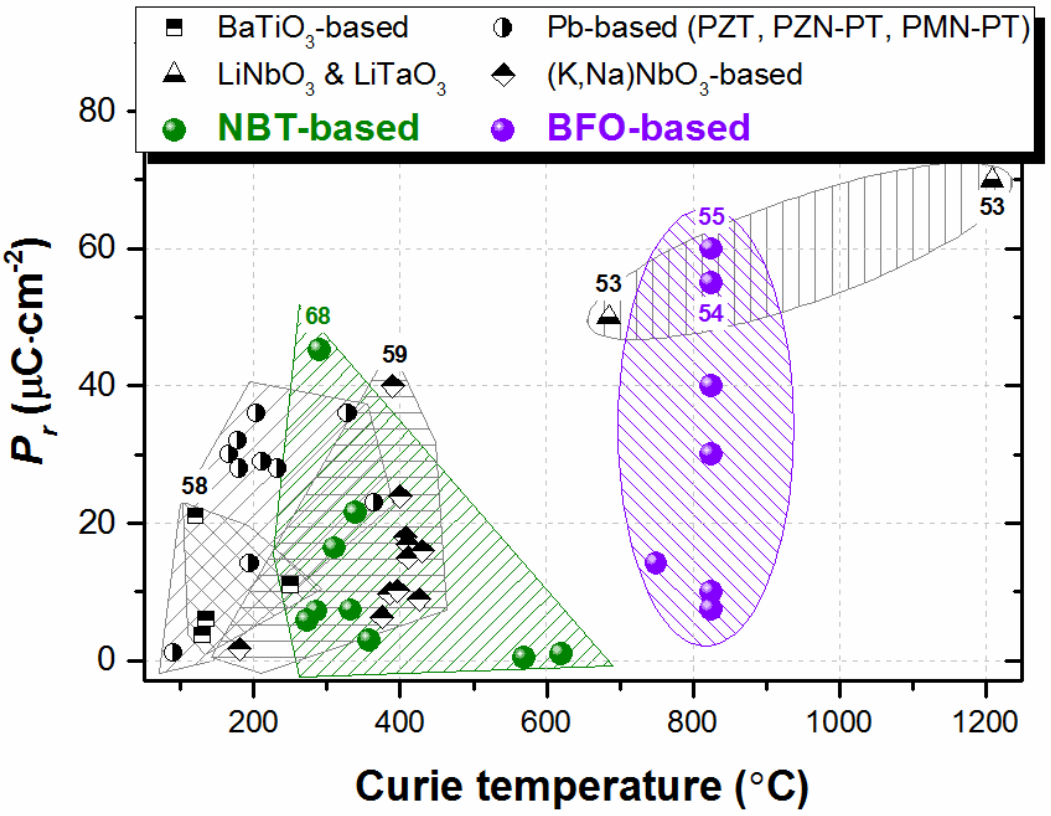

Figure 2-7. Relationship between the Curie Temperature (T_C) and remanent polarization (P_r) for selected groups of lead-based and lead-free ferroelectric materials (with selected references embedded) [40, 51-73]. In particular, BFO possesses high T_C and P_r, thus it can be implemented in devices working at high temperatures.

Hereafter we describe the main known characteristics for the two lead-free compositions (BFO and NBT) studied in the present thesis.

2.2.1. Bismuth ferrite – $BiFeO_3$

Complex oxides represent a giant class of materials including an extensive range of crystal structures and functionalities. Among these interesting properties and aiming at optimized responses, magnetic, ferroelectric, and, more recently, multiferroic properties in these oxide materials have driven significant interest and research.

According to the definition proposed by Hans Schmid multiferroics are "materials, in which two or all three of the properties *ferroelectricity*, *ferromagnetism* and *ferroelasticity* occur simultaneously in the same phase" [74]. Nowadays, multiferroism often refers to any combination of ferroelectric order and magnetic order (both ferromagnetism and antiferromagnetism) as well as, the so called ferrotoroidic order [75]. As presented in Figure 2-8 only a small subgroup of all magnetically and electrically polarizable materials are either ferromagnetic or ferroelectric and fewer simultaneously exhibit both order parameters. In materials called magnetoelectrics electric fields cannot only reorient the polarization but also control magnetization; similarly, a magnetic field can change electric polarization. Magnetoelectricity is an independent phenomenon that can arise in any material with both magnetic and electronic polarizability, regardless of whether it is multiferroic or not.

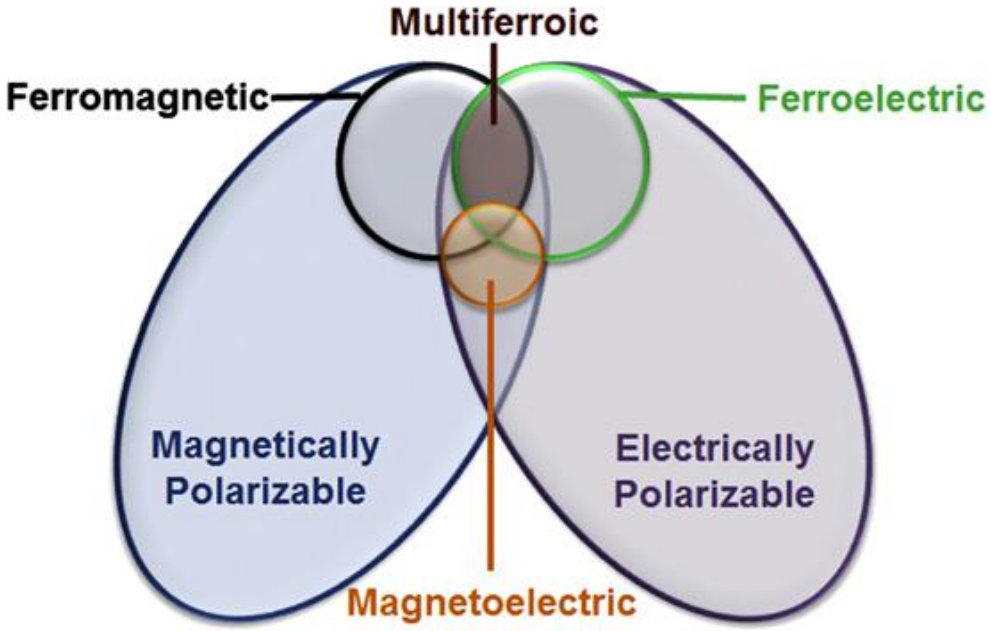

Figure 2-8. The relationship between multiferroic and magnetoelectric materials [76].

Among single phase multiferroics BFO stands out due to its true multiferroic nature and above room temperature. Therefore, BFO is a prime candidate for a number of potentially important applications, as memories, sensors, micro-electro-mechanical systems (MEMS) and spintronics [18]. The optical bandgap of BFO of 2.2-2.8 eV is interesting for applications utilizing photoconductivity (as sensors), the photovoltaic effect or the photocatalytic properties; BFO nanoparticles have been proposed as photocatalysts [77-79].

The state-of-the-art experiments on BFO have been carried out on single-crystals or epitaxial thin films fabricated on single crystal substrates. Such an approach is indeed too expensive to be used in practical applications, as for consumer electronics. Fundamental physical questions and exciting device concepts have been explored using BFO fabricated via sophisticated physical vapor deposition methods, however these are indeed inappropriate for mass production. Therefore, preparation methods that allow the fabrication of thin films and nanostructures at low cost and low temperature are of high interest. As mentioned above, chemical solution deposition offers a number of advantages, including comparatively low capital investment costs, good homogeneity and thickness uniformity over a large area, enhanced compositional control and ability to be scaled-up for massive production [80]. Although some progress has been achieved in the preparation of thin films by chemical solution deposition, more efforts have to be made in order to obtain BFO films with robust functional properties and also able to meet the current needs of the microelectronics as functionality and flexibility.

2.2.1.1. The structures of bismuth ferrite

The room temperature phase of BFO has a rhombohedrally distorted perovskite structure with *R3c* space group [81]. The unit cell of BFO can be described by pseudo-cubic, rhombohedral or hexagonal settings, where (111)pc || (111)rh || (001)hex [20, 81, 82], as presented in Figure 2-9. The lattice constants determined by X-ray diffraction are: a_c = 3.965 Å, α_c = 89.35° for the pseudo-cubic unit cell, a_{rh} = 5.6343 Å and α_{rh} = 59.348° in the rhombohedral unit cell, and a_{hex} = 5.578 Å and c_{hex} = 13.868 Å for the hexagonal unit cell [81]. In the cubic perovskite structure (Figure 2-9 c), the two distorted oxygen octahedral of the cells connected along the (111)pc are rotated clockwise and anti-clockwise around this direction by ~13.8°, and Fe ions are shifted by 0.135 Å along the same axis.

The structure of BFO is very flexible, and can be easily modified by many factors, such as strain and composition modification by doping. The crystal structure of epitaxial BFO films can be tuned by the strain induced using different substrates: monoclinic, tetragonal, rhombohedral, orthorhombic, and triclinic [83]. Detailed information about distinct phases in epitaxial BFO films can be found elsewhere [84].

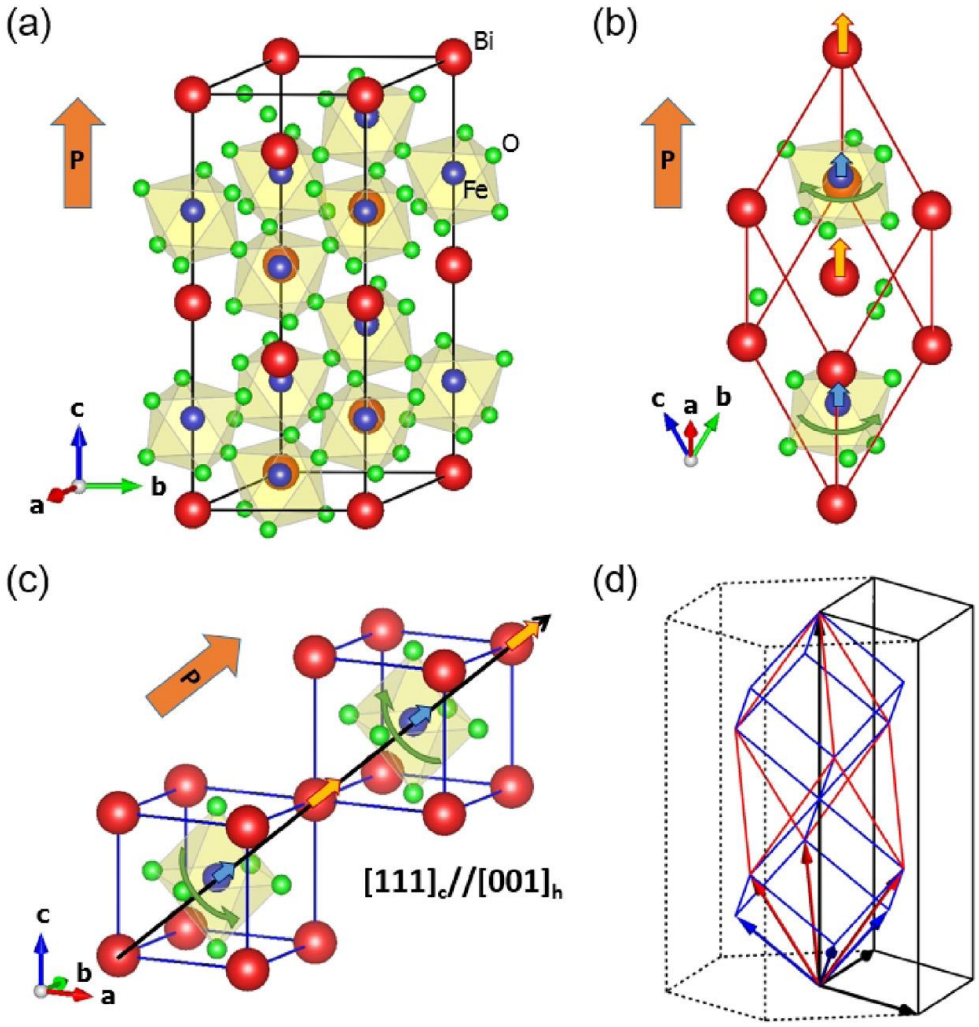

Figure 2-9. BFO crystal structure representations: (a) hexagonal unit cell (six formula units), (b) rhombohedral unit cell (two formula units), and (c) pseudo-cubic unit cell (one formula unit). Red balls represent the Bi ions, blue ones the Fe ions and green the O ions. Yellow/blue/green arrows symbolize a shift of the Bi/Fe cations and the octahedral rotation, respectively. (d) Unit vectors and unit cell in the hexagonal (black), rhombohedral (red), and pseudocubic (blue) notations [82].

BFO shows spontaneous polarization along one of the eight pseudo-cubic (111)pc axes. The analysis by Ravindran and co-workers showed that the Bi^{3+} $6s^2$ lone-pair electrons is responsible for displacements of the Bi atoms from the centrosymmetric to the non-centrosymmetric structure, and hence the ferroelectricity [85]. A high Curie temperature of ~1100 K was established [86].

During the 1980s, the magnetic structure of BFO was studied in detail by Sosnowska *et al*. [87, 88]. The studies indicated that BFO is a G-type antiferromagnet with a Néel temperature of ~643 K. The magnetic moments can be described as a cycloid with modulation of period length ~64 nm (Figure 2-10) [89]. This spin structure was found to be incommensurate with the structural lattice and was superimposed on the antiferromagnetic order [88]. This spiral spin structure leads to a cancellation of any macroscopic magnetization and also inhibits the observation of the linear magnetoelectric effect. However, if the magnetic moments are oriented perpendicular to the (111) direction, the symmetry also permits a canting of the antiferromagnetic sublattices resulting in a macroscopic magnetization, so-called weak ferromagnetism, the Dzyaloshinskii-Moriya type [90].

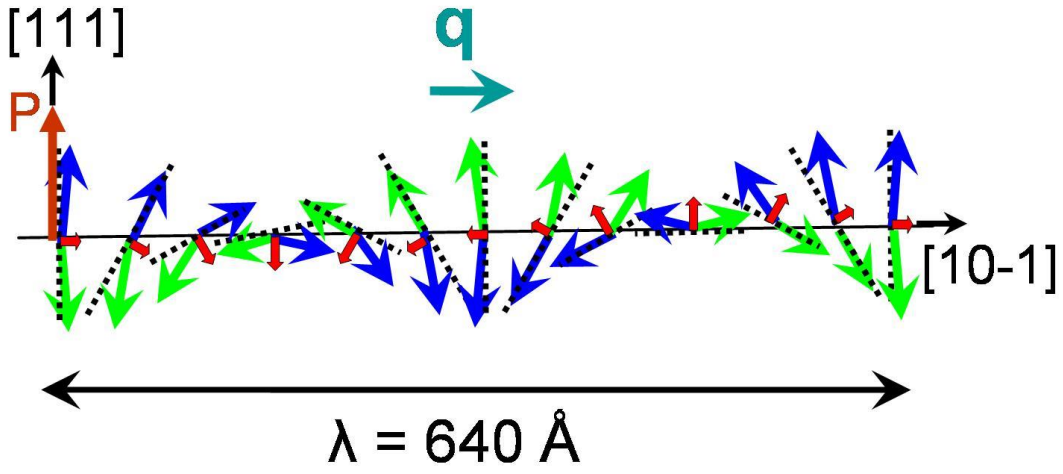

Figure 2-10. Scheme of the antiferromagnetic structure of BFO, the magnetic moments describe a cycloid with a period of 64 nm [89].

2.2.1.2. Physical properties of $BiFeO_3$

First measurements of ferroelectric hysteresis in single crystals of BFO have been reported by Teague *et al.* [91]. They found a spontaneous polarization of 3.5 μC/cm^2 in fields of 55 kV/cm along the (001)pc direction at liquid helium temperature. At room temperature the samples were too conductive to allow the hysteresis experiments.

Later on, Wang *et al.* [54] reported ferroelectric hysteretic behavior in epitaxial thin films with a remanent polarization of 55 μC/cm^2 under electric field of 500 kV/cm. The exceptionally large polarization of those films was initially thought to be due to strain enhancement [54, 92]. However, the large remanent polarization measured in thin films has been confirmed by hysteresis loop measurements on good quality single crystals. Lebeugle *et al.* [55] determined a ferroelectric hysteresis response in a 40 μm thick single crystals along the hexagonal (012) axis (corresponding to the (001)pc direction) in fields of 125 kV/cm. The saturation polarization was 60 μC/cm^2 and the $E_C \sim 12$ kV/cm (~100 μC/cm^2 in the (111)pc direction). The crystallographic orientation of the films has significant effect on the physical properties of BFO. The out-of-plane P_r for (111), (101), and (001) $BiFeO_3$ films were measured by Li *et al.* [93], and were found to be $P_{111} \approx 100$ μC/cm^2, $P_{101} \approx 80$ μC/cm^2, and $P_{001} \approx 55$ μC/cm^2. Figure 2-11 shows $P_{111} \approx \sqrt{2}\, P_{101} \approx \sqrt{3}\, P_{001}$ as a function of E for the variously oriented films. In this figure, the values of the projected polarizations can be seen to be nearly equivalent. This reveals that the direction of spontaneous polarization lies close to (111)pc, and that the values measured along (110)pc and (001)pc are simply projections onto these orientations.

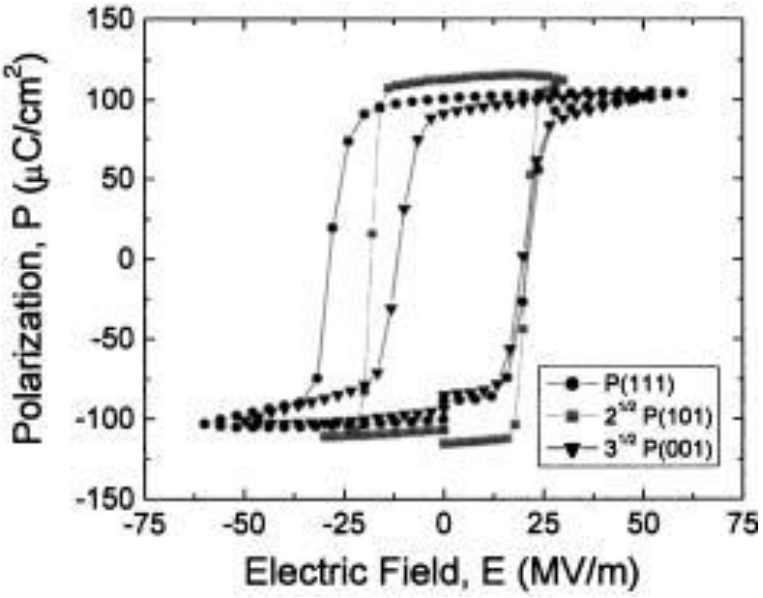

Figure 2-11. P–E response for BFO epitaxial thin layers grown on (001)pc, (110)pc, and (111)pc $SrTiO_3$ substrates by pulsed laser deposition, projected onto (111) [93].

Polycrystalline BFO thin films show higher coercive field and leakage current density in comparison to epitaxial BFO films. Generally, it is believed that the leakage current may arise from microstructure, impure phase, formation of defects and chemical fluctuation, which are associated with oxygen vacancies caused by the coexistence of Fe^{2+} ions and volatilization of Bi^{3+} ions in BFO films [94]. For improvement in electrical properties, ion substitution is one of the most common approaches for BFO thin films and bulk ceramic, including substitutions at either Bi or Fe or both sites. It is now well known that the ion substitution for Bi site can modify the ferroelectric properties by decreasing oxygen vacancy concentration and therefore decreasing the leakage current. On the contrary, the transition metal elements are mainly substituted for the Fe site and they are used to suppress the valence fluctuation of Fe ions, by which decrease in the leakage current can be expected [95]. Figure 2-12 shows *P–E* characteristics of undoped, 5 at%, and 10 at% Mn-substituted BFO films derived by CSD and measured at RT at a frequency of 1 kHz [96]. The hysteresis loops in the undoped and 10 at%-Mn-substituted films are rounded in shape and thus it is difficult to determine the exact values of the P_r, because of the large leakage current component. On the other hand, well saturated hysteresis loops are obtained in the 5 at% Mn-substituted BFO

film, with P_r of 100 μC/cm^2 and E_C of 330 kV/cm. More impurity substitution effects in BFO films are reviewed by Ishiwara [95].

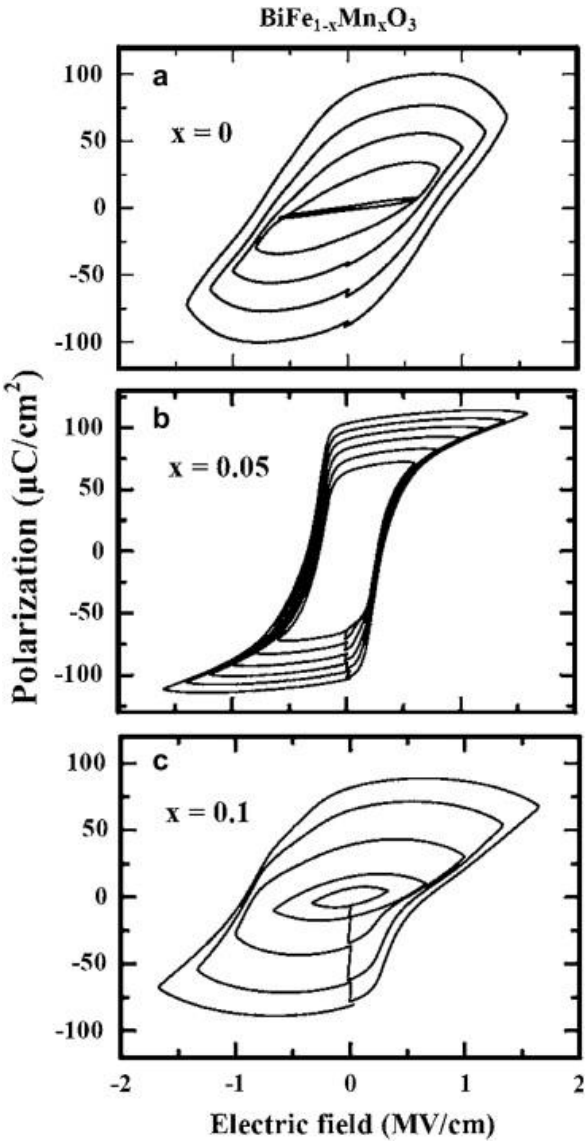

Figure 2-12. P–E hysteresis loops of (a) BFO, (b) $BiFe_{0.95}Mn_{0.05}O_3$, and (c) $BiFe_{0.9}Mn_{0.1}O_3$ films on Pt/Ti/SiO_2/Si substrates [96].

In rhombohedral BFO, the ferroelectric polarization can point along any of the four diagonals of the perovskite unit cell with two antiparallel polarities for each direction; hence, there are eight different polar domains in BFO. Accordingly, there are three possible types of boundaries separating the domain regions: 71°, 109° and 180° domain walls [97]. Seidel *et al*. have reported that certain ferroelectric domain walls of BFO are much more

conductive than the domains themselves, which is called domain-wall conductivity [98]. The origin of electronic conductivity in domain walls in BFO has been attributed to either vacancy aggregation dipole at the wall or local band gap lowering due to a significant distortion of the rhombohedral symmetry of the BFO unit cell at the domain wall [98]. It is also suggested that the conductivity of the walls is directly related to the type of domains they separate. Consequently, 180° walls are the most conductive, followed by 109° walls, and finally the 71° ones. The recent discovery of enhanced/reduced conductance at domain walls in PZT films and $LiNbO_3$ single crystals suggests that the domain wall conductivity is universal in ferroelectrics [99, 100].

The temperature dependence of the dielectric constant (ε_r) from room temperature up to >1000 K at microwave frequencies were measured in bulk BFO by Krainik *et al.* [101]. The ε_r linearly increases from a room temperature, ~45, to ~150 at 1150 K, and the dielectric loss remained almost constant, $\tan\delta = 0.09$. A number of dielectric measurements have been performed on ceramics and thin films, revealing that the intrinsic dielectric constants scatter from 50 to 300 at room temperature. Recent dielectric measurements on single crystals and ceramics showed a number of anomalies close to 50, 140 and 200 K (Figure 2-13), assigned to structural or magnetic (spin glass and spin reorientation) phase transitions [102].

Piezoelectric constant of BFO is relatively low (between 15-60 pC/N) [18]. However, in epitaxial BFO thin films with strain induced morphotropic phase boundary (mixed rhombohedral and tetragonal structure), enhanced piezoelectric responses were achieved with a d_{33} value of ~120 pC/N and associated strains of the order of 2 % [103]. Moreover, in solid solution of BFO and BTO ceramics much higher piezoelectric constant was obtained, ~240 pC/N [104].

BFO is a semiconductor with a moderate room-temperature band gap in the visible range. The band gap was calculated to be indirect; however most experiments evidence a direct gap with a band edge at ~440 nm [105, 106]. In semiconductor physics, band gap is called direct if the momentum of electrons and holes is the same in both the conduction band and the valence band (an electron can directly emit a photon). In an indirect gap, a photon cannot be emitted because the electron must pass through an intermediate state and transfer momentum to the crystal lattice [107]. The complex refractive index (~3.65 at ~420 nm [105]) of BFO thin films shows a real part that is quite high for ferroelectrics, while

the imaginary part is negligible for wavelengths above ~600 nm, indicating that absorption is very low in the IR region [97]. This characteristic makes BFO a good candidate for advanced photonic devices such as electro-optical modulators. BFO exhibits a bulk photovoltaic effect, thus the light-induced charge carriers are driven by the intrinsic electric field caused by the non-centrosymmetry of the crystal lattice. Photocurrent density of ~7.5 μA/cm^2 with green light (532 nm) was reported [79].

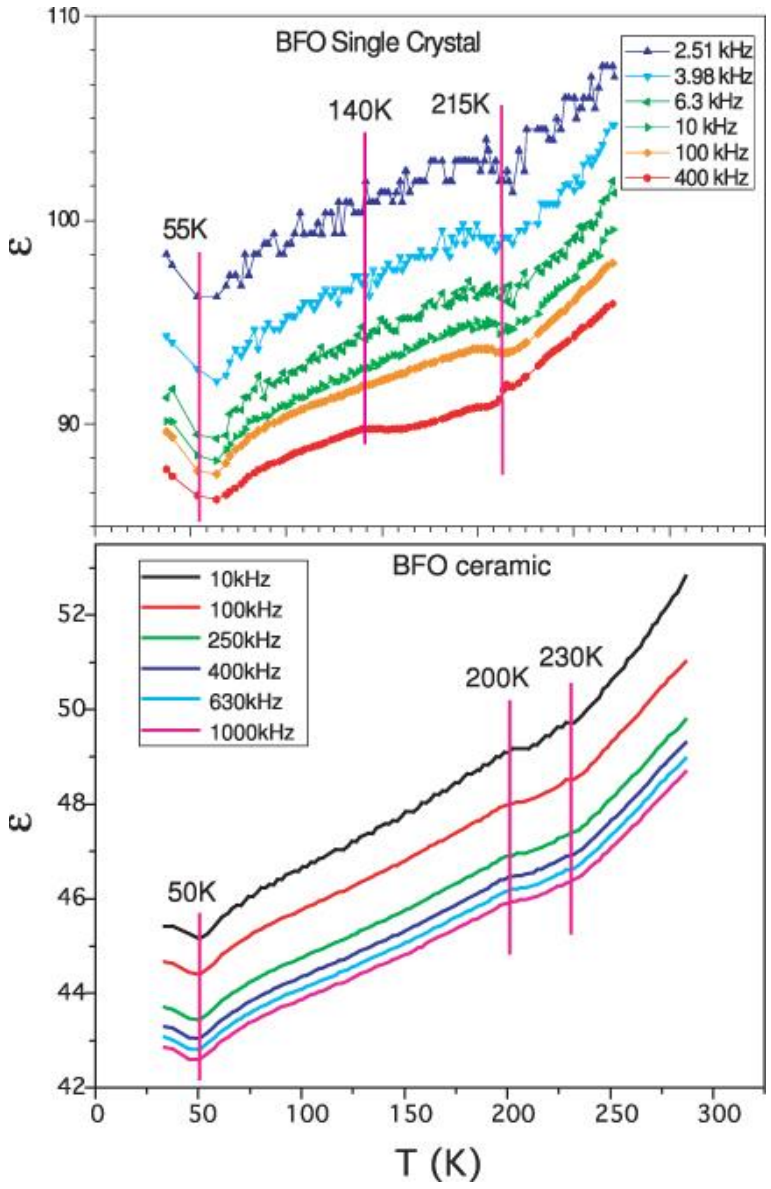

Figure 2-13. Dielectric constant of single crystal and bulk ceramic BFO at low temperatures. A small anomaly at 140 K can be seen in the single crystal data at the highest frequency [102].

Magnetic measurements revealed that BFO single crystals with a size bigger than the spin cycloid wavelength, *i.e.* 64 nm have a pure antiferromagnetic response [55]. However, this spin cycloid structure can be perturbed leading to a ferromagnetic response, by using different strategies: (i) application of of high magnetic fields, in bulk crystals; (ii) imposing epitaxial constraints, in thin layers; and (iii) local orthorhombic distortions induced by rare-earth substitution, $Bi_{1-x}R_xFeO_3$(R =La, Gd, Dy) [108]. Figure 2-14 depicts improved magnetic properties of epitaxial BFO films in comparison with bulk single crystal [109]. Enhanced magnetic properties were also reported for BFO nanoparticles and it was attributed to increased suppression of the antiferromagnetic spiral spin structure (period length of ~62 nm) with decreasing nanoparticle size and uncompensated spins and strain anisotropies at surface of those BFO nanoparticles [110].

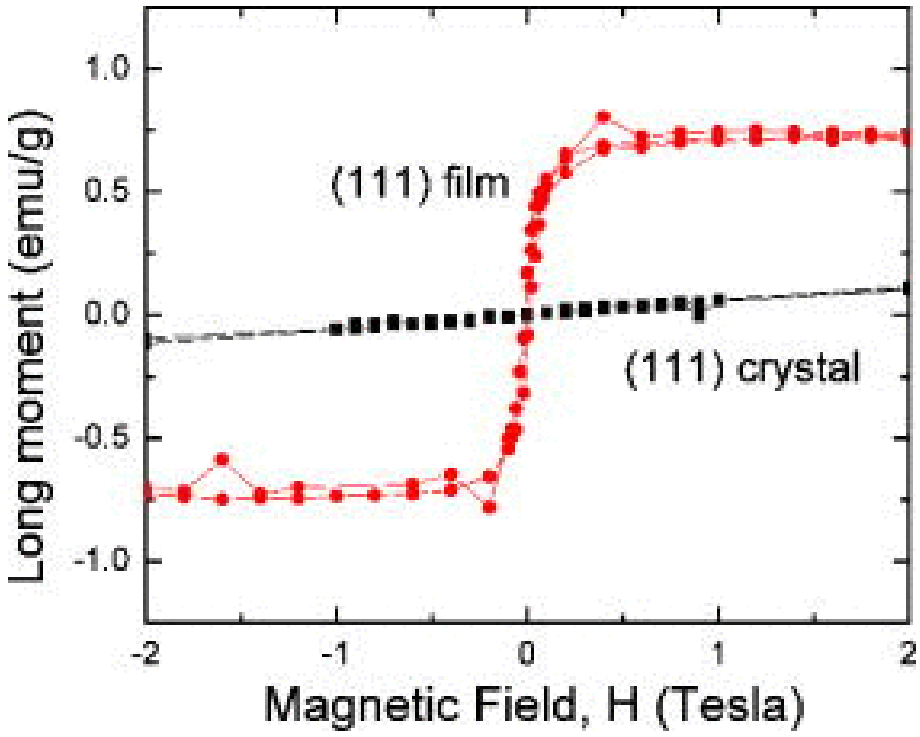

Figure 2-14. Magnetization properties for (111)c BFO films grown on (111) $SrTiO_3$ and corresponding single crystal [109].

The coupling of magnetic and electric subsystems is manifested in BFO by magnetoelectric effect. The magnetoelectric effect offers exciting possibilities for the use of multiferroics in new types of magnetic memory (*e.g.* read only memory, ROM). The magnetoelectric effect could also potentially be used to create high-precision equipment for

working with radiation in the microwave range, and to wirelessly transmit power to miniaturized electronic devices [111]. Due to the spin cycloid structure, the volume average of the linear magnetoelectric effect equals to zero in BFO. Therefore, firstly only the quadratic magnetoelectric effect had been observed in BFO single crystals, and the value found for the obtained magnetoelectric susceptibility tensor elements was of the order of 10^{-19} s/A [112]. The spin cycloid structure of BFO can be destroyed and the linear magnetoelectric effect can be recovered by applying an external magnetic field of a large magnitude and mechanical stress. Latest studies reported the value of the linear magnetoelectric coefficient of ~4.2 V/cm·Oe in BFO films [113]. Very recently, Popkov *et al* developed a theoretical justification for the occurrence of the linear magnetoelectric effect based on the Ginzburg-Landau theory, supporting the previously reported large experimental value of the effect. They also showed that the magnetoelectric effect could be enhanced in the presence of an electrostatic field [111]. They demonstrated that the antiphase oxygen octahedra rotation is responsible for occurrence of magnetoelectricity in BFO.

2.2.1.3. Device applications

The multifunctional character of BFO offers opportunities to design a wide variety of devices exploiting a single functionality (ferroelectricity, piezoelectric response, *etc*.) or the interaction between multiple functionalities (for instance through the magnetoelectric effect). As a case study BFO based non-commercialized non-volatile memories are presented in the following section.

2.2.1.3.1. Ferroelectric random access memories

Ferroelectric random access memory (FeRAM) devices are non-volatile memories that uses a ferroelectric film in the memory cell by associating "1" and "0" data states with the spontaneous polarization direction of the ferroelectric material. Commercial available FeRAMs were for example Fujitsu 64 Kb made of lead free material, PZT-based FeRAM fabricated by Samsung (64 Mb), and 32 Mb FeRAM by Matsushita made from strontium bismuth tantalate ($SrBi_2Ta_2O_9$, SBT). FeRAM is the new generation of non-volatile memory,

consumes less power, and offers higher speed and endurance to multiple read-and-write operations. FeRAMs are used in a variety of applications including smart cards, radio-frequency identification tags (RFID), security and many other applications that require high-performance non-volatile memory.

Fujitsu has announced in 2006 the development of 65 nm FeRAMs using an Mn-doped BFO thin-film capacitors [114]. The P_r of Mn-doped BFO is very large, ~100 μC/cm^2, along the polar [111] direction, being much larger than the polarization of the most widely used material in ferroelectric memories, like Pb(Zr, Ti)O_3 (Figure 2-15). Mn-doped BFO shows a square-shaped hysteresis at room temperature, and stable operation, as reported 1 year later by the company [115].

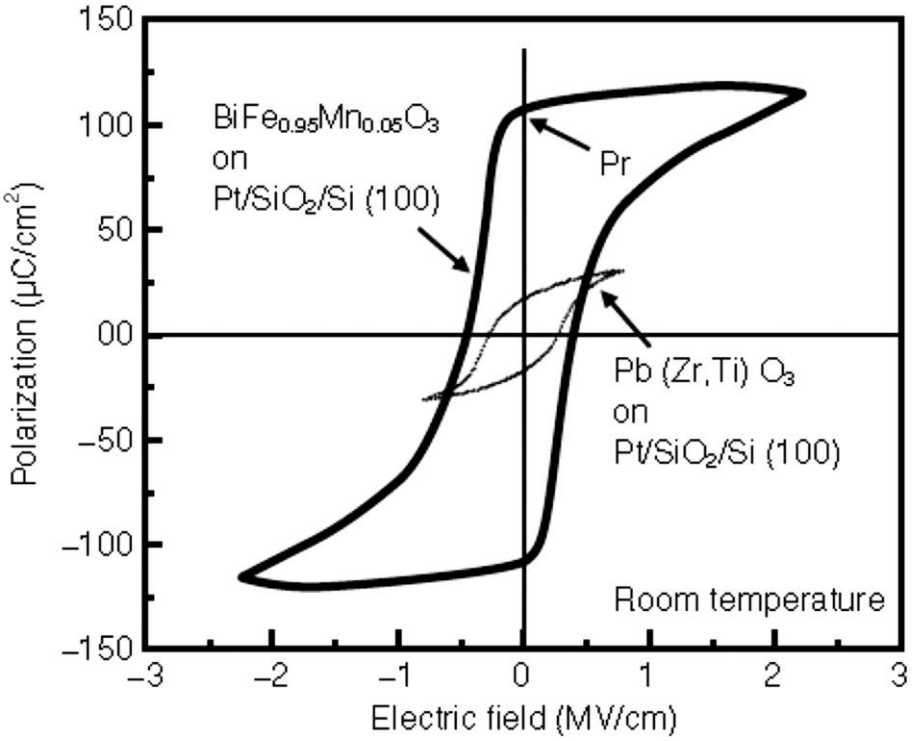

Figure 2-15. Hysteresis loop of Mn-doped BFO and Pb(Zr, Ti)O_3 thin films grown on platinized silicon substrates by chemical solution deposition. The remnant polarization of BFO is very large, ~100 μC/cm^2, along the polar [111] direction - much larger than the polarization of the most widely used material in ferroelectric memories, as PZT or SBT [115].

For commercialization of FeRAMs using BFO films, however, some important problems must be solved [115]:

- its high conductivity (and thus also dielectric losses) must be reduced;
- high coercive electric field must be reduced;
- passivation film must be selected to prevent Fe diffusion. Fe is considered an undesirable in the silicon process, because it rapidly diffuses into silicon substrates. Therefore, ferroelectric oxide layers are covered with passivation films for protection;
- low temperature deposition method compatible with microelectronic technology must be adopted.

2.2.1.3.2. Magnetoelectric and multiferroic memories

BFO is a prime candidate for magnetoelectric memories, where bits can be written by an electric field, utilizing the ferroelectric polarization, and read from the associated magnetic field. A possible Magnetoelectric Random Access Memory (MERAM) element using BFO is shown in Figure 2-16. Bibes *et al.* proposed to use the interfacial exchange bias coupling between the antiferromagnetic phase of the multiferroic and a magnetic soft layer in order to induce the magnetization reversal and the two-resistance state of the MRAM element [116]. The binary information is stored by the magnetization direction of the bottom ferromagnetic layer (blue), read by the resistance of the magnetic trilayer, and written by applying a voltage across the multiferroic ferroelectric–antiferromagnetic layer (FE-AFM being BFO; green). If the magnetization of the bottom ferromagnetic layer is coupled to the spins in the multiferroic (small white arrows), and if the magnetoelectric coupling is strong enough, reversing the ferroelectric polarization *P* in the multiferroic changes the magnetic configuration in the trilayer from parallel to antiparallel, and the resistance from *Rp* to antiparallel (*Rap*). A hysteretic dependence of the device resistance with voltage is achieved (blue curve).

A voltage (*V*) controls the ferroelectric state of BFO, which then can change the antiferromagnetic planes, and thereby reorient the direction of the lower ferromagnetic layer (FM, blue colour in Figure 2-16) [116]. The ferromagnetic layers can thus be controlled to be parallel or antiparallel by the ferroelectric state of the BFO layer. These FM layers give a

lower resistance across the FM-Metal-FM trilayer, corresponding to the binary state "0". The antiparallel alignment of the ferromagnetic layers gives a higher resistance, corresponding to the binary state "1".

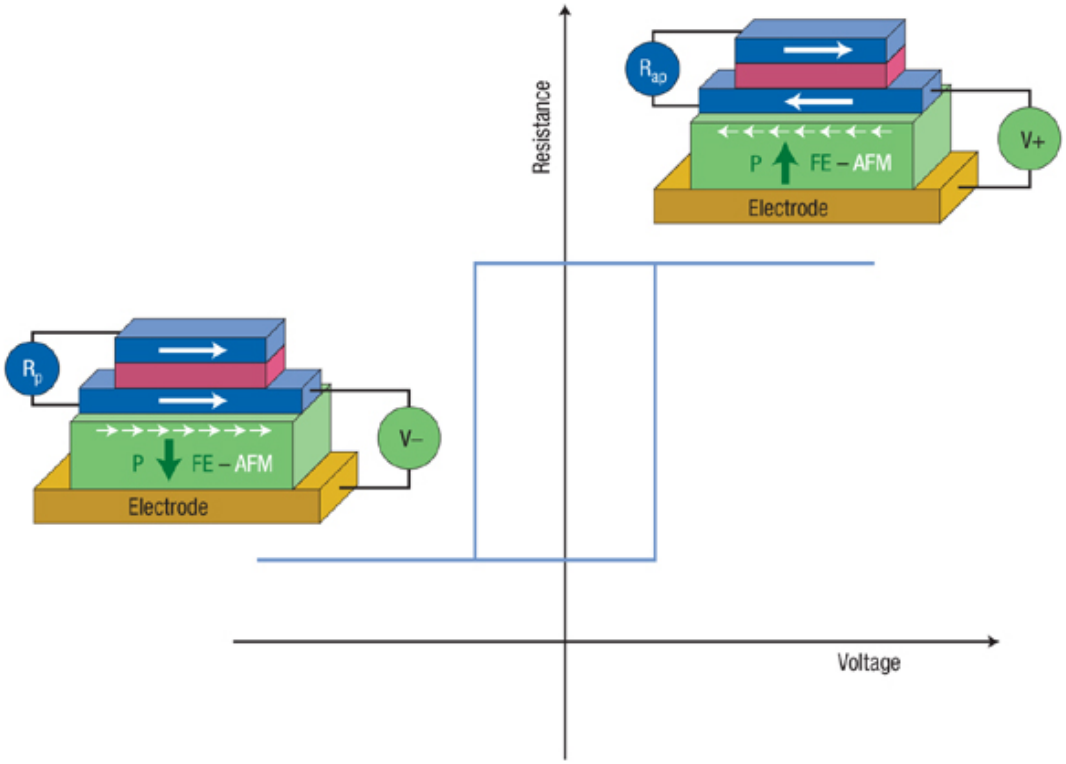

Figure 2-16. Sketch of a possible MERAM element using BFO [116]; description in the text.

BFO has been also used in the fabrication of tunneling magnetoresistance (TMR)-based memory devices. The ultrathin BFO film is used as a tunnel barrier layer. When BFO is placed between two ferromagnetic materials, *e.g.* $La_{2/3}Sr_{1/3}MnO_3$/BFO/Co, an electrical polarization rotation induced by an applied electric field can bring about rotation of the sublattice magnetization in the multiferroic layer, this in turn can change the spin configuration in the ferromagnetic layers, for example, from parallel to antiparallel, resulting in a resistance change and the data could be read using the variation of magnetoresistance. The additional advantage is that magnetic bits can be written electrically with lower power consumption [117].

The photovoltaic effect observed in BFO with a band gap in the visible range was proposed to be used to sense the polarization direction in a ferroelectric memory. A 16-cell memory prototype device was successfully tested [118], as presented in Figure 2-17. Upon illumination with a uniform light field, the bulk photovoltaic effect induces a voltage across the memory cell that is dependent on the ferroelectric polarization. This can serve as the read-out signal in a memory device. The prototype showed good retention properties and low fatigue.

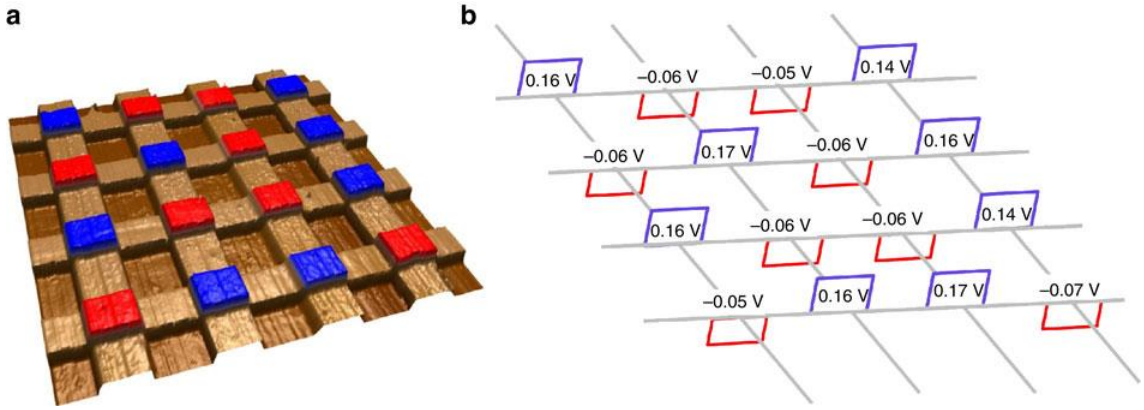

Figure 2-17. A ferroelectric photovoltaic memory prototype device [118]. (a) Topography of the device with pre-set polarization direction (polarization up and down). (b) V_{oc} of all cells measured under 20 mW/cm^2 light.

2.2.1.4. Processing of BFO

2.2.1.4.1. BFO single crystals

Reports on single crystals are rare and BFO single crystals have been obtained mainly using the self-flux method. In pioneering studies on single-crystal growth a 1.75:1 mol ratio Bi_2O_3–Fe_2O_3 flux was first employed [91]. The mixture was heated to 860 °C in nickel crucible and then cooled at a rate of 1.5 °/h to 760 °C, with a holding time of 18-20 h at 820 °C. The major faces of the crystals were (100)pc planes. Authors pointed out for some problems in preparing BFO crystals, such as: loss of Bi_2O_3 due to volatilization and reaction with crucible. Later a 3.34:1 mol ratio Bi_2O_3–Fe_2O_3 flux was employed [119].

Ferroelastically twinned single crystals with fernlike dendritic habit and 180° ferroelectric domains were obtained due to processing temperature above the ferroelectric phase transition temperature. In order to growth crystals below ferroelectric phase transition temperature (830 °C) and avoiding particular microstructure formation, B_2O_3 was added and a 4:1:1 $Bi_2O_3/Fe_2O_3/ B_2O_3$ mole ratio was used [81] and a 4:1:0.8 ratio [120], permitting growth of dendritic polar single domain crystals with (100)-pseudocubic habitus. Single crystals were grown in platinum crucibles placed in an evacuated sealed quartz tube by heating to 850 °C for 4 h and cooling down to 620 °C (initial growth temperature). Dendritic BFO single crystals obtained by flux method are presented in Figure 2-18.

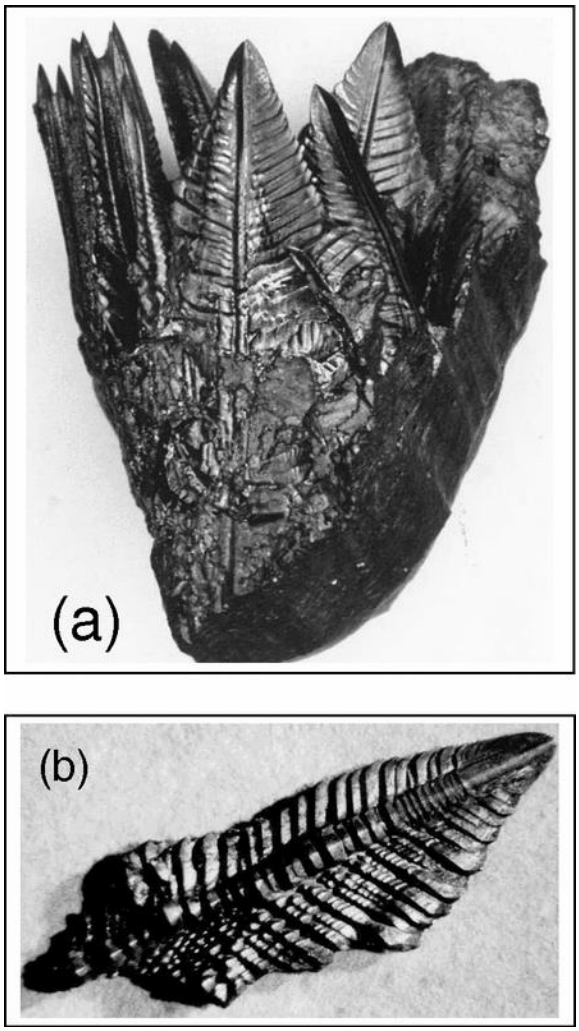

Figure 2-18. Fernlike dendritic single crystals of BFO (a) group of leaves grown in a Pt crucible; (b) individual leaf [121].

Lebeugle *et al.* reported the growth of single crystals from a Bi_2O_3-Fe_2O_3 flux with a mole ratio 3.5:1 using alumina crucibles. The mixture was heated up to 850 °C at a rate of 150 °C/h, held for 4 h at this temperature and cooled down slowly to 750 °C, followed by furnace cooling. The crystals grown in this way were millimeter-sized black platelets [122]. Another flux, Bi_2O_3/Fe_2O_3/NaCl, was also employed with constituent mole ratio of 4.2:1:0.36. By spontaneous crystallization of this flux with a cooling rate of 0.5 °C/h within the interval (870-820 °C) the BFO crystals were obtained with size up to 10 mm on edge [123].

More recently, in 2011 BFO single crystals were also grown by the laser-diode heating floating-zone (LDFZ) method [124]. In this method equivalent laser diodes are placed on a circle around the rotation axis of the sample at equal intervals and the laser beams are irradiated on the molten zone cooperatively. Powders of Bi_2O_3 and Fe_2O_3 for the feed rod and the solvent were mixed at the molar ratios of 1:1 and 8:2~9:1, respectively, calcined at 720 and 650 °C for 12 h. Then they were pulverized, pressed in rubber tubes, and sintered at 750 and 680 °C for 2 h, respectively. The sintered feed rod was premelted with the solvent and passed through the molten zone at the speed of 10 mm/h to make its density higher. Crystals were grown at the speed of 0.5 mm/h in oxygen mixed with argon. Obtained single crystal had a size of 4 mm in diameter and more than 50 mm in length [124].

Practical use of BFO single crystals is limited because they suffer the mechanical damage caused by repeated polarization reversal, as reported by Lebeugle *et al.* [55]. The large changes in shape result in the formation of cracks and defects that affects ferroelectric properties. The defects have much smaller resistivities, so during successive electrical cycling the leakage current heats and degrades the sample, decreasing the remnant polarization. It was demonstrated that the remnant polarization in single crystals can initially reach up to 100 $\mu C/cm^2$, but show appreciable degradation after few switching cycles [55].

2.2.1.4.2. BFO bulk ceramics

Preparation of single-phase BFO ceramics is extremely difficult due to particular thermodynamics and kinetics of the Bi_2O_3–Fe_2O_3 system. The Bi_2O_3–Fe_2O_3 phase diagram (Figure 2-19) indicates three equilibrium phases: the orthorhombic $Bi_2Fe_4O_9$, the rhombohedral perovskite BFO, which decomposes to $Bi_2Fe_4O_9$ and a liquid phase, and the

cubic $Bi_{25}FeO_{39}$ (or $Bi_{25}FeO_{40}$) that exhibits decomposition to Bi_2O_3 and a liquid phase [121, 125].

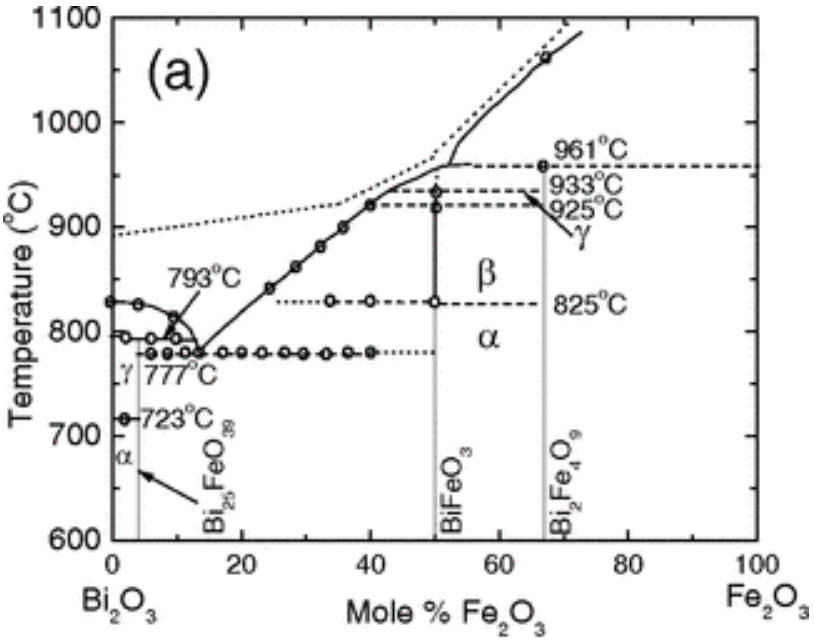

Figure 2-19. Phase diagram of the Bi_2O_3–Fe_2O_3 system. The α, β, and γ phases are rhombohedral, orthorhombic, and cubic, respectively [121].

Based on the thermodynamic studies by Selbach *et al.* [126] the $Bi_{25}FeO_{39}$ and $Bi_2Fe_4O_9$ phases are slightly more thermodynamically stable than the BFO in the temperature range 447-767 °C, that is, the $\Delta_rG°_m$, the Gibbs free energy of the equilibrium reaction between BFO and the Bi- and Fe-rich phases, is slightly positive in this temperature interval as shown in Figure 2-20 a). Secondary phases $Bi_{25}FeO_{39}$ and $Bi_2Fe_4O_9$ form at the expense of the perovskite BFO phase within the temperature instability range at 600 °C, but react back to the perovskite phase at higher temperatures [126].

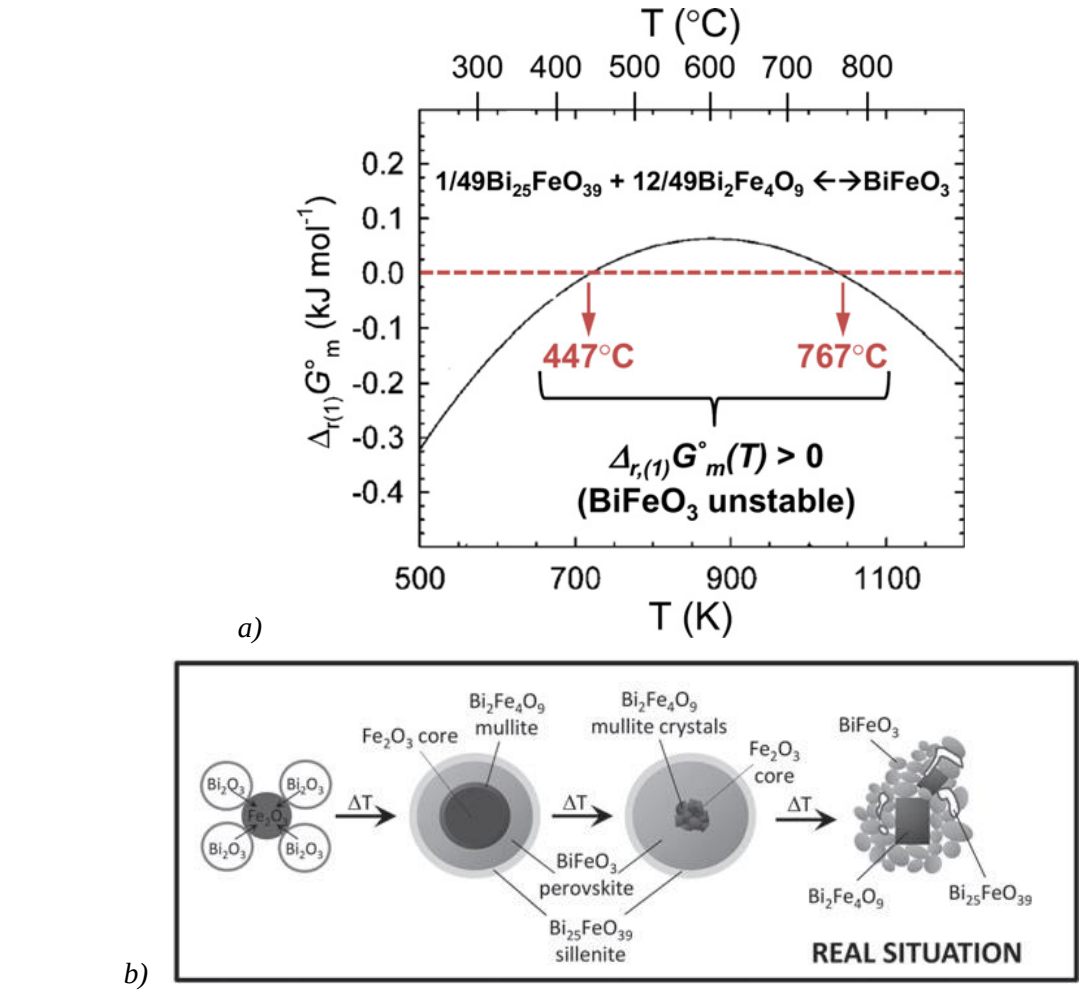

Figure 2-20. Thermodynamic instability of BFO and reaction kinetics in the Bi_2O_3–Fe_2O_3 system: a) Calculated temperature dependence of the Gibbs free energy ($\Delta_r G°_m$) of the equilibrium reaction between BFO and the Bi- and Fe-rich phases [126]; b) Proposed reaction pathway mechanism for the solid-state synthesis of BFO from Bi_2O_3 and Fe_2O_3 [127].

Moreover, analysis of the diffusion and solid state reactivity of the Bi_2O_3–Fe_2O_3 system revealed that the diffusion of Bi^{3+} ions into Fe_2O_3 governs the solid state synthesis of BFO [127]. As proposed by Bernardo *et al.* at the beginning of the Bi_2O_3–Fe_2O_3 solid state reaction, a $Bi_{25}FeO_{39}$ sillenite-type phase is initially formed at the shell whereas a $Bi_2Fe_4O_9$ mullite-type phase is formed at the reaction/diffusion front towards the iron oxide core (see Figure 2-20 b). Once crystallized, the $Bi_2Fe_4O_9$ primary particles are exceptionally stable and, consequently the reaction is stopped in a situation in which BFO coexists with small

amounts of the other two phases [127]. This proposed reaction pathway explains the commonly observed microstructural features in BFO ceramics, that is, a Fe-rich region inside a BFO grain with the Bi-rich sillenite phase close to the BFO grain boundary. Furthermore, sublimation or evaporation of volatile Bi_2O_3 at elevated temperatures may also result in $Bi_2Fe_4O_9$ formation [67]. Those secondary phases have detrimental impact on BFO piezo/ferroelectric properties, therefore should be avoided.

Due to the mentioned problems BFO ceramics were prepared using a variety of different processing methods such as: conventional sintering, rapid liquid-phase sintering, and spark plasma sintering (SPS). Usually BFO powders prepared by conventional solid state method do not exhibit good sinterability. Single phase ceramics with high density are very difficult to fabricate, because at temperatures ranging from 675 to 830 °C, BFO decomposes slowly into $Bi_2Fe_4O_9$, above 830 °C BFO separates rapidly into $Bi_2Fe_4O_9$, whereas below 675 °C the density of BFO ceramics is very low. Conventional sintering of BFO requires temperatures higher than 800 °C and several hours of sintering time even if small sized powders are used [128].

Pure BFO ceramics free from impurity phases have been reported by Shvartsman *et al.* [56]. In this work BFO powders were prepared by conventional solid state reaction using high purity Bi_2O_3 and Fe_2O_3. After mixing in stoichiometric proportions, powders were calcined twice at 820 °C for 3 h. To obtain the ceramics powders were hydrostatically cold pressed (2.5 kbars) and sintered once or twice at 820 °C for 6 h. A remanent polarization and a coercive field were reported to be 40 $\mu C/cm^2$, and 2.3 kV/cm, respectively for those BFO ceramics.

Differently from the previous work, it has been shown that single phase BFO ceramics with electrical resistivity ~5×10^{12} Ω cm and porosity ~8 % can be also synthesized by using Bi_2O_3 and Fe_2O_3 powders of <1 μm size and a rapid liquid-phase sintering process at 855 °C for 5 min. These single phase ceramics revealed a saturation polarization of 16.6 $\mu C/cm^2$ and a piezoelectric d_{33} coefficient of 27 pC/N. Deviation from these synthesis conditions leads to multi-phase samples with charged defects, and pores [129].

BFO ceramics were also successfully synthesized by SPS. The proper processing temperature and sintering time in order to obtain a single perovskite structure were determined to be 750 °C for 5 min. In SPS during heating and sintering, a pressure of 50 MPa

was used. The relative density and average grain size of the SPS-prepared ceramics were 95 % and 200 nm, respectively. A remanent polarization and a coercive field were reported to be 7.5 μC/cm^2, and 6.6 kV/cm, respectively [70].

2.2.1.4.3. BFO epitaxial thin films

The growth of high quality BFO epitaxial thin films was initiated in 2003. Wang *et al.* reported the growth of heteroepitaxially constrained BFO thin films on $SrTiO_3$ substrates by pulsed laser deposition and stimulated following research on the topic due to the presented enhancements in the polarization (up to ~90 μC/cm^2), piezoelectric strain coefficient (d_{33} = 70 pC/N), magnetoelectric effect (dE/dH = 3 V/cm Oe) of these BFO films [54]. Since then, epitaxial BFO films have been prepared by pulsed laser deposition (PLD) [54, 130], radio-frequency (RF) sputtering [131, 132], metalorganic chemical vapor deposition (MOCVD) [133], molecular beam epitaxy [103], chemical solution deposition (CSD) [134] on various substrates.

It is well established now that epitaxial strain imposed by the substrate enables the control of the crystal structure of the grown films: tetragonal, rhombohedral, orthorhombic and monoclinic structures are form in BFO epitaxial thin films as a function of the strain as presented in Figure 2-21. For thicker BFO films, the structure starts to relax and tends towards the bulk-like rhombohedral symmetry.

In BFO epitaxial films enhanced functional properties have been reported. In highly compressively strained tetragonal-like BFO films a remanent polarization of 130 μC/cm^2 was measured [135], due to Fe-ion displacement relative to the oxygen octahedra and the contribution of Bi *6s* lone pair electrons. Additionally the enhancement of piezoelectric d_{33} coefficient with a value of ~115 pC/N was obtained in mix phase (rhombohedral and tetragonal) BFO films [136]. Furthermore, the magnetic properties of strained BFO films are subsequently changed and measurements prove that the bulk cycloidal structure has been broken, which leads to a weak ferromagnetic moment arising from canting of the antiferromagnetic moments [109]. The richness of the structures, the phase coexistence and associated functional properties were widely explored in epitaxial BFO films and thorough reviews are available by Sando *et al.* [97] and Yang *et al.* [137].

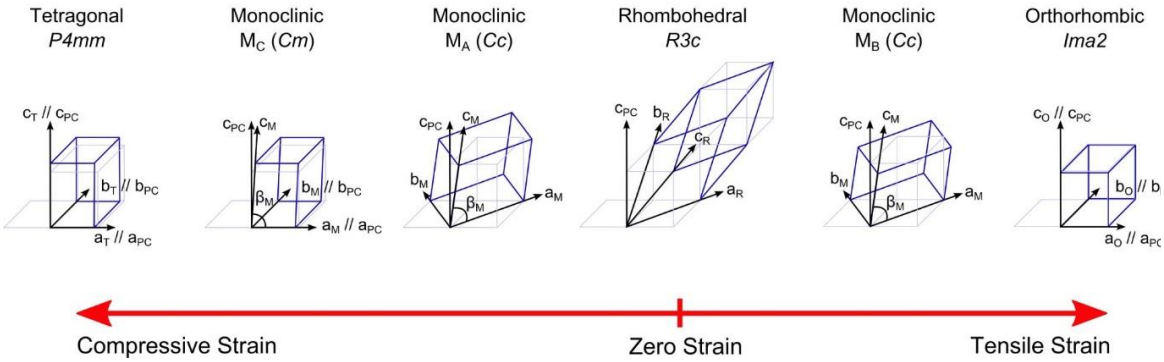

Figure 2-21. Symmetry-strain dependence for epitaxial BFO thin films. Epitaxial strain imposed by the substrate enables the control of the crystal structure of the grown films: tetragonal, rhombohedral, orthorhombic and monoclinic structures are form in BFO epitaxial thin films as a function of the strain (from [97]).

2.2.1.4.4. BFO polycrystalline films

Since epitaxial films are so expensive and laborious to prepare, their practical applications are, as a consequence, reduced. Within this context, many methods have been used to grow polycrystalline BFO thin films, however, the chemical solution deposition (CSD) technique is of particular interest for industrial use; as mentioned before because of its low-cost, good stoichiometric control, and ease processing of large areas they are quite promising from the application point of view.

In what concerns CSD, one of the key steps involved to fabricate thin films is the preparation of a stock solution of the necessary cation species that can later be coated onto a substrate. The fabrication of thin films by CSD generally involves four basic steps, as illustrated in Figure 2-22 [80, 138]:

- synthesis of the precursor solution;
- deposition by spin-coating, dip-coating or spraying on the substrate;
- low-temperature heat treatment, *i.e.* drying and pyrolysis of organic species (300-400 °C);

- high temperature heat treatment, crystallization of the coating into the desired oxide phase (up to 1100 °C).

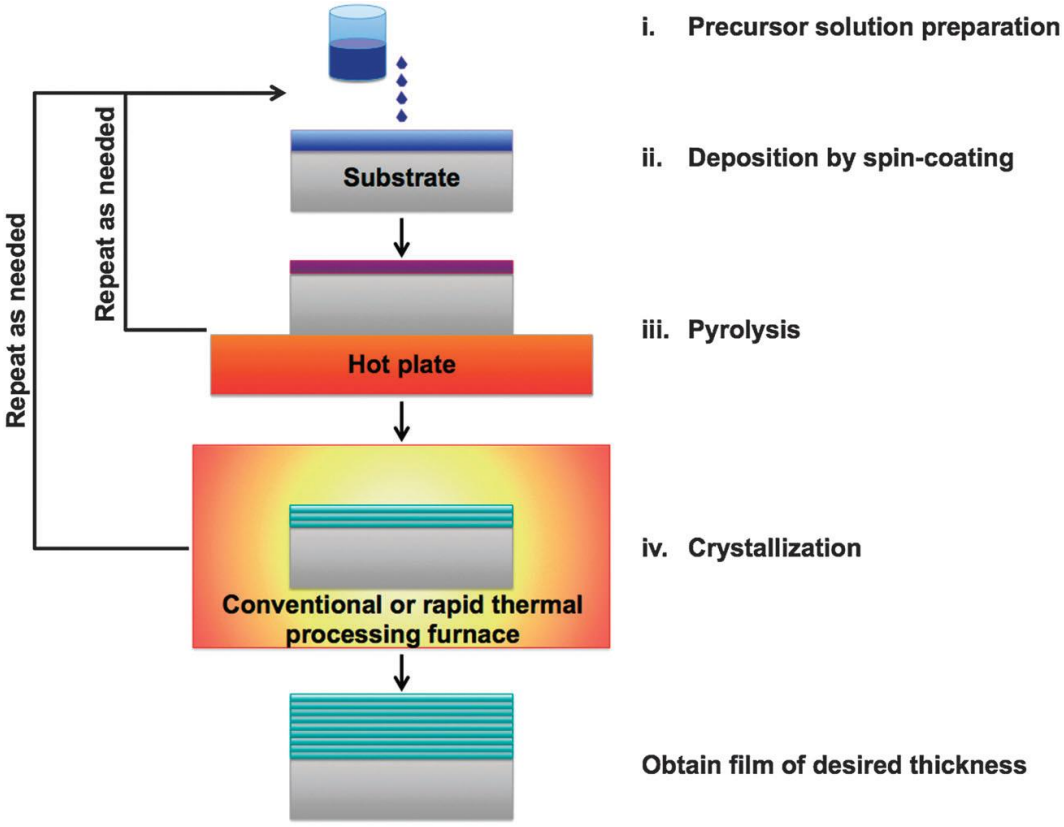

Figure 2-22. Schematic representation of the fundamental steps in CSD preparation of ferroelectric oxide thin films [80].

Various combinations of precursors for BFO thin films processing by CSD have been implemented. Table 2-1 summarizes the typical synthesis routes used for the fabrication of BFO thin films, including details on the precursor preparation and crystallization temperature. Chemical solution deposited BFO thin films was first reported in 1997 by Teowee *et al.* [139]. Thin films were synthesized from Bi and Fe ethylhexanoates in methanol. In that work, sol-gel derived BFO films were prepared on platinized Si substrates and XRD indicated that the films were crystalline perovskite-type when fired between 400 °C and up to 700 °C for 30 min. The film contained non-perovskite phases, such as $Bi_2Fe_4O_9$ when fabricated at 700 °C. The appearance of this Bi deficient secondary phase was attributed to Bi loss due to diffusion of Bi into the substrate or Bi volatilization.

Polarization values obtained for the films annealed at temperatures lower than 600 °C were quite low (<1 pC/cm^2). When crystallized at 650 °C, the hysteresis loops become more developed exhibiting a remanent polarization and a coercive field of 5.5 μC/cm^2 and 180 kV/cm, respectively.

Table 2-1. Selected processing parameters for typical CSD routes used for BFO thin films fabrication.

Precursors and solvents	Bi:Fe ratio	Annealing conditions	Substrate	Ref
Bi/Fe ethylhexanoates methanol	1:1	400-700 °C for 30 min	Pt/TiO_2/SiO_2/Si	[139]
$Bi(NO_3)_3 \cdot 5H_2O$, $Fe(NO_3)_3 \cdot 9H_2O$ Ethylene glycol, citric acid	1.05:1	500 °C for 60 min, air, O_2, N_2	Pt/TiO_2/SiO_2/Si	[140]
$Bi(OCO(CH)(C_2H_5)C_4H_9)_3$, $Fe(C_5H_7O_2)_3$ toluene	1:1 1.05:1 1.1:1 1.2:1 1:1.1	450 C for 15 min (RTA)	Pt/TiO_2/SiO_2/Si	[141, 142]
$Bi(t–OBu)_3$, $Fe(t–OBu)_3$ 2-metoxyethanol	1:1 1.1:1	500-700 For 20 min	Pt/TiO_2/SiO_2/Si	[143]
Bi $(CH_3CO_2)_3$, $Fe(C_5H_7O_2)_3$ de-ionized water, acetic acid	1:1	600 °C for 60 min (UV-assisted pyrolysis)	Pt/TiO_2/SiO_2/Si	[144]
$Bi(NO_3)_3 \cdot 5H_2O$, $Fe(NO_3)_3 \cdot 9H_2O$ 2-methoxyethanol, glacial acetic acid	1.05:1	500 °C for 30 min	LNO coated SiO_2/Si	[27]
$Bi(NO_3)_3 \cdot 5H_2O$; $Fe(C_5H_7O_2)_3$ acetic acid, 1,3-propanediol	1.05:1	500 °C for 1 min (RTA)	Pt/TiO_2/SiO_2/Si	[145]
Bi $(CH_3CO_2)_3$,$Fe(CO_2CH_3)_3$ propionic acid, ethanolamine	1.05:1	450-700 °C	Pt/TiO_2/SiO_2/Si	[146]

Later, much work has been done in order to obtain monophasic perovskite BFO thin films by CSD with optimized ferroelectric properties and reduced leakage currents. In 2009 Simões *et al.* [147] investigated effect of annealing atmospheres (air, N_2 and O_2) on the crystallization and electrical properties of BFO films. They reported intense effect of annealing conditions on the conductivity of the films. The films annealed in air showed better crystallinity and the presence of a single BFO phase leading to low leakage current density and superior ferroelectric hysteresis loops at room temperature. The films annealed in air

showed a leakage current density of ~10^{-5} A/cm^2 at 10 V. These films presented a remnant polarization of 32 μC/cm^2 and a coercive field of 540 kV/cm, and fatigue free properties up to 10^{10} cycles. The microstructure and phase composition of the films were also found to depend on the annealing conditions. A pure perovskite phase was only reported for films treated in air, while second phases, such as $Bi_2Fe_4O_9$ and $Bi_{36}Fe_{24}O_{57}$, were present in films annealed in N_2 and O_2 atmospheres.

Differently from the previous works, Nakamura *et al.* studied the effect of Bi/Fe ratio on the structure and ferroelectric properties of BFO films. BFO films were prepared via precursor solutions of various elemental ratio (Bi:Fe = 1.00:1.00, 1.05:1.00, 1.10:1.00, 1.20:1.00 and 1.00:1.10) on Pt/TiO_2/SiO_2/Si substrates [142]. Thin films were annealed at 450 °C for 15 min in nitrogen atmosphere using rapid thermal annealing (RTA) process. All deposited films were mainly polycrystalline perovskite. However, for 10 % Fe excess films $Bi_2Fe_4O_9$ was the major secondary phase while for 20 % Bi excess films Bi_2O_3 was present as the impurity phase. Microscopy analyses revealed that all films had a non-common rosette type structure consisting of circular regions with an uneven texture surrounded by regions with flat surfaces. The roughness of these circular regions increased with increasing Bi/Fe ratio. Further probing with Raman spectroscopy revealed that the circular regions were crystalline BFO while the outer regions were amorphous BFO. Remanent polarization at maximum applied voltage of 1.2 MV/cm were 38, 28, 85, 53 and 30 μC/cm^2 for the ratio of Bi:Fe = 1.00:1.00, 1.05:1.00, 1.10:1.00, 1.20:1.00 and 1.0:1.1, respectively. Films with excess Bi showed high leakage currents [141].

Another work by Tyholdt and co-workers reported that a small Bi excess (10 %) is necessary to obtain dense, pore-free BFO films. BFO films were fabricated using a sol prepared by alcoholysis of Fe(t-OBu)$_3$ and Bi(t-OBu)$_3$ in 2-methoxyethanol [143]. The stoichiometric and 10 % Bi excess precursor solutions were deposited on platinized Si substrates, and the films were crystallized at 500-700 °C for 20 min. Phase pure (012)-oriented films were obtained with the preferred texture being more enhanced in films prepared from 10 % Bi excess sol and using higher crystallization temperature. Stoichiometric BFO films were single phase according to XRD for crystallization temperatures up to at least 600 °C. At 700 °C, bismuth evaporation leads to the formation of secondary phases unless Bi-excess is adopted in the synthesis. Moreover, the observed (012)

texture is believed to originate from the growth mechanism as no relation to the substrate was found. This is also confirmed by observing (012) texture for films on glass substrates.

Habouti *et al.* showed a substantial improvement in leakage resistance for BFO films using UV-assisted CSD method on (111)Pt/Ti/SiO_2/Si substrates [144]. UV assisted pyrolysis was conducted in oxygen atmosphere in order to obtain a fine and homogeneous grain structure. The UV treated films and post annealed at 600 °C were well crystallized with strong (012) preferred orientation, and their microstructure was fine and homogeneous, comparing to not UV treated ones. It was speculated that UV treatment caused early breaking of C–H bonds and formation of highly activated oxygen species that led to efficient pyrolysis resulting in the observed fine morphology. The leakage currents were several orders of magnitude lower than those observed in conventionally pyrolized films (~10^{-6} A/cm^2 for the BFO UV treated and ~10^{-3} A/cm^2 for non-UV treated films), but the ferroelectric polarization remained poor for those UV treated films with the ferroelectric hysteresis curves resembling a lot like those of leaky dielectrics.

In 2010, Zhang and co-workers reported the preparation of BFO thin films by CSD using $LaNiO_3$ (LNO) metal oxide electrodes instead of the noble metal electrodes like Pt [27]. LNO was chosen among the oxide electrodes, due to its low resistivity with (10^{-4} Ω · cm) and pseudo-cubic perovskite structure with the lattice parameter of 0.384 nm, which is compatible with that of BFO (0.396 nm). Using metal nitrates as precursors dissolved in the glacial acetic acid and 2-methoxyethanol purely polycrystalline films were obtained without any impurities. Films were characterized by a smooth and dense surface morphology with well-distributed fine grains. The dielectric constant and dielectric loss at 10 kHz of BFO thin film on LNO electrodes were 202 and 0.057, respectively. Unsaturated loops were observed, which were attributed to the large leakage current contribution. A remanent polarization of ~45 μC/cm^2 and a coercive field of ~370 kV/cm were measured.

Calzada and co-workers reported a low-cost synthesis strategy based on the use of non-hazardous route, using 1,3-propanediol as a one of the solvents [145]. Crystallization was carried out by Rapid Thermal Processing (RTP) in the wide temperature range 400-750 °C, in air or oxygen atmospheres, but only BFO films crystallized in air at 500 °C were fully characterized. These films had a microstructure formed by large columnar grains with lateral size of 225-325 nm and small grains with lateral size of 75-150 nm. The ferroelectric

switching at room temperature was hindered by the charged defects, thus a ferroelectric response at room temperature could only be obtained after an electric-conditioning treatment at a low temperature that produces the depinning of the polarization. Functional properties of those films were presented: a remanent polarization, ~67 μC/cm^2, a magnetization of 2.50 emu/g for the ~42-nm-thick films, and a direct band gap in the visible range, E_g ~ 2.82 eV, for BFO films on Pt(111)/Ti/SiO_2/Si substrate annealed at 500 °C.

Recently, Jin *et al.* reported the fabrication of (111)-oriented BFO films on silicon-based substrates by CSD [146] In BFO the P_r is largely dependent on the orientation of the thin films and the largest theoretically predicted value of polarization for BFO film oriented along (111) direction is ~100 μC/cm^2 in the rhombohedral phase. To obtain (111)-oriented BFO thin films, an appropriate substrate or buffer layer with specific orientation is usually used. This work reports (111)-oriented BFO thin films on Pt(111)/Ti/SiO_2/Si substrates without a buffer layer. The (111)-oriented BFO films could only be achieved when Bi and Fe acetates were used as precursors, and the annealing atmosphere was N_2. Bismuth acetate and iron acetate were used as metal precursors, dissolved in propionic acid and stabilized with ethanolamine. The films were crystallized in air at distinct temperatures, 450-700 °C, and it was demonstrated that with increasing annealing temperature, the (111) texture was enhanced. BFO films annealed at 450 °C were amorphous and the ones annealed at higher temperatures showed relatively dense and crack-free microstructure. Additionally, annealing temperatures >600 °C lead to second phase formation and the deterioration of the ferroelectric properties. Monophasic BFO thin films exhibited a low leakage current density (10^{-5} to 10^{-6} A/cm^2 at 200 kV/cm), well-shaped hysteresis loops with a remanent polarization of ~65 μC/cm^2 and a coercive field of ~400 kV/cm.

As a summary note on the properties of BFO, Table 2-2 presents the selected reported ferroelectric properties of BFO in single crystals, ceramics and thin films form. It can be deduced that depending on processing method and conditions ferroelectric properties of BFO differ. While well saturated polarization hysteresis loops with high remnant polarization and low leakage currents were reported for epitaxial BFO films, polycrystalline BFO films have been in contrast found to have a large scatter in the polarization properties. Processing conditions like pyrolysis, annealing temperature and annealing atmospheres play a prominent role in controlling the ferroelectric properties [148] and more work is needed to

establish appropriate processing routes for high quality BFO films, including precursor solution, pyrolysis and annealing conditions as well as substrate choice.

Table 2-2. Summary of ferroelectric properties of pure BFO single crystals, bulk ceramics and thin films.

Method	P_r (μC/cm^2)	E_C (kV/cm)	Conditions	Ref
Single crystals				
Flux growth	60 [100]pc	12	RT	[55]
Floating zone growth	50 [100]pc 85 [111]pc	~60 ~90	RT	[124]
Ceramics				
Conventional solid-state reaction	40	2.3	RT	[56]
liquid-phase sintering	~9	~60	RT	[129]
spark plasma sintering	7.5	6.6		[70]
Epitaxial thin films				
CSD BFO/LSMO/STO(001)	50	96	RT	[149]
CVD BFO/SRO/STO(001)	60	~250	RT	[150]
PLD BFO/SRO/STO(001)	55	~150	RT	[151]
RF sputtering BFO/SRO/STO(001)	71	~150	RT	[131]
Polycrystalline thin films				
CSD BFO/Pt/TiO_2/SiO_2/Si	85	~400	RT	[152]
CSD BFO/LNO/Si	~7	~20	RT	[153]
CSD Pt/Ti/SiO_2/Si(100)	92	500	80 K	[154]
CSD Pt(111)/Ti/SiO_2/Si	31	560	RT	[155]

RT – room temperature.

2.2.2. Sodium bismuth titanate – $Na_{0.5}Bi_{0.5}TiO_3$

2.2.2.1. Structure of NBT

In 1960 Smolenskii *et al.* [156] found $Na_{0.5}Bi_{0.5}TiO_3$ (NBT) to be a perovskite-type ferroelectric at room temperature. NBT is a relaxor ferroelectric with a diffuse phase transition from rhombohedral to tetragonal phase between 200 and 320 °C and from tetragonal to cubic phase at 540 °C [157-160]. Relaxor ferroelectrics or relaxors are a class of disordered crystals possessing peculiar structure and properties. At high temperature they exist very much like normal ferroelectrics in a non-polar paraelectric phase. Upon cooling they transform into the ergodic relaxor state in which polar regions of nanometer scale with randomly distributed directions of dipole moments appear [161]. The region between 200 and 320 °C has been discussed controversially as either being antiferroelectric [162] or exhibiting a coexistence of rhombohedral and tetragonal phases with polar regions [157-159]. Recently, *in situ* temperature TEM studies suggest that there is a phase transition from ferroelectric rhombohedral to antiferroelectric orthorhombic phase proceeded via an antiferroelectric modulated phase consisting of orthorhombic sheets in a rhombohedral matrix in the temperature range from 200 to 300 °C. A second phase transition from orthorhombic to tetragonal phase occurs near 320 °C, which corresponds to the antiferroelectric/paraelectric phase transition [163, 164]. The possible high temperature phase transitions of NBT based on TEM and X-ray/neutron diffraction experiments are presented in Figure 2-23.

The room temperature, average structure of NBT has long been accepted to be of rhombohedral *R3c*. The rhombohedral structure of NBT is characterized by ferroelectric off-center displacements of the Na/Bi ions along a [111]pc direction and $a^-a^-a^-$ octahedral tilt rotation of the parent perovskite sub-structure around a [111]pc direction. More recently, it has been suggested [165] that the true average structure of NBT at room temperature is actually monoclinic *Cc*, characterized by $a^-a^-c^-$ octahedral tilt rotation. This *Cc* symmetry does not deviate dramatically from the *R3c* symmetry in terms of the unit cell dimensions; the pseudocubic unit cell of the *Cc* symmetry displays lattice constants of $a = b = 3.887$ Å, $c = 3.882$ Å, $\alpha = \beta = 89.944°$, $\gamma = 89.646°$, while that of the *R3c* symmetry exhibits the lattice constants of $a = b = c = 3.885$ Å, $\alpha = \beta = \gamma = 89.83°$ [165]. The rhombohedral (in the

hexagonal setting) and monoclinic unit cell consists of six and four formula units of NBT, respectively (Figure 2-24). Several experiments have probed the local structure of NBT and found the short-range ordering to be significantly different from the long-range order [163, 166, 167].

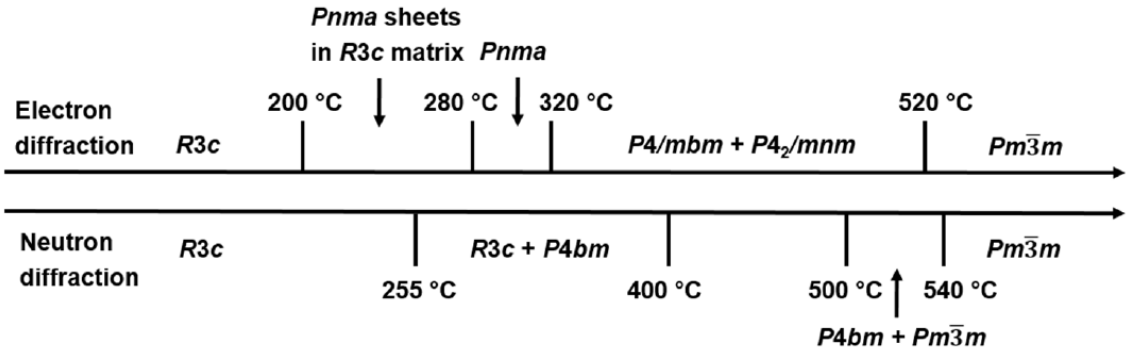

Figure 2-23. Reported possible phase transition routes based on TEM and X-ray/neutron diffraction studies for NBT ceramics [168].

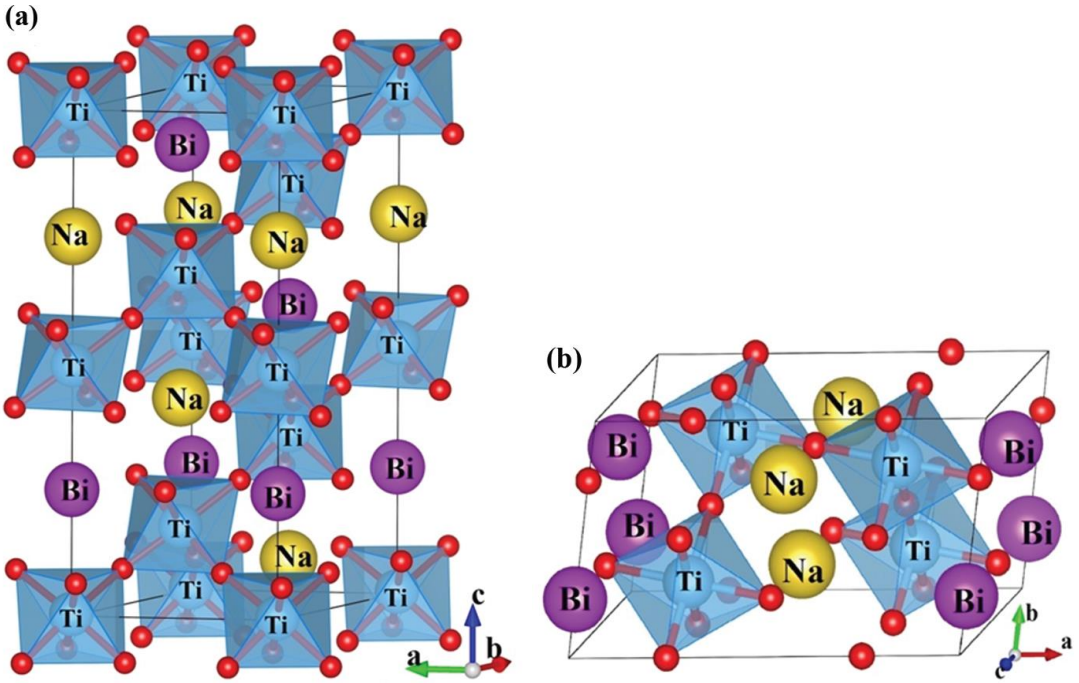

Figure 2-24. Crystal structures of NBT: (a) rhombohedral R3c (hexagonal setting) and (b) monoclinic Cc [169].

2.2.2.2. Physical properties of $Na_{0.5}Bi_{0.5}TiO_3$

NBT ceramics shows ferroelectric properties with a significant remnant polarization of P_r ~ 38 μC/cm^2. However, these ceramics have disadvantages such as high conductivity and large coercive field (Ec ~ 75 kV/cm), which cause problems in the poling process. Single crystals of NBT show P_r ~ 40 μC/cm^2 and Ec ~ 28 kV/cm at 20 °C [50].

Piezoelectric properties of the NBT ceramics, polarized by field 40 kV/cm at ~200 °C, were reported to be: k_{31} = 0.10, d_{31} = 15 pC/N, d_{33} = 70 pC/N, ε_r = 300, $tan\delta$ = 0.011, calculated k_{33}=0.40. Piezoelectric properties of single crystals (the (001) plates of the rhombohedral NBT) are: d_{31} = 160 pC/N, d_{33} = 60 pC/N, k_{31} = 0.55, k_{33} = 0.40 [50].

A high sintering temperature (>1200 °C) needs to be used to obtain dense samples. Nagata *et al.* using secondary ion mass spectrometry revealed that the difficulty in the poling treatment of NBT ceramics is attributed to the pinning of domain walls caused by oxygen vacancies due to Bi vaporization at high sintering temperatures [170].

The piezoelectric properties and room-temperature dc conductivity of NBT depend on the nominal starting composition. Effects of Bi and Na non-stoichiometry on NBT ceramics were investigated by Sung *et al.* [171, 172]. Either Na deficiency or Bi excess in the nominal starting composition enhances the dc resistivity and piezoelectric coefficient d_{33}, but lowers depolarization temperature T_d. On the other hand, either Na excess or Bi deficiency decrease the DC resistivity and d_{33} but enhances T_d. Figure 2-25 shows the variations of d_{33}, T_d, with Na and Bi stoichiometry.

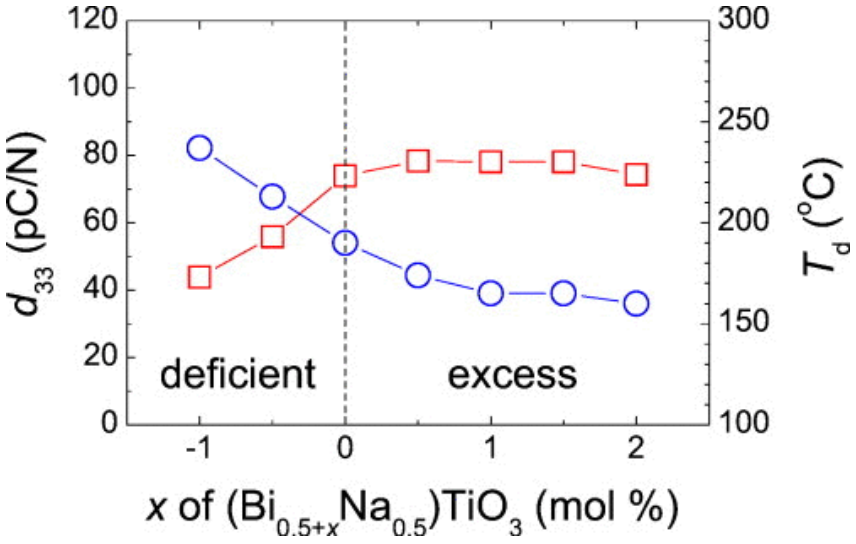

a)

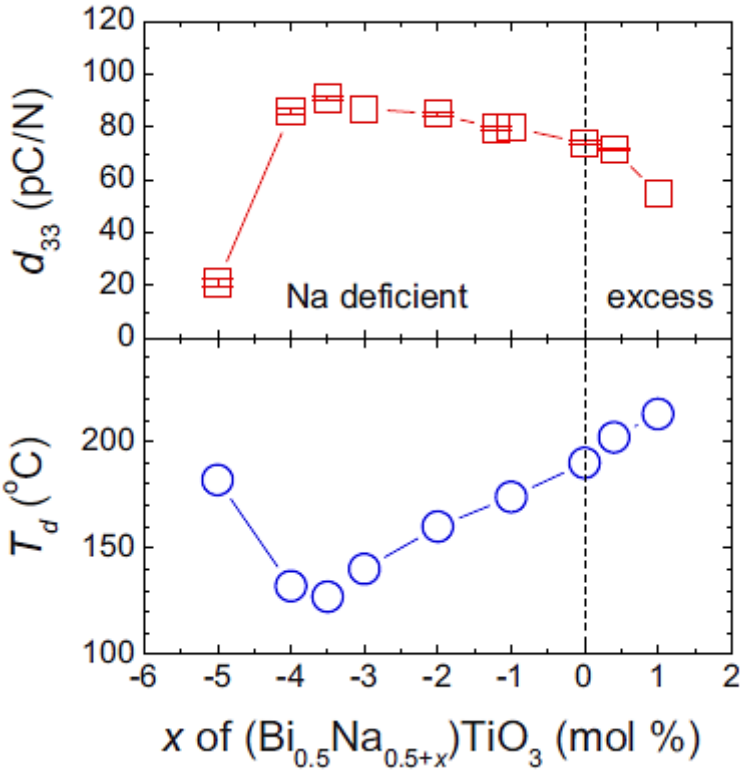

b)

Figure 2-25. Influence of a) Bi and b) Na non-stoichiometry on piezoelectric coefficient d_{33} and depolarization temperature T_d. Na deficiency and Bi excess in the nominal starting composition enhances the DC resistivity and piezoelectric coefficient d_{33}, but lowers depolarization temperature T_d. Na excess or Bi deficiency decrease the DC resistivity and d_{33} but enhances T_d [171, 172].

Recently, NBT was reported as a new family of oxygen ionic conductors by Li *et al.* [173]. In this experimental study, Mg doped NBT, $Na_{0.5}Bi_{0.49}Ti_{0.98}Mg_{0.02}O_{2.965}$, achieved an oxygen conductivity of ~0.01 S/cm at 600 °C. The fast oxygen ion diffusion of NBT is attributed to the high polarizability of Bi^{3+} cations and is mediated by oxygen vacancies, generated through Bi deficiency and/or Mg doping [173].

Arrhenius-type plots of bulk conductivity (Figure 2-26) show that NBT-based with slightly different starting compositions can be divided into two groups [174]. Based on combination of impedance spectroscopy, ^{18}O tracer diffusion studies, and transport number measurements for oxide-ion conductivity, stoichiometric NBT exhibits near-intrinsic electronic conduction, and is an excellent dielectric. Starting compositions with Bi/Na > 1 will lead to such insulating composition(s), which are suitable for dielectric/piezoelectric applications. Bi-deficient compositions exhibit high oxide-ion conductivity. Hence starting compositions with Bi/Na ≤ 1 will lead to such conducting materials, and these may be suitable (with appropriate doping) for intermediate-temperature solid oxide fuel cells electrolyte/electrode applications [174]. Clearly, electrical properties of NBT are highly sensitive to low levels of non-stoichiometry, therefore careful control of starting compositions and processing conditions is critical to obtain desirable and reproducible NBT materials.

2.2.2.1. Processing of NBT

Bi and Na are volatile elements with the consequent variation in the stoichiometry of the final NBT. Attempts to obtain NBT-based crystals have been widely reported using many growth methods, *e.g.* high temperature solution (flux) [175-177], Czochralski [178-182], and Bridgman [183]. The NBT-based crystals had various sizes (many of them were mm-level) in the flux method, and 15×15×25 mm^3 in the Czochralski method.

The synthesis of NBT ceramics is usually carried out via a conventional mixed oxide route with Bi_2O_3, Na_2CO_3 and TiO_2 as starting materials. Given the fact that high temperatures are needed for calcination and sintering, problems with the volatility of Bi_2O_3 and Na_2CO_3 may occur. Both materials have low melting points ($T_m(Bi_2O_3)$ = 826 °C, $T_m(Na_2CO_3)$ = 851 °C) and therefore high vapour pressures at processing temperatures. The

resulting loss of A-site cations leads to nonstoichiometric compositions. This non-stoichiometry causes vacancies, and/or formation of secondary phases, that can have detrimental impact on piezo/ferroelectric properties [184]. Therefore, some recent works proposed the synthesis of NBT powders by various wet chemical routes, such as the hydrothermal method [185, 186] and sol-gel [187], among others.

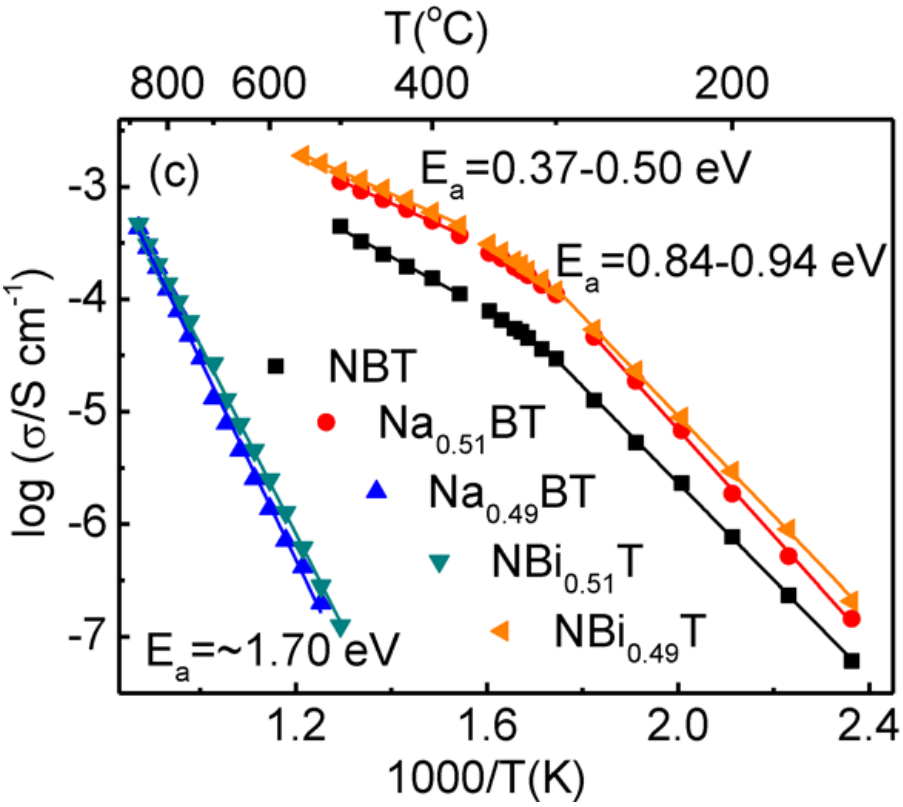

Figure 2-26. Arrhenius-type plots of bulk conductivity for nominal compositions NBT, $Na_{0.51}Bi_{0.5}TiO_{2.985}$ ($Na_{0.51}BT$), $Na_{0.49}Bi_{0.5}TiO_{3.015}$ ($Na_{0.49}BT$), $Na_{0.5}Bi_{0.51}TiO_{2.995}$ ($NBi_{0.51}T$) and $Na_{0.5}Bi_{0.49}TiO_{3.005}$ ($NBi_{0.49}T$) [174].

NBT crystals with different morphology, *e.g.* wires, plates and cubes, were synthesized by hydrothermal method [186]. NBT ceramics sintered from these crystals show different grain and domain sizes. NBT ceramics sintered from plate crystals present the largest grain with a mean size of 2.56 μm and expanded domain width with an optimum size of 350 nm, due to the weak clamping effect among large neighbouring grains. The NBT ceramics sintered from plate crystals possess the largest domain width, and exhibit the optimum

piezoelectric coefficient and remnant polarization of 87 pC/N and 36.7 μC/cm^2, respectively, which are 55 % and 37 % higher than those of the NBT ceramics sintered from cube crystals. NBT fine-grained and single phase ceramics were also prepared by SPS method [188]. Dense ceramics with the typical grain size ~200 nm were sintered only at 900 °C for 5 min. The X-ray diffraction study revealed that NBT ceramic corresponded to a mixture of tetragonal and rhombohedral symmetry. The SPS derived NBT ceramics possessed dielectric constants of approximately 1550 at room temperature and at a frequency of 100 kHz and a remnant polarization and coercive field of 19.9 μC/cm^2 and 23.4 kV/cm, respectively. This method demonstrated a unique opportunity to obtain densification with limited grain growth, being an effective method to fabricate NBT-based piezoceramics.

There are only few reports on lead-free NBT thin films. NBT thin films were synthesized by sol-gel [3, 189, 190], RF magnetron sputtering method [191] and Pulsed Laser Deposition (PLD) [192]. Firstly, highly (111)-oriented sol-gel NBT thin films were fabricated on Pt/Ti/SiO_2/Si (Pt/Si) substrates by Tang *et al.* [193]. In this work, the authors reported the highest P_r value measured in the literature up to date for pure NBT thin films: P_r ~ 20.9 μC/cm^2, for a corresponding coercive field E_C of 112 kV/cm.

For polycrystalline NBT synthesized by the sol–gel, the dielectric constant was 280-300, $tan\delta$ ~ 2 %, P_r ~ 8.3 μC/cm^2, and E_C ~ 200 kV/cm. Those films were fabricated on Pt/Ti/SiO_2/Si and crystallized at 650 °C for 60 s by RTP. P_r was lower than in NBT bulk material because full poling could not be achieved [194]. For NBT thin films synthesized by the RF magnetron sputtering method and subsequent annealing at 675 °C for 1 h, P_r ~ 12 μC/cm^2, E_C ~ 53.79 kV/mm and dielectric constant between 650 and 470 were obtained [191]. More recently, pure NBT films were epitaxially grown by PLD on (100)Pt layers supported by (100)MgO single crystals [192]. A well-defined shape of the *P-E* hysteresis loops was recorded with a P_r value of 14.1 μC/cm^2 and a coercive field of ~85 kV/cm. Table 2-3 summarizes the reported electrical properties of NBT thin films.

Table 2-3. Electrical properties of reported NBT thin films [191, 192, 194, 195].

	Chemical methods		**Physical methods**	
	Polycrystalline film [194]	***(111)-oriented film [193]***	***RF-sputtering [191]***	***Pulsed Laser Deposition [192]***
Crystallization conditions	RTA, 650 °C, 60 s	RTA, 650 °C, 10 min	Conventional annealing, 675 °C, 1 h	560-580 °C, oxygen pressure, 0.2 mbar
Remnant polarization ($\mu C/cm^2$)	8.3	20.9	12	14.1
Coercive field (kV/cm)	200	112	125	85
Dielectric constant	277 (100 kHz)	196 (1 kHz)	520 (1 MHz)	410 (100 kHz)
tanδ	0.02 (100 kHz)	0.064 (1 kHz)	0.032 (1 MHz)	0.06 (100 kHz)

As presented here the fabrication of NBT thin films has been rarely reported. The effects of the processing conditions such as annealing temperature requires further investigation.

2.3. Low temperature preparation of thin films

As mentioned in the motivation part of this thesis, the low temperature preparation of piezoelectric and ferroelectric thin films is strongly demanded. In order to be compatible with the existing high density semiconductor processes, the ferroelectric processing temperature should be decreased below 450 °C. The deposition of complex oxides on base metal substrates and polymer films represents an important extension of thin-film technology to substrate materials, more compatible with innovative applications and allow the fabrication of much thinner and lighter electronics. They decrease manufacturing costs and enhance design flexibility. On the other hand, polymer substrates are incompatible with typical processing temperatures of ferroelectric thin films, for example, most of the synthesis methods require temperatures that exceed 600, 700 and 650 °C to prepare the perovskite based ferroelectric films of PZT, $Ba_xSr_{1-x}TiO_3$ (BST) and KNN, respectively [196-198]. Normally, polyimide substrates for applications related to the electronics industry are thermally stable below 400 °C. Therefore, in order to directly integrate the ferroelectric films with silicon or flexible metal and polymer substrates, low temperature processing is strongly demanded.

For several years now the low temperature synthesis of ferroelectric thin/thick films has been attempted by chemical deposition methods with modifications at the "precursor/green state film level" and at the "post deposition processing level".

2.3.1. Modifications at the "precursor/green state film level"

Lowering the crystallization temperature can be achieved by forming the metal complexes or coordination compounds, which have the same arrangement of metal and oxygen ions as in the final crystalline state already in the solution, and/or by increasing the homogeneity of the solution. The crystallization of the perovskite phase often occurs via a transient non-ferroelectric phase and if such phase persists in the final film it can lower its functional response. In the process of crystallization of $BaTiO_3$ and $SrTiO_3$ thin films from short alkyl-chain carboxylate-alkoxide based precursors, a transient oxocarbonate phase is formed which shifts the crystallization of the perovskite phase to higher temperatures. This is not the case, if longer-chain carboxylates are used. For example, $BaTiO_3$ films, prepared

from barium propionate or acetate, crystallize at 700 °C, while the films prepared from barium ethylhexanoate crystallize at 600 °C [199]. But even when carboxylate free precursors are used and the formation of the transient oxocarbonate phase is avoided $BaTiO_3$-based films were found not to crystallize bellow 600 °C [200].

The use of seed-layers and of excess of the volatile components to decrease fabrication temperature (*e.g.* excess PbO in PZT and lead-contained systems; Bi_2O_3 in strontium bismuth tantalate and bismuth-containing systems) are widely reported in the literature [5, 6]. By using a lead titanate ($PbTiO_3$, PT) seed layer, the perovskite crystallization temperature was reported to decrease from 600 to 550 °C for 15 min for PZT thin films [3]. With a PT seeded layer plus 50 mol% excess PbO, a single perovskite phase of PZT(53/47) films was obtained on Pt/Ti/SiO_2/Si at 500 °C for 2 h [5].

In the lead-based perovskite films, another effect has been implemented to promote the heterogeneous nucleation at the film/electrode interface and consecutively to lower the energy barrier for the nucleation of perovskite phase. Upon heating of the as-deposited ('gel') film, a reducing local atmosphere may form as a consequence of the oxygen consumption in the process of thermal decomposition/oxidation of organics. A fraction of Pb^{2+} species may be reduced to Pb^0. In case of films on platinized silicon substrates, a Pt_xPb intermetallic phase may form. The intermetallic phase serves as an efficient nucleation layer for the (111) oriented perovskite phase due to a good lattice match to the PZT [201]. Upon further heating the Pb^0 may re-oxidize again to Pb^{2+}. By implementing this approach, the (111) oriented PZT(30/70) films with the values of remanent polarization, P_r, coercive field E_C, and pyroelectric coefficient γ of 36 $\mu C/cm^2$, 66 kV/cm, and 1.8×10^{-4} $C/m^2 K$, respectively, have been prepared at 480 °C [4]. Perovskite crystallization temperature of 440 °C for 100 min for PZT(30/70) films has also been reported and it is attributed to the formation of a Pt_xPb interlayer [202]. By using 10 % excess PbO and either a 10 nm Pt or TiO_2 nucleation layer, perovskite crystallization at 400 °C for 5 min for PZT(30/70) and PLZT(5/30/70) has been reported [6]. Precursor solutions containing Bi_2SiO_5 with large molar ratios of this compound to the ferroelectric phase make possible the CSD crystallization of ferroelectric thin films at temperatures 150-200 °C lower than those of the original ferroelectric layer [203]. For example, 0.4 Bi_2SiO_5-0.6 $Bi_4Ti_3O_{12}$ system was successfully crystallized at 500 °C, while pure $Bi_4Ti_3O_{12}$ required crystallization

temperatures higher than 620 °C. Concomitantly, the control of the solution chemistry to increase the homogeneity at the molecular level and thus, reactivity of the precursor, has been used for the preparation of ferroelectric thin films at low temperatures as well [6, 7]. In this way, PZT crystalline thin films in the titanium rich part have been obtained at ~450 °C for very long annealing times and at 550 °C in the MPB region; similarly, lead free films (*e.g.* SBT) have been also prepared at ~600 °C. In general, the ferroelectric response of the films prepared by these low temperature methods are very weak, clearly denoting the incipient degree of crystallization of the perovskite films, what supports the reported need to post heat treat the films at higher temperatures. For example, SBT thin films crystallized at temperatures below 500 °C, required further annealing at 650 °C to improve film crystallinity in order to obtain saturated hysteresis loops [7].

Another approach to low temperature processing of thin films is a combination of sol-gel, or more generally CSD, and hydrothermal methods. This combination offers the advantages of both techniques, control of the film stoichiometry, thickness and temperature of crystallization. Amorphous gel films, containing Pb/Zr/Ti in the stoichiometric ratio corresponding to PZT(52/48), on platinized silicon substrate were immersed into the 2M KOH + 0.1M $Pb(OH)_2$ solution and hydrothermally treated in an autoclave at 160 °C for 1 h. The KOH supplied a large enough amount of OH^- ions for the reaction as the solubility of the $Pb(OH)_2$ was not high enough. The perovskite phase with (111) preferred orientation crystallized upon hydrothermal treatment. The authors proposed a dissolution-reaction-crystallization mechanism for the perovskite formation. The Pb-species dissolved in the KOH + $Pb(OH)_2$ mixture, while the dissolution of ZrO_2 and TiO_2 was slower, and consequently a porous skeleton of these two compounds remained on the substrate. PZT as the product of the hydrothermal reaction in the solution precipitated on the substrate. The as-prepared films had poor ferroelectric properties. However, after post-heating at 400 °C the $P_r = 26\ \mu C/cm^2$ and $E_C = 40.1$ kV/cm were obtained. The improvement was most probably due to the removal of the adsorbed water [204]. Besides PZT, $BaTiO_3$ films were also deposited at low temperatures using this approach. Similarly, post-annealing at 500 °C contributed to improved dielectric properties [205]. $Ba_xSr_{1-x}TiO_3$ (x = 1, 0.9, 0.7, 05, 0.3, 0.1, and 0) polycrystalline thin films were fabricated at low temperature (120 °C) and for a short time (1 h) by a hydrothermal process on commercial flexible polymeric Kapton films.

Electrical characterization of $BaTiO_3$ thin films showed dielectric constant of 140 and tanδ of 0.04 (at 100 kHz) for the films after post-annealing in oxygen at 200 °C [206].

Recently, an innovative synthesis strategy for the low temperature processing of ferroelectric thin films based on the photocatalytically assisted decomposition at room temperature of liquid precursors incorporating TiO_2 particles was reported. The photocatalytic effect induced by TiO_2 particles upon light absorption causes a modification on the molecular structure of the precursor, promoting the partial decomposition of organics and polycondensation among the metal reagents. PZT thin films fabricated by this method were crystallized at 350 °C on polyamide flexible substrate. The hysteresis curve of those films showed a remanent polarization of 5.5 $\mu C/cm^2$. This solution method was additionally used for the preparation of BFO multiferroic thin films. The formation of the perovskite phase was achieved at 325 °C together with the presence of the secondary crystalline phase $Bi_2Fe_4O_9$. The local piezoelectric hysteresis loops were obtained, in order to confirm the ferroelectric character of those BFO thin films on flexible substrates. However, no macroscopic ferroelectric or magnetic functionality was presented [207].

2.3.2. Modifications at the "post deposition processing level"

The most widely used methodology in this set of methods is processing by rapid thermal annealing (RTA), thus transferring to ferroelectric films a processing technology typical of the semiconductor industry [208, 209]. RTA is a flexible technology that provides fast heating and cooling to processing temperatures of ~200-1250 °C with ramp rates typically 20-200 °C/s, usually using infrared radiation [210]. In contrast to conventional furnace annealing with lower heating rates, typically less than 20 °C/min, RTA offers shorter processing time and excellent gas ambient control [211].

RTA of lead-based perovskite films minimizes the formation of fluorite/pyrochlore intermediate phases, detrimental substrate/film interfaces or volatilization of lead. Also, it greatly reduces the thermal budget required for crystallization, although the required process temperatures are still too high for some applications [8]. For example, PZT thin films prepared by CSD require annealing at 700 °C for 1 h in a conventional electric furnace and at 700 °C for 60 s, using a RTA [212]. In the meantime other alternative methods such as

laser-assisted crystallization [8, 213], and microwave-assisted crystallization [214], or laser lift-off [9] are being used for the preparation of ferroelectric thin films.

Laser-assisted crystallization makes use of the local heating generated by the laser for the crystallization of the electroceramic layer. In microwave-assisted crystallization the microwave energy is transferred to the material through molecular interactions with the electromagnetic field, resulting in a fast and uniform heating of the whole volume. The last method, laser lift-off implies the fabrication of the crystalline layer onto a UV-transparent host-substrate at a high temperature (1000 °C) and then a transference to the semiconductor substrate by UV laser radiation at a low temperature (~100 °C). Extensive and uniform films are not obtained by these methods, which difficult their industrial utilization.

Laser-assisted crystallization approach has not been widely used in processing of electroceramic thin films and the amount of studies in the literature is very limited. The reasons are poor thermal conductivity and a very high absorption coefficient of ferroelectric materials at excimer laser wavelengths, which may cause surface melting. Bharadwaja *et al.* used KrF laser to crystallize amorphous, sputter-deposited $(Pb_{1.048}La_{0.037})(Zr_{0.28}Ti_{0.72})O_{3.26}$ thin films on $LaNiO_3$ (LNO)-coated silicon substrates at temperature as low as 250 °C in oxygen atmosphere [8]. The best electrical properties were obtained upon activation of the films for 10 min at 400 °C at 200 mJ/cm^2. The dielectric constant, tanδ at 10 kHz, remanent polarization and coercive field were 406, 0.0027, 14 μC/cm^2 and 95 kV/cm, respectively. The author estimated the surface temperature of the film upon laser irradiation (pulse duration: 20 ns) to about 3400 K.

Wang *et al.* [214] reported the crystallization of perovskite $Pb(Zr_{0.52}Ti_{0.48})O_3$ films on platinized Si-substrates upon 28 GHz microwave heating at 480 °C. The 1 μm thick films were deposited from an acetate-alkoxide based solution with a 20 mol% PbO excess and pyrolyzed at 400 °C. The film crystallized in the perovskite phase with a strong (110) orientation. For comparison, the PZT films were also crystallized at 600 and 480 °C for 30 min using a conventional furnace. The PZT films crystallized at 480 °C for 30 min by conventional thermal processing exhibited a broad diffraction peak of (222) planes of the pyrochlore phase, and no peak of the perovskite phase was detected in the films. The PZT films crystallized at 600 °C for 30 min by conventional thermal processing exhibited a similar XRD pattern to that of the PZT films crystallized by microwave irradiation. The

dielectric permittivity, tanδ, remanent polarization and coercive field of the films were 1100, 0.04, 40 μC/cm^2 and 50 kV/cm, respectively.

In the case of BFO it was reported by Lee *et al.* that highly (100)-oriented BFO films were coherently grown on LNO-buffered Pt/TiO_x/SiO_2/Si substrate at a temperature as low as 300 °C [215]. In that work, the films were deposited by RF sputtering in a high vacuum system with a base pressure lower than 5×10^{-5} torr. The 200 nm thick BFO films were grown on LNO/Pt/TiO_x/SiO_2/Si and Pt/TiO_x/SiO_2/Si substrates. The target with a nominal composition of $Bi_{1.1}FeO_3$ was prepared by conventional ceramic procedure. The crystallization temperature of the pure BFO perovskite phase was effectively reduced from 350 °C (on Pt) to 300 °C by the LNO bottom electrode. The BFO films were (100)-oriented and randomly oriented on LNO and Pt substrates, respectively, and the crystallinity of the films were greatly improved by the use of LNO electrode [215]. However, this sophisticated physical vapor deposition methods are inappropriate for low cost mass production.

2.3.3. Photo Chemical Solution Deposition

Photo Chemical Solution Deposition (PCSD) technique was initially employed in the low-temperature processing of single oxide films, such as Ta_2O_5, ZrO_2 or SiO_2 [216, 217]. In the case of ferroelectric multioxide films, UV irradiation of sol-gel deposited layers has been used for the photo-patterning of the films [218-221]. Recently, PCSD was used and exploited for the fabrication of lead titanate based perovskite thin films [222]. PCSD is based on the use of sol gel precursors sensitive to the UV light [14] and on the use of UV radiation sources of high intensity (excimers lamps) [15] to catalyze the chemical reactions within the precursors towards the oxide crystallization. The photo excitation of certain organic compounds present in the sol-gel precursor solutions favors a rapid dissociation of alquil group-oxygen, reducing the temperature of formation of metal-oxygen-metal (M–O–M) of the final oxide material. This enhances the decomposition of the organic species within the film prior to the crystallization of the material by a further thermal annealing at a relative low temperature.

A schematic representation of the process is depicted in Figure 2-27. By this method, two phenomena are promoted in the films using UV light. First, the activation of chemical

bonds due to $\pi \rightarrow \pi^*$ electronic transitions would lead to the photo-excitation of the gel films. This enhances the quick decomposition and easier elimination of organic species from the system, thus advancing the crystallization of the films. On the other hand, ozonolysis would be produced when the films are irradiated under oxygen atmosphere. Oxygen (O_2) is readily dissociated under UV-light, forming active oxygen species O(1D) and subsequent development of ozone (O_3). Ozone is a strong oxidant agent that produces the rapid combustion of the organic compounds. The active oxygen species can react with suboxides present in the film, thus improving the stoichiometry and decreasing the density of defects and oxygen vacancies [223, 224]. Using PCSD, ferroelectric lead titanate and modified PT (lead substituted by alkaline earth or lanthanide cations) thin films were prepared at temperatures over 450 °C onto Si-based substrates [225-228]. This approach has not been used for the low-temperature fabrication of lead free multi-oxide ferroelectric thin films yet.

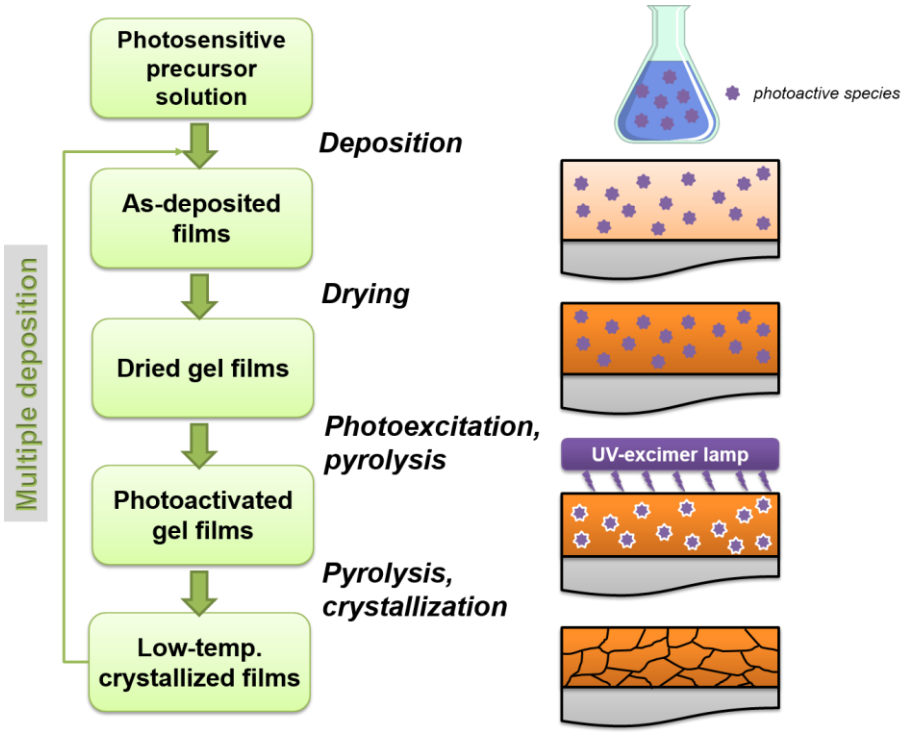

Figure 2-27. Flow chart of the Photochemical Solution Deposition technique.

2.3.4. *Seeded Diphasic Sol-Gel*

This methodology involves the utilization of diphasic precursor in which nanoparticles are dispersed and act as seeds to promote the nucleation of the perovskite phase in the thin films at low temperatures. Schematic illustration of Seeded Diphasic Sol-Gel (SDSG) method is presented in Figure 2-28. Perovskite PZT thin films were synthesized by this method at 410 °C, when using 5 mol% of seeds. Temperatures of 600-700 °C are common temperatures to obtain single phase PZT films without seeds [13]. The crystallization kinetics of PZT films were studied and the overall activation energy was reduced from 219 kJ/mol (unseeded) to 174 kJ/mol for 1 wt% seeded PZT film and to 146 kJ/mol for 5 wt% seeded PZT films [11]. Due to the presence of nanometric particles, the kinetics of the phase crystallization is enhanced. The multiple nucleation centers generated by the seeds change markedly the microstructure of the films and, consequently, improve their electrical properties. PZT thin films prepared at 430 °C by SDSG exhibit reasonable ferroelectric properties adequate for applications that require metallic or even polymeric substrates [12, 13, 201]. Concomitantly SBT thin films were prepared by this technique at 720 °C, while 800 °C is regular temperature to obtain single phase SBT without seeds [229].

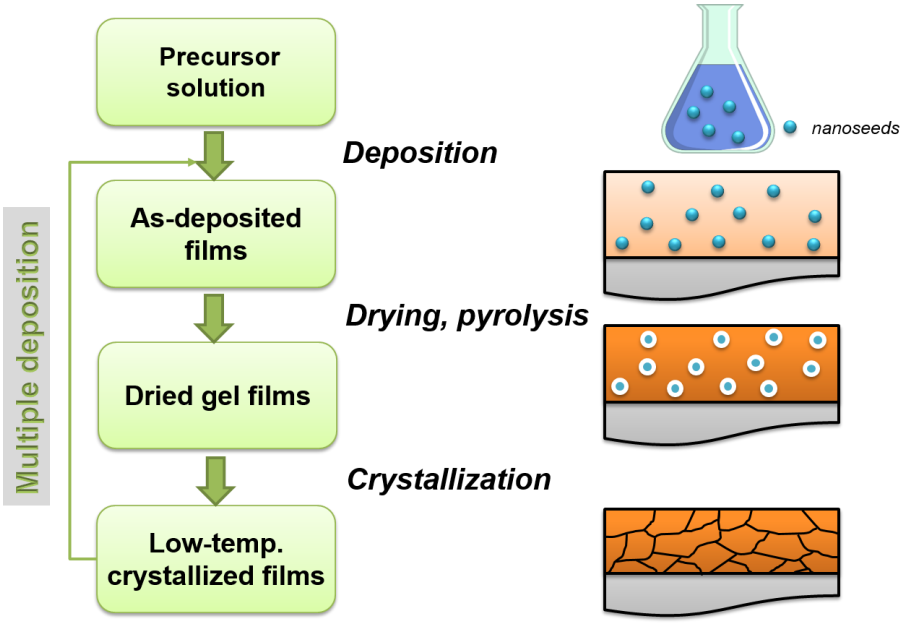

Figure 2-28. Flow chart of the Seeded Diphasic Sol-Gel technique.

2.3.5. Seeded Photosensitive Precursor Method

A novel solution method was presented very recently called Seeded Photosensitive Precursor Method developed by Paula Vilarinho and Lourdes Calzada research groups. This method enables the processing of functional oxides under low-temperature conditions that allows the compatibility of high temperature functional oxides with low temperature melting polymeric substrates [16]. The concept was presented for the most important multifunctional oxide, PZT. It reaches the lower limit temperature of crystallization at 300 °C, using a strategy that combines seeded diphasic precursors and photochemical solution deposition.

In this method Seeded Photosensitive Precursor Method, the "photoactive sol" displays an increased absorption in the UV-range. Elimination of organic compounds from these photosensitive systems is known to be accelerated by the irradiation due to (i) ozonolysis and (ii) the prompt dissociation of the alkyl group–O bonds with the subsequent formation of the metal-O-metal bonds Incorporation of seeds into the photoactive sol ("photoactive sol + seeds"), increases the number of nucleation sites in the resulting film, which produces a further reduction of the crystallization temperature.

The mechanism proposed for the low-temperature processing of PZT thin films by Seeded Photosensitive Precursor Method is shown in Figure 2-29.

A remarkable enhancement in the formation of the ferroelectric PZT perovskite is inferred for the films prepared using strategy that combines seeded diphasic precursors and photochemical solution deposition. The large UV-absorption of the gel layer together with the crystalline nanoseeds contained in it, decrease the Gibbs free energy barrier for the perovskite nucleation, leading to a significant reduction in the crystallization temperature of the films. This made the deposition of inorganic ferroelectrics on low-melting point substrates possible. Ferroelectric response of PZT thin film directly deposited onto the flexible polyimide with remanent polarization values of $P_r \sim 15\ \mu C/cm^2$ was presented (Figure 2-30) [16]. This method was not applied to produce lead free multi-oxide thin films.

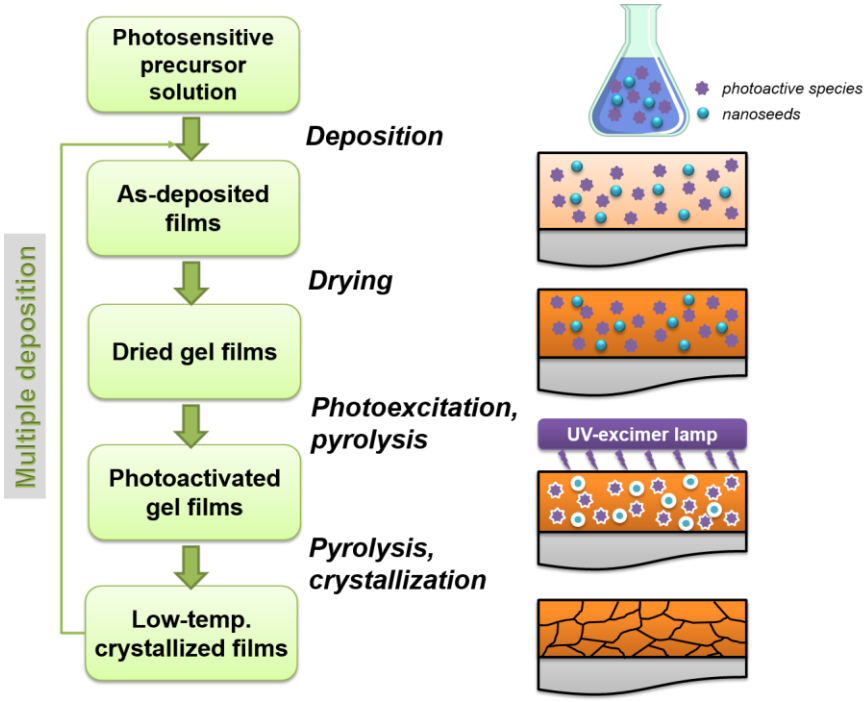

Figure 2-29. Flow chart of Seeded Photosensitive Precursor Method that combines PCSD and SDSG techniques.

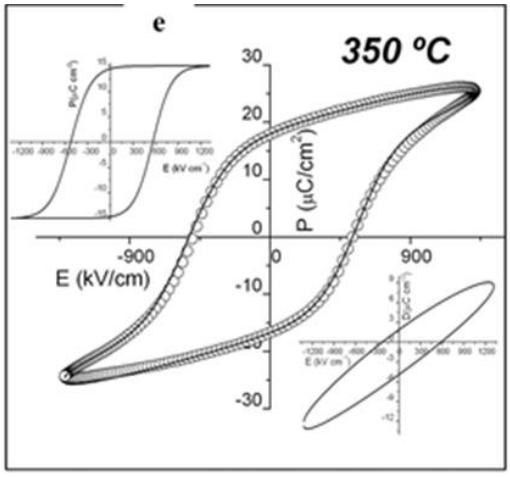

Figure 2-30. Ferroelectric hysteresis loop of a PZT film on flexible polyimide with a thickness of ~190 nm, showing values of P_r ~ 15μC/cm², from the compensated loop; the upper inset corresponds to the compensated ferroelectric hysteresis loop, and the lower inset corresponds to the non-switching contribution to the polarization [16].

2.4. Summary

Thin film ferroelectrics have received wide attention because of their growing use as non-volatile memories, pyroelectric detectors, miniaturized piezoelectric transducers and tunable microwave devices and currently PZT is most widely used material. The major problem with PZT is toxicity of lead. Therefore, lead free materials have great attention due to environmental and health concerns to replace lead based ones. This chapter reviewed the properties of various lead based and lead free families. Among these, BFO and NBT are promising material, based on the high Curie temperature and multi-functionality (multiferroic BFO). Therefore, BFO and NBT perovskites were selected to prepare in this work. Table 2-4 presents some of their structural, physical and chemical characteristics in comparison with PZT.

An overview of the state-of-the-art of the knowledge on BFO and NBT was presented. Limitations for these compounds are related to the high annealing temperatures necessary for the crystallization of these perovskite phases and volatilization of Bi at the temperatures required for the film fabrication. Bi volatilization leads to secondary phases or non-stoichiometry in BFO and NBT and determines the reproducibility of the electrical response. This emphasises the need for the low temperature fabrication method. Moreover, the reported properties of polycrystalline BFO thin films are strongly processing dependent, therefore systematic studies on the phase formation, microstructure and functional properties are desired.

Table 2-4. Some of the structural, physical and chemical characteristics of NBT [50] and BFO [54, 55], as well as PZT [52].

	NBT	**BFO**	**PZT-4/5A/5H**
Density (g/cm^3)	5.98	8.34	7.4-7.7
Crystallographic data:			
Crystal system (at RT):	rhombohedral	rhombohedral	rhombohedral/ tetragonal – MPB (morphotropic phase boundary)
Space group(at RT):	*R3c*	*R3c*	
Lattice parameters (at RT):	a_{hex} = 5.4887 Å, c_{hex} = 13.5048 Å	a_{hex} = 5.5779 Å, c_{hex} = 13.8670 Å	
Curie temperature, T_C (°C)	320	830	330
Neel temperature, T_N (°C)	-	370	-
P_r (μC/cm^2)	40 (single crystal)	60 (single crystal)	12-31
E_C (kV/cm)	28 (single crystal)	12 (single crystal)	5-15
d_{33}	60 (single crystal)	60	225-585

PZT-4/5A/5H – Navy type I, II and VI commercial ceramics.

Chapter 3. EXPERIMENTAL METHODS

Abstract: This chapter describes the experimental strategy followed to fulfil the defined objectives of this thesis. The materials under study include NBT and BFO. The synthesis techniques used comprise chemical solution deposition as well as hydrothermal for nanoparticle processing. The different fabricated thin films and nanoparticles were characterized by a variety of techniques that include: thermal analyses (DTA/TG), X-Ray diffraction (XRD), Raman spectroscopy, Scanning Electron Microscopy (SEM), Transmission Electron Microscopy (TEM), UV-Vis spectroscopy, Scanning Probe Microscopy (SPM), and others. For each composition the particularities of the experimental procedure are described in detail later in the corresponding chapters.

3.1. Experimental procedures

This chapter presents a detailed description of the experimental methods applied for the processing and characterization of the as-prepared thin films and powders.

Chemical solution deposition, as the main synthesis approach, is briefly introduced, and experimental protocols used for BFO and NBT precursor solutions preparations and films deposition are presented. Hydrothermal process for nanoparticles fabrication is also described.

3.1.1. Chemical solution process

Chemical solution deposition (CSD) synthesis is a technique widely used to fabricate electronic oxide thin films [138]. CSD typically begins with the solution synthesis. The main precursors are salts, carboxylates, or other metallo-organic compounds such as metal alkoxides and metal β-diketonates. The precursors are dissolved in appropriate solvents, sometimes with intermediate distillation steps, and mixed in the correct stoichiometric ratio. Therefore, precursor solutions are obtained, which usually contain the desired thin film stoichiometry. Often additives such as chemical stabilizers are added during synthesis to adjust the properties of the final coating solution. In chemical solution deposition, thin films are usually deposited through spin coating or dip coating of the solution on a substrate. After deposition, the as-deposited films are amorphous and contain solvents and organics. To obtain the crystalline phase, generally the film is first heat treated at low temperature (200-400 °C) for drying and organic pyrolysis and then subjected to higher temperature (500-700 °C) for crystallization and densification [80]. CSD has some unique advantages such as: i) stoichiometric and homogeneous composition can be obtained due to the reactions at the molecular level, ii) it can be used to fabricate large film areas, and iii) deposition methods are inexpensive; *i.e.* spin coating and dip coating are very attractive for industrial production [138].

The principles and the examples of metal oxide thin films processing by chemical solution deposition are well described elsewhere [230]. Chemical solution deposition

method was used to obtain thin films of BFO and NBT in the current work, as presented in Figure 3-31.

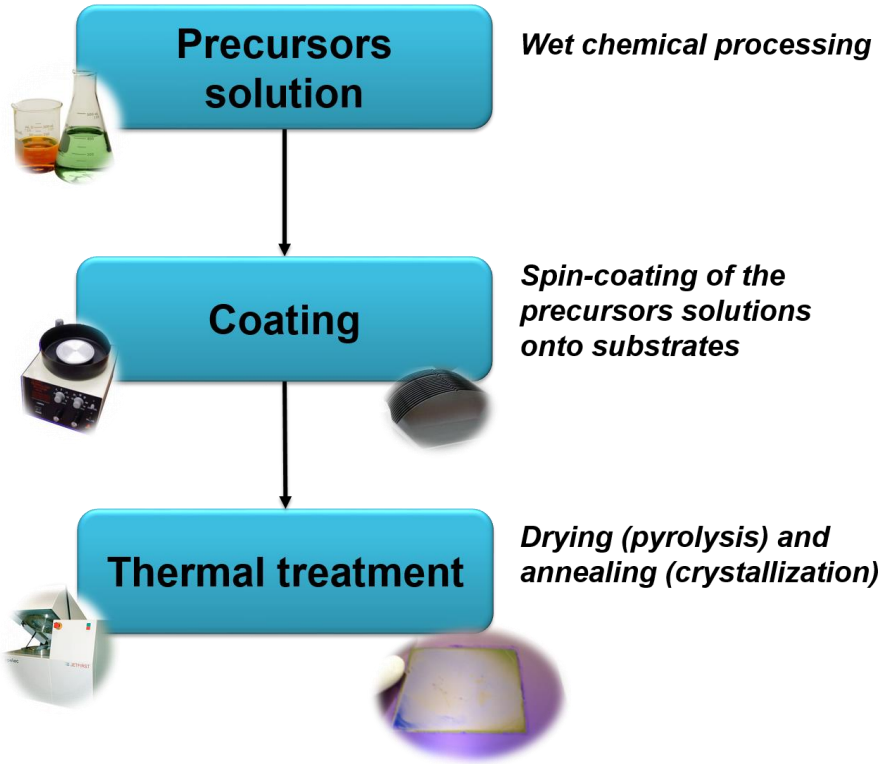

Figure 3-31. Thin films preparation via chemical solution deposition.

3.1.1.1. Precursor solutions preparation

BFO precursor solution was prepared using bismuth nitrate ($Bi(NO_3)_3 \cdot 5\ H_2O$, Sigma Aldrich, 99.99 %) and iron acetylacetonate ($Fe(CH_3COCHCOCH_3)_3$ – $Fe(acac)_3$, ABCR, 99 %). Acetic acid ($C_2H_4O_2$ – AcOH, Merck, 100 %) and 1,3 propanediol ($C_3H_8O_2$, Aldrich, 98 %) were used as solvents. The scheme of BFO precursor solution preparation is illustrated in Figure 3-32.

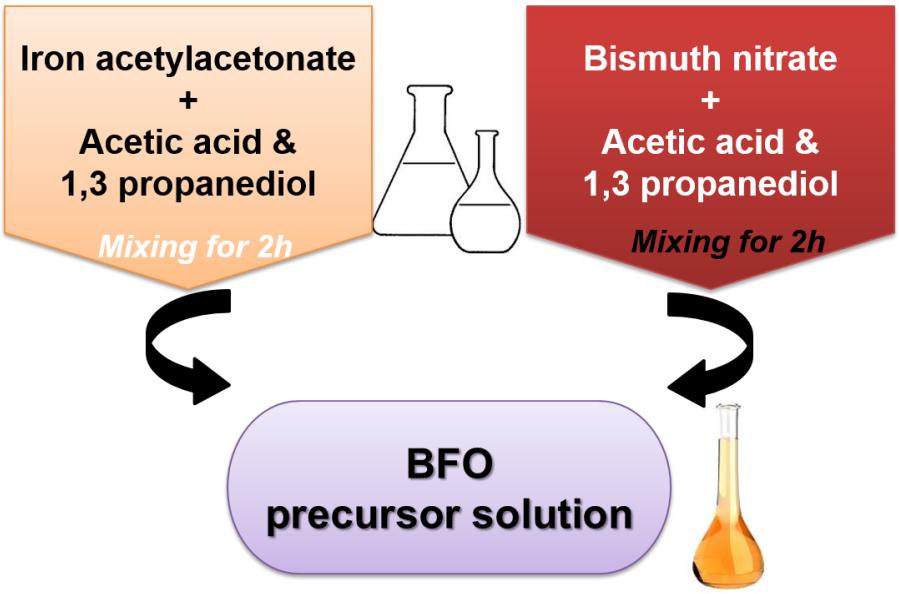

Figure 3-32. BFO precursor solutions preparation via sol-gel process. Detailed experimental protocol is described in text.

Firstly, bismuth nitrate and iron acetylacetonate were dissolved in a mixture of glacial acetic acid and 1,3 propanediol (4:1 vol. ratio) separately, by mixing at room temperature. Then, individual solutions were joined into one glassware and further stirred for 12 h to form a fine solution with the concentration of 0.125M. Solutions containing a 5 mol% excess of Bi(III) and without excess were prepared. The acetylacetonate ligand of the iron reagent provides an appreciable photosensitivity to these BFO solutions (Figure 3-33). The absorption band corresponds to the $\pi \rightarrow \pi^*$ electronic transition of acetylacetonate complexes. Elimination of organic compounds from the photosensitive wet films is known to be accelerated by the certain light irradiation leading to ozonolysis and then to dissociation of the alkyl group–O bonds with the subsequent formation of the metal–O–metal bonds (electronic excitation) [16].

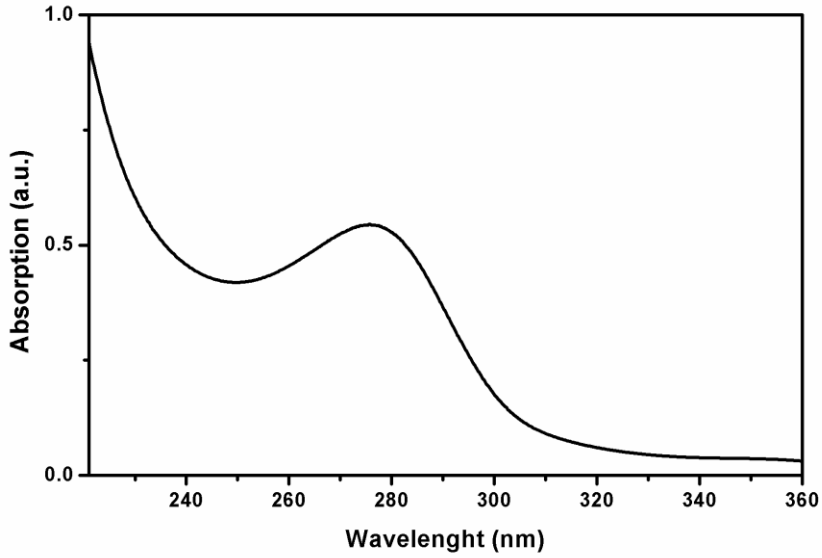

Figure 3-33. UV-absorption spectrum of BFO precursor solution. The absorption band at ~275 nm corresponds to the $\pi \rightarrow \pi^*$ electronic transition of acetylacetonate complexes that activate decomposition of metal precursors and oxidation of organic species while UV-irradiated.

Sodium acetate ($NaOOCH_3$ - NaOAc, Sigma-Aldrich, 95 %), bismuth acetate ($Bi(COCH_3)_3$ – BiOAc, ABCR, 99 %) and titanium tetra isopropoxide ($Ti[OCH(CH_3)_2]_4$ – $Ti(OiPr)_4$, Fluka, 97 %) were chosen as starting organic precursors in the sol-gel process, for the synthesis of NBT together with absolute ethanol (HOC_2H_5 - EtOH, Merck 99.9 %) as a solvent. Acetic acid ($C_2H_4O_2$ – AcOH, Merck, 99.8 %), 1,2 propanediol ($C_3H_6O_2$, Riedel-de Haen, 99.5 %) and acetylacetone ($C_5H_8O_2$ – Hacac, Merck, 99 %) were added to stabilize the sols. The scheme of NBT sol preparation is illustrated in Figure 3-34. Firstly, bismuth acetate and sodium acetate were refluxed for 3 h in air in a mixture of 1,2 propanodiol and acetic acid. Titanium tetra isopropoxide was refluxed in acetylacetonate for 5 h in air. Then, individual solutions were joined into one glassware and mixed for 3 h at 70 °C. The stable sols were further diluted with ethanol to 0.3M and 0.2M concentrations.

Figure 3-35 presents UV-absorption spectrum of the NBT solution. A maximum in the UV-absorption at <280 nm is observed, which is in the range where the acetylacetonate groups absorb UV-light. Thus, the use of acetylacetone in the synthesis procedure provides NBT solutions, which are photosensitive under UV light, as in the case of BFO.

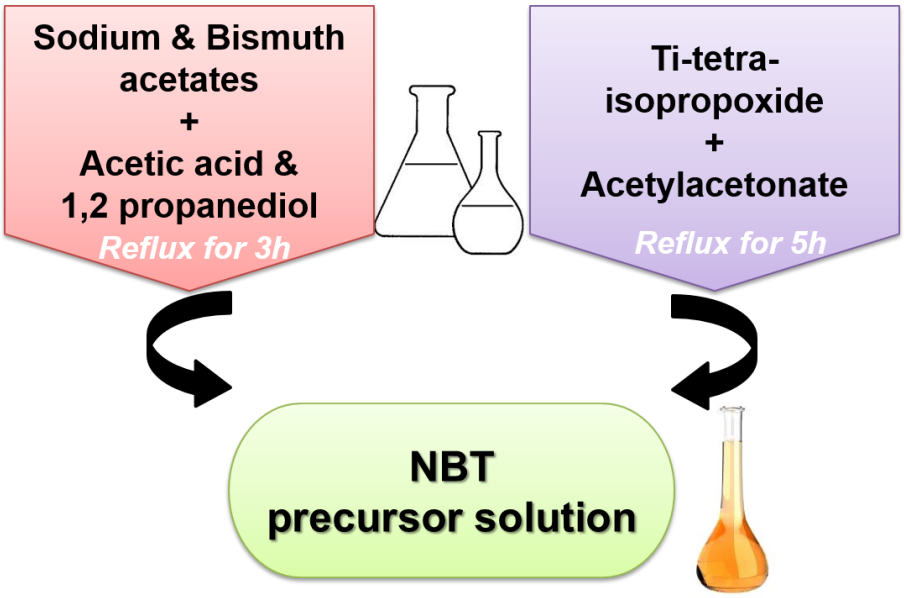

Figure 3-34. NBT precursor solutions preparation via sol-gel process. Detailed experimental protocol is described in text.

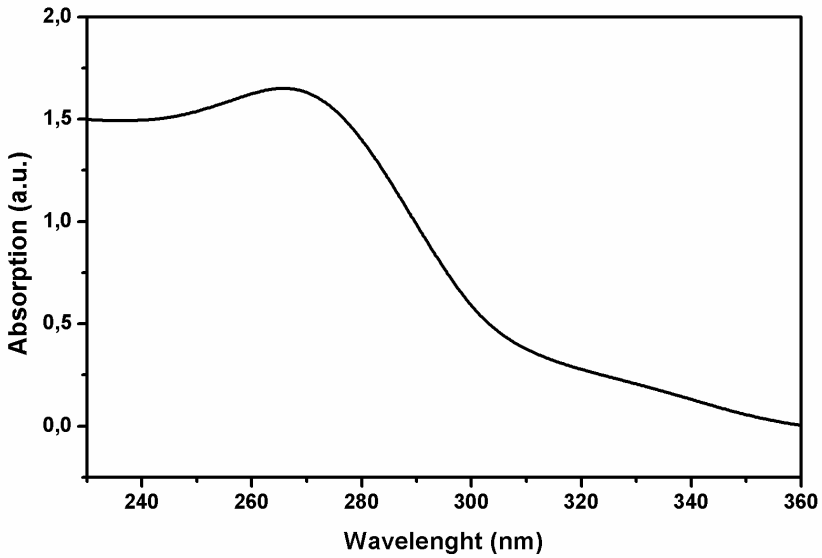

Figure 3-35. UV-absorption spectrum of NBT precursor solution. The absorption maximum at ~270 nm matches to the π → π electronic transition developed by the acetylacetonate molecules.*

Summary of the used precursors, solvents and experimental conditions for BFO and NBT solutions preparations are listed in Table 3-5.

Table 3-5. Experimental details of BFO and NBT precursor solutions preparation by solution methods.

	Metal precursors	**Solvent / modifiers**	**Remarks**
BFO	$Bi(NO_3)_3 \cdot 5\ H_2O$, $Fe(acac)_3$	AcOH, 1,3 propanediol	Mixing at room temperature
NBT	NaOAc, BiOAc, $Ti(OiPr)_4$	EtOH, AcOH, Hacac 1,2 propanediol,	Reflux (3 h + 5 h)

3.1.1.2. Thin films deposition – spin-coating

Precursor solutions have been deposited onto distinct substrates, depending on processing objectives. Primarily, platinized Si substrate was used: $Pt/TiO_2/SiO_2/(100)Si$ provided by Inostek, Inc., or Radiant Technologies, Inc.

For the studies on bottom electrode effects (Chapters 4.3 and 4.4), additionally commercial $IrO_2/TiO_2/SiO_2/(100)Si$ (Inostek, Inc.) were used, as well as LNO coated Pt-Si. LNO was deposited on commercial Pt-Si by CSD method. LNO was synthesized as follows: lanthanum nitrate hexahydrate ($La(NO_3)_3 \cdot 6H_2O$, Merck, 99 %) and nickel (II) nitrate hexahydrate ($Ni(NO_3)_2 \cdot 6H_2O$, Fluka, 98.5 %) were dissolved respectively in 5 ml of deionized water, and mixed in the stoichiometric ratio of La:Ni=1:1. To improve the solution wettability and avoid film cracking during heating 1 ml of formamide ($HCONH_2$, Merck, 99.5 %) was used. Finally, ethanol absolute (Merck, 99.8 %) was added until the resultant concentration of LNO solution was diluted to 0.2M. LNO films were deposited by spinning the solution on $Pt/TiO_2/SiO_2/Si$ substrates at 2500 rpm for 45 s and annealed by RTA at 700 °C for 5 min in O_2 atmosphere.

For the low temperature (<350 °C) preparation of BFO films (Chapter 4.5), flexible substrates were used: UPILEX-75S polyimide film; thickness of the substrate of 75 μm

(UBE Europe GmbH). Metallization of the bare polyimide substrate by successive layers of NiCr (nichrome alloy) and Pt (by sputtering) was performed for protection and metallization of the flexible plastic substrate.

All the substrates were cleaned using the same protocol: firstly, for 2 min in acetone (CH_3COCH_3, Panreac) and then for 2 min in 2-propanol ($CH_3CHOHCH_3$, Panreac, for analysis).

The deposition of the NBT and BFO thin films has been carried out by spin-coating. Glass syringes equipped with filters (Millipore) of 0.2 μm pore size were used for the deposition of the solutions. The commercial precision KW-4A Spin Coater (Chemat Technology, Inc.; located at DEMaC, University of Aveiro; 2500 rpm for 45 sec) or TP 6000 gyrset system (SET-Micro-Controle group model; located at ICMM-CSIC, Madrid; 1500-2500 rpm for 45 sec) were used for films deposition.

The wet films were dried and pyrolysed on a hot-plate at either 150 °C followed by 250 °C for 1 min, or 350 °C for 1 min. UV assisted drying/pyrolysis was implemented in PCSD using laboratory-scale prototype combining a high-intensity UV excimer lamp (Heraeus, BlueLight Excimer System, 222 nm wavelength) with an ultra-fast heating system (Watlow, UltramicTM 600 advanced ceramic heater) in oxygen atmosphere at 250 °C for 30 min, prior to the crystallization at different temperatures.

All the films prepared were crystallized by Rapid Thermal Processing (RTP, RTA) using Jetstar 100T JIPELEC (or Qualiflow JetFirst 100) equipment. A heating rate of 30 °C/s was used for the treatments, which were carried out in air for BFO or oxygen for NBT. The preparation of some of the NBT and BFO films has been carried out at the ICMM-CSIC Madrid, in a 100 class clean-room (less than 100 particles with <0.5 μm diameter per m^3) with a laminar flux hood (CAM-1300-V) and a sterile air circulator unit (Telstar FFU).

3.1.2. Hydrothermal preparation of seeds

Hydrothermal synthesis is a technique that Yoshimura defined as "... reactions occurring under the conditions of high temperature (>100°C) and high pressure (>1 atm) in aqueous solutions in a closed system" [231]. The main advantage of the hydrothermal synthesis method is the ability to process crystals of substances, which are unstable, near the

melting point. There is also a group of solvothermal synthesis methods, which is based on the use of organic solvents instead of water [232]. The main parameters of hydrothermal synthesis, which define both the processes kinetics and the properties of resulting products, are: i) initial pH of the medium, ii) duration and temperature of synthesis, and iii) pressure in the system. The synthesis is carried out in autoclaves, which are sealed cylinders.

BFO powders to be used as seeds were prepared by hydrothermal method [233], as illustrated in Figure 3-36. The chemical regents used to prepare BFO nanoparticles were bismuth nitrate ($Bi(NO_3)_3 \cdot 5H_2O$, Sigma Aldrich, 99.99 %), iron nitrate ($Fe(NO_3)_3 \cdot 9H_2O$, Sigma Aldrich, 98 %), potassium nitrate (KNO_3, Fluka, 98 %), poly(vinyl alcohol) (PVA, Sigma Aldrich, 98 %), and potassium hydroxide (KOH, ABCR, 85 %). The mineralizer-assisted hydrothermal process included the following steps: 0.005 mol $Bi(NO_3)_3 \cdot 5H_2O$ and 0.005 mol $Fe(NO_3)_3 \cdot 9H_2O$ were dissolved in 100 ml diluted HNO_3 (10 %) to form aqueous solutions. Then, the (12M) KOH solution was slowly added to the above solution to adjust its pH value to ~8 by constant stirring, and brown precipitates were formed. The precipitates were filtered and washed with distilled water to remove NO_3^- and K^+ ions. Then, precipitates were mixed with 30 ml KOH solutions (12M) and 15 ml PVA (4 g/l) solutions under constant magnetic stirring for 5 min. The suspension solution was transferred into Teflon lined stainless-steel autoclave for the hydrothermal treatment. The autoclave was sealed and maintained at 160 °C for 9 h. The obtained BFO powders were filtered and washed with distilled water and absolute ethanol several times, and then dried at 70 °C for 12 h.

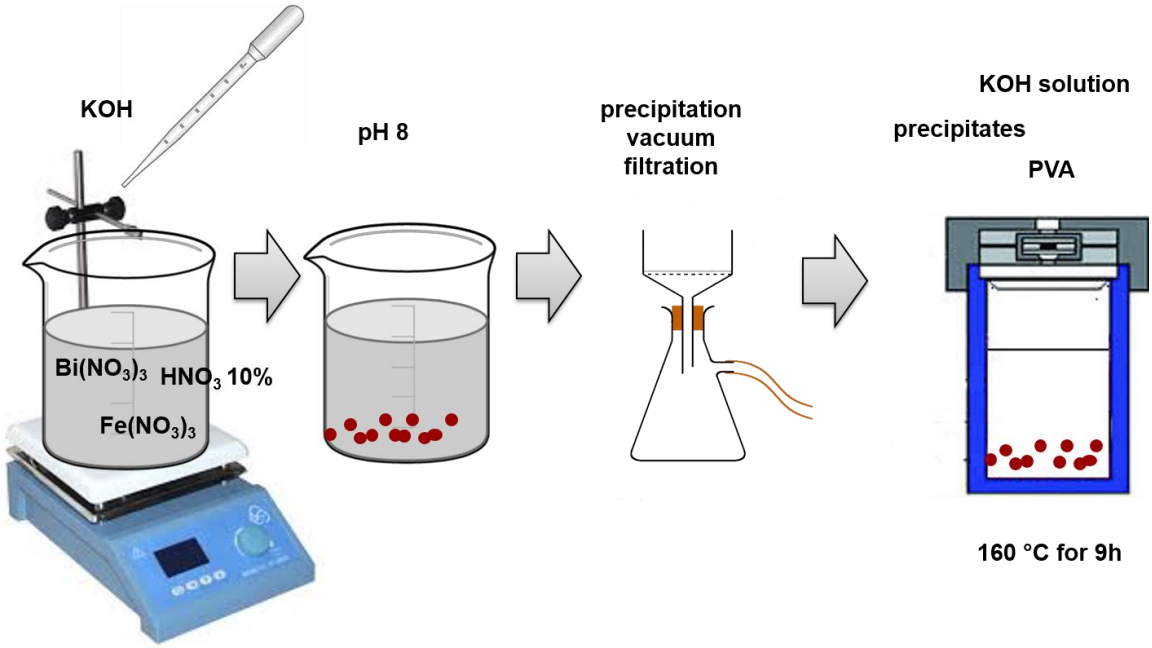

Figure 3-36. Scheme presenting the protocol for hydrothermal synthesis of BFO nanoparticles.

3.2. Characterization techniques

In the present work, various advanced characterization techniques have been used in order to determine the structural, microstructural, and electrical properties of as-prepared materials.

3.2.1. Thermal analyses

Differential thermal analysis (DTA) and thermogravimetric analysis (TG) are some of the most basic techniques, and listed among the powerful tools to evaluate the behavior of a material as a function of temperature. From the DTA and TG plots, various information can be extracted, among them: thermal stability, chemical and physical reactions (exothermic or endothermic), phase formation and transition, glass transition temperature, melting temperature, among others [234].

The working principle of DTA is based on the heat loss or gain due to the structural changes in the material as a function of temperature or time. DTA equipment uses two set of identical containers, one for the reference (generally, empty alumina crucible) and other for the sample. Both the columns undergo similar thermal cycle, while recording any temperature difference between the reference and the sample by thermocouples equipped within the chamber. These temperature changes occur due to the endothermic or exothermic reactions in the sample [234].

TG is a technique in which the mass of a sample is measured as a function of temperature while heating or cooling the sample at some predetermined and defined rate. Phenomena that can be studied by TGA can be easily grouped into mass gain processes (absorption, adsorption or oxidation) and mass loss processes (dehydration, vaporization, decomposition or reduction) [234]. Consequently, it can provide information about physical phenomena (phase transitions such as sublimation, desorption, *etc.*), chemical phenomena (chemisorption) and solid-gas reactions (oxidation, reduction).

Setaram Labsys DTA/TG instrument was used from ambient temperature to 800 °C with a heating rate of 10 °C/min.

3.2.2. X-ray Diffraction

Max von Laue, in 1912, discovered that crystalline substances act as three-dimensional diffraction gratings for X-ray wavelengths similar to the spacing of planes in a crystal lattice. XRD is now a common technique for the study of crystal structures and atomic spacing [235].

X-ray diffraction is based on constructive interference of monochromatic X-rays and a crystalline sample. These X-rays are generated by a cathode ray tube, filtered to produce monochromatic radiation, collimated to concentrate, and directed toward the sample. The interaction of the incident rays with the sample produces constructive interference (and a diffracted ray) when conditions satisfy Bragg's Law:

$$n\lambda = 2d \sin\theta \quad (3)$$

where: λ is the wavelength of the X-rays, d is the spacing of the crystal layers, θ is the incident angle, and n is an integer. This law relates the wavelength of electromagnetic radiation to the diffraction angle and the lattice spacing in a crystalline sample. These diffracted X-rays are then detected, processed and counted. By scanning the sample through a range of 2θ angles, all possible diffraction directions of the lattice should be attained due to the random orientation of the powdered material. Conversion of the diffraction peaks to *d*-spacings allows identification of the mineral because each mineral has a set of unique *d*-spacings. Typically, this is achieved by comparison of *d*-spacings with standard reference patterns.

The characterization of thin films using the conventional symmetrical Bragg Brentano configuration (θ/2θ) generally produces weak signals from the film itself and intense signal from the substrate, which is why it is not suitable. In these cases, it is convenient to use the technique of X-ray diffraction at grazing incidence to minimize the contribution related to the substrate [235].

In this geometry, the incident angle (ω) is fixed at a small angle (exceeding the critical angle of total reflection, typically between 1 and 3°) and the angle between the incident beam and the diffracted beam (2θ) is varied, moving only the detector arm. Thus, the incident beam goes over a long way on the film surface or interest, reinforcing its diffraction pattern, while the signal from the substrate is reduced due to the small incident angle. Under these

conditions, it can be shown that the depth of analysis (*z*), when alpha is very small, does not depend on the 2θ angle and, in that case, the depth of analysis is controlled by the angle of incidence and does not vary during the sweeping.

Unlike conventional powder diffraction geometry, which observes planes parallel to the surface of the sample, in the case of grazing incidence crystal planes inclined with respect to the surface of the sample are observed (GI-XRD), whose normal is the bisector of the angle formed by the incident and the diffracted beam (Figure 3-37). So, it is not suitable for studying orientation [235].

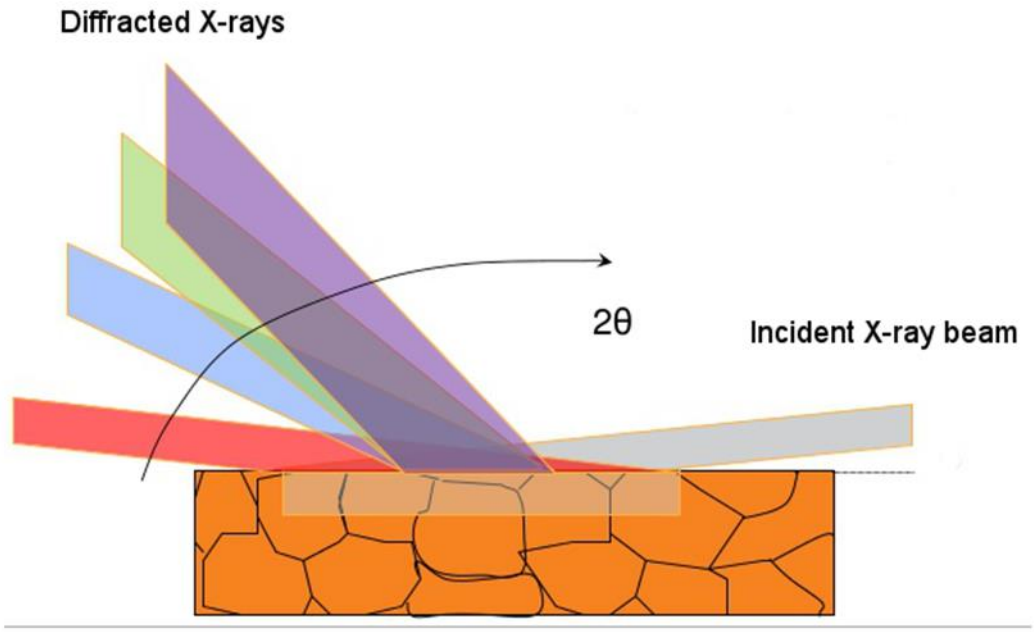

Figure 3-37. Scheme of grazing incidence XRD experiment.

In this work, powder measurements were performed by XRD with a Rigaku (D/Max-C series) X-Ray diffractometer, using Cu-Kα radiation (0.15064 nm), equipped with MDI data scan 3.2 controller software. The XRD was typically operated at 40 kV and 30 mA. The configuration of XRD experiment was θ/2θ scan technique adopted to collect diffraction intensity data with Cu-Kα radiation at rate 1 °/min. with step 0.02° between 10-60°. The X-ray patterns where processed afterward using Jade 8.0 software. The analysis of thin films was performed using PANalytical X'Pert Pro instrument, and XRD patterns were recorded using small angle geometry configuration (GI-XRD, an incidence angle, ω = 2°), in order to

suppress the substrate contribution. The XRD patterns were analyzed using HighScore Plus software.

3.2.2.1. Stress analysis by XRD

The components of the macroscopic mechanical stress tensor of a stressed thin film, coating, multilayer or the region near the surface of a bulk material can in principle be determined by XRD. The basic idea is sketched in Figure 3-38, where it is assumed that a polycrystalline specimen is subjected to a compressive stress parallel to the surface. Due to the presence of stress, the lattice spacing of the *hkl* lattice planes in a crystallite depends on the orientation of the crystallite in the specimen with respect to the specimen frame of reference [236].

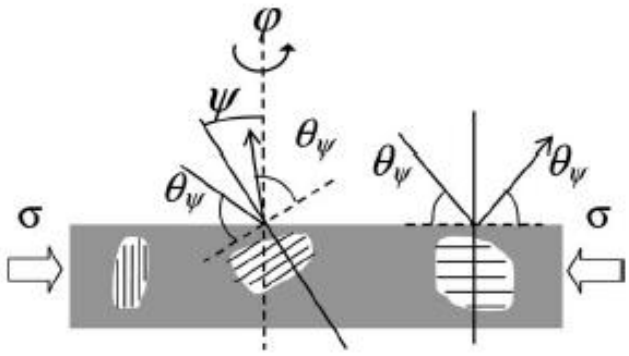

Figure 3-38. Concept of diffraction stress analysis [236].

In this thesis sin2ψ method was used. This method is based on the measurements of the shifts in the angle of diffraction by the planes, Δθ, due to changes in the inter-planar spacing, Δ*d*, caused by strain. By measuring the changes to the shifts in diffraction angles, we are able to deduce the strain, hence the stresses involved with formulas usually derived from linear isotropic elasticity theory. The relationship between inter-planar spacing and stress in a biaxial isotropic material is as follows [236]:

$$\sigma_{\phi} = \frac{E}{(1+\nu)\sin^2\psi}\frac{(d_{\psi} - d_n)}{d_n} \qquad (4)$$

where d_n is the measurement made in a plane normal to surface, d_ψ is the measurement made at a certain ψ direction, ψ is the angle between the surface normal and the direction of the strain being measured, E is the Young's modulus, and v is the Poisson's ratio.

In this method, a number of XRD measurements was made at different ψ tilts. Inter-planar spacing is plotted in a d vs sin2ψ plot. Assuming a zero stress at $d = d_n$, where d is the y-intercept, stress is given by:

$$\sigma_\phi = \left(\frac{E}{1+v}\right) m \quad (5)$$

where m is the gradient of the d vs sin2ψ plot. By substitution of the gradient, known E and v values of the films into equation, the stress in each film can be derived. Using this method, we assume our films are isotropic, and stresses normal to the substrate are zero.

3.2.3. Electron Microscopy

3.2.3.1. Scanning Electron Microscopy

The Scanning Electron Microscope (SEM) is an instrument that produces a largely magnified image by using electrons instead of light to form an image. A beam of electrons is produced at the top of the microscope by an electron gun. The electron beam follows a vertical path through the microscope, which is held within a vacuum. The beam travels through electromagnetic fields and lenses, which focus the beam down toward the sample. Once the beam hits the sample a variety of signals is produced. These signals include secondary electrons (that produce SEM images), backscattered electrons (BSE), diffracted backscattered electrons (EBSD that are used to determine crystal structures and orientations of minerals), photons (characteristic X-rays that are used for elemental analysis) visible light and heat. Secondary electrons and backscattered electrons are commonly used for imaging samples. Secondary electrons are most valuable for showing morphology and topography on samples and backscattered electrons are most valuable for illustrating contrasts in composition in multiphase samples [237].

In the current thesis SEM was used to characterize powders and thin films. For interface study, cross-sections of the films were prepared. For this, film's samples were cut and fixed

in a special sample holder using a conductive carbon paste. The samples were oriented with the surface up and lateral up in order to analyze the surface (plan view) and the interface (cross section) of the films, respectively.

The carbon deposition process was performed using an Emitech K950 carbon deposition chamber equipped with a turbo pump; 2-3 cycles with evaporation time of 1.2 s at ~9×10^{-3} mbar. Hitachi S-4100 and Hitachi SU-70 SEM/EDS microscopes were used to study the materials developed in this work.

3.2.3.2. Transmission Electron Microscopy

The Transmission Electron Microscope (TEM) has become the premier tool for the microstructural characterization of materials. The first practical TEM was built by Albert Prebus and James Hillier at the University of Toronto in 1938 using concepts developed earlier by Max Knoll and Ernest Ruska [238]. Since then, TEM has had considerable development and recently has become a versatile tool of characterization in material science and biology. The acceleration voltage of a routine instrument is 100-400 kV. Electrons are emitted in thermionic, Schottky, or field emission electron gun. A three- or four-stage condenser-lens system permits variation of the illumination aperture and the area of the specimen illuminated. The electron intensity distribution behind the specimen is imaged with a lens system, composed of three to eight lenses, onto a fluorescent screen. The image can be recorded by direct exposure of a photographic emulsion or an image plate inside the vacuum, or digitally via a fluorescent screen coupled by a fiber-optic plate to a CCD camera. Schematic of a transmission electron microscope is presented in Figure 3-39.

There are different conventional image modes in which the TEM can work [239]:

- Bright-Field (BF)
  - ✓ objective aperture passes the transmitted beam;
  - ✓ intermediate aperture is removed;
  - ✓ image is made of the image plane of the objective lens.
- Dark-Field (DF)
  - ✓ same as bright-field except objective aperture passes a diffracted beam.

- Selected Area Diffraction (SAD)
  - ✓ objective aperture is removed;
  - ✓ intermediate aperture passes the image of a selected region;
  - ✓ image is made of the back focal plane of the objective lens.

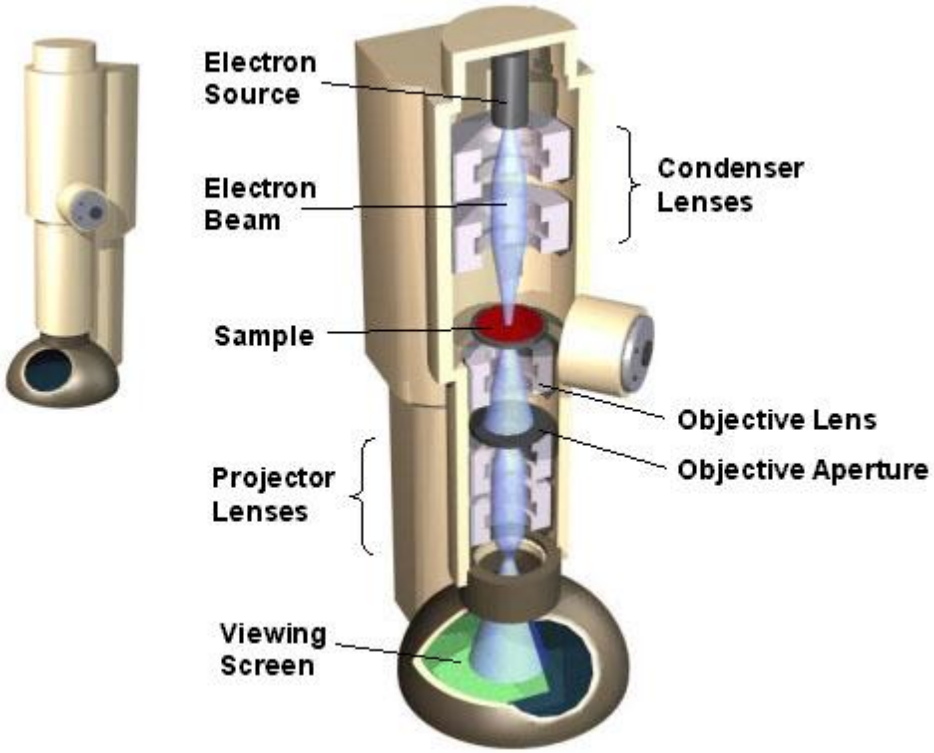

Figure 3-39. Schematic representation of a construction of TEM (http://barrett-group.mcgill.ca/tutorials/nanotechnology/nano02.htm).

Besides diffraction and spatial imaging, the high-energy electrons in TEM cause electronic excitations of the atoms in the specimen. "Analytical TEM" uses two types of spectrometry techniques to obtain chemical information from electronic excitations:

- In energy-dispersive X-ray spectrometry (EDS), an X-ray spectrum is acquired from small regions of the specimen illuminated with a focused electron beam, usually using a solid-state detector. Characteristic X-rays from the chemical elements are used to determine the concentrations of the different elements in the specimen.

- In electron energy-loss spectrometry (EELS), energy losses of the electrons are measured after the high-energy electrons have traversed the specimen. Information on local chemistry and structure is obtained from features in EELS spectra caused by plasmon excitations and core electron excitations [239].

A more detailed description of TEM operation can be found elsewhere [240].

3.2.3.3. Scanning Transmission Electron Microscopy

Scanning Transmission Electron Microscopy (STEM) combines the principles of transmission electron microscopy and scanning electron microscopy. STEM techniques can be generally described as sequential scans of a very finely focused electron beam over a selected region of the sample in a raster pattern [241].

The primary STEM imaging modes are differentiated based on the angle of the scattered electrons used to form the image. The most common mode uses an annular detector with an inner diameter set to collect electrons which have scattered more than 80 mrad known as a high-angle annular dark field (HAADF) imaging [242]. A first approximation of these scattering events by the Rutherford model indicates that their cross-section is dependent on the squared atomic weight (Z^2). The resulting HAADF images are often referred to as *Z*-contrast images. However, the occurrence of a channeling effect as electrons travel through the sample requires a much more complex analysis for reliable quantitative analysis of the HAADF signal [241].

Bright-field and dark-field TEM images of cross sections of thin films were taken using a JEOL, 2200FS electron microscope at 200 kV. HAADF micrographs were obtained on Titan 200 kV ChemiStem (FEI). Local chemical analysis was performed using high efficiency EDS detector. Nanoparticles were analyzed by using a Hitachi H9000-NA (300 keV).

3.2.3.4. TEM sample preparation

Specimen preparation for TEM is almost an art, at the same time technical skills alone are not enough for good specimen preparation; one should have basic knowledge about the

material and the preparation process may vary depending on the properties and nature of the specimen. Different methods are applied for different materials such as metals, ceramics, polymers, powder samples, thin films, bulk specimens, *etc*. The methods of sample preparation for different specimens are listed in the books by Williams and Carter [243] and by Egerton [244].

Powder samples for TEM analysis were grinded in agate mortar and after that dispersed in an absolute ethanol in the case of NBT powders, and a mixture of acetic acid and 1.3 propanediol (4:1 volume ratio) in the case of BFO powders, using ultrasonic bath for 10 min. The suspended particles were lifted on a carbon coated Formvar copper grid (Agar Scientific, Ltd., 400 mesh), with the help of forceps, by dipping the grid in the beaker gently and withdrawing horizontally. The grid was then dried in an oven.

Cross section specimens for TEM were prepared by a gallium focused ion beam (FIB) using Helios 450S (FEI). Prior to sectioning, a platinum metal layer was ion beam deposited using the FIB on the top of film. In order to prevent ion implantation and surface abrasion by the ion beam during the first moments of metal deposition, a few tens of nanometers of metal must first be deposited using the electron beam. Ionic milling was first conducted using an ion beam of 30 kV in normal incidence with regard to the sample surface. Two trenches (cuttings) define the exterior faces on both sides of the area of interest (Figure 3-40), so as to be close enough that they leave only a slice, a few 100 nm thick in the selected area. A needle-shaped micromanipulator is moved near the sample. The metal source and the ion beam are used to create a weld between the sample and the micromanipulator. After welding, final cutting of the slice is performed. The lamella is then moved to be welded to a TEM half-grid inside the FIB chamber. Final FIB milling was performed when the sample was on the TEM grid. Final thinning was done with low-energy (5 and 2 kV, respectively) to reduce possibility of FIB induced damage (surface roughness, deep ion implantation, amorphization, and temperature rise) [245].

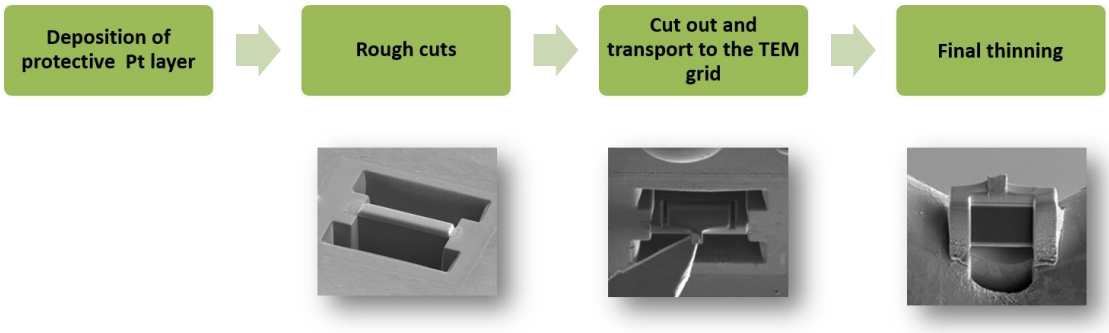

Figure 3-40. Scheme presenting sample preparation by FIB.

3.2.4. Raman Spectroscopy

Raman spectroscopy is a spectroscopic technique based on inelastic scattering of incident monochromatic light (usually from a laser source; Figure 3-41) in which the frequency of photons is changed upon interaction with a sample. Photons of the laser light are absorbed by the sample and then reemitted and their frequency is shifted up or down in comparison with original monochromatic frequency, so called the Raman effect. This shift provides information about vibrational, rotational and other low frequency transitions in molecules. Raman spectroscopy can be used to study solid, liquid and gaseous samples [246].

A Raman spectrum is presented as an intensity-versus-wavelength shift. A Raman system typically consists of four main components: excitation source (laser), sample illumination system and light collection optics, wavelength selector, detector [247].

Raman spectroscopy was performed using Renishaw spectrometer equipped with He-Ne laser source with 633 nm wavelength and optical lens of 50x at room temperature.

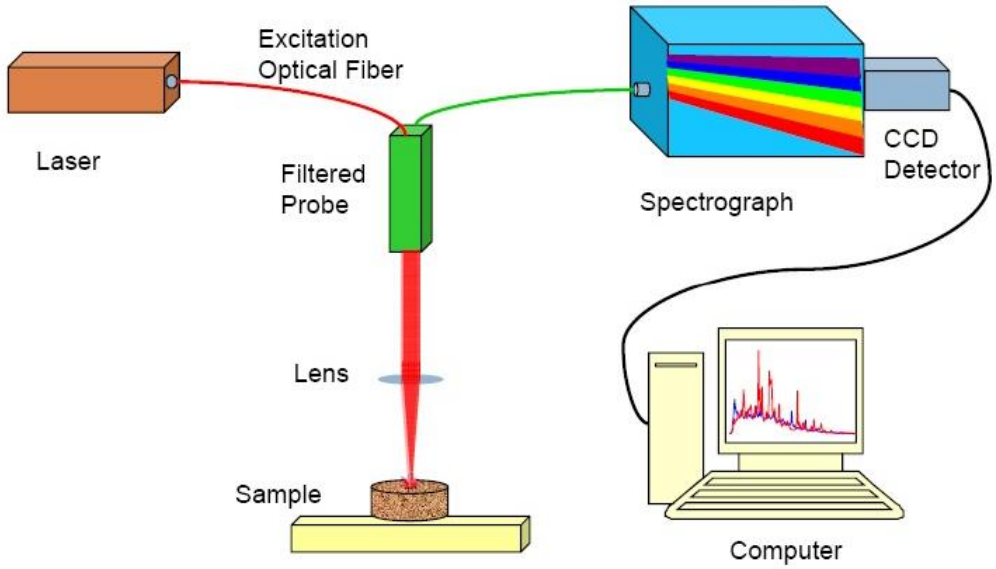

Figure 3-41. Schematic representation of the main components of Raman spectrometer (www.renishaw.com).

3.2.5. Electrical measurements

Dielectric properties were assessed on metal/film/metal capacitors using Signatone S-725-CRM micropositioners. Top Au electrodes were sputtered onto the films using an SEM coating unit (E5000, Polaron Equipment Limit) with an argon partial pressure of 2 mTorr, an acceleration voltage of 12 kV and an emission current of 12 mA. After the deposition, the electrodes were annealed in a conventional oven at 200 °C for 30 min., to release the stresses in the film caused by the deposition of the electrodes and improved the film-electrode quality.

Dielectric constant and loss tangent of the films were measured without DC bias using a precision impedance analyzer (Agilent E4980A). A small AC bias with 100 mV was applied to the capacitors at various frequencies. The capacitance was recorded and the dielectric constant evaluated from:

$$\varepsilon_r = \frac{C_p t}{\varepsilon_0 S} \tag{6}$$

where ε_r is dielectric constant, ε_0 is the dielectric constant of vacuum, and C_p is the capacitance of parallel circuit, t is the thickness of the sample and S is area of the electrode.

Loss tangent was calculated through the expression:

$$tan\delta = \frac{t}{f\varepsilon_0\varepsilon_r S R_p} \quad (7)$$

where, t is the thickness of the film, S is area of the electrode, f is the measuring frequency and R_p is the resistance of the parallel circuit.

The hysteresis loop measurement was performed using the ferroelectric analyzer TF Analyzer 2000, equipped with ferroelectric module. The method used to collect the data is the virtual ground feedback method, which is realized by a current to voltage converter. This method reduces the influence of parasitic capacitance and back voltage known from the Sawyer Tower measurements.

To record a hysteresis loop, an excitation signal like the triangular signal is generated. There will be a prepol pulse and three bipolar excitation signals generated. Each signal is followed by a relaxation time of 1 s.

The prepol pulse and the second pulse of the excitation signal establish defined polarization states. The prepol pulse has a negative state of relaxed remanent polarization. The second pulse ends in the positive state of relaxed remanent polarization.

The input parameters were selected in order to control the hysteresis measurement including variable frequency, variable amplitude of the driving voltage, signal waveform (triangular). The current applied to the films was auto-controlled by the acquisition software (aixPlorer Software).

Electrical characterization of thin films was also performed in parallel configuration and for some particular samples at Materials Science Institute of Madrid (ICMM) Consejo Superior de Investigaciones Científicas (CSIC), Madrid, Spain. Top Pt electrodes were sputtered on the films surfaces using a BAL-TEC SCD 050 sputter working at 40 mA for 150 s and at 60 mA for 200 s. A shadow mask with two dot sizes was used to obtain an array of capacitors with electrodes diameter of 500 and 300 μm. The dielectric constant and tanδ were measured at different frequencies between 100 Hz and 1 MHz using a precision LCR meter (Wayne Kerr 4300). Room temperature ferroelectric hysteresis loops were measured

with a modified Sawyer-Tower circuit. Experimental setup consisted of a HP 8116A pulse/function generator that allows the application of sinusoidal signals with electrical amplitude between 0.01-16 V and frequencies of 1-10 kHz. Current intensity generated values, after amplification with a Keithley 428 current amplifier, together with the voltage applied were collected with a Tektronix TDS 520 oscilloscope. Data acquisition and further processing of the data was carried out by homemade software.

3.2.6. UV-Vis spectroscopy

It is an analytical technique, which involves the measurements of absorption of electromagnetic radiation. Ultraviolet and visible (UV-Vis) absorption spectroscopy is the measurement of the attenuation of a beam of light after it passes through a sample or after reflection from a sample surface. As mentioned, it uses light in the UV (200-400 nm of wavelengths) and visible (400-800 nm of wavelengths) ranges. When electromagnetic radiation interacts with matter, a number of processes can occur, and when measuring UV-Vis spectra normally only absorbance takes place [248].

Absorption of visible and UV radiation corresponds to electronic excitations, in both atoms and molecules, from lower level to higher energy levels. Since the energy levels of matter are quantized, only light with the precise amount of energy can cause transitions from one level to another that is absorbed.

When light passes through or is reflected from a sample, the amount of light absorbed is the difference between the incident radiation, I_0, and the transmitted radiation, I. The amount of light absorbed is expressed either as transmittance, T, or absorbance, A.

$$T = \frac{I}{I_0} \Rightarrow A = -\log T \tag{8}$$

UV-Vis spectroscopy is primarily used to analyze liquids or solutions that is immersed into a cell. Generally, a cell (cuvette) is completely transparent to all wavelengths, and is made of plastic (acrylic), glass or quartz, depending on the measurement range. The measurement is carried out with two cuvettes, containing the sample solution in one and the solvent without the solute of the sample in other. By comparing the intensities collected by

the detectors, the wavelengths at which the solute absorbs UV-Vis light can be determined in the absorbance spectrum.

UV-Vis spectra were acquired using a Shimadzu UV 3100 spectrometer, covering a wavelength range between 220 and 800 nm.

3.2.7. Scanning Probe Microscopy

Scanning probe microscopy (SPM) is a technique used to probe ferroelectric domain configurations and local properties at micro- and nanometer scales. Depending on the type of the interaction force between the probing tip and the sample (attracting or repelling), SPM can operate in two different regimes: non-contact or contact, respectively [249]. SPM in contact mode provide distinct domain contrast due to a difference in mechanical, structural, electrochemical, dielectric and piezoelectric properties of ferroelectric domains. In the non-contact regime, domains can be visualized by detecting surface polarization charge and surface potential [250].

The most widely used SPM method for imaging domain structure of ferroelectrics is piezoresponse force microscopy (PFM). It is based on the detection of surface deformation due to the converse piezoelectric effect induced by external electric field applied to the conductive SPM tip. In PFM, a conductive tip is scanned across the surface of a piezoelectric sample in the contact mode. When AC voltage is applied to the tip (or, in some cases, to the bottom electrode while the tip is grounded), the ferroelectric sample undergoes the periodical expansion or contraction. The changes of the sample dimensions (cantilever deflection or bending) are detected by a reflected laser beam on a four sector photodiode as presented in Figure 3-42. The piezoresponse is defined as the first harmonic component of the tip oscillation. Oscillation amplitude and phase difference between the excitation signal and the resulting deformations are demodulated from the piezoresponse via a lock-in amplifier, thus providing information about the magnitude and orientation of the surface displacements, respectively [251]. PFM is frequently used to study ferroelectric materials, mainly for high resolution imaging, domain switching, local hysteresis measurements or switching of ferroelectric capacitors, and many excellent reviews can be found in literature [249, 251, 252].

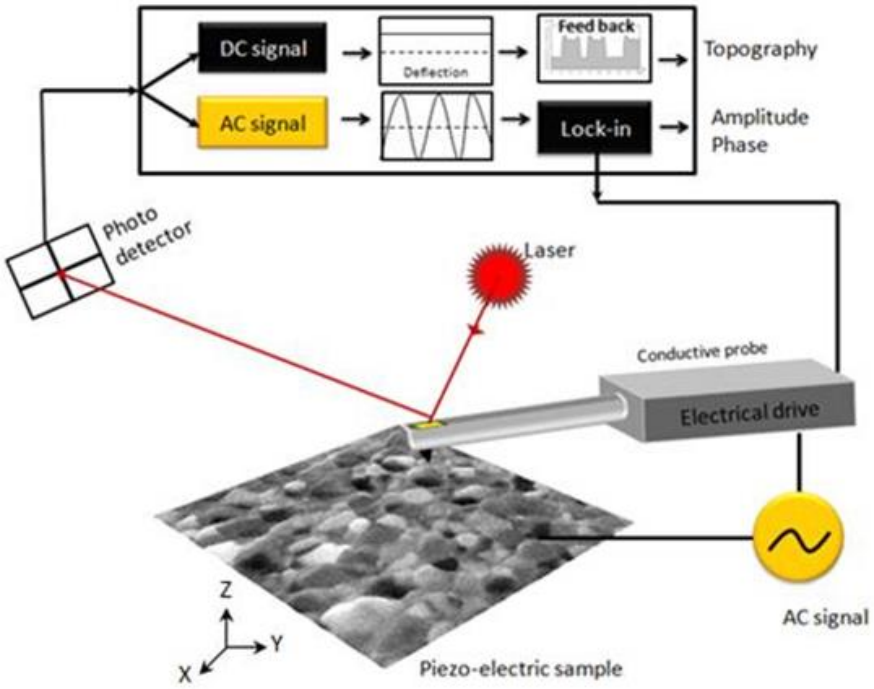

Figure 3-42. PFM experimental setup. When AC signal is applied between the tip and the bottom electrode the induced cantilever deflection is measured as an electrical signal by lock-in amplifier (www.csinstruments.eu).

An atomic force microscopy (AFM) system consisting of a commercial NT-MDT NTEGRA Aura SPM equipped with PFM mode was used to examine the domain structure of BFO thin films. Measurements were carried out using a cantilever Mikromash HQ: NSC35/PT with spring constant of 16 N/m and resonance frequency of 300 kHz. A small AC electric field of 5 V and frequency 70 kHz was applied to the tip to induce local vibration. The AFM tip signals (both amplitude and phase), originating from the induced vibration of the film, were detected by a lock-in amplifier (Stanford Research Systems, SRS 830). The topography and domain images were processed using WSxM v2.2 software.

3.2.8. Other methods

Other characterization techniques were utilized in the thesis as well however with less extend. Therefore, only experimental conditions and information about instruments are presented.

The particle size distribution of the obtained powders was accessed with a Coulter LS-230 equipment using the principle of laser diffraction. A sample placed in the fluid module is circulated through a sample cell at a constant speed. A beam of laser light shone through the cell is diffracted by particles within the sample, and the forward scattered (or diffracted) light is collected by a series of detectors. The distribution of light falling on the sensors enables the size distribution of the sample to be calculated [253]. The measurements were collected in the range from 0.04 to 2000 μm.

The surface area of the particles, SA_{BET} ($m^2 \cdot g^{-1}$) was evaluated by the Brunauer-Emmett-Teller (BET) method in which N_2 acted as adsorbate gas (Micromeritics Gemini 2375 equipment). Prior to the measurements, the samples were degassed at ~200 °C for 12 h.

A vibrating sample magnetometer (VSM) was used to measure the magnetic behaviour of BFO thin films. The principle of this measurement is as follows: firstly, the samples to be studied is placed in a constant magnetic field and magnetic moment will be induced in the sample. Then a sample is vibrated in the vicinity of a set of pick-up coils. The alternating magnetic field will cause an electric field in the pick-up coils according to Faraday's law of induction. This current will be proportional to the magnetization of the sample. More details about this technique can be found elsewhere [254].

In this work, Cryogenic VSM (Cryogenic Inc., UK) was used to measure the magnetic behavior of the samples up to 10 T at room temperature.

Chapter 4. RESULTS AND DISCUSSION

4.1. $Na_{0.5}Bi_{0.5}TiO_3$ thin films – an effect of annealing temperature on microstructure and electrical performance

Abstract: Aiming to the low temperature preparation of lead free NBT to make it compatible with low melting temperature substrates, in this chapter, the growth and properties of polycrystalline NBT thin films by chemical solution deposition method are presented. NBT thin films are fabricated by non-toxic chemical solution deposition on platinized Si substrates. The effect of crystallization temperature on the structure, microstructure and ferroelectric properties of the as-prepared films is studied. Crystalline NBT films are obtained at temperatures as low as 400 °C. All NBT films are composed of equiaxed grains which size is dependent on the crystallization temperature, and for the films annealed at temperatures >500°C a microcracking is observed. The remanent polarization of ~24 μC/cm^2 with corresponding coercive field of ~215 kV/cm is measured for films annealed at 650 °C. However, for films annealed at temperatures lower than 500 °C values of remanent polarization are <10 μC/cm^2, in spite of very low thermal budget used; NBT films annealed at 450 °C show a remanent polarisation of ~6 μC/cm^2 with corresponding coercive field of ~150 kV/cm.

Following the recent need for environmental friendly materials and technologies there has been an active search on lead free piezo and ferroelectric materials for sensors, actuators, motors and memory applications. Among the huge number of materials studied, sodium bismuth titanate stands out being a key lead-free piezoelectric material, *e.g.* single crystals of NBT show P_r ~ 40 μC/cm^2 and Ec ~ 28 kV/cm at 20 °C [50]. It shows ferroelectricity at room temperature, with a relatively large remnant polarization and high Curie temperature (T_C ~ 320 °C) [255]. However, NBT has serious disadvantages that may exclude it from practical applications: i) high conductivity, and ii) large coercive field. One way of overcoming these drawbacks is via the solid solution formation with other perovskites, such as $BaTiO_3$ or $K_{0.5}Bi_{0.5}TiO_3$ [255].

The crystalline structure of pure NBT perovskite has been deeply investigated by Jones and Thomas [256, 257]. The highest temperature phase of NBT is cubic (*Pm3m*), and it undergoes a phase transition to tetragonal (*P4mm*) at 540-530 °C, and to rhombohedral at about 200 °C (*R3c*). The tetragonal and rhombohedral phases are known to exhibit ferroelasticity and ferroelectricity, respectively. Two regions of coexistence of phases are found: a rhombohedral/tetragonal region around 255-400 °C and a tetragonal/cubic region in the range of 500-540 °C. Despite intensive studies of NBT, many important aspects of its crystal structure are still unclear, which complicates analyses of NBT-based solid solutions [256, 258, 259]. The electron-diffraction studies showed that NBT ceramics possess a complex and disorder local structure with a random distribution of the Bi^{3+} and Na^{+} (A-site cations), leading to an octahedral tilt disorder and to changes in crystal symmetry [167].

The research on NBT thin films has not been as intensive as for other lead-free perovskites, and most of the works have been focused on solid solutions. Nevertheless, in terms of processing and related properties, the published works can be categorized into physical deposition methods, such as sputtering and pulsed laser deposition (PLD), and chemical ones, as chemical solution deposition (CSD). Highly (111)-oriented sol-gel NBT thin films were prepared by CSD on platinized Si substrates by Tang *et al.* [195]. In this work, the authors reported the highest P_r value measured in the literature up to date for pure NBT thin films: ~21 μC/cm^2, and a corresponding high coercive field of ~112 kV/cm for films annealed at 650 °C for 10 min. The dielectric constant and tanδ with a grain size of ~200 nm were 171 and 0.024, respectively (measured at 100 kHz). They reported that their leakage current density ~4.5×10^{-5} A/cm^2, at an applied field of 167 kV/cm. They also evidenced that the leakage currents depended on the voltage polarity. A (110) preferential growth orientation was reported by Yang *et al.* for NBT films deposited on Pt/Ti/SiO_2/Si substrate by CSD [260]. The films presented monophasic perovskite phase with homogeneous microstructure with grains of ~120 nm in size after annealing at 700 °C for 10 min. However, for an applied electric field of 100 kV/cm, a remanent polarization of only 0.45 μC/cm^2 was measured. The applied voltage could not be raised further because of large leakage current. The dielectric constant and tanδ at 1 MHz were about 375 and 0.087. Zhou and co-workers fabricated NBT films by RF magnetron sputtering [191, 261]. The films exhibited a remanent polarization of 11.9 μC/cm^2 and a coercive field of 37.9 kV/cm at room

temperature. However, a rather high leakage current density was measured in those films, ~6×10^{-5} A/cm^2 at an applied electric field of 100 kV/cm. Finally, Bousquet *et al.* fabricated epitaxial NBT films by PLD [262, 263]. The thinner films (respectively 230 and 400 nm) displayed a quasiunique (100) orientation (close to 100 %), whereas for the thickest film, >600 nm, the proportion of (100)-oriented NBT crystallites decreases to ~85 vol.% (on MgO substrate). A P_r value of 12.6 μC/cm^2, associated to a coercive field of about 94 kV/cm was measured. On the other hand, mostly a (110)-oriented NBT films were grown on $SrTiO_3$ substrate. A remanent polarization value ranging from 7 to 14 μC/cm^2, associated with a coercive field in the range 68-85 kV/cm was obtained, depending on the target stoichiometry. The relative permittivity was about 255-410 and the tanδ were 6-7% (at 100 kHz).

Aiming to the low temperature preparation of NBT to make it compatible with low melting temperature substrates, in this chapter the growth and properties of polycrystalline NBT thin films by chemical solution deposition method are presented. Up to date, the lowest crystallization temperature for NBT films derived from a classic 2-methoxyethanol sol-gel route on platinized silicon was reported to be 460 °C [264]. Only local piezoelectric activity was reported by using PFM. However, no macroscopic ferroelectric properties were observed. 2-methoxyethanol is rather common solvent used in traditional sol-gel alkoxide chemistry. However, this solvent is a known teratogen, being hazardous substance to health and environment, thus it should be avoided. Therefore, in this study, non-toxic CSD route is used based on metal carboxylates, and carboxylic acid (acetic acid) and glycol (1,2 propanediol) as solvents. Using this precursor solution deposited on platinized silicon substrate, various annealing temperatures were tested in order to find the low temperature limit to obtain crystalline NBT films with reasonable ferroelectric properties. To our knowledge, there is no other example of such studies of low temperature processing of the NBT thin film prepared by CSD method.

4.1.1. Experimental methods

NBT precursor solution was prepared as detailed in experimental section (Chapter 3). NBT films were deposited onto Pt/TiO_2/SiO_2/(100)Si provided by Inostek, Inc. The deposition of the NBT thin films was carried out by spin-coating and wet films were dried

and pyrolysed on a hot-plate at 350 °C for 1 min. All the films prepared were crystallized by Rapid Thermal Processing (RTP) using Jetstar 100T JIPELEC equipment. A heating rate of 30 °C/s was used for the treatments, which were carried out in oxygen.

The electrical characterization was conducted using gold (Au) top electrodes deposited on the films by DC sputtering and followed by an annealing treatment at 300 °C for 30 min in air. Ferroelectric hysteresis loops, currents and leakage currents were measured with a ferroelectric analyzer TF Analyzer 2000, equipped with a ferroelectric module, at room temperature.

4.1.2. Results and discussion

The thermal decomposition of the as-prepared non-toxic NBT sol, dried at 80 °C for 1 h was studied by Differential Thermal and Thermogravimetric Analysis (DTA-TG). Figure 4-43 shows the DTA and TG curves recorded in air atmosphere. Here, a subtle endothermic energetic process is detected (peak at 90 °C), associated to a small weight loss. This is produced by the elimination of residual solvent and volatiles entrapped in the powdered precursor. Between 100 and 400 °C, a well-defined and quite intense exothermic anomaly at 312 °C is recorded, associated to the major weight loss (~20 %) of the TGA curve. These are mainly due to the pyrolysis and combustion of the organic compounds. At higher temperatures, a very small weight loss is observed probably associated to the small exothermic reaction that takes place at 485 °C and it is associated with the perovskite formation. Indeed the perovskite formation in NBT prepared by a 2-methoxyethanol sol–gel route was reported to occur at 492 °C as exothermic reactions [265]. Above ≥500 °C no other energetic anomalies are observed. Therefore, the major decomposition process of the precursor is produced at temperatures below 400 °C, the conversion of this amorphous precursor into a full crystalline material should proceed properly at temperatures ≥500 °C.

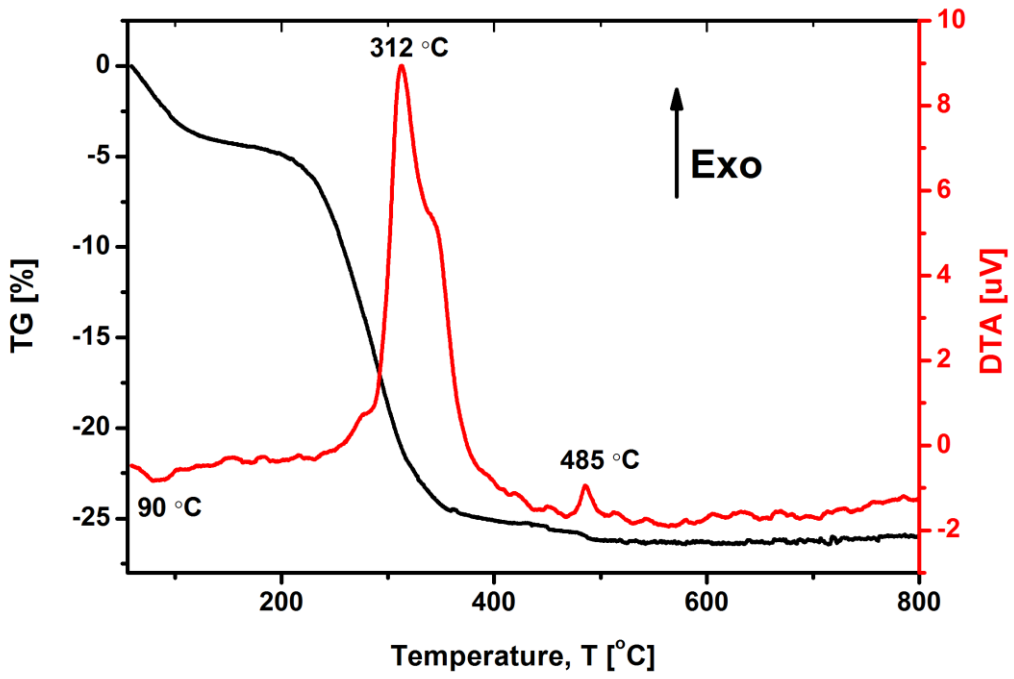

Figure 4-43. DTA/TG curves for NBT gel powders, at 5 °C/min heating and cooling rates. The conversion of the amorphous precursor into a full crystalline material proceeds in the temperature ≥500 °C.

A number of thin films of NBT were initially deposited onto the substrates by spinning, and then heat treated in a wide range of temperatures from 400 to 650 °C, in order to crystallize the desired perovskite phase. A total of four layers were successively deposited, dried and crystallized accordingly. Figure 4-44 presents the XRD diffraction patterns of NBT films crystallized at different temperatures, for 60 s. It can be seen that all films, heat treated at temperatures ≥400 °C, are crystalline but as the annealing temperature increases, the diffraction peaks in the XRD patterns became more intense and sharper, showing enhanced crystallinity of the thin films. The indexation of the corresponding reflections is ascribed to the perovskite crystalline phase. No crystalline secondary phases were observed in the diffractograms, indicating the oxide is phase pure.

Lower crystallization temperature of NBT films in comparison to thermal profiles of the dried sol is associated with RTP and processing atmosphere that is O_2. RTP is known to be effective in reducing the processing time and temperature of perovskite systems in thin

films form [209]. Additionally oxygen atmosphere strongly affect the kinetics of subsequent amorphous-perovskite crystallization of perovskite oxides powders and thin films. It was observed that usage of oxygen instead of air as an atmosphere for crystallization of sol-gel derived $BaTiO_3$ powders speeds up the decomposition of Ba containing intermediates and lowers the crystallization temperature of perovskite phase [266]. Similar effect was observed for $SrBi_2Ta_2O_9$ films obtained by CSD [267].

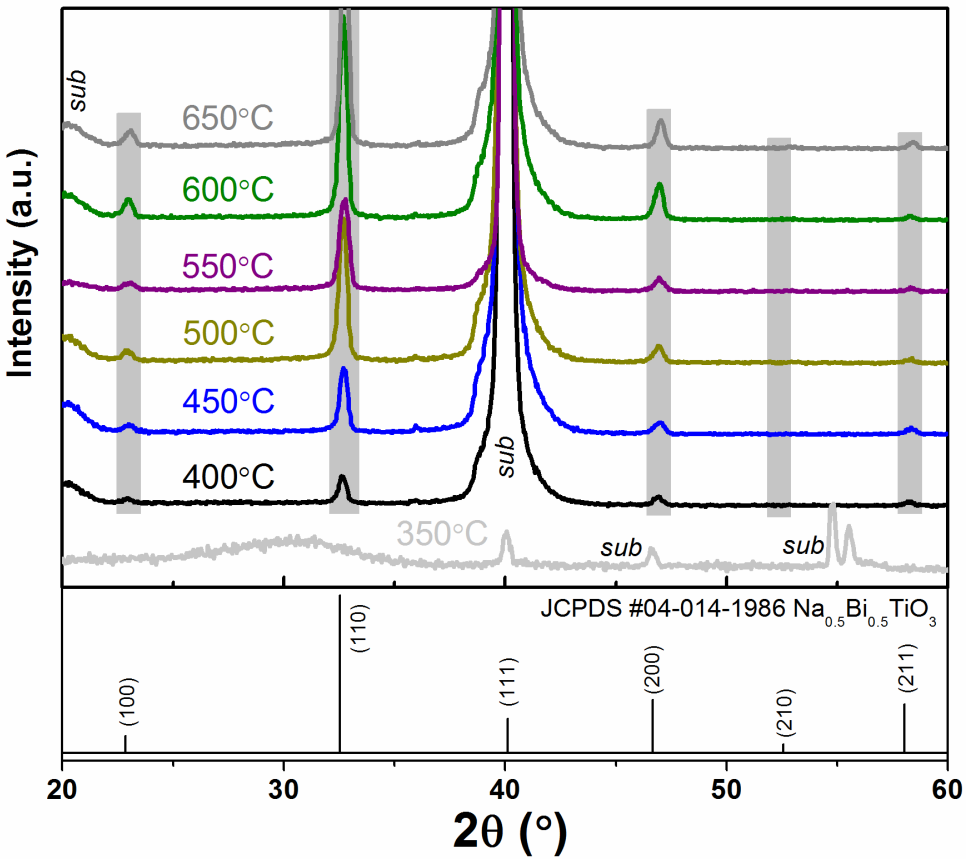

Figure 4-44. XRD patterns of NBT thin films annealed at distinct temperatures: 400, 450, 500, 550, 600 and 650 °C, for 60 s. It can be seen that all films, heat treated at temperatures ≥400 °C, are crystalline.

Figure 4-45 shows the typical surface and cross sectional morphology of the NBT thin films annealed at 400 (a), 450 (b), 500 (c), 550 (d), 600 (e), and 600°C (f). The microstructure of these films slightly varies depending on crystallization temperature. It is rather smooth formed by equiaxed grains for all of them, but there is clear evidence of cracking in the case

of films annealed at temperatures >500 °C. Those cracks follow the grain boundaries. Cracking of the chemical solution deposited thin films arise mainly from a mismatch in thermal expansion coefficients between the substrate and the film. Indeed, thermal expansion previously reported for NBT single crystals is ~16×10^{-6} /K [268] and for Pt is 8.8×10^{-6} /K [269]. Due to this mismatch in thermal expansion coefficient of the film (α_{film}) and substrate ($\alpha_{substrate}$), strain / stress develop between the substrate and the film upon cooling to room temperature. This thermal stress $\sigma_{thermal}$ can be calculated as [270]:

$$\sigma_{thermal} = \frac{E}{1-\nu}\int_{T_{RT}}^{T}\left(\alpha_{film} - \alpha_{substrate}\right)dT \qquad (9)$$

where, E is the Young's modulus, ν is the Poisson's ratio, α_{film} and $\alpha_{substrate}$ are the coefficient of thermal expansions of NBT film and substrate, respectively, and T and T_{RT} are the annealing temperature and room temperature, respectively. For NBT E = 110 GPa and ν = 0.26 [271]. This high $\sigma_{thermal}$ (670 MPa for NBT films annealed at 650 °C) results in the cracking of the films to relax film strain.

The film thickness of the NBT was estimated from SEM cross sections to be about 350 nm, as shown in the upper right insets of Figure 4-45. The films are quite dense with uniform thickness, however some porosity is also present. The high temperature heat treatments lead to increased densification and larger grains, due to the temperature-activated mobility of the ions [138].

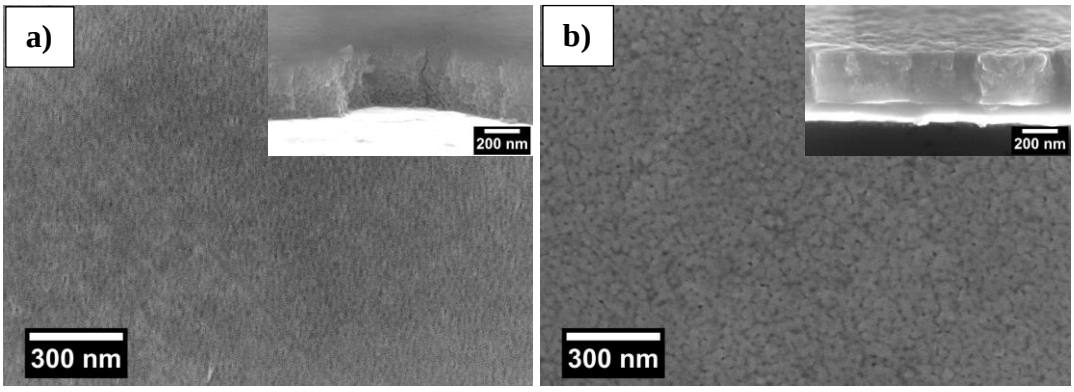

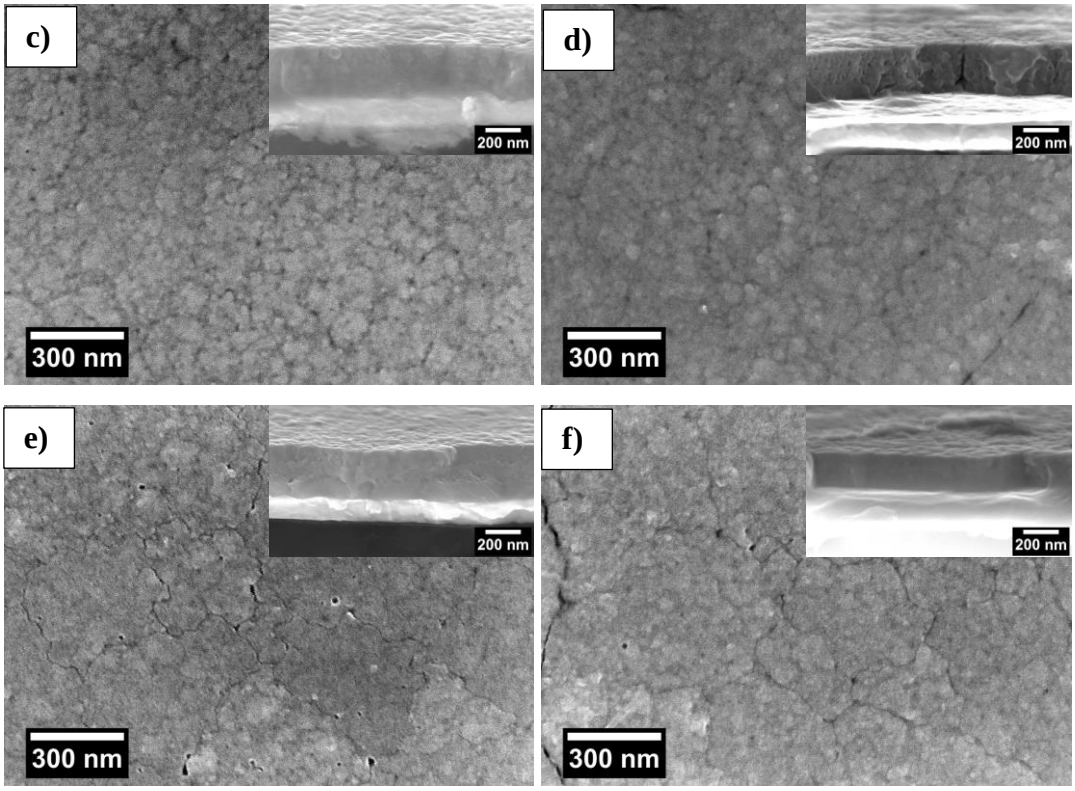

Figure 4-45.SEM top views and cross sections of NBT films annealed at 400 (a), 450 (b), 500 (c), 550 (d), 600 (e), and 600 °C (f). The microstructure of NBT films is rather smooth formed by equiaxed grains, and there is an evidence of cracking in the case of films annealed at temperatures >500 °C. The thickness of the NBT films was estimated to be ~350 nm.

The ferroelectric character of NBT films was analysed by the ferroelectric hysteresis loop. The room temperature *P-E* and *I-E* hysteresis loops of NBT films annealed at different temperatures are shown in Figure 4-46. We observe the characteristic maxima of the current curves related to the switching of the ferroelectric domains for the films annealed at ≥450 °C, and for NBT film crystallized at 400 °C no apparent contribution from domain switching is detected due to lack of current maxima, indicating the insufficient crystallization. Values of P_r are increasing with increasing of crystallization temperature reaching values of ~24 μC/cm^2 with corresponding coercive field of ~215 kV/cm, for films annealed at 650 °C. For films annealed at temperatures lower than 500 °C values of remanent polarization are lower than 10 μC/cm^2. The different ferroelectric response measured in these films can be ascribed to the lower porosity and larger grain size than of NBT films fabricated at lower

temperature as well as lower degree of crystallinity which corroborates XRD results. It is well-known that the polarization of polycrystalline films decreases as the grain size is lower [272] Moreover, the thin films prepared at higher temperature show an increase in E_C (~215 kV/cm for films annealed at 650 °C in comparison to films annealed at 600 °C, ~150 kV/cm). It is recognized that E_C is determined by the grain size, the defects and the thin film thickness [273]. Here, the thickness of all the derived NBT thin films is very close to each other, suggesting the small effects of thickness on the E_C. As annealing temperature increasing, the grain size and defects such as oxygen vacancies trapped at the grain are enhanced, which will lead to an increase in E_C [192].

Table 4-6 summarizes electrical properties of NBT thin films prepared at 650 °C in this work and reported in literature. The remnant polarization of NBT films is slightly higher that reported for (111)-oriented NBT thin films. Values of dielectric constant and tanδ obtained in this work are very similar to previously reported for NBT thin films. On top of this, NBT film annealed at 450 °C shows appreciable P_r of 6 μC/cm^2 and E_C of ~150 kV/cm despite the low thermal budget used.

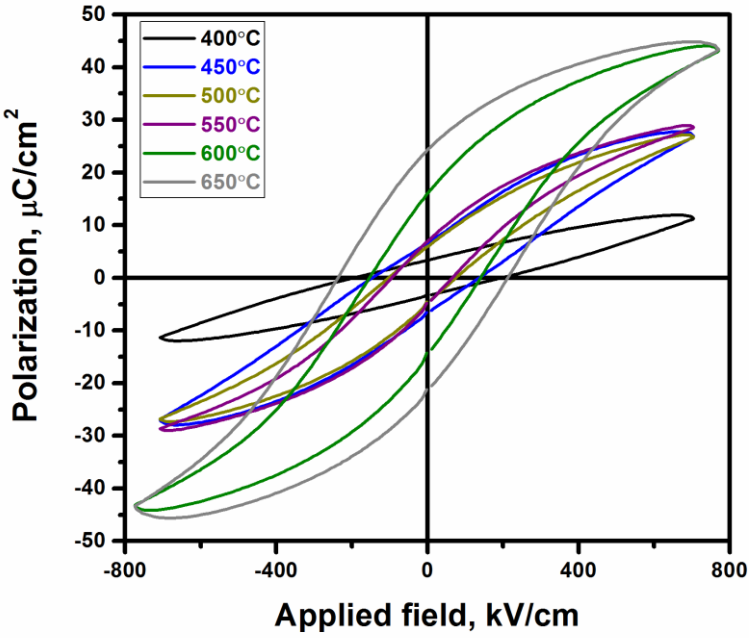

a)

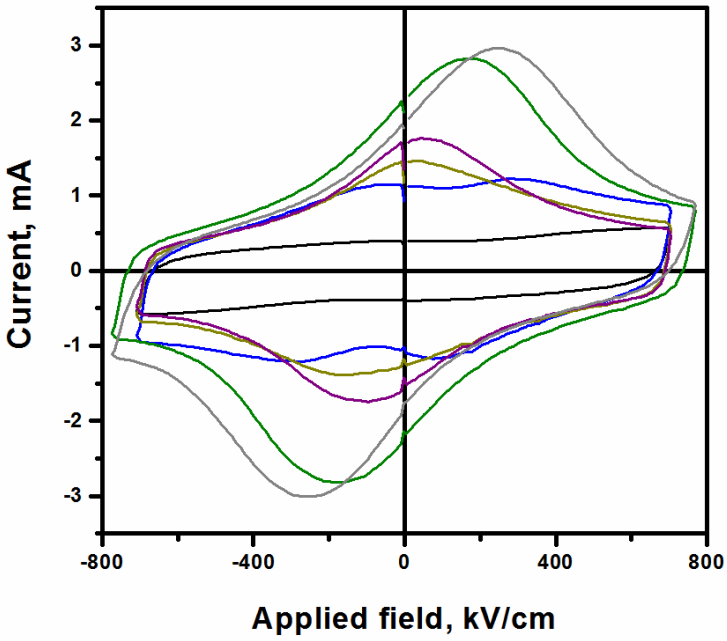

b)

Figure 4-46. Hysteresis loops a) and current loops b) of NBT thin films crystallized at different temperatures. The characteristic maxima of the current curves related to the switching of the ferroelectric domains are observed for the films annealed at ≥450 °C. However, almost linear, P-E loop was obtained for those NBT films crystallized at 400 °C due to an incipient crystallinity.

Table 4-6. Properties of NBT thin films prepared at this work and reported in literature.

	This work	***Tang et al. [195]***	***Yu et al. [276]***	***Xu et al. [275]***	***Zhou et al. [191, 261]***	***Daryapurkar et al. [274]***	***Bousquet et al. [262, 263]***
Preparation method	Sol-gel, RTA 650 °C, 1 min	Sol-gel, RTA 650 °C, 10 min, O_2	Sol-gel, RTA 650 °C, 5 min, air/O_2	MOD, RTA, 700°C, 30 min	RF-sputtering, 700 °C, 60 min	PLD, 650 °C	PLD, 560-580 °C
Remnant polarization ($\mu C/cm^2$)	24	20.9	8.3	10	11.9	21.4	14.1
Coercive field (kV/cm)	215	112	200	130	37.9	187	85
Dielectric constant	616 (1 kHz)	196 (1 kHz) 171 (100 kHz) 162 (1 MHz)	300 (100 Hz) 277 (100 kHz) 280 (1 MHz)	464 (1 kHz) 425 (100 kHz) 440 (1 MHz)	580 (1 kHz) 470 (100 kHz)	735 (1 kHz) 400 (100 kHz) 241 (1 MHz)	500 (1 kHz) 410 (100 kHz) 390 (1 MHz)
tanδ	0.032 (1 kHz)	0.064 (1 kHz) 0.024 (100 kHz) 0.03 (1 MHz)	0.02 (1-100 kHz) 0.05 (1 MHz)	0.04 (1 kHz) 0.035 (100 kHz) 0.05 (1 MHz)	0.05 (1-100 kHz)	0.07 (1 kHz) 0.07 (100 kHz) 0.3 (1 MHz)	0.09 (1 kHz) 0.06 (100 kHz) 0.06 (1 MHz)
Remarks		(111)-type preferential growth					Substrates: Pt/(110)$SrTiO_3$, Pt/(100)MgO

Summary: In this chapter, the growth and properties of polycrystalline NBT thin films by chemical solution deposition method were presented. These thin films were fabricated by non-toxic chemical solution deposition on platinized Si substrates. The effect of crystallization temperature on the structure, microstructure and ferroelectric properties of NBT was studied. Crystalline NBT films were obtained at temperatures as low as 400 °C. All films are composed of equiaxed grains which size is dependent on the crystallization temperature, and for the films annealed at temperatures >500 °C a microcracking was observed. The P_r of ~24 μC/cm^2 with corresponding E_C of ~215 kV/cm was obtained for films annealed at 650 °C. However, for films annealed at temperatures lower than 500 °C values of remanent polarization are <10 μC/cm^2, in spite of very low thermal budget used, and NBT films annealed at 450 °C show a P_r of ~6 μC/cm^2 and E_C of ~150 kV/cm. To our knowledge, this is the lowest crystallization temperature reported for NBT thin films up to date with measurable macroscopic properties.

4.2. $BiFeO_3$ thin films on Si: Bi-excess and temperature effect

Abstract: Pure BFO perovskite thin films have been prepared on Pt-coated silicon substrates by chemical solution deposition at temperatures below 500 °C. Precursor solutions with and without Bi(III) excess have been used. Perovskite films without crystalline secondary phases, as detected by XRD analysis, are obtained at the lowest temperature limit of 400 °C. Scanning electron micrographs of these films show surface microstructures formed by well-defined grains surrounded by a fine-grained phase, suggesting the appearance of a volume fraction of crystals in an early stage of crystallization. The films prepared with Bi(III) excess have better defined ferroelectric hysteresis loops than those without any excess, especially for the films annealed at 400 °C. BFO films prepared with Bi(III) excess and annealed at 400 and 450 °C can be poled at room temperature, obtaining an effective switching of the ferroelectric polarization with the electric field. Remanent polarization values of P_r ~ 46.1 and ~55.3 μC/cm^2 with coercive fields of E_C ~ 171 and 190 kV/cm were obtained for the films prepared at 400 and 450 °C, respectively; measured at 200 K.

Bismuth ferrite is a room temperature multiferroic material that exhibits ferroelectric and ferromagnetic ordering at room temperature in a single perovskite (ABO_3) phase [18]. The coupling between these ferroic orders is of interest to produce additional and novel functionalities with applications in devices (*e.g.*, spintronics, electrically switchable magnets or magnetoelectric non volatile memories). However, the spontaneous polarization, P_S, values usually measured in bismuth ferrite materials are significantly smaller than the spontaneous polarization expected for a ferroelectric with such a high Curie temperature, T_C (~830 °C, P_S up to 100 μC/cm^2). This is because of the high leakage current densities and dielectric losses of the material produced by the difficulty to prepare pure BFO perovskite materials [126]. The BFO perovskite is a metastable phase between 447 and 767 °C with respect to the bismuth-rich ($Bi_{25}FeO_{39}$) and the iron-rich ($Bi_2Fe_4O_9$) phases, the stable

compounds on each side of the BFO in the phase diagram. Formation of defects associated to the two oxidation states of the iron (Fe^{2+} and Fe^{3+}) and to the volatility of bismuth (melting point of Bi_2O_3 = 817 °C) are easily produced during the processing of BFO materials.

Nowadays, key applications of multiferroic compounds, such as BFO, are envisaged for the material in thin film form [277]. It was demonstrated that it is possible to prepare high quality (001)-pseudocubic epitaxial BFO thin films by physical methods at temperatures >500 °C with ferroelectric polarization of ~60 μC/cm^2 [278]. But for future applications in large areas and flexible electronics the epitaxial thin films are not essentially needed and solution deposition methods are more suitable. Therefore, solution derived polycrystalline BFO thin films with reasonably good ferroelectric and ferromagnetic properties have been synthesized at temperatures >500 °C [140, 145, 279], but at the limit of integration in Si-technology (International Technologies Roadmap for Semiconductors (ITRS), 2013 Update).

In this chapter, Bi excess and reduced crystallization temperatures were utilized to prepare BFO thin films with ferroelectric properties, deposited using chemical solution deposition method. BFO thin films were annealed by rapid thermal processing in air at temperatures in the range 400-500 °C, with or without Bi(III) excess in the precursor solutions. Under these processing conditions, it was possible to reduce the temperature limit of formation of the pure BFO perovskite to 400 °C showing ferroelectric switching. Structural and microstructural characteristics of the films were studied in details.

4.2.1. Experimental methods

Precursor solutions of BFO were prepared as presented in experimental section of this thesis. Two solutions were obtained, with and without a 5 mol% of Bi(III) excess. These solutions were spin-coated at 3000 rpm for 45 s onto Pt/TiO_2/SiO_2/(100)Si substrates. Wet layers were dried on a hot plate at 350ºC/60s. Rapid thermal treatments (RTP, JetStar 100T JIPELEC) in static air (1 bar), were carried out at temperatures of 400, 450 and 500 °C, with a soaking time of 60 s and a heating rate of 30 °C/s. Deposition, drying and RTP treatment were repeated up to a maximum of 10 layers to fabricate crystalline films with a thickness of ~200 nm.

The crystalline phases developed in the films were studied by XRD, using a Siemens D500 powder diffractometer with a Cu anode (λ = 1.5406 Å). Surface and cross-section images of the films were obtained by high-resolution scanning electron microscope (SU-70, Hitachi). Thicknesses of the films were calculated from the cross-section images.

A planar array of capacitors was fabricated by sputtering Pt/Au top electrodes on the film surfaces, with diameter sizes between 140 and 640 μm. Variation of the charge current density with the electric field (*J-E*) loops were measured, with an in-house made system based on a virtual ground circuit. The loops were traced by a Tektronix TDS520 oscilloscope. This equipment coupled to a home built cryostat equipped with micro-manipulators allowed thin films hysteresis loops measurements in the temperature range 100-400 K.

4.2.2. Structure and microstructure

XRD patterns of BFO thin films crystallized in air at 400, 450 and 500 °C, and prepared from stoichiometric precursor solution are shown in Figure 4-47 a), while from 5 mol% Bi excess in Figure 4-47 b). In both cases, crystalline perovskite phase is not clearly observed in the patterns of the films treated at 350 °C. Traces of nano-crystalline phase can be observed as bumps in the diagram close to the position of the (012) reflection and (024) in both preparations. This indicates that the main volume of the films remains amorphous but some nano-sized region of the BFO phase have been developed at 350 °C. On the other hand, all the films treated at temperatures in the range 400-500 °C are crystallized and the perovskite phase was formed. However, small traces of other phases are observed in the films annealed at 500 °C, 2θ ~28° (marked with an asterisk in Figure 4-47), probably associated with a nano-crystalline phase with a composition $Bi_2Fe_4O_9$ (JCPDS #01-080-8638). Thus, the appearance of the Fe-rich phase is attributed to the Bi_2O_3 loss, as and can be represented by a reaction: 8 $BiFeO_3$ (s) → 2 $Bi_2Fe_4O_9$ (s) + BiO (g) + O_2 (g), where "s" and "g" refer to the solid and vapor phases, respectively [67]. Reflections of perovskite BFO with rhombohedral *R3c* crystal structure (JCPDS #00-086-1518) are indexed in the patterns. No preferred orientation was observed for those BFO thin films. The 202 and 024 BFO diffraction lines are overlapped with 111 and 200 peaks of the Pt-bottom electrode (JCPDS #00-04-0802), respectively.

An improvement in the crystallinity of the films can be hypothesized from the decrease of the broadening of the perovskite peaks and the splitting of the 104/110 reflections produced with the increase of the annealing temperature and the Bi(III) excess. It was observed that these reflections appear in all of the films at slightly higher 2θ values than those of the JCPDS card of BFO perovskite. This indicates smaller cell parameters of our BFO films due to a strain induced by the substrate [280], and a lower content of defects in the perovskite cell [126].

Figure 4-48 shows the plan-view and cross-section micrographs of the BFO thin films processed at distinct temperatures and precursor solutions. The thickness of the films was estimated from the cross sections, and for all of them it is ~200 nm. Noticeable differences are observed in the film surfaces. BFO films prepared from stoichiometric precursor solution at 400 °C show areas morphologically differentiated, *i.e.* zones with well-defined grains surrounded by a fine grained phase. Microstructure development with temperature leads to a final film microstructure with a uniform average grains size ~200 nm. BFO films crystallized at 500 °C. The films with Bi excess follow a similar evolution with increasing temperature, but BFO films processed at 400 °C seems to be one step forward in comparison with the film from stoichiometric precursor solution. The former is now formed by clusters of grains that convert into well-defined grains at higher processing temperatures, 500 °C, with an average size ~135 nm, slightly lower than those of the films from stoichiometric precursor solution. It was reported that the 5 and 10 % Bi excess in BFO films enhance the grain growth and gives uniform topology [281].

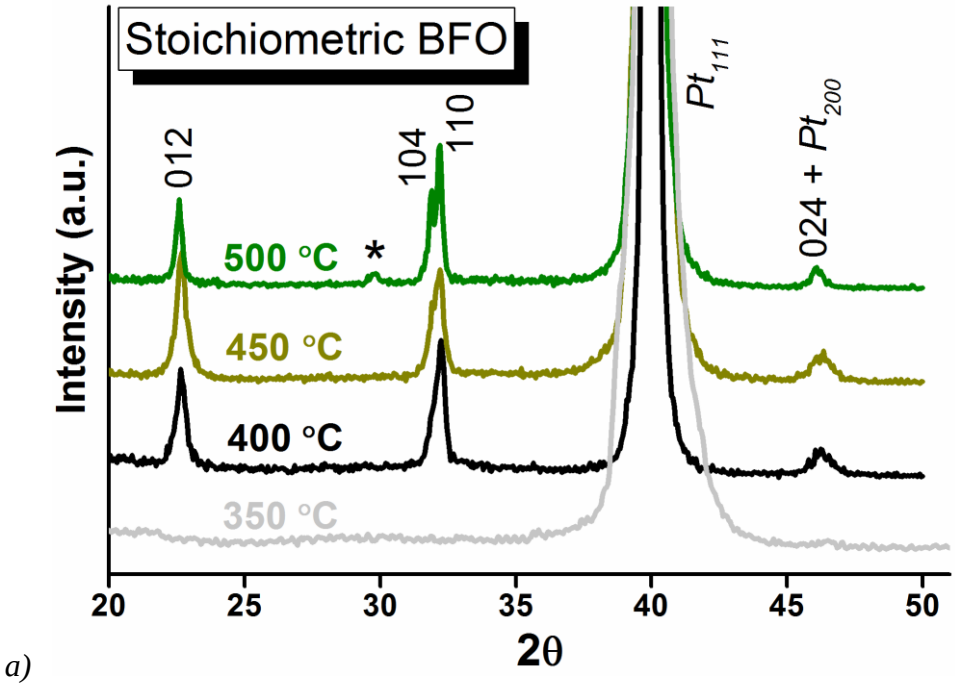

a)

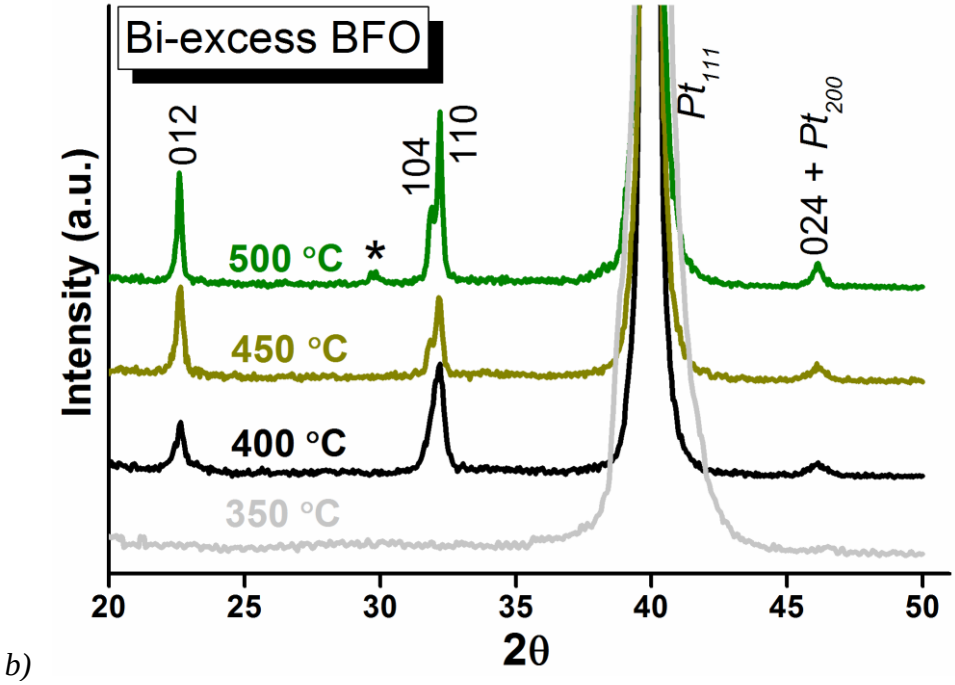

b)

Figure 4-47. XRD results of BFO thin films prepared from stoichiometric precursor solution a), and from Bi excess b). All peaks may be attributed either to the electrode or a BFO perovskite phase whereas BFO annealed at 500 °C also exhibits a weak, broad peak attributed to $Bi_2Fe_4O_9$ (*).

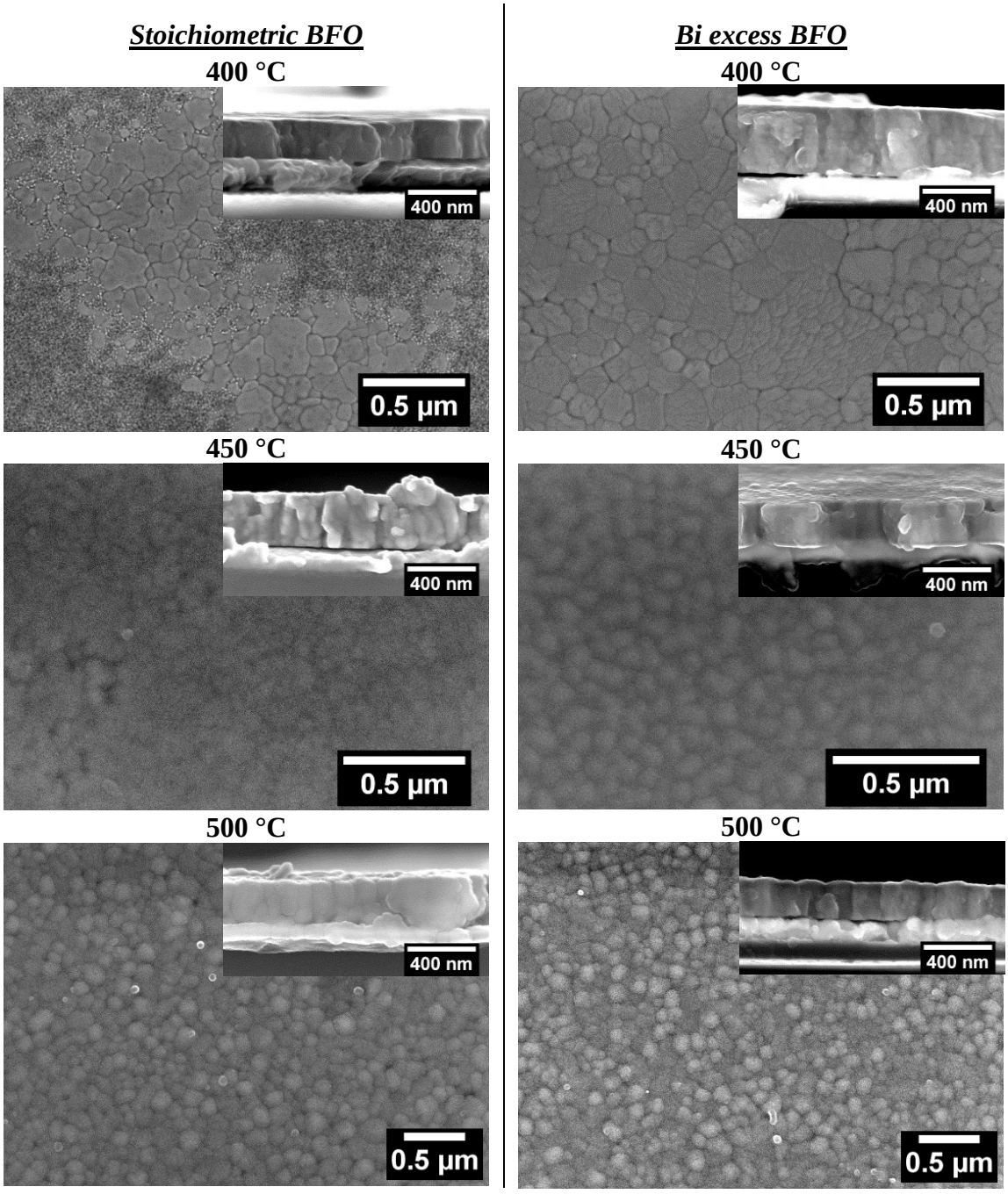

Figure 4-48. SEM micrographs (top view and cross section) of BFO films annealed at distinct temperatures and deposited from stoichiometric or Bi excess precursor solutions. The average thickness of the films is ~200 nm, not observing noticeable dissimilarities in the cross-section microstructure images. As the annealing temperature increases, a large amount of grains seems to grow at the expense of the fine-grained phase.

4.2.3. Electrical characterization

The ferroelectric characterization of BFO thin films was conducted at distinct temperatures due to the high leakage contribution. The measurements were carried out from low temperature to room temperature in order to switch the domains preventing electrical break-down. For all the samples, the temperature was lowered to 150 K and then the amplitude of the sinusoidal electrical signal was gradually increased to prevent any conductivity degradation and to act as an electrical conditioning treatment. After the switching was observed in the loops the temperature was increased till 250-300 K.

Figure 4-49 depicts the experimental *P–E* and *J–E* ferroelectric loops of BFO annealed at distinct temperatures and deposited from stoichiometric precursor solutions. The characteristic current maxima in *J-E* loops are related to the switching of the ferroelectric polarization and are observed in all of the films. BFO films derived from stoichiometric precursor solution could be only measured at temperatures up to 250 K. BFO films prepared at 400 °C show hysteresis loop with degraded shape due to leakage current.

Figure 4-50 depicts the experimental *P–E* and *J–E* ferroelectric loops of BFO annealed at distinct temperatures and deposited from Bi excess precursor solutions.

The films prepared with Bi excess can be switched at room temperature when annealed at 400 and 450 °C. The one crystallized at 500 °C suffers a dielectric breakdown during switching at temperatures higher than 225 K. It can be observed from those curves that on approaching room temperature the contribution from non-linear leakage currents increases in the films with Bi excess, in contrary to stoichiometric BFO as evidenced by the non-lineal behaviour in the J-E curves at high electric field. In order to make a quantitative comparison of the ferroelectric response of the films, the data collected for BFO films at 200 K are presented in Table 4-7. At this temperature all the measured capacitors were subjected to the same electrical conditioning thus the electrical situation is for all films more comparable.

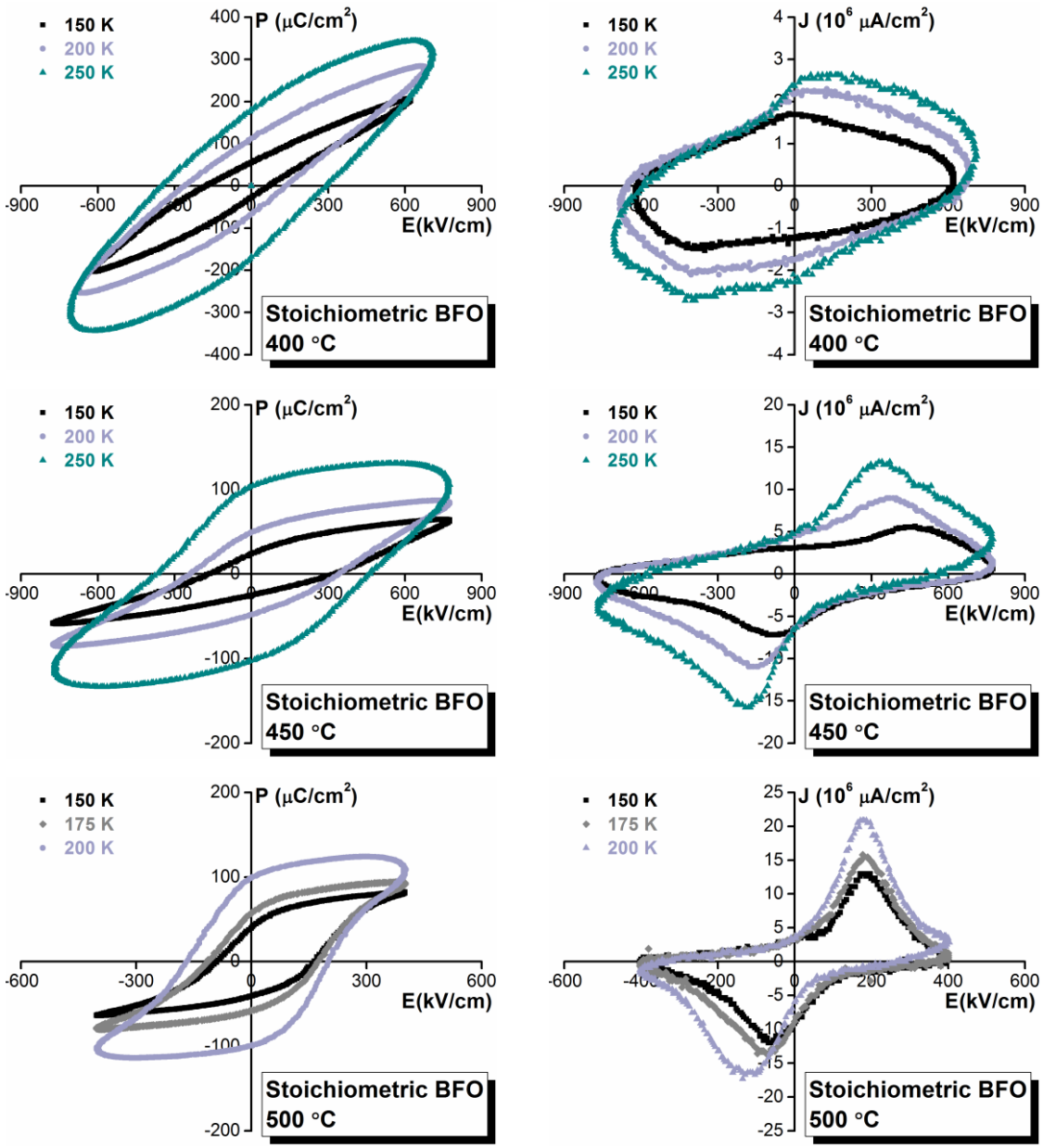

Figure 4-49. Polarization and current density hysteresis loops, traced at 1 kHz measured at different temperatures. BFO films crystallized at distinct temperatures and derived from stoichiometric precursor solutions. The characteristic current maxima in J-E loops are related to the switching of the ferroelectric polarization and are observed in all of the films.

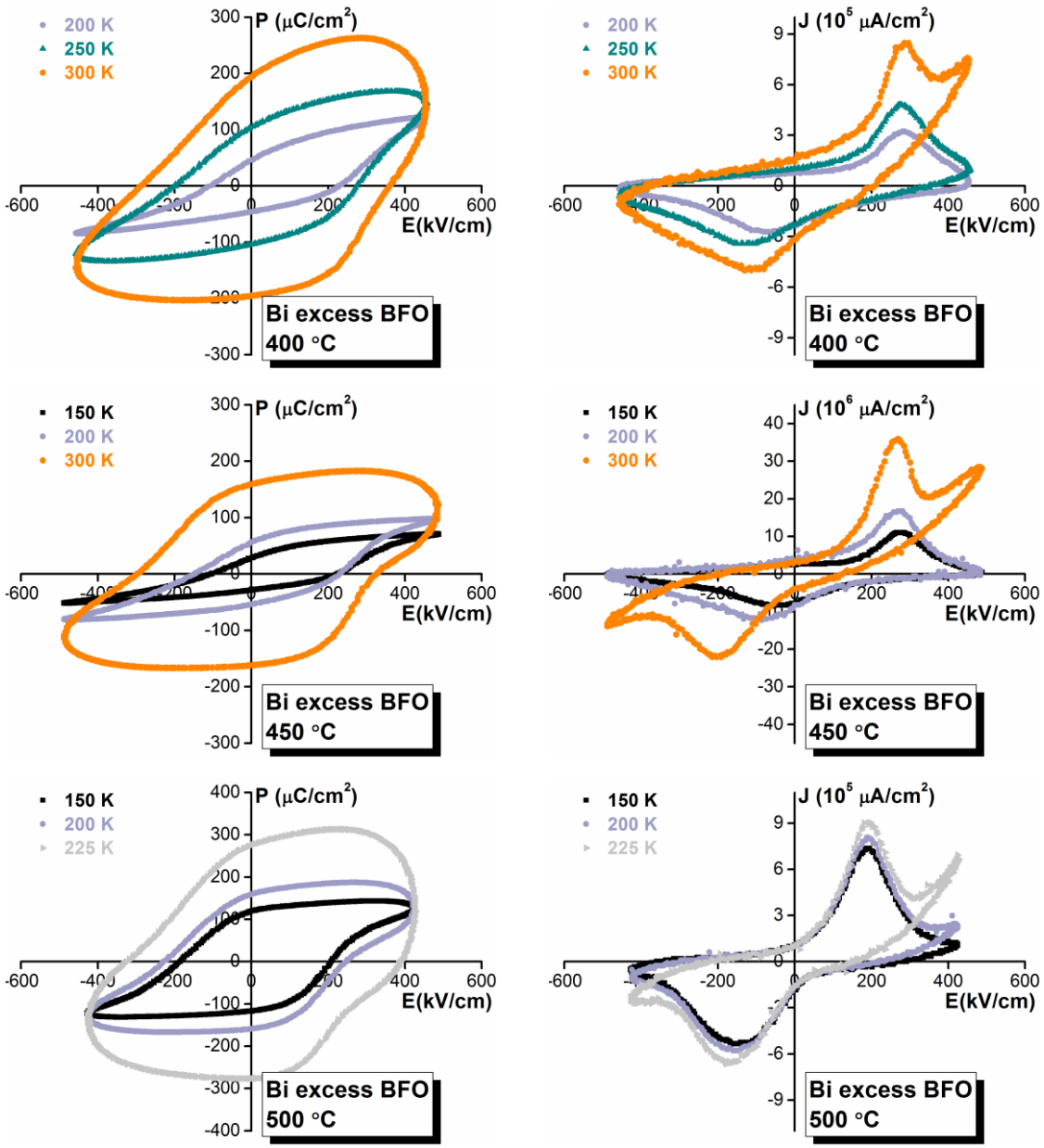

Figure 4-50. Polarization and current density hysteresis loops, traced at 1 kHz measured at different temperatures. BFO films crystallized at distinct temperatures and derived from Bi excess precursor solutions. The one crystallized at 500 °C suffers a dielectric breakdown during switching at temperatures higher than 225 K.

Table 4-7. Results derived from the current density loops measured at 200 K and 1 kHz for BFO films annealed at distinct temperatures and deposited from stoichiometric or Bi excess precursor solutions.

Precursor solution	Annealing temp. (°C)	P_r (μC/cm^2)	E_C (kV/cm)
Stoichiometric BFO	400	88.2	200
	450	48.5	290
	500	98.7	186
Bi excess BFO	400	46.1	171
	450	55.3	190
	500	159	240

The values of P_r are larger in the films with the Bi excess. It is also important to note that the films with Bi excess can be switched at temperatures close to RT except the films crystallized at 500 °C that cannot be switched at 250 K due to an electrical break-down.

The results show that the values of the polarization (P_r) are larger in the films prepared from solution with Bi excess, for the same crystallization temperature. When the structural characteristics and microstructures of films crystallized at the same temperature are compared, no significant changes can be observed that explain these differences. As the polarization values are related to the volume of ferroelectric phase that can be switched in the films, it must be assumed that the introduction of an excess of Bi in the precursor solution is increasing the volume fraction of defect-free, well-crystallized crystals.

Apart from the differences of the polarization values of the films prepared from solutions with and without Bi excess, already discussed, it is clear that the increase of the crystallization temperature, which in both cases produces films with larger and better crystallized grains according to the structural and microstructural results, leads to an increase of the polarization values.

Summary: BFO perovskite thin films have been prepared on Pt-coated silicon substrates by chemical solution deposition at temperatures below 500 °C. Precursor solutions with and without Bi(III) excess have been used. Perovskite films without secondary phases, as detected by X-ray diffraction analysis, are obtained at a lower temperature limit of 400 °C. Due to high leakage contribution *P-E* hysteresis loops were recorded at low temperature (150 K-RT). The films prepared with Bi(III) excess had better defined ferroelectric hysteresis loops that those without Bi(III) excess, especially for the films annealed at 400 °C. Room temperature hysteresis loops could be obtained only for films prepared from solution with Bi(III) excess and annealed at 400 °C and 450 °C. Due to larger P_r values observed in the films prepared from solution with Bi excess, Bi excess BFO solution derived films were chosen to be analyzed in more detail in next chapters.

4.3. Bottom electrode effect on the microstructure of $BiFeO_3$ thin films

Abstract: BFO thin films were grown by chemical solution deposition on a range of electrodes to determine their role in controlling phase formation and microstructure. The crystallization on oxide electrodes followed the sequence: amorphous → $Bi_2O_2(CO_3)$ → perovskite, while those on Pt crystallized directly from the amorphous phase. IrO_2 electrodes promoted perovskite phase formation at the lowest temperature and LNO additionally induced local epitaxial growth. All compositions exhibited fully coherent Fe-rich precipitates within the grain interior of the perovskite matrix, whereas incoherent $Bi_2Fe_4O_9$ second phase was also observed at the grain boundaries of BFO grown on Pt electrodes. The latter could be observed by XRD as well as TEM but coherent precipitates were only observed by TEM, principally evidenced by their Z contrast in annular dark field images. These data have pronounced consequences for the extended use of BFO films under applied field for actuator, sensor and memory applications.

In recent years, attention has been paid to materials possessing two or more of the following ferroic properties: ferroelasticity; ferroelectricity and (anti)ferromagnetism, a class of materials now referred to as multiferroics. Due to their potential technological applications in modern electronic devices, such as memory elements, sensors, and spintronics, they have become the subject of intense research [282]. Rich in properties and functionality, bismuth ferrite has been studied more extensively than any other multiferroic, being hailed the most promising lead-free single phase multiferroic candidate for devices due to its intrinsic multiferroic nature above room temperature [20]. However, its compositional instability, often resulting in variation in functional properties is a major obstacle to full practical utilization [20].

Early studies, dating back to the 1960's, pointed out the difficulties in the preparation of BFO free from non-perovskite, parasitic phases [283]. Moreover, BFO exhibits high

electrical conductivity, creating difficulties in applying large electric fields [91]. This high electrical conductivity is mainly attributed to the presence the Bi-rich sillenite type, $Bi_{25}FeO_{39}$ (or $Bi_{25}FeO_{40}$) phase and the Fe-rich mullite-type, $Bi_2Fe_4O_9$, and to defects in the crystal structure, such as oxygen vacancies originating from the reduction of Fe^{3+} to Fe^{2+} [18]. Preparation of monophasic BFO is extremely difficult due to the thermodynamics and kinetics of Bi_2O_3–Fe_2O_3 system. Based on studies by Selbach *et al.* [126], $Bi_{25}FeO_{39}$ and $Bi_2Fe_4O_9$ phases are slightly more stable thermodynamically than BFO in the temperature range 447-767 °C. During the solid state reaction between Bi_2O_3 and Fe_2O_3, $Bi_{25}FeO_{39}$ forms at the shell whereas a $Bi_2Fe_4O_9$ is formed at the reaction/diffusion front towards the iron oxide core. Once crystallized, $Bi_2Fe_4O_9$ is stable and consequently, the reaction is arrested so that BFO coexists with small amounts of $Bi_{25}FeO_{39}$ and $Bi_2Fe_4O_9$ [127]. Furthermore, sublimation or evaporation of volatile Bi_2O_3 at elevated temperatures may also result in $Bi_2Fe_4O_9$ formation [67].

In contrast to bulk materials described above, the crystallization pathway to form thin films of BFO is quite different. BFO thin films have been grown via numerous methods including physical vacuum-based and chemical-based techniques but each deposition technique has drawbacks. BFO thin films grown by PLD under incorrect oxygen pressures can develop parasitic iron oxide phases, such as α-type Fe_2O_3 or γ-type Fe_2O_3 [284] and in some cases nano-scale precipitation of Bi_2FeO_{6-x}, an Aurivillius compound (n = 1) with an orthorhombic crystal structure has been reported. More recently, using advanced TEM, the existence of a new Fe_2O_3-rich perovskite nanophase, fully coherent with the matrix of Ti and Nd doped BFO was reported with an approximate formula, $(Fe_{0.6}Bi_{0.25}Nd_{0.15})^{3+}$ $Fe^{3+}O_3$ [285].

Similarly the preparation of monophasic BFO thin films by CSD requires accurate control of the processing parameters and Bi:Fe stoichiometry. Bi deficiency in the starting composition or from volatilization of Bi during the annealing steps leads to the formation of secondary phases and highly conductive films [286]. To compensate for the Bi volatility, Bi excess is normally used in CSD BFO films. However, in the case of high Bi excess, phases such as Fe substituted α-Bi_2O_3 are formed at the BFO/Pt interface. Moreover, other common impurity phases such as: Bi_2O_3, Fe_2O_3, $Bi_2Fe_4O_9$, $Bi_{46}Fe_2O_{72}$ and $Bi_{24}Fe_2O_{39}$, have also been reported [140, 154, 279]. This broad spectrum of possible secondary phases in BFO thin

films, sometimes difficult to detect by XRD, due to their small particle size and volume fraction, determines the reproducibility of the electrical response.

The electrical properties of ferroelectric capacitors are not only affected by the intrinsic nature of the ferroelectric films but also by the electrodes due to differences in chemical nature, lattice parameter, work function and surface roughness [197]. The bottom electrode also serves as a template for growth and promotes phase stability . Bottom electrodes for ferroelectric thin films can be either metal or oxide-based. The former group includes: platinum; iridium; ruthenium and copper, most commonly used due to their chemical and thermal stability. The latter group includes the rutile-type iridium (IrO_2) and ruthenium oxides (RuO_2) and perovskite-structured oxides, such as strontium ruthenate ($SrRuO_3$, SRO) and lanthanum nickelate (LNO). Among them, IrO_2 is easily and reproducibly deposited on Si substrates on a large scale at low cost [287]. Generally, Pt is used as a bottom and top electrode for thin film ferroelectric capacitors due to its high electrical conductivity, good stability at high temperatures and high Schottky barrier which lowers leakage current [197] whereas SRO, IrO_2, RuO_2 and LNO have been reported to offer lattice matching, structural and chemical compatibility, a high diffusion barrier for oxygen, phase stability at high temperatures, and superior fatigue properties over Pt electrodes [22]. It is believed that oxygen vacancies in PZT thin films can easily be filled with oxygen from the oxide-based electrodes, resulting in a reduction in their build up at interfaces [22, 288]. Oxide electrodes also have an important role in the processing of other lead-based and lead-free ferroelectric thin films. IrO_2 enhances the electrical performance of 0.37 $BiScO_3$-0.63 $PbTiO_3$ [289] and LNO interlayers promote (001) texture and improve the dielectric properties of $Ba_{0.5}Sr_{0.5}TiO_3$ [290].

The use of oxide electrodes for fabrication of BFO thin films has to date been mainly limited to epitaxial thin films grown on SRO [97] with only a few reports describing BFO films grown on oxide electrodes such as LNO and IrO_2. LNO and IrO_2 electrodes were studied for La and Nb co-doped BFO (BLNF) thin films fabricated by PLD. BLNF films on LNO/Si substrates showed strong (012) texture due to the lattice matching between BLNF(012) and LNO(001) whereas no preferred orientation was observed for IrO_2/Si. Moreover, BLNF films using LNO as the bottom electrode showed well-saturated ferroelectric loops with large remnant polarization, but poor fatigue resistance. BLNF thin

films using IrO_2 as the bottom electrode displayed ferroelectric loops with high leakage current, but better fatigue resistance [291]. Comparative studies between Pt and LNO electrode for BFO films produced by RF sputtering showed that LNO reduces crystallization temperature and improves the crystallinity of BFO films. Moreover, the electrical conductivity is greatly reduced due to improvements in the film/electrode interface, chemical homogeneity and surface roughness of the BFO on LNO interlayer [215]. The reduction of electrical conductivity in BFO films prepared by CSD was also suggested to originate from the absence of parasitic phases and better quality of film/electrode interface, due to the use of LNO as bottom electrode but no preferred orientation was reported [25]. Although, oxide electrodes such as LNO have been shown to improve crystallinity and chemical homogeneity of BFO, reduce the crystallization temperature and induce texture and improve film/electrode interfaces in BFO thins films, the microstructure and phase formation have not been addressed.

In this part, we use annular dark field (ADF) scanning transmission electron microscopy (STEM), high resolution TEM, energy dispersive X-ray spectroscopy (EDS) complemented by grazing incident XRD to identify the crystallization pathway and microstructure of BFO films prepared by a chemical solution deposition route on $Pt/TiO_2/SiO_2/(100)Si$, $LNO/Pt/TiO_2/SiO_2/(100)Si$ and $IrO_2/TiO_2/SiO_2/(100)Si$ electrodes.

4.3.1. Experimental methods

Lanthanum nitrate hexahydrate ($La(NO_3)_3 \cdot 6H_2O$, Merck, 99%) and nickel (II) nitrate hexahydrate ($Ni(NO_3)_2 \cdot 6H_2O$, Fluka, 98.5%) were dissolved in 5 ml of deionized water, and mixed in the stoichiometric ratio of La:Ni=1:1. To improve the solution wettability and avoid film cracking during heating, 1 ml of formamide (Merck, 99.5%) was used. Finally, ethanol absolute (Merck, 99.8%) was added until the resultant concentration of LNO solution was diluted to 0.2M. The LNO films were deposited by spin-coating (KW-4A Spin Coater) the solution on $Pt/TiO_2/SiO_2/Si$ substrates at 2500 rpm for 45 s and annealed by rapid thermal processing (Qualifllow JetFirst 100) at 700 °C for 5 min in O_2 atmosphere.

BFO precursor solutions were prepared using bismuth nitrate ($Bi(NO_3)_3 \cdot 5H_2O$, Sigma Aldrich, 99.99%) and iron acetylacetonate ($Fe(CH_3COCHCOCH_3)_3$, ABCR, 99%). Acetic

acid ($C_2H_4O_2$ – AcOH, Merck, 100%) and 1,3 propanediol ($C_3H_8O_2$, Aldrich, 98%) were used as solvents [145]. Bismuth nitrate and iron acetylacetonate were dissolved in a mixture of glacial acetic acid and 1,3 propanediol (4:1 vol. ratio) separately room temperature. Individual solutions were poured into a beaker and stirred for 12 h to form a solution with the concentration of 0.125M. Solutions were prepared with 5 mol% of Bi(III) excess. Precursor solutions were deposited onto $Pt/TiO_2/SiO_2/(100)Si$ and $IrO_2/TiO_2/SiO_2/(100)Si$ (Inostek Inc) and LNO coated $Pt/TiO_2/SiO_2/(100)Si$, cleaned in acetone (CH_3COCH_3, Panreac) and in 2-propanol ($CH_3CHOHCH_3$, Panreac, for analysis). The deposition of the BFO thin films was carried out by spin-coating at 2500 rpm for 45 s. Wet films were dried and pyrolysed on a hot-plate (IKA C-MAG HS7) at 350 °C for 1 min, followed by rapid thermal processing at 500 °C for 1 min. Deposition, drying and annealing was repeated 10 times to fabricate films with the desired thicknesses.

A grazing incidence (2°) X-ray diffraction (GI-XRD, PANalytical X'Pert Pro diffractometer, Cu-Kα radiation, 45 kV and 40 mA, 10° to 50° 2θ, step size 0.025°;) was used to assess the phase assemblage and crystal structure. Residual stress analysis was carried out by XRD using sin2ψ method [236], described well in Chapter 3.

The microstructure of the thin films was observed at low resolution using an Hitachi SU-70 SEM. Specimens for TEM were prepared by a gallium FIB using Helios 450S (FEI). Bright-field and dark-field TEM images were taken using a JEOL, 2200FS electron microscope at 200 kV. High-resolution (HR) TEM and ADF micrographs were obtained on Titan 200 kV ChemiStem (FEI). EDS was perform using the Oxford INCA Energy TEM 250 spectrometer.

4.3.2. Results and discussion

Figure 4-51 shows the GI-XRD traces of BFO/Pt, BFO/LNO and BFO/IrO_2 films. All peaks for BFO/IrO_2, BFO/LNO may be indexed according to either the electrode or a rhombohedrally distorted perovskite phase with *R3c* symmetry [145, 292] with no evidence of any second phase. In addition to perovskite and electrode peaks, films prepared on Pt, exhibited a weak broad peak at $2\theta \sim 28.2°$ (marked with an asterisk in Figure 4-51, attributed to a low volume fraction of a nanocrystalline $Bi_2Fe_4O_9$ (JCPDS #01-080-8638) phase.

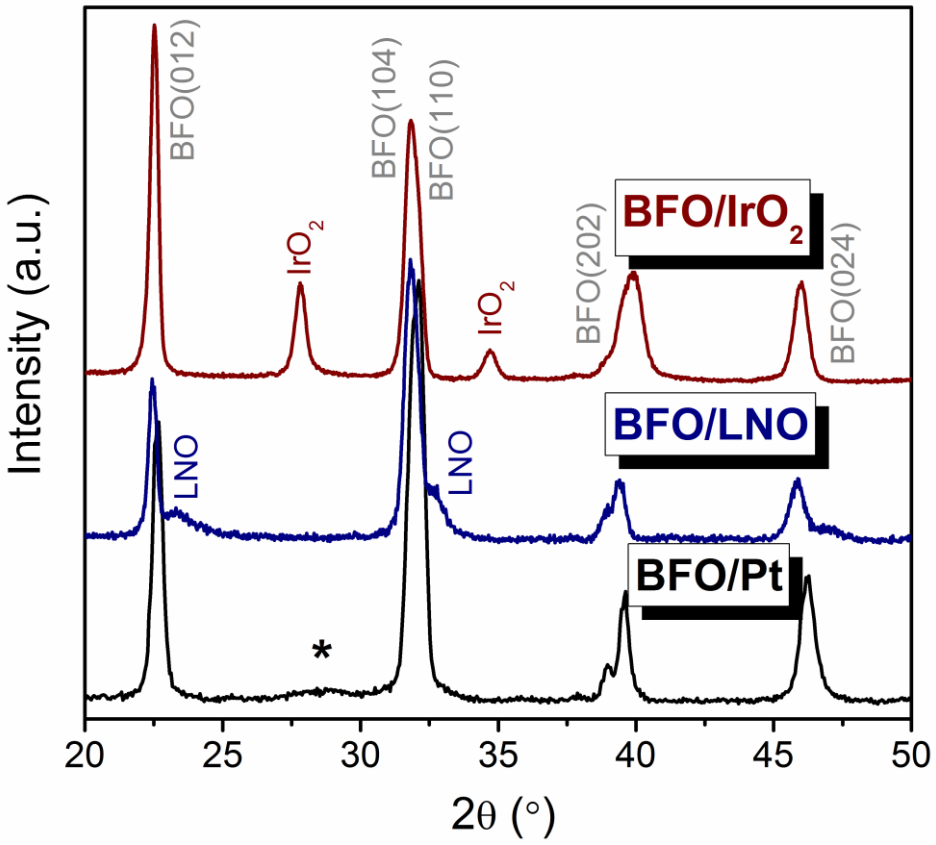

Figure 4-51. GI-XRD traces of BFO films fabricated by chemical solution deposition on Pt/Si (BFO/Pt), LNO/Pt/Si (BFO/LNO) and IrO_2/Si (BFO/IrO_2) and annealed at 500 °C. All peaks associated with BFO/IrO_2 and BFO/LNO may be attributed either to the electrode or a BFO perovskite phase whereas BFO/Pt also exhibits a weak, broad peak attributed to $Bi_2Fe_4O_9$(*).

To study the phase formation on each type of bottom electrode, BFO films were deposited on (a) Pt, (b) LNO, and (c) IrO_2 and annealed at 500 °C for periods of 1, 2 and 3 s with a heating rate of 100 °C/s, and 1, 5 and 30 s with a heating rate of 30 °C/s. BFO/Pt films (Figure 4-52 (a)) were initially amorphous (1 s, 100 °C/s) as indicated by the presence of the broad hump centered at 2θ ~ 29° but as annealing time increased to 3 s (100 °C/s), they began to crystallize into perovskite BFO with complete conversion at longer times. In BFO films deposited on LNO and IrO_2, an intermediate $Bi_2O_2(CO_3)$ phase was detected at 2θ ~ 12.9 and 30.3°. $Bi_2O_2(CO_3)$ is a mineral with a tetragonal structure (a=b=3.867 Å and c=13.686 Å) and space group I4/mmm (JCPDS #04-017-6012). Sun *et al.* identified

$Bi_2O_2(CO_3)$ as an initial phase which nucleates at pre-existing metal-organic clusters in amorphous films prepared on an electron-transparent SiN_x membrane by sol-gel [293].

The crystallization of BFO films deposited on the oxide electrodes (Figure 4-52 b) and c)) appears to follow the same sequence: amorphous → $Bi_2O_2(CO_3)$ → perovskite. However, the conversion to perovskite occurs more rapidly on IrO_2 than LNO. Perovskite peaks appear after 1 s (100 °C/s) for BFO/IrO_2 but only after 2 s (100 °C/s) for BFO/LNO. It is proposed that the relatively slow amorphous to perovskite conversion for BFO/Pt allows a longer time for Bi volatilization since the vapour pressure of Bi_2O_3 above an amorphous phase is higher than that above an equivalent crystalline composition, similar to PbO above PZT [294]. As a consequence, BFO films on Pt may be Bi deficient despite 5 % excess added to the precursor solution. This results in the presence of broad peaks in XRD traces arising from Bi deficient phases, Figure 4-51.

Figure 4-53 shows images of cross-sections of BFO/LNO, BFO/Pt and BFO/IrO_2 thin films. The thickness of BFO layers measured from TEM images is 150, 170 and 200 nm with a columnar microstructure in each case with lateral grain size, 80, 140 and 200 nm for BFO_3/LNO, BFO_3/Pt and BFO/IrO_2, respectively. The columnar grains extend through the entire film thickness which indicates layer-by-layer homoepitaxy for BFO growth within a grain [138]. As discussed in the literature, crystallization of solution-based films is characterized by competition between bulk nucleation within the amorphous matrix, and heterogeneous nucleation at the interfaces [138]. Columnar grain growth in thin films can only be achieved if interface nucleation is favoured over bulk nucleation [138]. Low solution concentration and the thermal treatment conditions at which each layer is crystallized before the next layer is deposited, promotes interfacial nucleation and columnar grain growth. For $SrTiO_3$ and $BaTiO_3$ films, depositing thin layers (10-20 nm) and annealing induces nucleation at the interfaces between the layers and encourages local epitaxial growth [295]. In this study, 10 layers were spin coated onto the substrates, dried and annealed at 500 °C, leading to columnar grain growth with layer thicknesses of 12-18 nm, as deduced from TEM images in Figure 4-53.

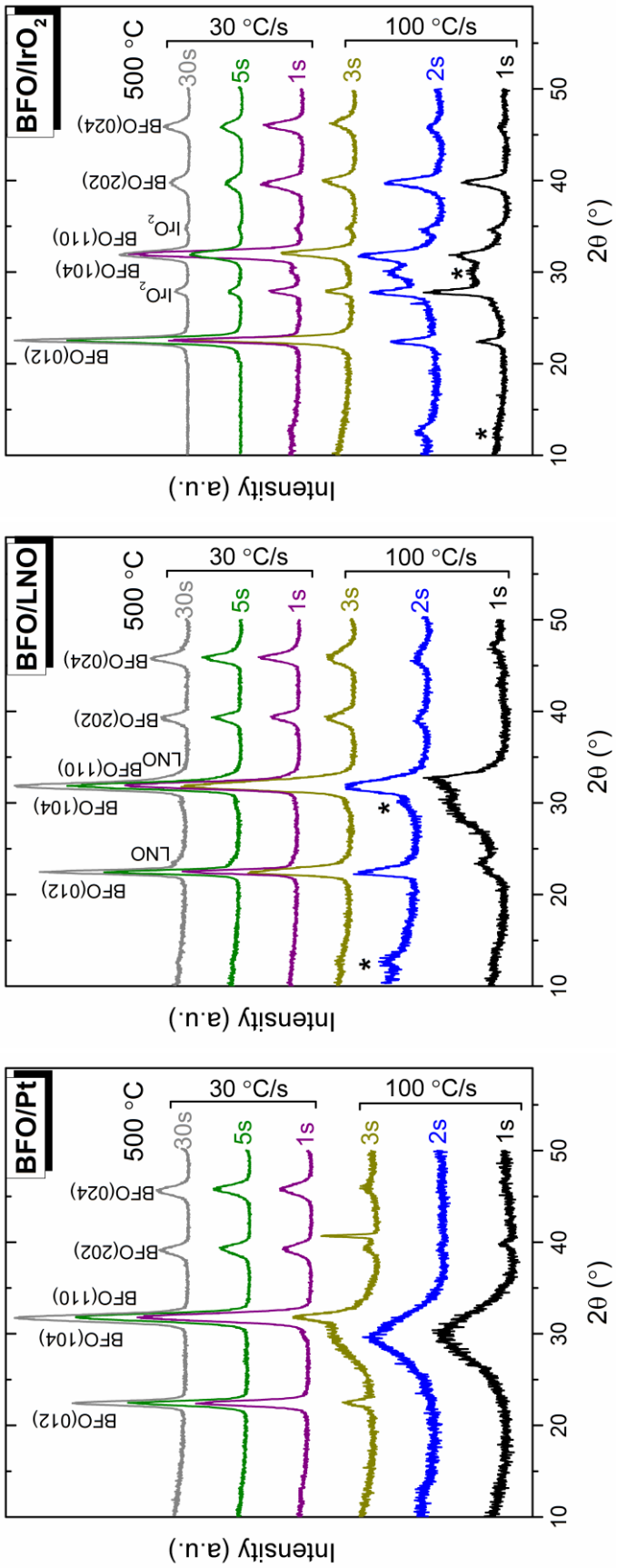

*Figure 4-52. GI-XRD patterns of BFO thin films annealed at 500°C for different times using heating rates of 30 and 100 °C/s. (a) BFO/Pt, (b) BFO/LNO, and (c) BFO/IrO_2. * denotes $Bi_2O_2(CO_3)$.*

In addition to the individual layers, Figure 4-53 revealed inclusions of bright contrast in the interior of the BFO grains, often between the deposited layers. This contrast could arise due to the segregation of light elements, the formation secondary phase with high quantity of lighter elements, or the formation of pores. Porosity has been previously reported in sol–gel processed 0.9 PMN–0.1 PT thin films and attributed to fast crystallization [296].

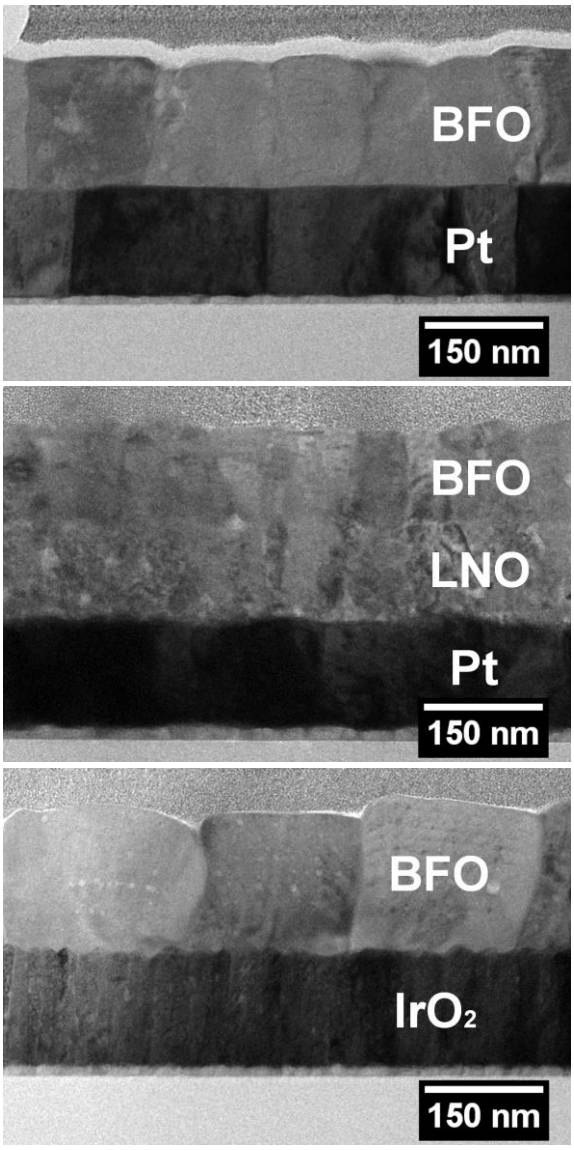

Figure 4-53. Bright-field TEM images of cross-sections of a) BFO/Pt, b) BFO/LNO and c) BFO/IrO_2 thin films showing a columnar grain structure. The average width of the columnar grains is 80, 140 and 200 nm for BFO/LNO, BFO/Pt and BFO/IrO_2, respectively.

Figure 4-54 however, presents higher magnification ADF images in which the brightness at each atomic position is approximately proportional to the square of atomic number (Z) [241]. Therefore, the bright areas in Figure 4-53 correspond to scattering from Bi atoms with the highest Z and the darkest to Fe atoms with lower Z. The bright contrast inclusions in Figure 4-54 exhibit dark contrast in the ADF images, indicating that these regions are deficient in Bi compared with the neighboring bright contrast areas. For BFO on IrO_2, the precipitates are <10 nm and generally located away from the grain boundaries, Figure 4-54 (c). For BFO films on LNO, larger inclusions (10-15 nm) are present within the film interior, whereas smaller inclusions (5nm) exist at the interfaces between the crystallization layers (Figure 4-54 (b)). For BFO on Pt, small inclusions (10 nm) are present in the grain interior but larger elongated inclusions with dark contrast occur at the grain boundaries, Figure 4-54 (a).

To clarify the chemical composition of the grain boundary secondary phase in BFO on Pt, EDS line-scans were performed, as denoted by the white line in Figure 4-55 (a), with the traces inset. The line-scans reveal that the particles are poor in Bi and rich in Fe with respect to the matrix, corroborating the XRD data (Figure 4-51) and ADF images (Figure 4-54) which suggests the presence Bi deficient phases. High resolution images (Figure 4-55 (b)) reveal lattice fringes with a measured spacing of 0.552 nm, consistent with d_{110} (0.579 nm) of orthorhombic $Bi_2Fe_4O_9$ (JCPDS #01-080-8638).

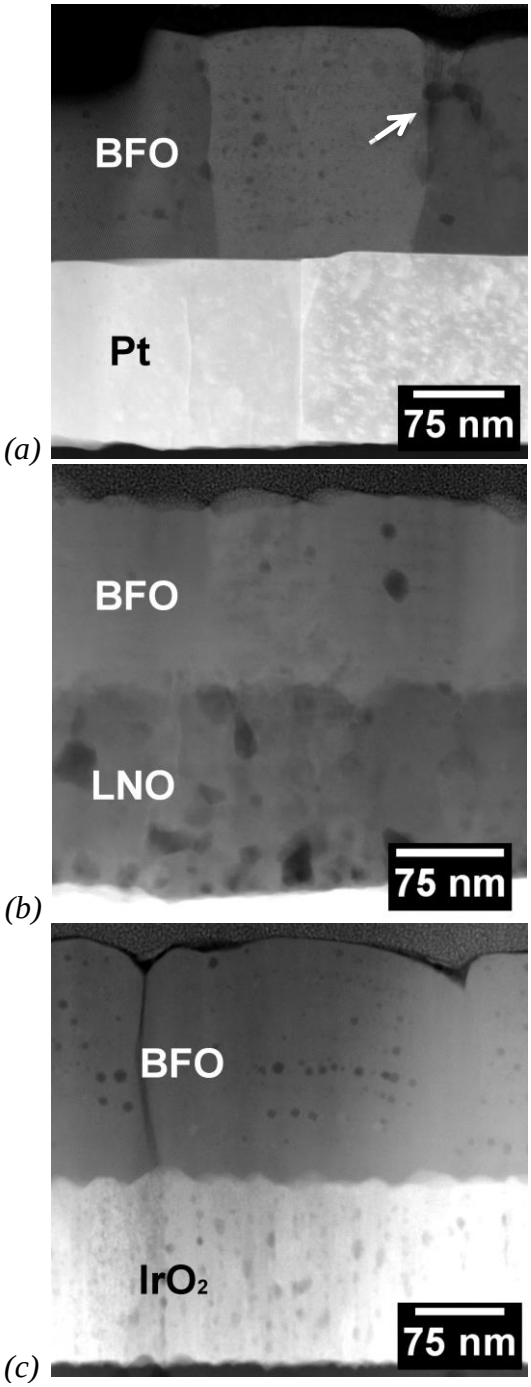

Figure 4-54. ADF TEM cross-sectional micrographs of the (a) BFO/Pt, (b) BFO/LNO and (c) BFO/IrO_2 thin films. A grain boundary with second phase (indicated by the arrowhead) is shown in (a). Inclusions inside the columnar grains exhibit dark contrast in ADF images, indicating that these regions are poor in heavier elements compared with the bright contrast in neighboring areas.

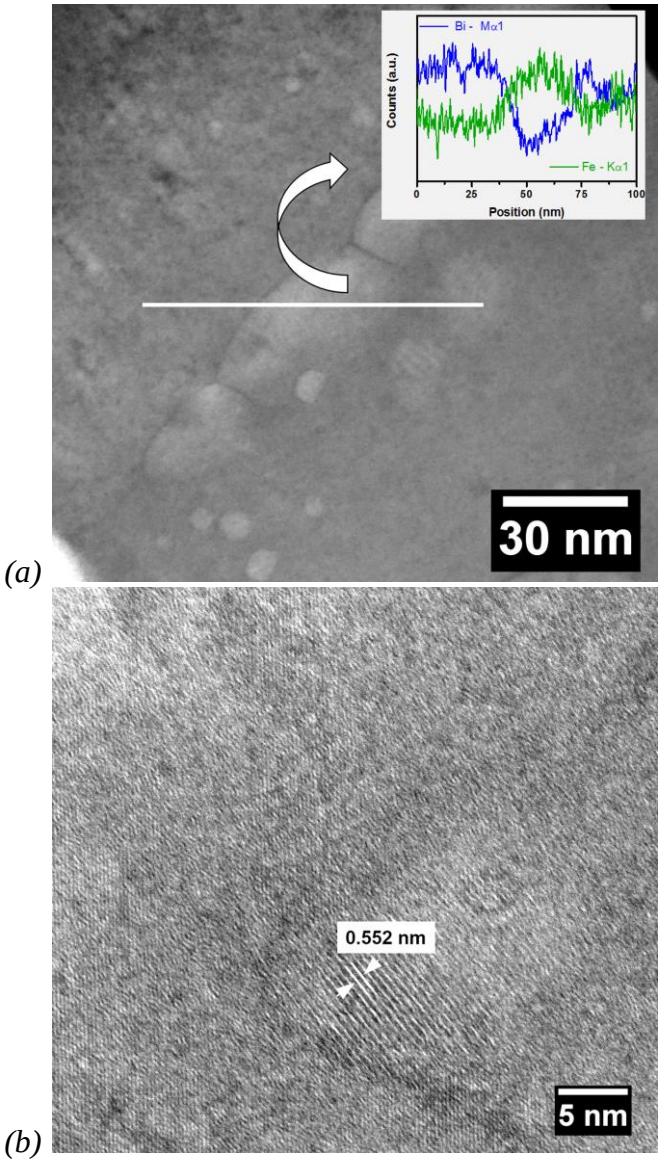

Figure 4-55. (a) STEM micrographs of second phase at the grain boundary of a BFO/Pt thin film with inset line-scan EDS plots obtained along the white line. The grain boundary phase is poor in Bi and rich in Fe with respect to the matrix, (b) high resolution lattice image of a second phase, grain boundary particle whose d-spacings are consistent with d_{110} (0.579 nm) $Bi_2Fe_4O_9$ phase.

In contrast, high resolution images of the grain interior (Figure 4-56 (a)) illustrate that the small inclusions are fully coherent with the matrix, despite being Fe rich according to the contrast within ADF images, Figure 4-54. Their location, primarily at the layer interfaces, suggests that their occurrence relates to Bi loss at the surface of each individual layer, the

mechanism for which is illustrated in Figure 4-56 (b). The high surface/volume ratio of thin films make them prone to Bi loss. In layer by layer deposition used in this study, the perovskite crystals in lower are nucleation sites for those in upper layers and grains transmit their orientation, leading to columnar growth. The precipitates do not disrupt this epitaxial nucleation process, consistent with the notion that they are fully coherent.

During the preparation of Bi-containing films, problems relating to interdiffusion and chemical fluctuations have been previously reported [297]. Yakovlev *et al.* using X-ray photoelectron spectroscopy (XPS) analysis, showed a wide film–electrode interface reaction due to interdiffusion in BFO films grown on Pt/Si substrates, pointing to the formation of Pt–Bi and Pt–Fe intermetallic compounds at the bottom electrode-film interface [297]. High-magnification ADF images of BFO/Pt, BFO/LNO and BFO/IrO_2 interfaces are shown in Figure 4-57. The BFO/Pt interface (Figure 4-57 (a)) appears sharp with the Pt relatively flat compared to IrO_2 and LNO. Figure 4-57 (b) shows that the BFO/LNO interface is broadened by the slight curvature of the grain boundaries of LNO. Figure 4-57 (c) reveals that the BFO/IrO_2 interface is not flat but consists of a series of roughly curved boundaries reflecting the topography of columnar grains of IrO_2. Experimental and theoretical studies have demonstrated that the interface roughness has a great influence on the electrical properties of dielectric films, especially leakage current [298]. All interfaces between BFO films and electrodes are free from interaction layers and secondary phases.

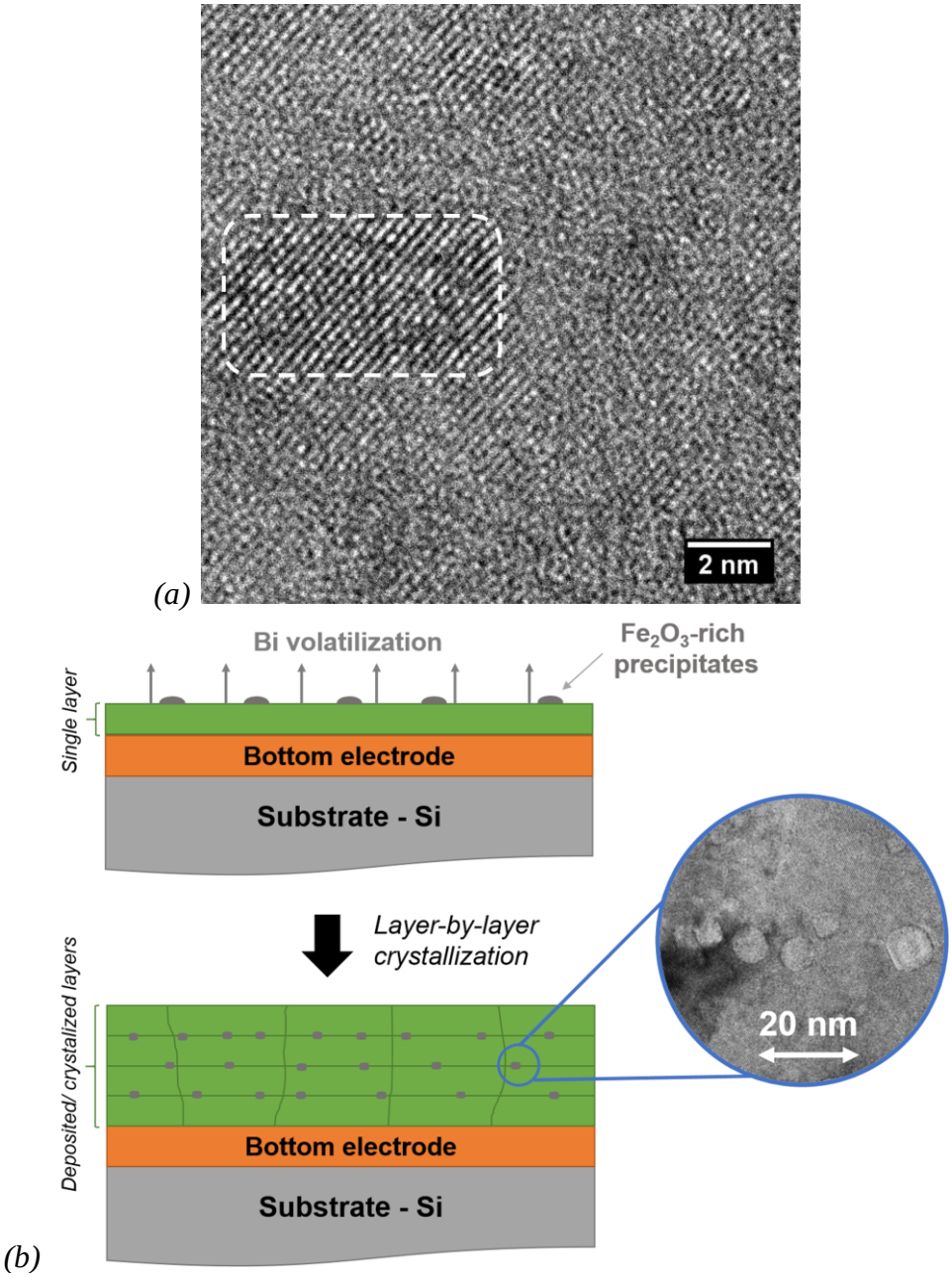

Figure 4-56. (a) HRTEM micrograph of the inclusion in the grain interior which indicates that they are coherent and (b) proposed mechanism of inclusion formation.

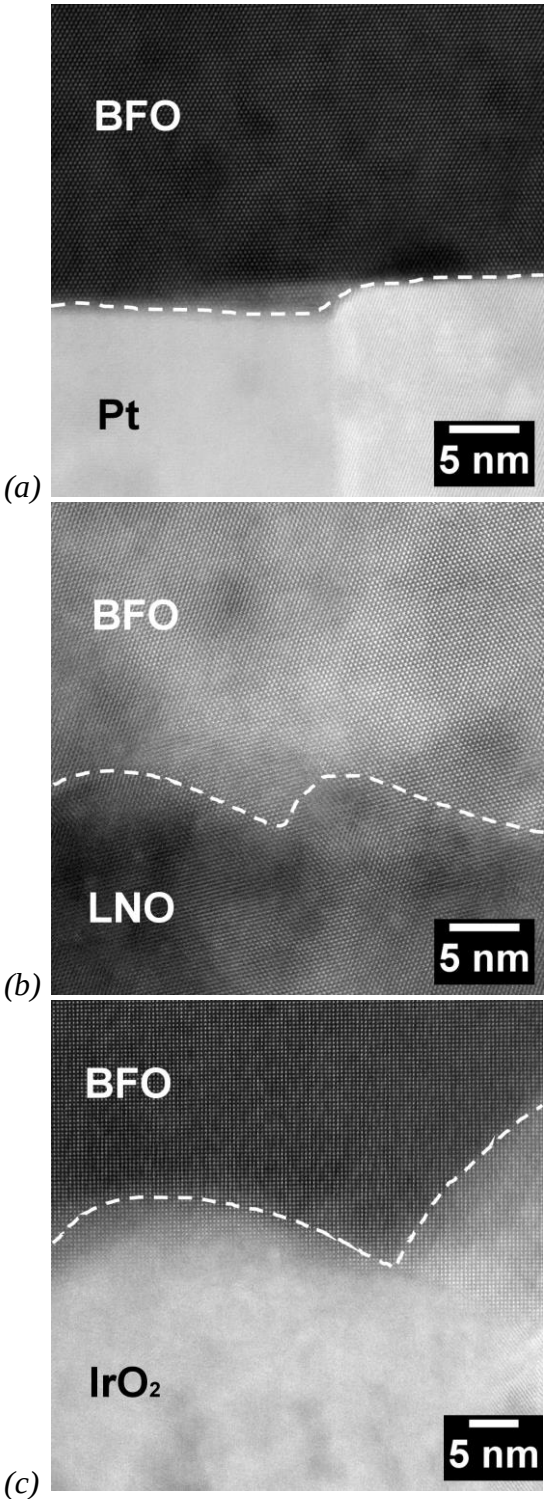

Figure 4-57. ADF TEM micrographs of (a) BFO/Pt, (b) BFO/LNO and (c) BFO/IrO_2 interfaces. No secondary phase was detected at the interface between BFO and bottom electrodes.

The effect that the bottom electrode has on residual stress in BFO films was also addressed. In a film, the total residual stress consists of: i) intrinsic stress induced by the formation of the grain boundaries during the crystal grain growth; ii) thermal stress due to the difference between thermal expansion coefficients of the film and the substrate and iii) extrinsic stress that originates from the lattice parameter mismatch [299]. The average residual stresses calculated by XRD $\sin^2\psi$ method are 0.72, 0.49 and 0.77 GPa for BFO/Pt, BFO/LNO and BFO/IrO_2, respectively, as presented in Figure 4-58. The stresses are tensile in all cases. Grain growth can contribute substantially to tensile stresses in a constrained film through elimination of the excess volume associated with grain boundaries and grain size has a dominant impact on the residual stress [300, 301]. In BFO thin films residual stress decreases with decreasing grain size. The highest residual stress was observed for BFO/IrO_2 film which has the largest grain size. In contrast, the stress state in BFO/LNO is lowered due a smaller lateral grain size.

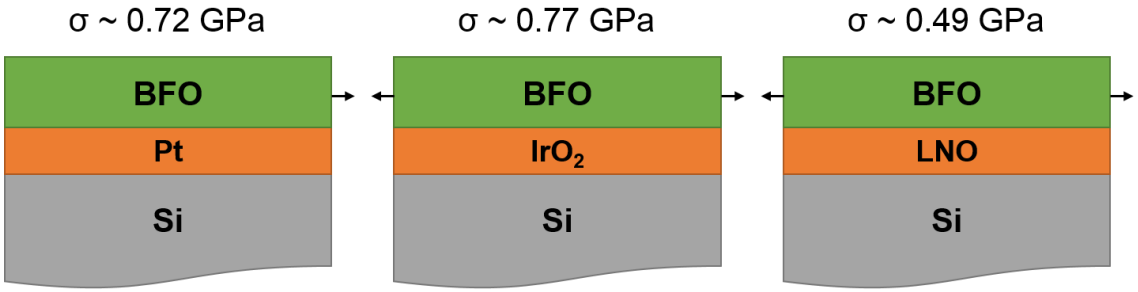

	Thermal expansion coefficient [×10^{-6} K^{-1}]	Lattice parameters [nm]
BFO	10.9	0.396
Pt	8.8	0.392
IrO_2	4.8	0.451 (*a*=*b*) 0.316 (*c*)
LNO	8.2	0.384

Figure 4-58. Schematic illustrating the average residual stresses calculated by XRD $\sin^2\psi$ method for BFO films on distinct electrodes. The lattice and thermal expansion coefficient of the BFO and bottom electrode materials were listed [269, 302, 303]. The stresses are tensile in all cases. The highest residual stress was observed for BFO/IrO_2 and the lowest in BFO/LNO thin films.

Figure 4-59 is a dark-field image of one of the columnar grains in a BFO films on LNO. This grain has an epitaxial relationship with a grain in the LNO layer. In contrast, films grown on Pt and IrO_2 did not exhibit an epitaxial orientation relationship with the electrode. Unlike IrO_2 and Pt, LNO has the perovskite structure with lattice parameter a = 0.384 nm, compatible with that of BFO, a = 0.396 nm and thus epitaxy is more likely [153] and may contribute to lowering of residual stress.

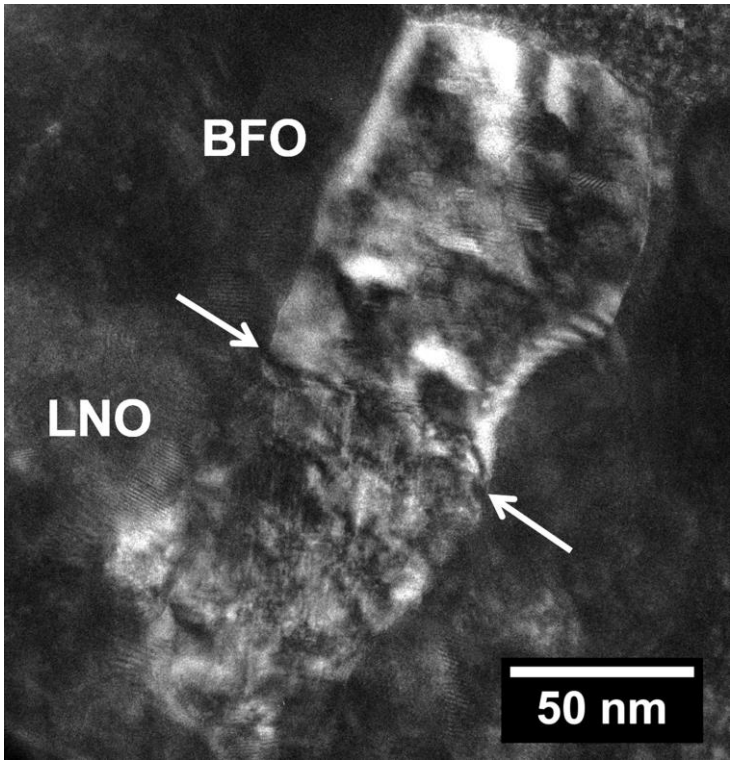

Figure 4-59. Dark-field image of a columnar grain in the BFO film on LNO. Local epitaxial growth of BFO on LNO was observed.

Summary: ADF imaging, STEM, HRTEM and EDX complemented with grazing incident XRD were used to analyse the microstructure and phase formation of BFO thin films prepared by the chemical solution deposition on $Pt/TiO_2/SiO_2/(100)Si$, $LNO/Pt/TiO_2/SiO_2/(100)Si$ and $IrO_2/TiO_2/SiO_2/(100)Si$ substrates. All the BFO films showed a columnar structure with the grain size depending on the electrode. Formation of $Bi_2Fe_4O_9$ was observed at the grain boundaries of BFO/Pt but coherent Fe-rich

precipitates were observed in the grain interior for all studied films. The crystallization of BFO films deposited on the oxide electrodes followed the sequence: amorphous → $Bi_2O_2(CO_3)$ → perovskite, while BFO on Pt crystallized directly from amorphous phase. IrO_2 was the most effective at promoting transformation to perovskite whilst LNO induced local epitaxial growth. Residual stress analysis of BFO films revealed that they are subject to tensile stress whose magnitude depends on the bottom electrode.

4.4. Correlation of electrodes with orientation and electrical performance of $BiFeO_3$ thin films

Abstract: The development of high quality BFO thin films fabricated by chemical solution deposition methods is currently relevant. For that the knowledge on the correlations between bottom electrodes and crystallographic orientation and electrical performance is needed. Here we provide a set of experimental evidences on the role of metallic (Pt) and oxide (IrO_2 and LNO) electrodes on the texture development and functional properties of BFO thin films. All BFO films are composed of columnar grains which size is dependent on the bottom electrode. No texture was observed for 320 nm thick films fabricated on (111) oriented Pt. Films on oxide electrodes, in particular on LNO are highly (012) oriented. The large remanent polarization in BFO/Pt and BFO/IrO_2 is attributed to the high leakage current contribution. 400 nm thick BFO films on LNO possess a low leakage current density ~4×10^{-6} A/cm^2, a large remanent polarization of 50 μC/cm^2 and a small coercive field of 180 kV/cm at room temperature. We demonstrate that LNO layers enhance the crystallinity and orientation of BFO thin films, which is reflected in their functional properties. This analysis shows that besides the simple need of monophasic films metal oxide electrodes have a relevant impact on the development of high quality BFO thin films fabricated by chemical solution deposition methods. These results have a broad implication for the fabrication of BFO thin film based devices.

Epitaxial BFO films with robust ferroelectric properties have been fabricated by pulsed laser deposition (PLD) [54], radio-frequency (RF)-sputtering [131], chemical solution deposition (CSD) [134, 149], metalorganic chemical vapor deposition (MOCVD) [133] and molecular beam epitaxy [103] on various single crystal substrates. For example, a large remanent polarization, P_r, ~55 μC/cm^2 and a piezoelectric coefficient d_{33} of approximately 70 pC/N was recorded in (100)-pseudocubic epitaxial BFO films grown on $SrRuO_3$/$SrTiO_3$ (STO) [54].

On the other hand, and in contrast, polycrystalline BFO films, in particular prepared by CSD, have been found to have a large scatter in the polarization properties. CSD derived BFO thin films usually exhibit high leakage currents and formation of secondary phases. It has been advocated that leakage currents in BFO are related to the existence of charge defects, as oxygen and bismuth vacancies. Those oxygen vacancies are due to reduction of Fe^{3+} species to Fe^{2+} $[Bi(Fe^{2+}Fe^{3+})]O_{3-\delta}$. It is also believed that B-site substitution with proper cations may reduce the oxygen vacancy concentration, thereby reducing the leakage currents. Several reports that recently discuss this drawback of polycrystalline BFO films proposed improvements, either by doping with La, Mn, Cr and Ni, or by introducing of an intermediate layer in between the substrate and BFO films [304-310], as well as by modifying film thickness [311]. Mn-doped BFO thin films deposited on a FTO/glass substrates by CSD presented a large P_r of 105 μC/cm^2 and low leakage current density of 1.42×10^{-5}A/cm^2 at 150 kV/cm [312]. This enhancement of the ferroelectric and the ferromagnetic properties was attributed to a structure transition from rhombohedral to tetragonal, the mixed-valence states of Mn^{2+} and Mn^{4+}, the improved surface morphology and the decrease of oxygen vacancies. Similar enhancements of properties have been reported for Ti-doped BFO films [313]. Moreover, thickness of BFO thin films has a great effect on the electric properties [153, 314, 315]. Tang *et al.* [315] found that the dielectric constant is enhanced and the leakage current is reduced as the thickness of BFO thin films deposited by CSD on Pt/Ti/SiO_2/Si (100) increases. By varying the thickness from 40 to 115 nm, BFO films grown on LNO-buffered Si substrates gradually transform from (100)-preferentially oriented to randomly oriented and the thicker films show better ferroelectric properties. Although no explanation was presented, the P_r values varied from 3 to 14.3 μC/cm^2 for 40 and 115 nm thick films, respectively [153]. It was also found that the ferroelectric domain size increases with increasing thickness of BFO thin films [314].

To construct ferroelectric devices, a sandwich structure is usually needed, including top electrode/BFO/bottom electrode. The top electrode is typically selected as Au or Pt. For the bottom electrode, metals such as Pt, Ni, Ru and Ir, and metallic oxides such as $SrRuO_3$, IrO_2, LNO, $La_{0.7}Sr_{0.3}MnO_3$ and Nb doped $SrTiO_3$ are normally utilized [25, 97, 149, 215]. As for the metals, the poor ferroelectric-electrode interface leads to the degradation of the ferroelectric properties [316], making it more desirable to use metallic oxides as bottom electrodes in BFO thin films structures. Nb and La co-doped BFO thin films have been

fabricated on oxide bottom electrodes, as LNO/Si and IrO_2/Si, by PLD [291]. These PLD doped BFO thin film capacitors on LNO exhibited a P_r higher than 75 μC/cm^2 in a saturated hysteresis loop. The same PLD La and Nb co-doped BFO thin film capacitors on IrO_2 showed a larger P_r of 93 μC/cm^2 while with a significant contribution from the leakage current, attributed by the authors to the nature of the interfacial layer between the doped BFO thin films and IrO_2. Furthermore, these doped BFO capacitors on LNO presented worse fatigue resistance than films on IrO_2. Doped BFO thin film capacitors on LNO showed remnant polarization dropping by up to 50 % after 10^7 read and write cycles. However, for the doped BFO films on IrO_2, almost no fatigue was observed after 10^7 read and write cycles.

In spite of this only a few investigations have been conducted on chemical solution deposited BFO films on LNO and IrO_2 bottom electrodes when compared with Pt. Moreover, the electrical properties of CDS BFO thin films on IrO_2 have not been reported yet.

According to our recent work on the growth of BFO thin films by chemical solution deposition, the bottom electrode (Pt, IrO_2 and LNO) strongly affects the microstructure and phase formation of ~150 nm BFO thin films prepared by CSD [317]. All our BFO films presented a columnar structure with the grain size depending on the electrode underneath. The formation of $Bi_2Fe_4O_9$ was observed at the grain boundaries only for BFO/Pt but coherent Fe-rich precipitates were observed for the first time in the grain interior of all studied films. Worth to highlight that IrO_2 was the most effective bottom layer to promote the transformation to perovskite whilst LNO induced local epitaxial growth [317].

The use of LNO as a bottom electrode was also reported for BFO thin films grown by CSD in other works. 160 nm thick BFO films on LNO/$SrTiO_3$ (111) single crystals were highly (012) oriented but the reported remnant polarization was very low: 0.86 μC/cm^2 under 375 kV/cm electric field at 80 K [23]. 250 nm thick BFO films on LNO/Si presented a P_r of 6.4 μC/cm^2 under 160 kV/cm electric field at room temperature [24]. The weak dielectric properties observed for films annealed at 600 °C was attributed to interfacial reactions [24]. For 480 nm thick BFO films on LNO/Si the dielectric constant (ε_r) and dielectric loss (tanδ) at 10 kHz were 202 and 0.057, respectively [27]. The P_r of these Pt/BFO/LNO/SiO_2/Si configurations was determined to be 45.5 μC/cm^2 for an applied field of ~745 kV/cm, although a round-shaped hysteresis was recorded. With a similar substrate configuration Liu *et al.* reported for 380 nm thick BFO films on LNO/Si substrates a room temperature

saturated hysteresis loops with a large P_r of ~60 μC/cm^2 at 10 kHz. These films showed low leakage current density of ~10^{-4} A/cm^2 at 450 kV/cm [25].

Table 4-8 summarises the available and above described data. The limited amount and scarcity of data on CDS BFO films on different substrates suggest the need of more and systematic studies. Indeed, up to now the consistent effect and comparative study of CDS BFO film thickness on the ferroelectric properties and its dependence on the bottom electrode has not been reported before. It is therefore interesting and opportune to investigate the effect of distinct bottom electrodes and film thickness, on the growth and electrical properties of BFO thin films prepared by CSD.

This contribution aims to establish and compare the electrical behaviour between IrO_2, LNO and Pt based BFO capacitors and to illustrate the dependence of the film thickness of these BFO/IrO_2, BFO/LNO and BFO/Pt capacitors on the ferroelectric properties.

Table 4-8. Electrical properties of BFO thin films on different bottom electrodes / substrates prepared by CSD and other related methods for comparison.

Method of deposition	Film Thickness (nm)	Bottom Electrode / Substrate	ε_r	tanδ	P_r (μC/cm^2)	E_C (kV/cm)	Leakage current density (A/cm^2)	Ref
PLD (La/Nb-doped BFO)	600	LNO/Si	-	-	75	~350	-	[291]
PLD (La/Nb-doped BFO)	600	IrO_2/Si	-	-	93 (round-shaped loop)	~300	-	[291]
CSD	160	LNO/STO	62-76	0.05-0.2	0.86	375	~10^{-6} @20kV/cm	[23]
CSD	250	LNO/Si	>100	0.2-2.4	6.4	160	~10^{-3} @320kV/cm	[24]
CSD	480	LNO/Si	202 @10kHz	0.057 @10kHz	~45 (round-shaped loop)	~372	~10^{-5} @10V	[27]
CSD	380	LNO/Si	-	-	60	1220	~10^{-4} @450kV/cm	[25]
CSD	>400	LNO/Si	140-170	0.07-0.1 @1MHz	65	600	~10^{-3} @250kV/cm	[318]

4.4.1. Experimental methods

BFO thin films were prepared by CSD. The details of the preparation of BFO precursor solution are presented in our previous work [317, 319]. Precursor solutions were deposited onto (111)Pt/TiO_2/SiO_2/Si (hereafter assigned as Pt/Si) and IrO_2/TiO_2/SiO_2/Si (hereafter assigned as IrO_2/Si) provided by Inostek Inc., and LNO coated Pt/TiO_2/SiO_2/Si (hereafter assigned as LNO/Si). Lanthanum nitrate hexahydrate ($La(NO_3)_3 \cdot 6H_2O$, Merck, 99 %) and nickel (II) nitrate hexahydrate ($Ni(NO_3)_2 \cdot 6H_2O$, Fluka, 98.5 %) were dissolved, respectively in 5 ml of deionized water, and mixed in the stoichiometric ratio of La:Ni=1:1. To improve the solution wettability and avoid film cracking during heating 1 ml of formamide (Merck, 99.5 %) was used. Finally, ethanol absolute (Merck, 99.8 %) was added until the resultant concentration of LNO solution was diluted to 0.2M. LNO films were deposited by spinning the solution on Pt/TiO_2/SiO_2/Si substrates at 2500 rpm for 45 s and annealed by RTP (Qualifllow JetFirst 100) at 700 °C for 5 min in O_2 atmosphere. The substrates were firstly cleaned in acetone (CH_3COCH_3, Panreac) and then in 2-propanol ($CH_3CHOHCH_3$, Panreac, for analysis).

The deposition of BFO thin films was carried out by spin-coating. Coatings were obtained with a spinner (KW-4A Spin Coater, Chemat Technology Inc.) working at 2500 rpm for 45 s. The wet films were dried and pyrolysed on a hot-plate at 350 °C for 1 min. BFO thin films were crystallized by RTP at 500 °C for 1 min. Deposition, drying and annealing steps were repeated 20 or 30 times in order to fabricate BFO thin films with desired thicknesses: BFO/Pt-20L, BFO/Pt-30L, BFO/IrO_2-20L, BFO/IrO_2-30L, BFO/LNO-20L and BFO/LNO-30L, where 20L and 30L denotes films prepared with 20 and 30 deposition layers. The schematic representation of BFO/Pt, BFO/IrO_2 and BFO/LNO films structures is presented in Figure 4-60.

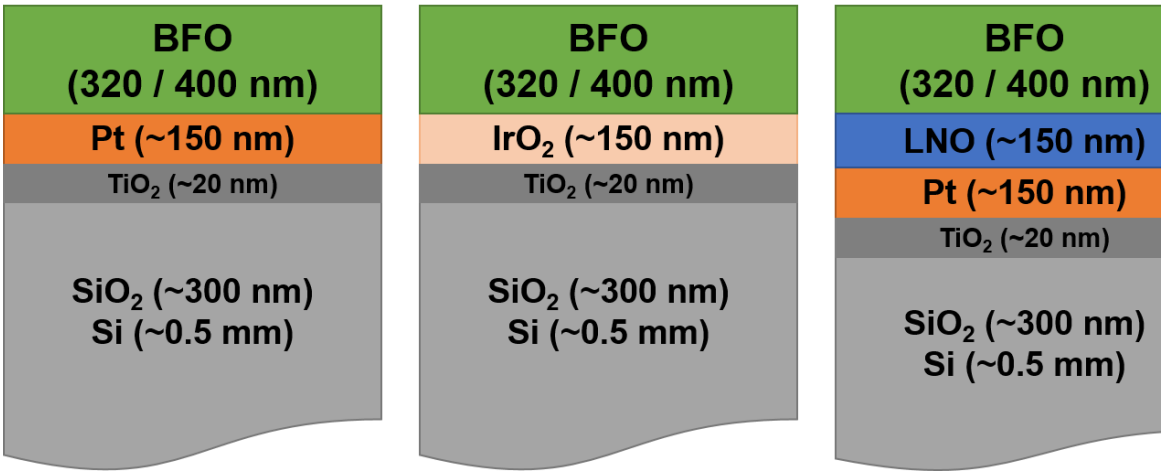

Figure 4-60. Schematic representation of BFO/Pt, BFO/IrO_2 and BFO/LNO thin films structures.

The crystallographic structure and phase content of BFO films were analyzed by X-ray diffraction (PANalytical X'Pert Pro diffractometer, Cu-Kα radiation, 45 kV and 40 mA, 10° to 50° 2θ, step size 0.025°). The texture fraction of (012) planes in the obtained BFO thin films was calculated from the XRD patterns in terms of the Lotgering factor.

XRD rocking curves were obtained by tilting the BFO films through the Bragg angle of (012) plane. In the measurements of pole figures the diffracted intensity was collected at a step-size of 5° in the tilting and rotating angles in the whole hemisphere, at a fixed θ-2θ angle of the open detector that corresponds to the (012) reflections of BFO films on Pt, IrO_2 and LNO. The specimens were tilted and azimuthally rotated in relation to the incident beam.

Raman spectroscopy was performed using Renishaw spectrometer equipped with He-Ne laser source with 633 nm wavelength and optical lens of 50x at room temperature. The microstructure of the thin films was observed using scanning electron microscopy (SEM) coupled with EDS (Hitachi SU-70). The thickness of the films was calculated from the cross-sectional SEM micrographs. The estimated thickness of the films was ~320 nm for BFO/Pt-20L, BFO/IrO_2-20L and BFO/LNO-20L, while for BFO/Pt-30L, BFO/IrO_2-30L and BFO/LNO-30L it was ~400 nm. The average grain intercept method was used to determine the average grain size of these films.

In order to perform the electrical characterization gold (Au) top electrodes with a diameter of 250 μm were deposited on the films by DC sputtering using a shadow mask followed by an annealing treatment at 300 °C for 30 min in air. Ferroelectric hysteresis loops, currents and leakage currents were measured with a ferroelectric TF Analyzer 2000, equipped with a ferroelectric module, at room temperature and a frequency of 4 kHz.

4.4.2. Results

Figure 4-61 presents the XRD patterns of BFO/Pt, BFO/IrO_2, and BFO/LNO films, with: (a) 20L and (b) 30L. Films exhibit monophasic perovskite phase with no evidence of any extra phase within the XRD detection limits. The XRD peaks are indexed to the rhombohedrally distorted perovskite structure with space group *R3c*, as previously reported for polycrystalline BFO films grown by CSD [139].

For BFO films deposited on Pt, no preferred orientation was observed only for BFO/Pt-20L ones. However, for BFO/Pt-30L the ratio of the intensity of the (012) to (104/110) peaks changes and the films become slightly (012) oriented. For BFO/LNO-20L and BFO/LNO-30L films (012) diffraction lines are significantly higher than (104/110) peaks, thus these films hold a (012) preferred orientation. In the case of BFO films on IrO_2, BFO/IrO_2-20L films show an appreciable (012) orientation, however with the progressive increase in the thickness (from 320 nm to 400 nm), the texture decreases.

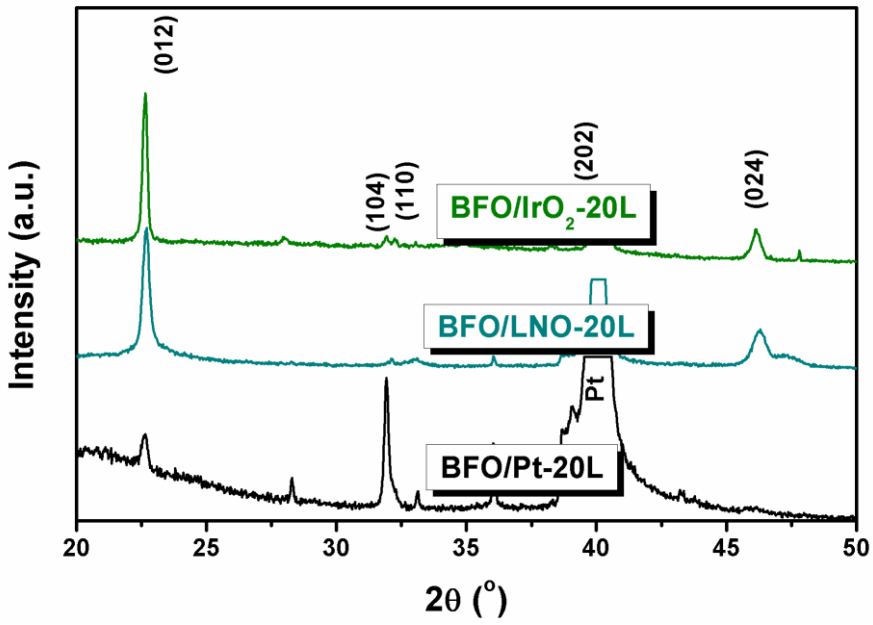

(a)

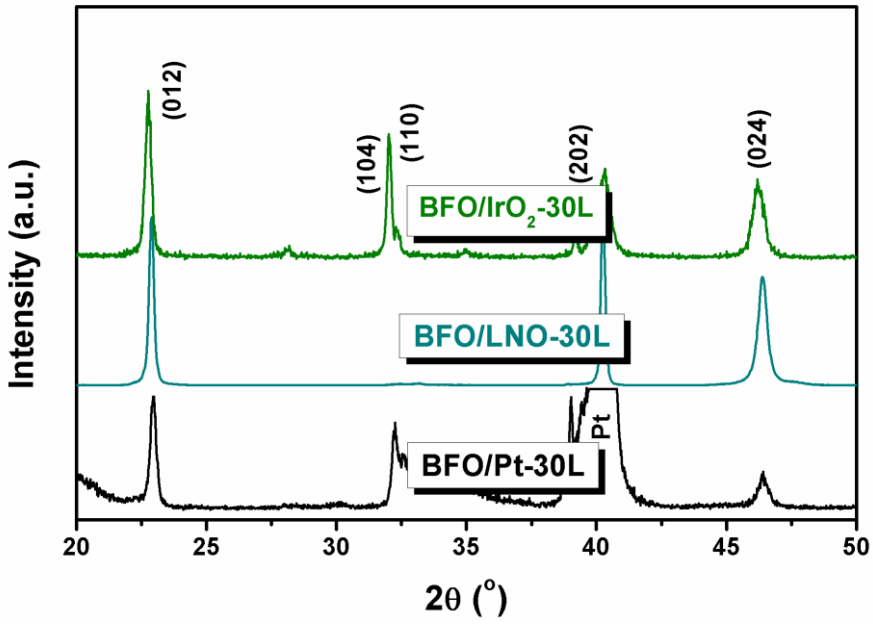

(b)

Figure 4-61. XRD patterns of BFO thin films on Pt/Si, LNO/Si and IrO_2/Si, with (a) 20L (320 nm) and (b) 30L (400 nm), and annealed at 500 °C. Diffraction lines of crystallographic planes of R3c space group are marked. All peaks associated with BFO/Pt, BFO/IrO_2 and BFO/LNO may be attributed to either the electrode or the BFO perovskite phase.

Therefore, texture analyses of the films by XRD were conducted in order to analyze in detail their preferred orientation, and XRD rocking curves and pole figures corresponding to (012) diffraction line ($2\theta \approx 22.65°$) were recorded. Figure 4-62 shows the 2D projection of pole figures and rocking curves of BFO films on distinct substrates and with different thicknesses. The intensity of a single peak as a function of tilt (-90° to 90°) and rotation (360°) of the sample is represented on the pole figure maps, and the lines of the same colour depicts the points with the same intensity. The center of pole figures, at a tilt angle of 0°, corresponds to the normal of the lattice plane that is parallel to the film surface normal, thus if most of the crystallites in the films have the planes arranged in parallel manner to the selected 2θ, the film is considered to be preferentially oriented to this lattice plane. According to Figure 4-62, the pole figure maps of the films deposited on Pt/Si: BFO/Pt-20L and BFO/Pt-30L, are rather similar with diffuse distribution of the lines, however, for BFO/Pt-30L the map is more clustered meaning that the films are slightly more oriented than BFO/Pt-20L, corroborating the XRD results. Similar pole figure map to BFO/Pt-20L is observed for the case of BFO/IrO_2-30L, *i.e.* these films are also randomly oriented. However, for the other films: BFO/IrO_2-20L, BFO/LNO-20L and BFO/LNO-30L, the projected intensities are all grouped in a central circle near a tilt angle of 0°. It is an obvious indication that these films are oriented along (012), as XRD results suggested. Additionally, the rocking curves match well the pole figure distributions. The full width at half maximum (FWHM) of the (012) diffraction for oriented BFO films are 3.27, 3.29 and 2.29° for BFO/IrO_2-20L, BFO/LNO-20L and BFO/LNO-30L, respectively. A low FWHM value indicates a strong film texture. It can be clearly stated that LNO bottom electrode promotes (012) texture of BFO films and the orientation increases with thickness increasing, while for IrO_2 the degree of orientation decreases with increasing thickness of BFO films.

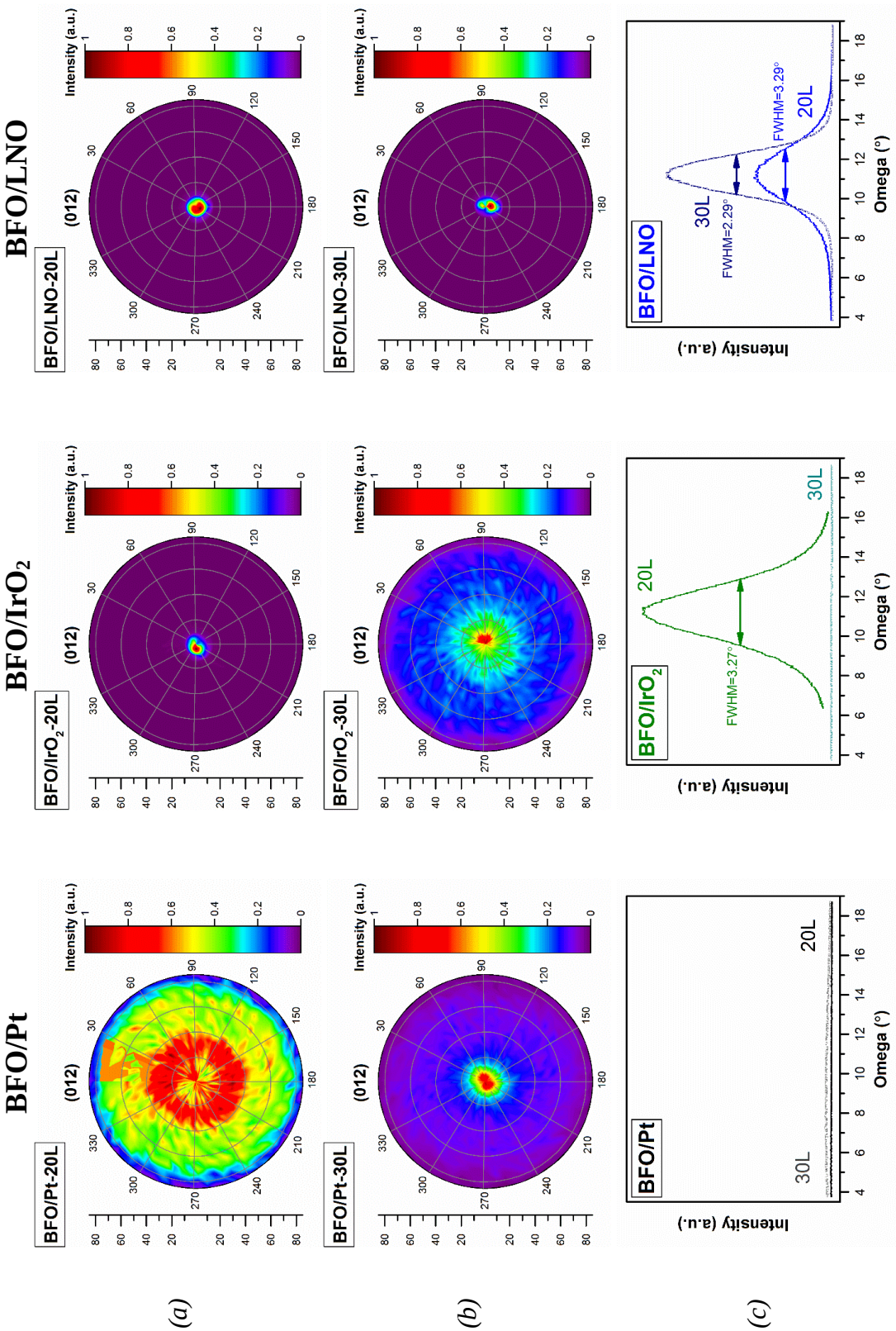

Figure 4-62. XRD pole figure maps corresponding to (012) diffraction reflection of BFO thin films on Pt/Si, LNO/Si and IrO_2/Si, with 20L (a) and 30L (b). Rocking curves are also presented (c). Strong (012) texture is observed for BFO/IrO_2-20L and BFO/LNO independently on the film thickness, in this last case.

Figure 4-63 displays Raman spectra of BFO films on distinct substrates and with different thickness, acquired in the range of 100 to 400 cm^{-1}. The rhombohedral *R3c* structure of BFO presents 13 distinct Raman-active modes, using the representation: $\Gamma_{R3c} = 4A_1 + 9E$ [320, 321]. In BFO films only three A_1 modes with strong scattering intensities (~140, ~170 and ~220 cm^{-1}) in the low-frequency region can be clearly detected, assigned to A_1-symmetry longitudinal-optical phonons [A_1(LO)]. The three E-symmetry transverse-optical phonons, E(TO), are located in the frequency range 250-400 cm^{-1} (marked in Figure 4-63), but they are barely visible. Another E(TO) peak ~116 cm^{-1} is overlapped by A_1-1 mode. These observations are in good agreement with previously reported Raman spectra of BFO films grown by PLD [322], proving that the films are well crystallized with proper crystallographic arrangement. The results strongly confirm the distorted rhombohedral structure of the BFO thin films; this is in agreement with the XRD results.

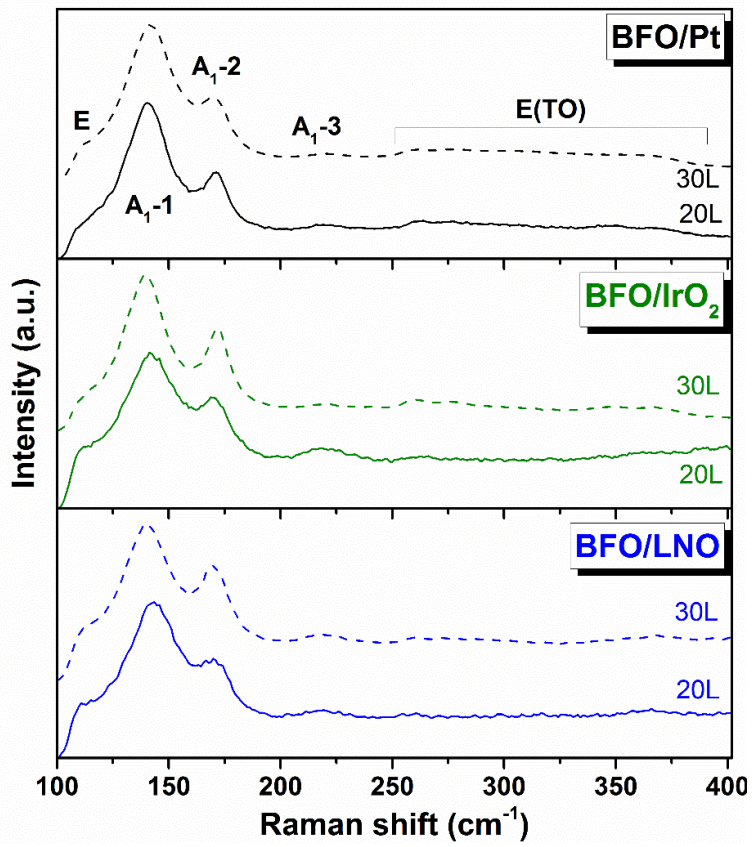

Figure 4-63. Raman spectra of BFO thin films on Pt/Si, LNO/Si and IrO_2/Si, with 20 (solid lines) and 30 (dashed lines) deposition layers.

Figure 4-64 shows SEM top view micrographs and cross-sections of BFO/Pt, BFO/LNO and BFO/IrO_2 films. Some pinholes can be observed from the top view SEM micrographs but cross-sections indicate that all films are dense and uniform. The morphology of the films is composed of columnar grains regardless of the type of bottom electrode used, similarly to our previous study [317], and thickness.

The grain size of BFO thin films changes with the type of bottom electrodes used. The largest grains are observed for BFO films on IrO_2 (~210 and 310 nm for 20L and 30L films, respectively) and the smallest for LNO (~100 and 85 nm for 20L and 30L films, respectively) bottom electrode. Average grain size of BFO/Pt films is ~115 and 135 nm for 20L and 30L, respectively.

Figure 4-65 depicts the ferroelectric response of the films at room temperature. BFO/Pt-20L and BFO/Pt-30L thin films exhibit P_r of 65 μC/cm^2 and E_C of ~480 kV/cm (E_C was calculated for all films as $(+E_C+(-E_C))/2$), and P_r of 54 μC/cm^2 and E_C = 380 kV/cm, respectively. BFO/IrO_2-20L film suffers a dielectric breakdown for applied field larger than 450 kV/cm, preventing the full switching at room temperature. A very large remanent polarization of 71 μC/cm^2 and E_C = 320 kV/cm was obtained below the breakdown voltage for BFO/IrO_2-20L, and P_r = 136 μC/cm^2 and E_C = 330 kV/cm for BFO/IrO_2-30L. BFO/LNO-20L shows P_r of 40 μC/cm^2 and E_C = 540 kV/cm. In contrast, well saturated hysteresis loops for highly (012) textured BFO/LNO-30L exhibits well-shaped *P-E* hysteresis with P_r and *Ec* of 50 μC/cm^2 and 180 kV/cm, respectively, which is in consistence with the P_r value of 55 μC/cm^2 for epitaxial BFO films with the same orientation.

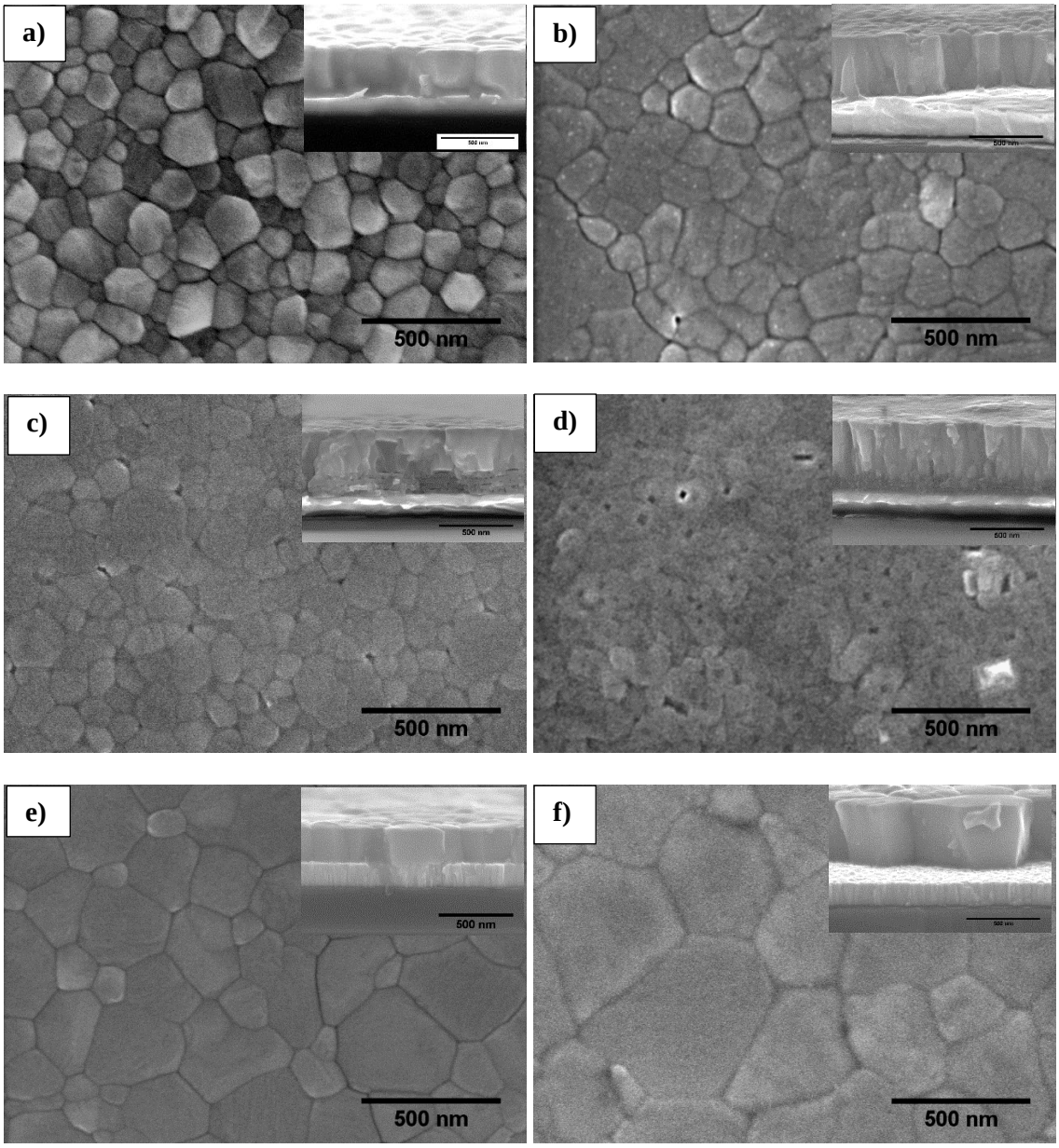

Figure 4-64. Plan view and cross section view (inset) SEM micrographs of BFO/Pt-20L (a), BFO/Pt-30L (b), BFO/LNO-20L (c), BFO/LNO-30L (d), BFO/IrO_2-20L (e) and BFO/IrO_2-30L (f). The estimated thickness of films was ~320 nm for BFO/Pt-20L, BFO/IrO_2-20L and BFO/LNO-20L, while for BFO/Pt-30L, BFO/IrO_2-30L and BFO/LNO-30L it is ~400 nm. The results show that the average grain sizes increase with increasing thickness, except for the BFO/LNO-30L.

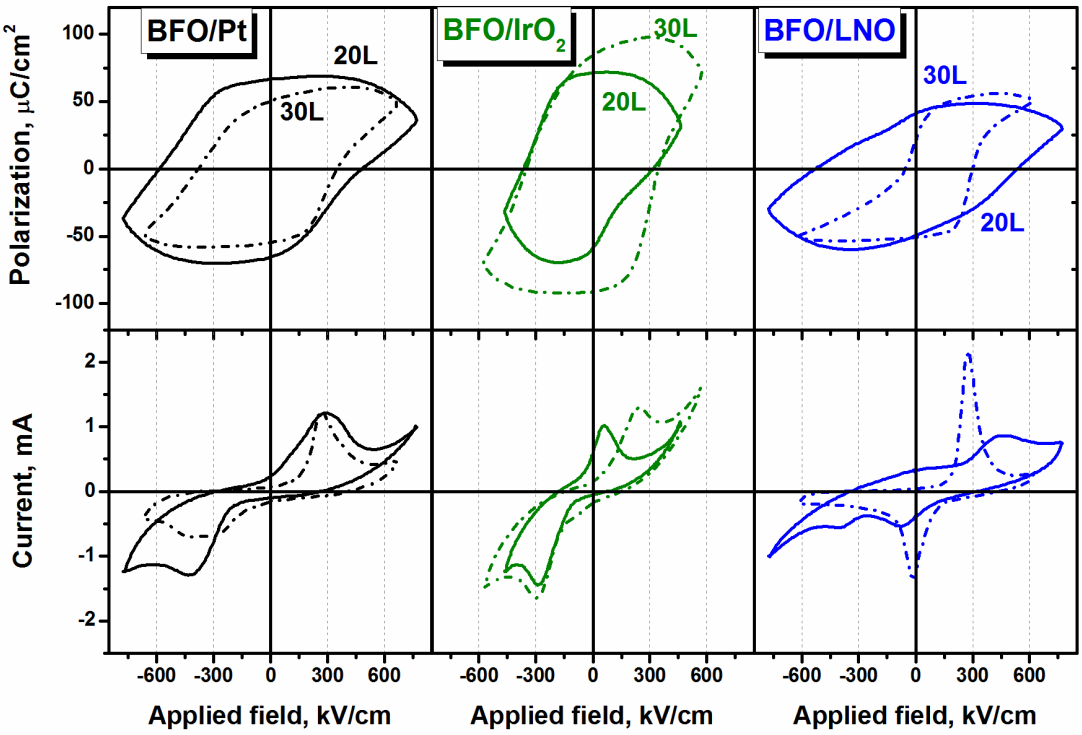

Figure 4-65. The polarization (P-E) hysteresis loops (top) and the switching currents versus applied field (I-E) (bottom), for BFO/Pt, BFO/LNO and BFO/IrO_2 measured at room temperature and at 4 kHz for films with thickness of 320 nm (solid line) and 400 cm (dashed line). A significant contribution from the leakage current was obvious, as evidenced by the round shape of the P-E loops for BFO/Pt, BFO/IrO_2 and BFO/LNO-20L.

The leakage current density (*J*) versus electric field (*E*) of the different BFO thin films on different electrodes was measured and is shown in Figure 4-66. BFO films grown on Pt exhibit leakage currents of 3.61×10^{-4} and 4.12×10^{-6} A/cm^2 at 400 kV/cm for 20L and 30L films, respectively, and BFO films grown on LNO exhibit the lowest leakage current of 5.28×10^{-7} and 4.04×10^{-6} A/cm^2 at 400 kV/cm for 20L and 30L films, respectively. BFO films grown on IrO_2 exhibit high leakage current of 4.27×10^{-2} and 3.58×10^{-1} A/cm^2 at 400 kV/cm for 20L and 30L films, respectively. With increasing film thickness, the leakage current density decreased strongly for BFO/Pt. Different leakage currents under a positive and negative bias can be attributed to the asymmetric electrodes.

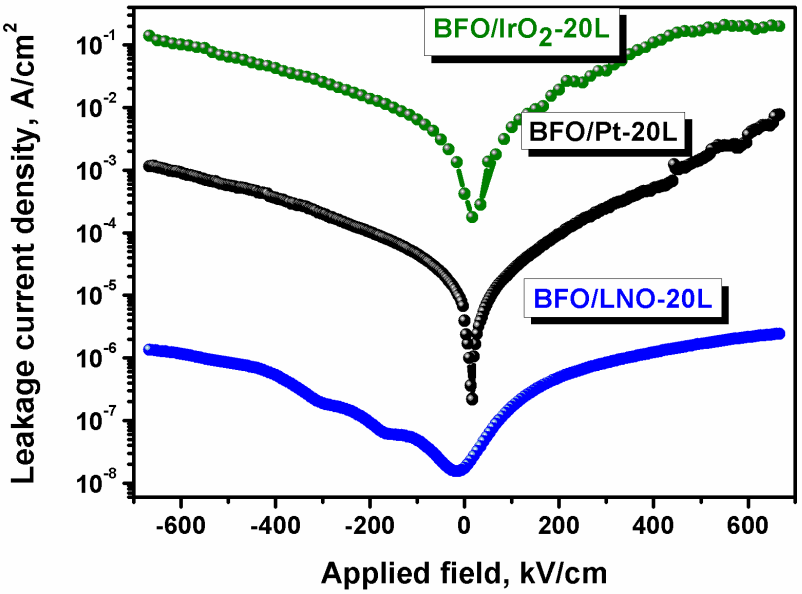

(a)

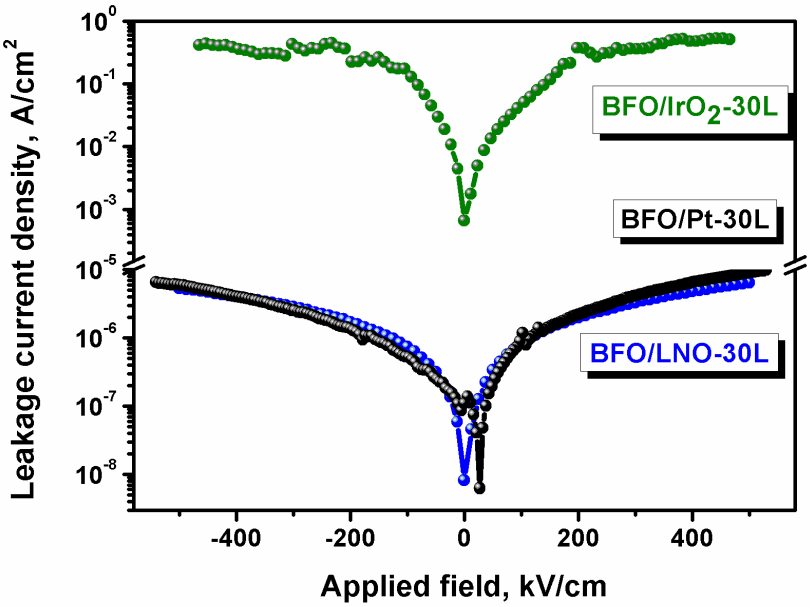

(b)

Figure 4-66. The leakage current density (J) versus electric field (E) of BFO thin films on different electrodes having thickness of (a) 320 nm (20L) and (b) 400 nm (30L). For films with LNO used as a bottom electrode, the leakage current density was substantially reduced to 5.28 × 10^{-7} and 4.04 × 10^{-6} A·cm^{-2} for BFO/LNO-20L and BFO/LNO-30L consistent with saturated hysteresis curves.

4.4.3. Discussion

From the above described results is clear that the underneath electrode layer has a marked effect on the structure, microstructure and electrical performance of BFO thin films fabricated by CSD. Well known is that a combination of strain and interface effects are responsible for the differences in the dielectric properties of thin films and single crystals [323]. It is then expected that the differences in the lattice mismatch and thermal expansion coefficient between BFO and Pt, IrO_2 and LNO (Table 4-9), will affect strain state, crystallization, crystal orientation, microstructure and even defect chemistry.

Table 4-9. Some physical and crystallographic parameters of Pt, IrO_2, LNO and BFO.

Property / Material	Thermal Expansion Coefficient ($\times 10^{-6}$ /K)	Lattice Parameters (Å)	Crystallographic Structure and Growth Plane	Ref
Pt	8.8	3.92	Face centered cubic / (111)	[269]
IrO_2	4.8	4.51 (a=b) 3.16 (c)	Tetragonal Rutile / polycrystalline	[302]
LNO	8.2	3.84	Rhombohedral perovskite / polycrystalline	[303]
BFO	10.9	3.96	Rhombohedral perovskite / (012)	[269]

Generally, residual stresses come from the sum of lattice misfit strain, thermal stress, phase transition stress and intrinsic stress. Another source of strain / stress in thin films is related with the annealing process after or during film´s fabrication. High temperatures are usually required for the film crystallization (perovskite phase for the case of BFO) and due to the difference in the thermal expansion coefficients of the film (α_{film}) and substrate ($\alpha_{substrate}$) strain / stress develop between the substrate and the film upon cooling to room temperature. This thermal stress $\sigma_{thermal}$ can be calculated according to equation (9). The stress value for each film is obtained by substituting E = 133 GPa and ν = 0.25 [324]. The

thermal expansion coefficient (α) of BFO, Pt, IrO_2 and LNO is 10.9, 8.8, 4.8 and 8.2×10^{-6} /K, respectively [317]. Therefore, tensile $\sigma_{thermal}$ of BFO/Pt, BFO/IrO_2 and BFO/LNO is 176, 512 and 226 MPa.

Studies have been proving that $\sigma_{thermal}$ may induce stress driven preferred orientation and structural changes in the thin films that results in an extreme case in the cracking of the films that may lead to short circuiting between their top and bottom electrodes and also alterations in their dielectric intrinsic response.

In addition as BFO is a rhombohedral perovskite it crystallizes in the same structure as LNO, consequently with a minimal lattice mismatch. So, from the strain point of view it is expected that the nucleation and growth of BFO on LNO will be facilitated in relation to the nucleation on the other electrodes and less strained and defective films developed.

Indeed it was observed that the formation of BFO perovskite phase occurs at lower temperatures for the BFO on LNO [317], and the grain size of the annealed films is much smaller (85-100 nm for BFO/LNO versus 210-310 nm for BFO/IrO_2).

Columnar grain growth as observed in our BFO films can only be achieved when a nucleation at the substrate interface is favoured over the bulk nucleation. By preparing thinner layers using a highly diluted solution and performing crystallization of each layer before the next layer is deposited, bulk nucleation within the film was avoided, and surface of prior-crystallized BFO layer serves as new nucleation sites without lattice mismatch and induce local epitaxial growth within each columnar grain [295].

Based on the microstructural observations, we can assume that BFO have lower nucleation barriers when deposited on LNO compared to IrO_2 and Pt, due to similar perovskite structure of BFO and LNO (small lattice mismatch, ~3 %). A lower nucleation barrier means more nuclei can form at a particular annealing temperature and smaller grain size is expected in the fully crystallised film, as indeed observed in the case of LNO bottom electrodes. On the other hand, in the case of IrO_2 with tetragonal structure with $a = b = 4.51$ Å and $c = 3.16$ Å and Pt with cubic structure ($a = 3.92$ Å), much fewer nuclei are formed and, consequently, most of the nuclei can grow into much larger grains [3]. The results show that the average grain sizes increase with increasing thickness, except for the BFO/LNO, what is related with the above discussion.

Due to the presence of these induced strains and stress levels modifications and to the different crystal structures of BFO films and substrate layers we may expect different texture degree for the different films. Indeed, XRD pole figures and rocking curves identified different preferred orientation and texture degree for the different films. To quantify the crystallographic texture of the films, we calculated the Lotgering factor (*f*) of BFO films based on XRD patterns. The Lotgering factor (*f*) is defined as the fraction of the area oriented with the crystallographic plane of interest as:

$$f = \frac{\sum \frac{I_{0kl}}{I_{hkl}} - \sum \frac{I^0_{0kl}}{I^0_{hkl}}}{1 - \sum \frac{I^0_{0kl}}{I^0_{hkl}}} \cdot 100\ (\%) \qquad (10)$$

where, I_{hkl} and I^0_{hkl} being the intensities of (hkl) peaks for the oriented and randomly oriented samples, respectively. The Lotgering factor varies between zero to 100 %; 0 corresponds to the random orientation, and 100 % to the full orientation. In the current work BFO thin films grown on polycrystalline (non-textured) oxide electrodes, such as LNO and IrO_2, exhibit *f* of 72, 95, 49 and 21 % for BFO/LNO-20L, BFO/LNO-30L, BFO/IrO_2-20L and BFO/IrO_2-30L, respectively. The highest Lotgering factor, or the highest texturization, is observed for BFO/LNO films. In this case the textured nature of BFO is independent on the film thickness for LNO bottom electrodes, effectively inducing a (012) textured structure. BFO grown on highly (111) oriented Pt exhibit *f* of 13 and 25 % for BFO/Pt-20L and BFO/Pt-30L, respectively. BFO thin films on Pt are randomly oriented for the thinner films and become more oriented as the film thickness increases. While for IrO_2 bottom electrode films become more randomly oriented as the film thickness increases.

The observed results can be understood based on the fact that as-grown BFO single crystals reflect exclusively (012) reflections suggesting a natural growth habit along this plane [325]. So unless an external factor, in this case the underneath layer, restricts the crystallographic growth within a specific crystallographic direction, as is the case of the highly (111) textured Pt, the growth of BFO will be preferentially (012) oriented. This is the case for BFO films grown on IrO_2 and LNO of this work. In the case of BFO on Pt there is a direct conflict between the natural growth habit of BFO along the (012) plane and the texturization imposed by the Pt layer (111). This conflict originates a random oriented BFO film. But as expected this conflict is lost as the film thickness increases and thicker BFO

films on Pt start to be more (012) oriented as the bulk crystallization dictates. A similar phenomena was observed for Pb(Zr, Ti)O_3 (PZT) films on Pt/Si substrates. The change in the crystallographic orientation in PZT films is attributable to the competition between the interfacial energy and the inherent kinetics of the system [326]. When the film is thin, it grows with a (111) orientation to minimize the interface energy between the underlying (111) oriented Pt and the newly nucleating PZT film. However, as the film becomes thicker, films became (100) oriented, because (100) plane has the lowest activation energy for nucleation (natural growth habit) [326]. In the case of BFO and similarly to our work, Tyhold *et al.* described the growth of 120 nm thick (012)-textured BFO by CSD on Pt electrode with low degree of texture [286]. No relation to the Pt structure was found and the very same (012) texture of BFO was even obtained when deposited on glass. Therefore, we advocate that the (012) BFO texture originates from the growth mechanism. This means that, unless we use a substrate which restricts growth within a specific crystallographic relationship (for example highly (111) textured Pt), the growth of BFO is preferentially (012) oriented.

These are crucial observation because some orientation-sensitive physical properties, such as P_r and E_C, may vary with the degree of orientations, which is different for BFO films grown on Pt/Si, IrO_2/Si or LNO/Si.

It was reported from both theoretical and experimental investigations that P_r of BFO thin films is largely dependent on the orientation of the films, and the largest P_r is found in the thin films with $(111)_{pc}$ orientation (easy direction of spontaneous polarization) [109, 327]. In epitaxial BFO thin films prepared by PLD, a P_r of ~55 μC/cm^2 for $(001)_{pc}$ films, ~80 μC/cm^2 for $(101)_{pc}$ films, and ~100 μC/cm^2 for $(111)_{pc}$ (pseudocubic settings) films was reported [93]; similarly to BFO single crystals where P_r = 60 μC/cm^2 along (012) [55]. Thus, for the films with $(001)_{pc}$ (*i.e.* $(012)_{hex}$) texture, as in our case for BFO/IrO_2-20L, BFO/LNO-20L and BFO/LNO-30L, the expected value of P_r is ~55 μC/cm^2.

A significant contribution from the electrical conductivity was obvious, as evidenced by the round shape of the *P-E* loops and the very high current at the maximum applied field in *I-E* curves for BFO/Pt, BFO/IrO_2 and BFO/LNO-20L. The contribution of electrical conductivity cannot be avoided in measurements of ferroelectric hysteresis loops, and the obtained polarization can be characterized as [328]:

$$P = P_i + \frac{\sigma E t}{2} \quad (11)$$

where P_i is the intrinsic polarization, σ is the electrical conductivity, E is the applied field and t is the measuring time. Therefore, we advocate here that the very high values of P_r obtained for BFO/IrO_2 and BFO/Pt are associated with high electrical conductivity.

The decrease of P_r for BFO/Pt-30L in comparison to BFO/Pt-20L can be attributed to the decrease of electrical conductivity in thicker films, as better-shaped *P-E* hysteresis loop was obtained for BFO/Pt-30L. This decrease of electrical conductivity in BFO/Pt-30L is due to the decreased contribution of structural defect density such as oxygen vacancies between Pt electrode and BFO as the film thickness increases due to enhanced crystallinity of BFO/Pt-30L [315].

It should be noted that the *P-E* and *I-E* loops measured for all the films are asymmetric due to imprint. This asymmetry can be induced by various factors such as: defect charges present in the ferroelectric material, differences in the work function of the top and the bottom electrodes, and interfacial charges [329]. Usually asymmetries of *P-E* loops are attributed to the electrode asymmetry in terms of work functions between the bottom and top electrodes. In addition, due to their work functions, these electrodes give rise to different barrier height at the bottom and top interfaces, resulting in different leakage currents under a positive and negative bias [329]. Indeed, in this study Pt, LNO and IrO_2 were used as bottom electrodes and Au as a top electrode. The work function of Au and Pt accounts for 5.1 and 5.3 eV, and 4.6 and 4.2 eV for LNO and IrO_2, respectively [330, 331].

The leakage current density of the BFO/Pt 400 nm (30L) films was nearly two orders of magnitude smaller than that observed for the 320 nm (20L) ones. The decrease in leakage current density is usually attributed to the enhanced crystallinity, a general decrease in defect density between bottom electrode and BFO film and increasing grain size, with increase in film thickness [332]; indeed BFO/Pt-30L possesses higher crystallinity (as deduced from Raman spectra based on FWHM increase) and bigger grain size than BFO/Pt-20L. For BFO/IrO_2 and BFO/LNO films thickness do not have strong effect on the leakage current of BFO films. Therefore, the observed well-shaped hysteresis loop for BFO/LNO-30L, cannot be attributed only to low leakage current but to the combined effect of enhanced (012) texture and crystallinity along with low leakage current. The highest leakage current is observed for

BFO films on IrO_2 and the lowest for BFO on LNO. A large number of experiments have found that the surface/interface roughness has a great influence on the electrical properties of dielectrics, especially the leakage current [298]. Indeed our recent TEM study revealed that the BFO/IrO_2 interface is rough (reflecting the topography of columnar grains of IrO_2) in comparison with BFO/Pt and BFO/LNO [317]. This roughness of BFO/IrO_2 interface may contribute to the observed high leakage currents. Since top electrodes usually suffered little thermal process, they only provide ohmic contact in ferroelectric capacitors and bottom electrodes are believed to have the greatest impact on the leakage properties [333]. Among the studied electrodes LNO is the most effective in obtaining BFO films with low leakage current and well-shaped hysteresis loops due to combined effect of enhanced (012) texture and crystallinity along with low leakage current.

In what concerns Pt based metallic electrodes, BFO films on (111) Pt/TiO_2/SiO_2/Si films are randomly oriented without specific texture development, they exhibit a columnar growth and an average grain size of ~115 and 135 nm for 320 nm and 400 nm thick films, respectively. These films show an increase of the grain size with the increase of the film thickness. 320 nm thick BFO/Pt-20L and 400 nm thick BFO/Pt-30L exhibit P_r of 65 μC/cm^2, E_C of ~480 kV/cm and J of 3.61×10^{-4} A/cm^2 at 400 kV/cm, and P_r of 54 μC/cm^2, E_C = 380 kV/cm and J of 4.12×10^{-6} A/cm^2 at 400 kV/cm, respectively.

In what concerns IrO_2, BFO films on IrO_2/TiO_2/SiO_2/Si show an appreciable (012) orientation, however with the progressive increase in the thickness (from 320 nm to 400 nm), the texture decreases, they exhibit a columnar growth and the large average grain size of ~210 and 310 nm for BFO/IrO_2-20L and BFO/IrO_2-30L, respectively. 320 nm thick BFO/IrO_2-20L and 400 nm thick BFO/IrO_2-30L exhibit P_r of 71 μC/cm^2, E_C of ~320 kV/cm and large J of 4.27×10^{-2} A/cm^2 at 400 kV/cm, and P_r of 85 μC/cm^2, E_C = 330 kV/cm and J of 3.58×10^{-1} A/cm^2 at 400 kV/cm, respectively.

In what concerns LNO, BFO films on LNO coated (111) Pt/TiO_2/SiO_2/Si show strong (012) texture and its increase with films thickness increasing. They exhibit a columnar growth and the small average grain size of is ~100 and 85 nm for 320 nm and 400nm thick films, respectively. 320 nm thick BFO/LNO-20L and 400 nm thick BFO/LNO-30L exhibit P_r of 40 μC/cm^2, E_C of ~540 kV/cm and small J of 5.28×10^{-7} A/cm^2 at 400 kV/cm, and P_r of 50 μC/cm^2, E_C = 180 kV/cm and J of 4.04×10^{-6} A/cm^2 at 400 kV/cm, respectively.

Table 4-10 presents the values of P_r, E_C and J for BFO thin films prepared by CSD with different bottom electrodes reported in this work and in the literature.

Table 4-10. Comparison of functional properties of BFO thin films on different electrodes fabricated by CSD. Large ferroelectricity in BFO/Pt-20L and BFO/IrO_2 (20L and 30L) is attributed to the high leakage current contribution.

	Texture / thickness (nm)	**P_r (μC/cm^2)**	**E_C (kV/cm)**	**J (A/cm^2) @400 kV/cm**	**Ref**
BFO on Pt-20L	No / 320	65	480	$3.61 \cdot 10^{-4}$	This work
BFO on Pt-30L	No / 400	54	380	$4.12 \cdot 10^{-6}$	This work
BFO on LNO-20L	(012) / 320	40	540	$5.28 \cdot 10^{-7}$	This work
BFO on LNO-30L	(012) / 400	50	180	$4.04 \cdot 10^{-6}$	This work
BFO on IrO_2-20L	(012) / 320	71	320	$4.27 \cdot 10^{-2}$	This work
BFO on IrO_2-30L	No / 400	85	330	$3.58 \cdot 10^{-1}$	This work
BFO on LNO/Si	No / 380	60	~500	$\sim 10^{-5}$	[25]
BFO on LNO/Si	No / 185	100	500	-	[26]
BFO on LNO/Si	No / -	35.3	310	$\sim 10^{-3}$	[334]
BFO on LNO/Si	(012) / >400	65	600	$\sim 10^{-3}$ (@250kV/cm)	[318]

While comparing the listed results, it can be seen that the present BFO/LNO-30L films possess the lowest E_C and J amongst all BFO films reported on LNO bottom electrodes by CSD. Although high P_r (60-100 μC/cm^2) have been reported for randomly oriented BFO films on LNO, they exhibit high E_C (~500 kV/cm) what according to our opinion reflect their high leakage nature [25, 26]. Additionally, very high P_r = 65 μC/cm^2, with high E_C of 600 kV/cm and J of $\sim 10^{-3}$ A/cm^2 at 250 kV/cm were recently reported for >400 nm thick (012) oriented BFO films on LNO [318]. These films were annealed at relatively high

temperatures, 600 °C, and authors relate the enhanced P_r as a result of large grain size and/or decreased defects (grain boundaries). Our BFO/LNO-30L films show relatively high P_r of 50 μC/cm^2 and low J of ~10^{-6} A/cm^2.

Summary: This work discloses the role of metallic (Pt) and oxide electrodes, specifically LNO and IrO_2, on the texture development and functional properties of BFO thin films prepared by chemical solution deposition. No texture was observed for films fabricated on (111) Pt/TiO_2/SiO_2/(100)Si although they become more (012) oriented as the film thickness increases. On the contrary films are highly (012) oriented when deposited on conductive oxide electrodes. In addition to promoting (012) texture of BFO films for LNO electrodes the film orientation increases with thickness increasing, while for IrO_2 the degree of orientation decreases with increasing films thickness. The grain size of BFO films changes with the type of bottom electrode and thickness of BFO films. The largest grains are observed for films on IrO_2 and the smallest for films on LNO. LNO provides BFO films with lowest electrical conductivity and well-shaped hysteresis loops. 400 nm thick columnar BFO films on LNO exhibit a low leakage current density on the order of 4.04×10^{-6} A/cm^2 and a large remanent polarization of 50 μC/cm^2 and a small coercive field of 180 kV/cm at room temperature. LNO templates the BFO film growth and enhances its crystallinity and orientation. 320 nm thick BFO/IrO_2 and 400 nm thick BFO/IrO_2 exhibit large leakage current density of 4.27×10^{-2} and 3.58×10^{-1} A/cm^2 at 400 kV/cm, respectively. With increasing film thickness, the leakage current density decreased strongly for BFO/Pt.

4.5. Direct fabrication of $BiFeO_3$ thin films on polyimide substrates for flexible electronics

Abstract: One of the major challenges for the integration of functional oxides as ferroelectrics into flexible electronics is the reduction of their processing temperature below the degradation temperature of plastic substrates. Under this aim particular attention has been given to the low-temperature processing of oxide films by chemical solution deposition methods. In this work lead-free multifunctional and multiferroic BFO thin films have been fabricated for the first time at a temperature as low as 300 °C directly on flexible polyimide substrates by our own proprietary solution-based Seeded Photosensitive Precursor Method. The ferroelectric, piezoelectric and magnetic functionalities demonstrated for these films reveal their interest for applications in microelectronic devices as well as their feasibility for using in flexible electronics. The results here shown are a proof of concept of the Seeded Photosensitive Precursor Method for the successful integration of lead free ferroelectric thin films with flexible plastic substrates and have a broad impact in terms of an extended use of functional oxide thin films processed with low thermal schedules.

A solution-based process called Seeded Photosensitive Precursor Method has been recently developed by us, which enables the processing of functional oxide films under low-temperature conditions. This method combines two different approaches: i) seeded diphasic sol/solution-gel precursors (SDSG) with ii) photosensitive precursor solutions (PCSD; PhotoChemical Solution Deposition). The first approach (SDSG) introduces crystalline nanoseeds to the precursor solution in order to enlarge the number of nucleation sites leading to a reduction of the crystallization temperature [201]. The second approach (PCSD) is based on the synthesis of photosensitive precursors containing UV absorbing species (like β-diketonates) that after UV irradiation produces the pyrolysis and oxidation of the organic

components of the solution deposited layer, advancing the formation of the M–O–M bonds of the ferroelectric perovskite at low temperatures [222]. This proprietary technology (International patent PCT/IB2009/055699 [335]) was demonstrated for the most important multifunctional oxide, PZT. Ferroelectric response of PZT thin films directly deposited onto flexible polyimide with remanent polarization values of $P_r \sim 15\ \mu C/cm^2$ for the films annealed at 350 °C was reported [16]. The concept was initially proved for a lead-based complex composition, but this method has not been applied to produce lead free complex oxide thin films up to now.

In this work, we enlarge the concept by direct fabricating BFO thin films on polyimide for flexible electronics using the Seeded Photosensitive Precursor strategy.

Preparation of functional oxide thin films at very low temperatures, over large areas and compatible with low cost and flexible substrates, offers great industrial potential [336]. Flexible electronics are becoming crucial for light, small, portable and flexible microelectronic applications [336]. The deposition of crystalline complex oxides on polymer and base metals represents an important extension of thin films technology to substrate materials, more compatible with innovative applications. The intrinsic multifunctionality of ferroelectric thin films make them very attractive for high performance, flexible electronic devices such as ferroelectric random access memories (FeRAM), sensors, piezoelectric harvesters or photovoltaic solar cells [2, 337-339]. However, integration of functional ferroelectric oxides with flexible polymers has been prevented by the incompatibility of the respective processing conditions: polymer is unable to withstand the high temperatures required for electrical response development in the perovskite oxides; for example, most of the synthesis methods require temperatures that exceed 600 °C, 700 °C and 650 °C to crystallize the perovskite ferroelectric film of PZT, BST and KNN, respectively [196-198]. Normally, polyimide and polyester substrates for applications related to the electronics industry are thermally stable below 450 °C (short dwell time) and 150 °C, respectively. Naturally, this temperature difference inhibits the direct deposition of the inorganic ferroelectric films on polymeric substrates.

Up to now the most widely investigated method to fabricate ferroelectric thin films on flexible polymeric substrates is the transfer printing [340, 341]. This method is an indirect process: firstly, inorganic ferroelectric films are deposited on rigid substrates and heat treated

at high temperatures and then transferred to flexible substrates through a series of processes, such as etching, peeling off, and printing or laser lift off [342]. Although transfer printing has been widely investigated, it is a quite complex and expensive process. Therefore, the direct deposition of inorganic ferroelectric films on flexible substrates is highly demanded.

Solution based processes are very attractive to prepare functional oxide thin films owing to their wide range of advantages, as large-area deposition, easy control of composition, atmospheric processing, and low cost (due to the lack of sophisticated instrumentation). Among them, chemical solution deposition (CSD) has been widely used to obtain crystalline thin films at relatively low temperatures. Several attempts to reduce thin film growth temperatures using different or modifications of CSD based techniques, such as: UV-assisted annealing [343], laser or microwave heating [8, 214], seeding [10] and heterogeneous photocatalysis [207], to levels that are compatible with temperature-sensitive substrates (300-400 °C) have been carried out.

In what concerns materials, in recent decades, multiferroic BFO have attracted remarkable research interest due to its large switchable polarization, resistive switching as well as magnetoelectric properties [55, 344, 345]. These functionalities are crucial for applications in electronic devices and therefore BFO and its solid solutions hold a great potential for applications in spintronics and memory devices [277]. The optical bandgap of BFO in the visible range is interesting for applications utilising photoconductivity (sensors), photovoltaic effect (solar energy harvesting) or photocatalytic performance to be used for environmental waste management [77-79].

Up to date, BFO thin films have been deposited mainly on single crystal substrates, being the $SrTiO_3$ and $DyScO_3$ mostly used for the growth of epitaxial BFO films, or on platinized silicon wafers in the case of polycrystalline ones [54, 133, 346, 347]. From the application point of view those substrates are expensive and rigid. Moreover other limitations of Bi based compounds are related to the high annealing temperatures necessary for the crystallization of the perovskite phase and the consequent volatilization of the high-vapour pressure elements such as Bi, leading as a consequence to the appearance of parasitic phases [143]. Recently, BFO thin films were prepared on flexible metallic Ni tapes with $La_{0.5}Sr_{0.5}TiO_3$ buffer layers by chemical solution deposition [348]. Although, BFO films were successfully integrated with metallic foils, the reported crystallization temperature

(475-550 °C) for those BFO films is well above the temperature that flexible polymeric substrate can withstand. Nanocrystalline BFO thin films on $SrTiO_3$ single crystals prepared by low temperature atomic layer deposition (ALD) were reported as well. The BFO films were composed of BFO nanocrystals embedded in an amorphous matrix after the deposition at 250 °C. The ferroelectric behaviour of those films was assessed by piezoelectric force microscopy and a piezoelectric coefficient of $d_{zz} = 4$ pC/N was reported [349]. Low-temperature processing of BFO thin films compatible with flexible polymeric substrates was very recently reported by photocatalytically assisted decomposition method of metal precursors. The formation of the perovskite phase was achieved at 325 °C together with the presence of the secondary crystalline $Bi_2Fe_4O_9$ phase. Local piezoelectric hysteresis loops were obtained, in order to confirm the ferroelectric character of those BFO thin films on the flexible plastic substrates. However, no macroscopic ferroelectric or magnetic functionality was presented [207]. Indeed, a review of the literature reveals that the crystalline quality required for attaining macroscopic ferroelectric response in BFO thin films, is difficult to achieve for thin films fabricated at temperatures lower than 400 °C. Figure 4-67 depicts the reported experimental values of remanent polarization, P_r, as a function of the fabrication temperature for BFO single crystals [122], bulk ceramics [56, 70, 129] and thin films [54, 131, 134, 150, 318, 319, 350, 351] (Figure 4-67). It is clear from the graph that the ferroelectric properties of BFO show a strong regression as the processing temperature of thin films decreases.

In this work by using our own proprietary technique we directly fabricate BFO thin films on polyimide substrates for flexible electronics, demonstrating macroscopic ferroelectric switching. Our process not only addresses the issue of Bi volatilization at high temperature but also enables a facile production of thin films on low melting temperature substrates. This easy, low-cost solution method is used to prepare BFO multiferroic thin films for the first time at 300 °C, a remarkably low temperature of formation for this complex perovskite oxide.

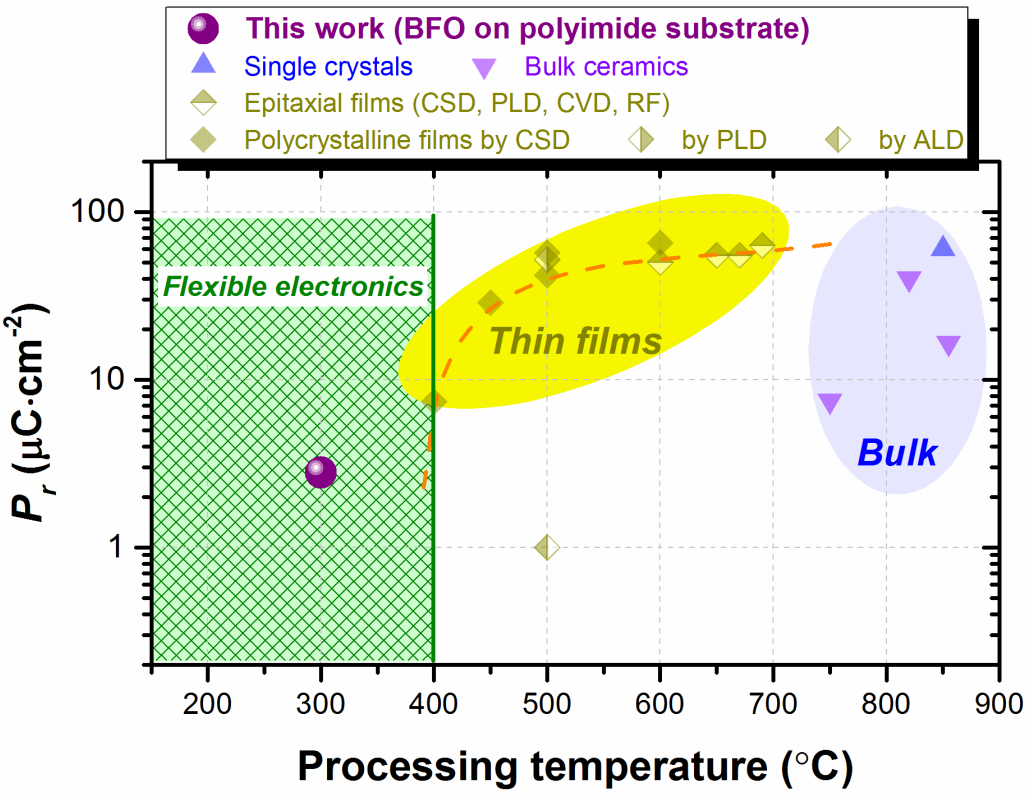

Figure 4-67. Remanent polarization, P_r, as a function of the BFO single crystals, bulk ceramics and thin films fabrication temperature. Clear regression of the BFO ferroelectric properties is observed for fabrication temperatures lower than 400 °C.

4.5.1. Experimental procedure

Synthesis of precursor solutions and nanosized seeds. 0.25M precursor solution of BFO was prepared using bismuth nitrate ($Bi(NO_3)_3 \cdot 5H_2O$, Sigma Aldrich, 99.99 %) and iron acetylacetonate ($Fe(CH_3COCHCOCH_3)_3$, ABCR, 99 %). Acetic acid ($C_2H_4O_2$ – AcOH, Merck, 100 %) and 1,3-propanediol ($C_3H_8O_2$, Aldrich, 98 %) were used as solvents [319]. No excess of Bi was used. The acetylacetonate ligand of the iron reagent provides an appreciable photosensitivity to this BFO solution [222]. BFO nanopowders to be used as seeds were prepared by hydrothermal method [233]. The chemical regents used to prepare BFO nanoparticles were bismuth nitrate [$Bi(NO_3)_3 \cdot 5H_2O$, Sigma Aldrich, 99.99 %], iron nitrate [$Fe(NO_3)_3 \cdot 9H_2O$, Sigma Aldrich, 98 %], potassium nitrate (KNO_3, Fluka, 98 %), poly(vinyl alcohol) (PVA, Sigma Aldrich, 98 %), and potassium hydroxide (KOH, ABCR,

85 %). The mineralizer-assisted hydrothermal process included the following steps: 0.005 mol $Bi(NO_3)_3 \cdot 5H_2O$ and 0.005 mol $Fe(NO_3)_3 \cdot 9H_2O$ were dissolved in 100 ml of diluted HNO_3 (10 %) to form aqueous solutions. Then, (12M) KOH solution was slowly added to the above solution to adjust its pH value to ~8 by constant stirring until brown precipitates were formed. The precipitates were filtered and washed with distilled water. Then, precipitates were mixed with 30 ml KOH (12 M) and 15 ml PVA (4 g/l) solutions under constant magnetic stirring for 5 min. The suspension solution was transferred into teflon lined stainless-steel autoclaves for the hydrothermal treatment. The autoclave was sealed and kept in the oven at 160 °C for 9 h. The obtained BFO powders were filtered and washed with distilled water and absolute ethanol several times, and then dried at 70 °C for 12 h. The obtained BFO powders were dispersed in a solution of acetic acid and 1,3-propanediol (AcOH:diol, 4:1 vol. ratio). High intensity ultrasonic processor (Vibra Cell 750) was then used to disperse the nanoparticles for 48 h. Suspensions were then left to settle for 3 days to allow sedimentation of the larger particles and aggregates, and supernatant was collected. Appropriate volume of seeds suspensions was added to the photoactive BFO precursor to obtain seeded photosensitive precursor solutions.

Preparation of thin films. The method used in this study for the direct fabrication of BFO films onto a polyimide substrate is presented in Figure 4-68 and consists of the following steps:

- The synthesis of the “photoactive sol”, which displays an increased absorption in the UV-range
- Incorporation of seeds into the photoactive sol (“seeds + photoactive sol”), that increases the number of nucleation sites in the resulting film producing a further reduction of the crystallization temperature.
- Deposition of seeded photoactive sol on the substrates and irradiation using a high-intensity UV excimer lamp. Elimination of organic compounds from these photosensitive systems is accelerated by the irradiation due to (i) ozonolysis and (ii) a prompt dissociation of the alkyl group–O bonds with the subsequent formation of the metal–O–metal bonds [222, 339].
- Thermal treatment of the irradiated layer by RTP.

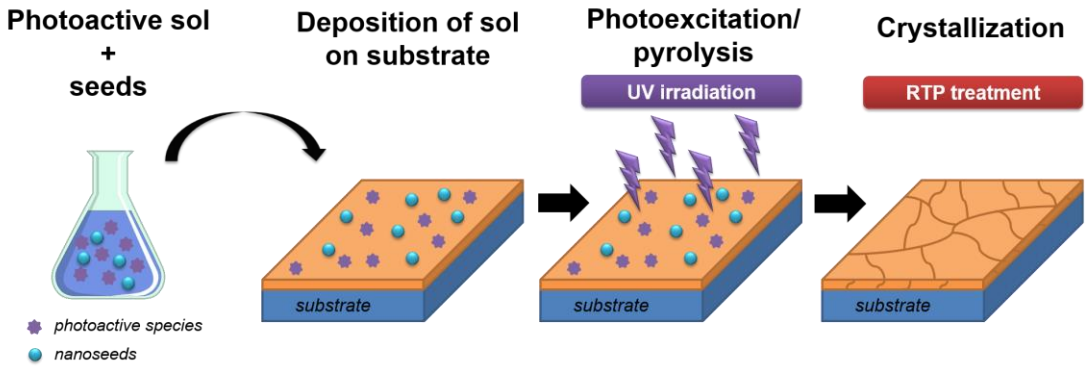

Figure 4-68. Schematic representation of the strategy that combines seeded diphasic precursors and photochemical solution deposition. This method consists in the preparation of activated sols, deposition of the precursor films, followed by photoexcitation/pyrolysis and final crystallization [16].

Precursor solutions were deposited on flexible polyimide substrates (UPILEX-75S polyimide film; thickness of 75 µm - UBE Europe GmbH). Metallization of the bare polyimide by a NiCr layer with a thickness between 5-10 nm, and a 150-200 nm thick layer of Pt was performed on both sides of the substrate by DC sputtering at room temperature. The deposition of BFO thin films was carried out by spin-coating at 1500 rpm for 45 s.

As-deposited *seeded* $BiFeO_3$ films were heated on a hot plate in air at 150 °C for 1 min to evaporate the solvents and pyrolyzed at 300 °C for 1 min to burn the residual organics. BFO thin films prepared by the combination of PCSD with SDSG (denoted as *seeded + UV*) were dried at 150 °C for 1 min and irradiated using laboratory-scale prototype combining a high-intensity UV excimer lamp (Heraeus, BlueLight Excimer System, $\lambda_{emission}$ = 222 nm, electrical power of 1.5 kW, frequency of 50 Hz, irradiation length of 30 cm and irradiance of 6.25 Wcm^{-2}) with a ultra-fast heating system (Watlow, UltramicTM 600 advanced ceramic heater) in oxygen atmosphere at 250 °C for 30 min. Deposition and drying steps were repeated 8 times before the RTP annealing in order to fabricate BFO thin films with desired thicknesses. The deposited films were crystallised by RTP using Jetstar 100T JIPELEC equipment. A heating rate of 30 °C/s and an air atmosphere were used for films treatments at 300 °C for different periods of time (from 60 to 120 min).

Characterization of materials. XRD analysis, under Bragg-Brentano (θ/2θ), using a Philips X'Pert, and Bruker D8 T2T SOLX Cu Kα diffractometer were performed to inspect the formed phases in BFO nanoparticles and thin films. Microstructures of BFO thin films were observed with SEM. Nanoparticles were analysed by using a Transmission Electron Microscopy (TEM) Hitachi H9000-NA (300 keV). The surface area of the particles, SA_{BET} ($m^2 \cdot g^{-1}$) was evaluated by the Brunauer-Emmett-Teller (BET) method in which N_2 acted as adsorbate gas (Micromeritics Gemini 2375 equipment). Prior to the measurements, the samples were degassed at ~200 °C for 12 h. Ferroelectric hysteresis behaviour was assessed with a virtual ground circuit. Experimental setup consisted of Agilent 33220A function/arbitrary waveform generator that allows the application of sinusoidal signal with electrical amplitude between 0.01-16 V and frequencies between 1 kHz and 10 kHz. Current intensity generated values, after amplification with a Keithley 428 current amplifier, together with the voltage applied were collected with a Tektronix TDS 520 oscilloscope. Data acquisition and further processing of the data was carried out by homemade software [352]. An AFM system consisting of a commercial NT-MDT NTEGRA Aura scanning probe microscope equipped with Piezoresponce Force Microscopy mode was used. Measurements were carried out using a cantilever Mikromash HQ: NSC35/pt with spring constant of 16 N/m and resonance frequency of 300 kHz. A small ac electric field of 5 V and frequency 70 kHz was applied to the tip to induce local vibration. The topography and domain images were processed using WSxM v2.2 software. Cryogenic vibrating sample magnetometer (VSM) instrument (Cryogenics, UK) was used to measure the magnetic behaviour of the sample up to 10 T at room temperature.

4.5.2. Results and discussion

4.5.2.1. Characterization of seeds

The powder morphology, particle size and its dispersion behaviour are equally important for the quality of the seeded films and, consequently determine the final functional properties. The XRD pattern in logarithmic scale of BFO particles to be used as seeds is shown in Figure 4-69 a). The nanoparticles present a single-phase BFO perovskite structure.

The diffraction pattern is indexed based on the rhombohedral *R3c* structure (JCPDS #04-009-3445 file). No characteristic XRD peaks of possible impurity phases, such as Fe_2O_3, Bi_2O_3, $Bi_2Fe_4O_9$, $Bi_{25}FeO_{40}$ or $Bi_{36}Fe_{24}O_{57}$ were observed within the resolution of XRD.

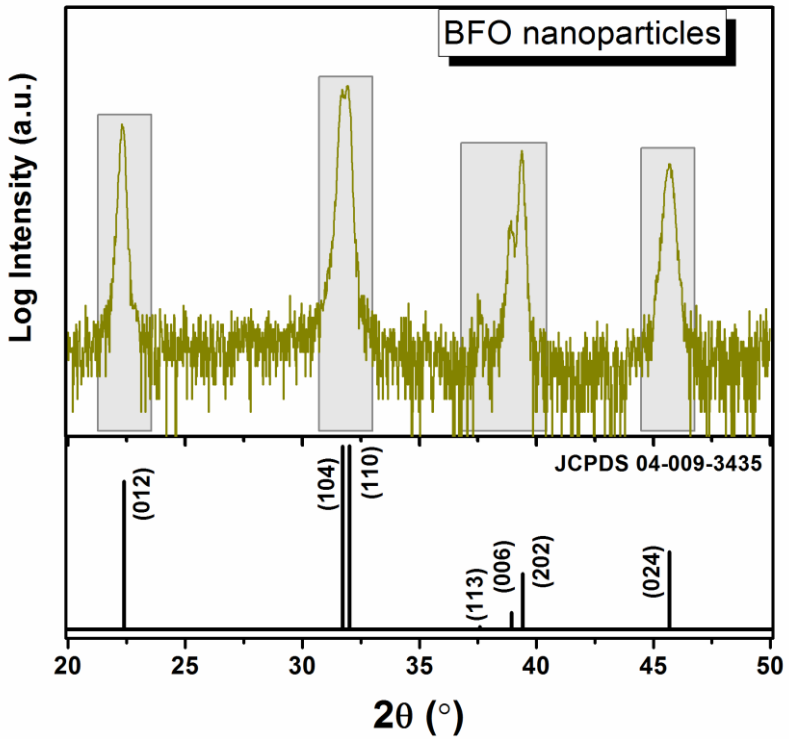

a)

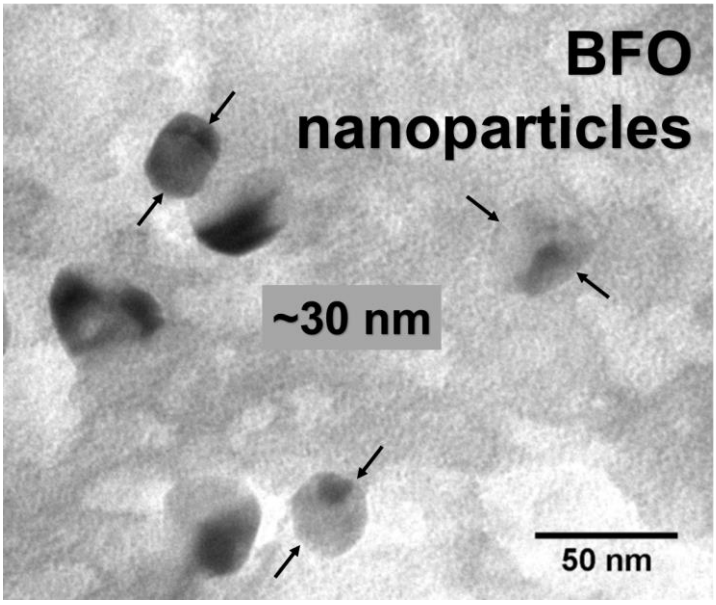

b)

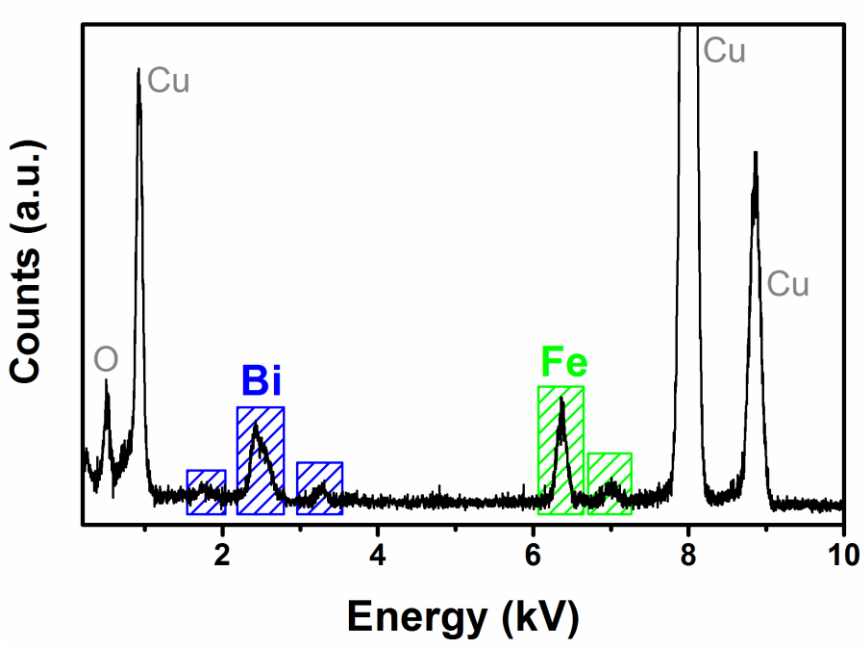

c)

Figure 4-69. XRD pattern (a), TEM bright field image (b) and EDS spectra (c) of BFO nanoseeds synthesized by the hydrothermal process. BFO nanoparticles present a single-phase perovskite structure and ultra-fine spherical morphology with the average particle size of about 30 nm.

The mean particle size of the powders (*D*) was also calculated from the specific surface area of BET, as $D_{BET} = 6000/SA_{BET} \cdot \rho$, in which SA_{BET} stands for the specific area (m^2/g) and ρ for the theoretical density (g/cm^3). The measured value of SA_{BET} was 25.19 m^2/g. Fine-grained powders have particularly high surface areas owing to small particle sizes. The mean particle size D_{BET} calculated assuming spherical particle morphology is ~29 nm for these BFO nanopowders. For comparison the specific surface area reported for BFO particles prepared by classical solid state reaction is SA_{BET} ~ 4.25 m^2/g, that correspond to average particles size of 15 μm [353]. The morphology of the powders disaggregated by sonication was studied by TEM and is shown in Figure 4-69 b). Ultra-fine spherical BFO powder particles with an original particle size of about 30 nm were obtained. This is consistent with the average size calculated from SA_{BET}. To confirm the chemical composition of these as-prepared structures, energy dispersive X-ray spectroscopy (EDS) spectra (Figure 4-69 c), taken at a number of selected positions of the sample, show the expected presence of Bi, Fe, and O. Copper signal detected by EDX comes from the used supporting grid.

4.5.2.2. Characterization of thin films

BFO films prepared on the flexible polyamide substrates present a very uniform aspect, they are adherent to the substrate and when bended they do not crack, as presented in Figure 4-70 a).

XRD patterns of BFO thin films processed at 300 °C are presented in Figure 4-70 b). No evidence of crystallinity (*i.e.*, amorphous BFO film) is observed in the diffractogram of *unseeded* films after annealing at 300 °C. The diffraction peaks for the *seeded* and *seeded + UV* BFO films may be indexed according to either the electrode or a rhombohedrally (JCPDS #04-009-3445 file) distorted perovskite structure of BFO. Similarly, to our studies on PZT thin films, the BFO seeds distributed in the amorphous BFO layers act as preferential nucleation sites, and the perovskite phase formation is promoted at lower temperature in contrast to the films without seeds [16, 354].

a) 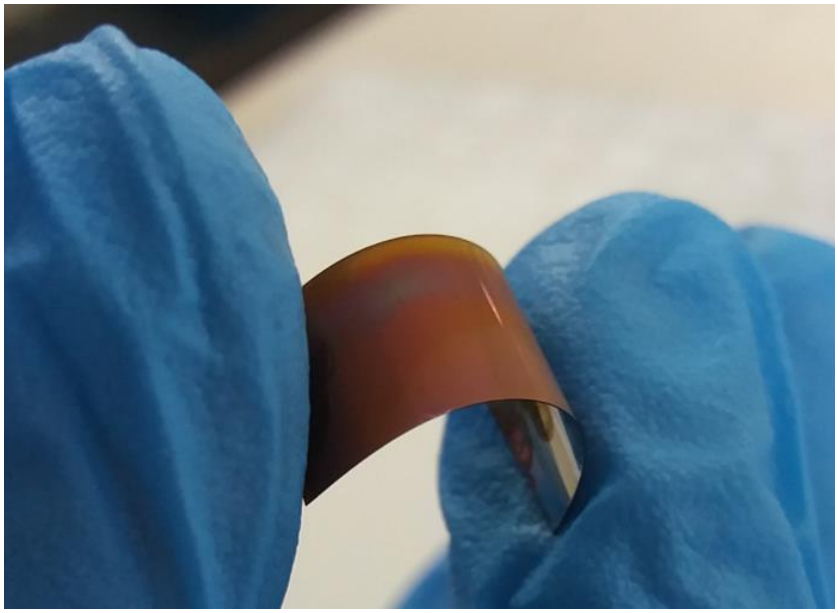

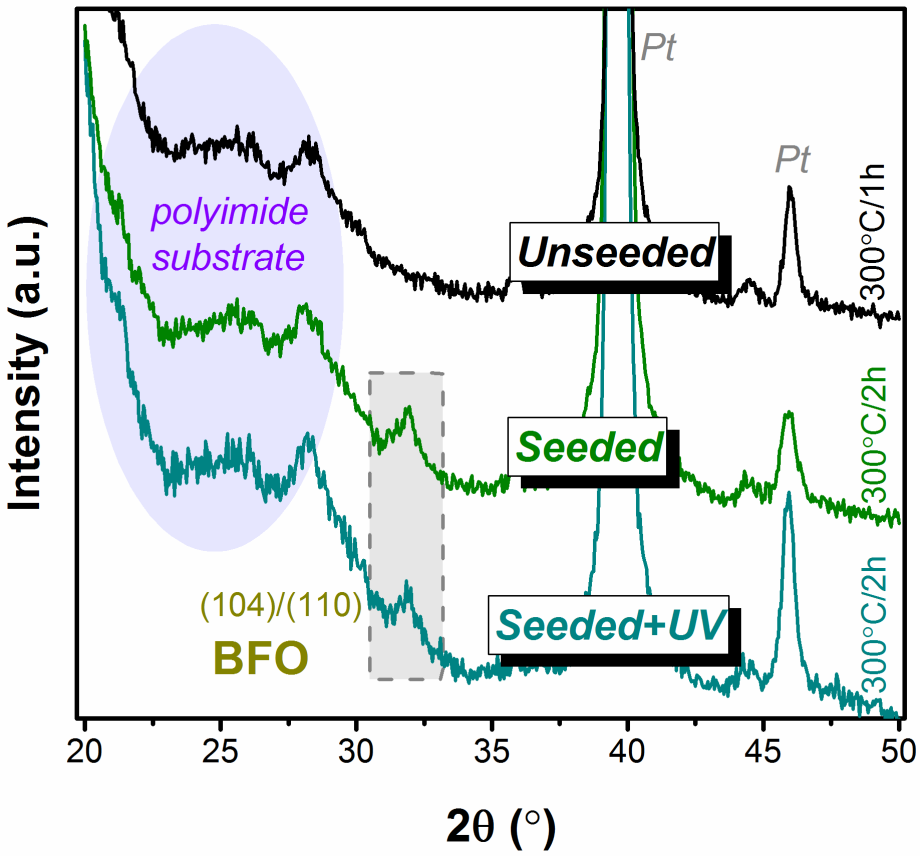

b)

Figure 4-70. (a) Photograph of a flexible BFO film fabricated on polyamide substrate. (b) XRD patterns of BFO thin films processed at 300 °C on flexible substrates. Unseeded films are amorphous. Reflections corresponding to the perovskite phase are detected for seeded and seeded + UV BFO films.

Surface morphologies of the crystalline *seeded* and *seeded + UV* BFO films were inspected by SEM. Typical micrographs are shown in Figure 4-71. All fabricated BFO films are crack free and composed of fine and densely compacted grains. The morphology of films consists of nanosized grains with a mean diameter of ~70 and ~100 nm for *seeded* and *seeded + UV* BFO thin films, respectively. The fine-grained morphology with nanosized grains obtained for those low-temperature thin films is consistent with our crystallization kinetic studies of seeded PZT films [12]. The presence of nanometric BFO seeds in the films lowers the barrier for BFO nucleation and those perovskite nanoseeds act as preferential nucleation sites within the amorphous films that result in large number of small and equiaxed grains. It is well documented that small grain size in thin films indicates high nucleation rate [355]. In

addition, UV irradiation of seeded amorphous films enhances the pyrolysis and oxidation of organic components in those films that further promotes the grain growth, therefore slightly bigger grains were observed for *seeded + UV* BFO thin films. Moreover, the surface of those films is compact but rather rough. From the inset in Figure 4-71 b) we can see that films possess uniform thickness along the substrate and the thickness is about 200 nm.

a)

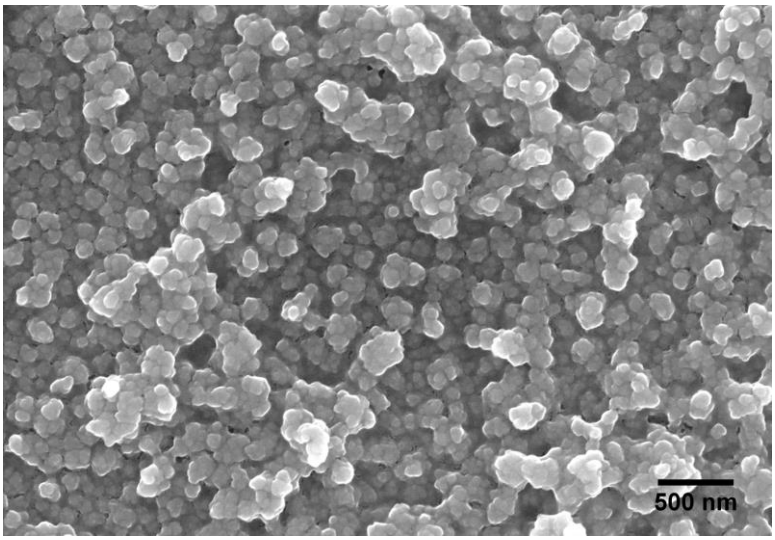

b)

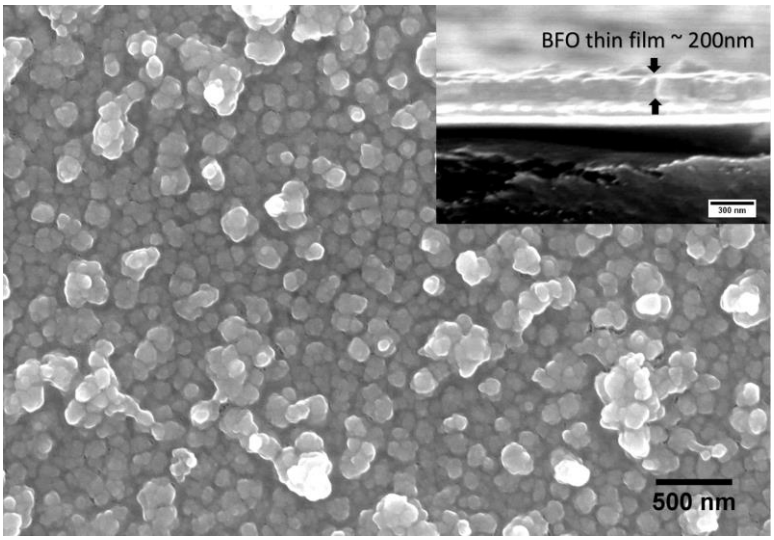

Figure 4-71. SEM micrographs of seeded (a) and seeded +UV (b) of BFO thin films on flexible polyamide substrate. The morphology of the films consists of nanosized grains with a mean diameter of ~70 and ~100 nm for seeded and seeded + UV BFO thin films, respectively.

The ferroelectric hysteresis curves measured at 140 K in *seeded* and *seeded + UV* BFO films are illustrated in Figure 4-72. Despite the low thermal budget that affects the crystal quality and microstructure of the films a remanent polarization P_r of 2.8 μC/cm^2 is obtained for the *seeded + UV* film, with a coercive field E_C of 300 kV/cm, which confirms the ferroelectric nature of the perovskite phase prepared at only 300 °C. Polarization current peaks can clearly be seen when the applied field reaches E_C. This is a clear evidence of ferroelectric domain switching. (Figure 4-72 b) [356]. In the case of *seeded* films an appreciable lower P_r of 1 μC/cm^2 is obtained.

The electrical properties of ferroelectric films depend on several factors, which include phase purity, microstructure, crystallite orientation, stresses, grain size or imperfections such as charged defects and vacancies [357]. The increase in P_r in *seeded + UV* films can be attributed to the decrease in the density of defects and oxygen vacancies. It is well-known that UV-irradiation of oxide layers in an oxygen atmosphere leads to the formation of ozone (O_3), a strong oxidant agent, and monoatomic oxygen O(1D) that reacts with sub-oxides, improving stoichiometry and decreasing defects [224, 354, 358, 359].

The local piezoelectric behaviour of *seeded* and *seeded + UV* BFO films were investigated using vertical piezoresponse force microscopy (VPFM). Figure 4-73 shows the simultaneously recorded topography and VPFM amplitude and phase responses with an AC bias (5 V, 70 kHz) applied to the tip. The topography of ferroelectric BFO thin films shows small grains with diameters of ~75 and ~100 nm for *seeded* and *seeded + UV* BFO thin films consistent with SEM micrographs. The RMS roughness of only seeded and seeded and UV-irradiated films were R_{RMS} = 40.8 ± 3.8 nm and R_{RMS} = 49.8 ± 5.8 nm, respectively. The dark areas in the VPFM phase images correspond to domains in which the polarization is oriented in the opposite direction to the applied field (phase = -180°), while bright regions correspond to domains with polarization oriented along the applied field (phase = 180°). The VPFM phase image is characterized by strong domain contrast: deep bright and dark areas indicate significant out of plane components of polarization. There is also a fraction of regions with poor contrast (indicated by blue dashed line in Figure 4-73) likely corresponding to areas of the films with incipient crystallization and domains with in-plane polarization. VPFM amplitude and phase images of *seeded + UV* BFO films show that the piezoelectric domains in these films are bigger than in the case of *seeded* BFO films

(highlighted in green for comparison in Figure 4-73) because neighbouring grains merge into one domain. The average domain size for *seeded* and *seeded + UV* BFO films was measured to be 60 and 100 nm, respectively. This fact is a consequence of higher crystallinity present in the films prepared by a strategy that combines seeded precursors and UV-irradiation of the photoactive deposited layers. This increase of domain size points toward the enhancement of the ferroelectric polarization. Indeed this local observation at the nanoscale is consistent with the macroscopic *P-E* loops results previously described.

The magnetic behaviour of BFO thin films was assessed at room temperature and given in Figure 4-74. *M-H* hysteresis curves of BFO films on flexible polyimide substrates depict unsaturated hysteresis loops, with weak ferromagnetic behaviour with a small coercivity ($2H_c$) of 200 Oe for *seeded + UV* BFO films (represented as inset of Figure 4-74). BFO is known to show a G-type antiferromagnetic ordering. In bulk BFO a small net magnetization due to the canting of adjacent Fe^{3+} spins is modulated by a long-range superstructure superimposed on the spin arrangement. The net magnetic moment is cancelled out due to the magnetization rotation following a cycloid with ~62 nm periodicity [122]. But in nanocrystalline BFO thin films and nanoparticles smaller than 95 nm, BFO shows a ferromagnetic behaviour due to the incomplete rotation of the spins along the antiferromagnetic axis [110, 360]. Indeed it is clear from the SEM micrographs of these BFO films that BFO grains are smaller than 100 nm, therefore the cycloid-like magnetic modulation was broken or significantly distorted in our films leading to this weak ferromagnetic behaviour.

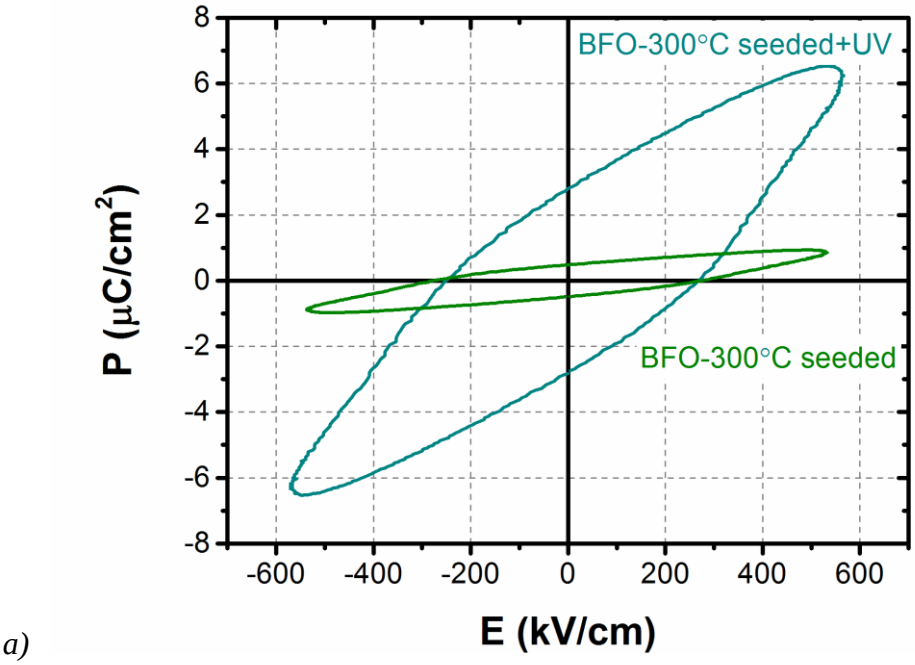

a)

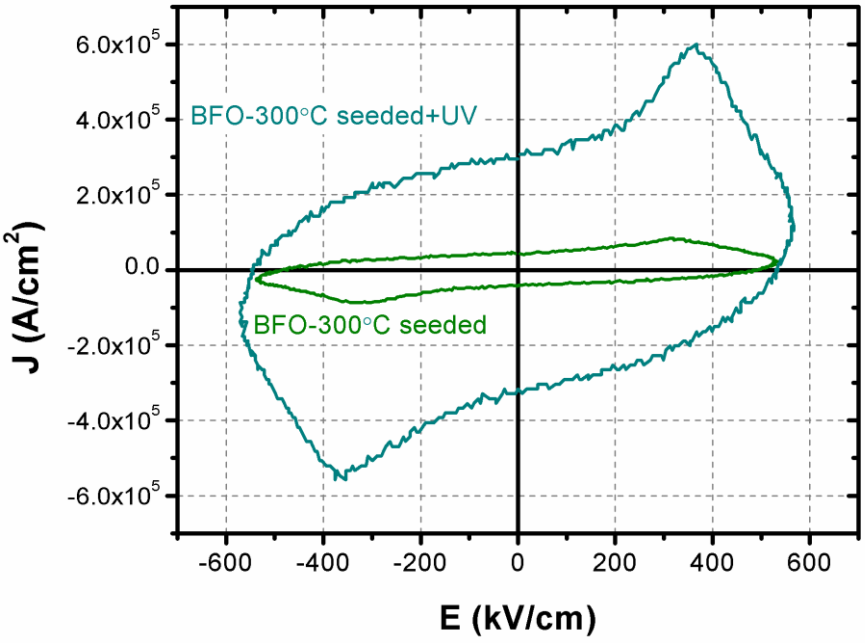

b)

Figure 4-72. The polarization (P-E) hysteresis loops (a) and the switching currents versus applied field (b), for seeded and seeded and UV-irradiated BFO films measured at 140 K and 10 kHz. A remanent polarization P_r of 2.8 μC/cm^2 is obtained for the seeded + UV film, with a coercive field E_C of 300 kV/cm confirm the ferroelectric nature of the perovskite phase prepared at only 300 °C.

Figure 4-73. Topographic and VPFM amplitude and phase images of seeded and seeded + UV BFO thin films on flexible polyimide substrates crystalized at 300 °C for 120 min. Both films depict obvious piezoelectric behaviour, however areas with poor contrast, indicated by blue dashed line, likely correspond to regions of the films with incipient crystallization and domains with in-plane polarization. Some of the domains are highlighted in green for comparison.

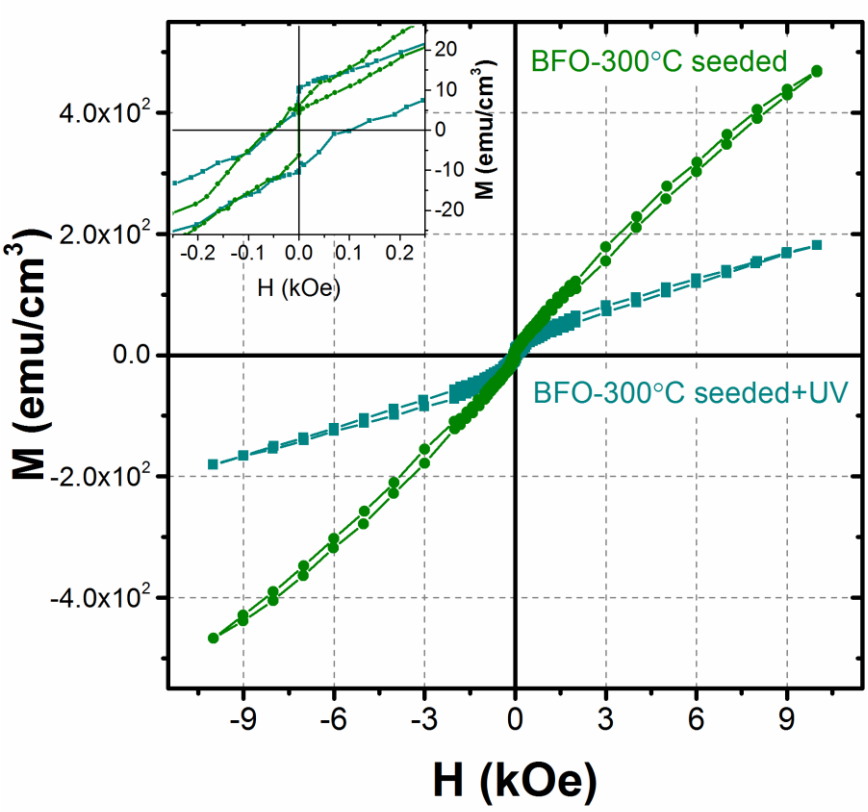

Figure 4-74. Magnetic hysteresis of seeded and seeded + UV BFO at 300 K up to 10 kOe. BFO on flexible polyimide substrates depict the weak ferromagnetic response. The magnetic response increases with decreasing grain size of BFO thin films.

Summary: Here we prove that it is possible the direct fabrication of lead-free BFO thin films on flexible polyamide substrates with ferroelectric and magnetic functionalites (multiferroicity) at room temperature. Our own proprietary novel solution-based Seeded Photosensitive Precursor Method was successfully used to decrease the crystallization temperature of BFO thin films down to a temperature as low as 300 °C, the lowest reported to now for the preparation of multiferroic BFO thin films. Despite this exceptionally low thermal budget a remanent polarization P_r of 2.8 μC/cm^2 is obtained for the *seeded +UV* films, with a coercive field E_C of 300 kV/cm. The

synthesis strategy based on the use of seeded photosensitive precursors can be transferred to any family of functional metal oxide. This concept allows direct fabrication of complex oxides thin films on polyimide substrates targeted for flexible and miniaturized electronic components to produce light, low cost, low power consumption, and portable electronic devices.

Chapter 5. SUMMARY

There is a need of high performance, high reliability and miniaturized electronic components integrated into various devices due to rapid development of the electronics industry. Low dimensional functional materials hold great promises to fulfil those requirements. As already mentioned in Chapter 2, crystallization temperature is a key parameter in preparation of perovskite ferroelectrics and many ferroelectric thin films are crystallized at temperatures >600 °C, which make them incompatible with low cost, low melting temperature flexible polymeric substrates. The compatibility of ferroic thin films with those last types of substrates could markedly widen the range of applications for those ferroelectric thin films.

In this thesis, lead-free BFO and NBT thin films with a competitive ferroelectric response at low temperatures were fabricated. Moreover, investigations of the effect of the bottom electrode on the ferroelectric properties of BFO thin films was conducted and the comparison between the behavior of IrO_2, LNO and Pt based BFO capacitors established. Additionally, the effects of these various bottom electrodes on the microstructure of BFO ferroelectric films was studied by high-resolution TEM.

From the work carried out in this PhD thesis the main output can be summarized as follows:

- Crystalline NBT thin films with perovskite structure have been successfully obtained on rigid Pt-coated silicon substrates by chemical solution deposition. Effect of annealing temperature on phase formation and ferroelectric properties of NBT thin films was studied. Heat treatment of the as deposited NBT films at 400-650 °C gives the pure perovskite phase. The remanent polarisation of ~24 $\mu C/cm^2$ with corresponding coercive field of ~215 kV/cm was obtained for films annealed at 650 °C. For films annealed at temperatures lower than 500 °C values of remanent polarization were <10 $\mu C/cm^2$. However, in spite of very low thermal budget used and NBT films annealed at 450 °C shows a remanent polarisation of ~6 $\mu C/cm^2$ with corresponding coercive field of ~150 kV/cm. Thermal annealing in an oxygen atmosphere is effective in promoting crystallization of the film into rhombohedral perovskite phase at a low temperature of 400 °C. However, almost linear, *P-E* loop was obtained for those NBT films crystallized at 400 °C due to incipient crystallinity.

- BFO perovskite thin films have been prepared on rigid Pt-coated silicon substrates by chemical solution deposition at temperatures below 500 °C. Precursor solutions with and without Bi(III) excess have been used. Perovskite films without secondary phases, as detected by XRD analysis, were obtained at a lower temperature limit of 400 °C. Due to high leakage contribution the *P-E* hysteresis loops were recorded at low temperature (150 K-RT). The films prepared with Bi(III) excess had better defined ferroelectric hysteresis loops that those without Bi(III) excess, especially for the films annealed at 400 °C. Room temperature hysteresis loops could be obtained only for films prepared from solutions with Bi(III) excess and annealed at 400 and 450 °C.
- BFO thin films were also grown by chemical solution deposition on a range of bottom electrodes to determine their role in controlling phase formation and microstructure. The crystallization on oxide electrodes followed the sequence: amorphous → $Bi_2O_2(CO_3)$ → perovskite, while those on Pt crystallized directly from the amorphous phase. IrO_2 electrodes promoted perovskite phase formation at the lowest temperature and LNO additionally induced local epitaxial growth. For the first time fully coherent Fe-rich precipitates within the grain interior of the perovskite matrix were observed for all the films, whereas incoherent $Bi_2Fe_4O_9$ second phase was also observed at the grain boundaries only of BFO grown on Pt electrodes. The latter could be observed by XRD as well as TEM but coherent precipitates were only observed by TEM, principally evidenced by their Z contrast in annular dark field images. These data have pronounced consequences for the extended use of BFO films under applied field for actuator, sensor and memory applications.
- 310 and 400 nm thick BFO thin films were grown by chemical solution deposition on a metallic (Pt) and oxide (IrO_2 and LNO) electrodes to determine their role in controlling the texture development and functional properties of BFO thin films. All BFO films are composed of columnar grains which size is dependent on the bottom electrode. No texture was observed for 320 nm thick films fabricated on (111) oriented Pt. Films on oxide electrodes, in particular on LNO are highly (012) oriented. The large remanent polarization in BFO/Pt and BFO/IrO_2 is attributed to the high leakage current contribution. 400 nm thick BFO films on LNO possess a low leakage current density ~4×10^{-6} A/cm^2, a large remanent polarization of 50 μC/cm^2 and a small coercive field

of 180 kV/cm at room temperature. We demonstrate that LNO layers enhance the crystallinity and orientation of BFO thin films, which is reflected in their functional properties. This analysis shows that besides the simple need of monophasic films metal oxide electrodes have a relevant impact on the development of high quality BFO thin films fabricated by chemical solution deposition methods. These results have a broad implication for the fabrication of BFO thin film based devices.

- Lead-free multifunctional and multiferroic BFO thin films have been fabricated for the first time at a temperature as low as 300 °C directly on flexible polyimide substrates by our own proprietary solution-based Seeded Photosensitive Precursor Method. The ferroelectric, piezoelectric and magnetic functionalities demonstrated for these films reveal their interest for applications in microelectronic devices as well as their feasibility for using in flexible electronics. The results here shown are a proof of the concept of the Seeded Photosensitive Precursor Method for the successful integration of lead-free ferroelectric thin films with flexible plastic substrates and have a broad impact in terms of an extended use of functional oxide thin films processed with low thermal schedules.

Scientific output

The list of publications:

1. M Tomczyk, I. Bretos, R. Jiménez, A. Mahajan, E. V. Ramana, M. L. Calzada, P. M.Vilarinho, "Direct fabrication of $BiFeO_3$ thin films on polyimide substrates for flexible electronics", submitted to *ChemSusChem*.
2. M. Tomczyk, A.Mahajan, A. Tkach, P. M.Vilarinho, "Correlation of electrodes with orientation and electrical performance of $BiFeO_3$ thin films by chemical solution deposition", submitted to *Acta Materialia*.
3. M. Tomczyk, D. G. Stroppa, I. M. Reaney, P. M. Vilarinho, "The role of electrodes in the growth of $BiFeO_3$ thin films by chemical solution deposition", accepted to *Physical Chemistry Chemical Physics*.
4. Levin, V. Krayzman, T.A. Vanderah, M. Tomczyk, H. Wu, M.G. Tucker, H.Y. Playford, J.C. Woicik, C.L. Dennis, P.M. Vilarinho, "Oxygen-storage behavior and local structure in Ti-substituted $YMnO_3$" *Journal of Solid State Chemistry*, 246 (2017) 29.
5. Bretos, R. Jiménez, M. Tomczyk, E. Rodríguez-Castellón, P. M. Vilarinho, M. L. Calzada, "Active layers of high-performance lead zirconate titanate at temperatures compatible with silicon nano- and microelectronic devices", *Scientific Reports*, 6 (2016) 20143.
6. A. Perez-Rivero, M. Tomczyk, R. Jiménez, I. Bretos, J. Ricote, P. M. Vilarinho, M. L. Calzada, "Polarization switching at room temperature of undoped $BiFeO_3$ thin films crystallized at temperatures between $400 \leq T \leq 500$ °C", *Journal of Materials Science: Materials in Electronic*, 26 (2015) 9373.
7. M. Tomczyk, A. M. R. Senos, I. M. Reaney, P. M. Vilarinho, "Reduction of microcracking in $YMnO_3$ ceramics by Ti substitution", *Scripta Materialia*, 67 (2012) 427.
8. M. Tomczyk, A. M. R. Senos, P. M. Vilarinho, I. M. Reaney, "Origin of microcracking in $YMnO_3$ ceramics", *Scripta Materialia*, 66 (2012) 288.
9. M. Tomczyk, P. M. Vilarinho, A. Moreira, A. Almeida, "High temperature dielectric properties of $YMnO_3$ ceramics", *Journal of Applied Physics*, 110 (2011) 064116.
10. M. Kempa, S. Kamba, M. Savinov, M. Marysko, Z. Frait, P. Vanek, M. Tomczyk, P. M. Vilarinho, "Bulk dielectric and magnetic properties of PFW–PZT ceramics: absence of magnetically switched-off polarization", *Journal of Physics: Condensed Matter*, 22 (2010) 44590.

The list of presentations:

1. "Strategies for the low temperature preparation of lead free $BiFeO_3$ ferroic thin films" Monika Tomczyk, I. Bretos, R. Jiménez, M.L. Calzada, P. M.Vilarinho, COST IC1208 Conference and MC meeting, September 8-9th 2016. Warsaw, Poland – ***oral*** presentation.
2. "Transmission Electron Microscopy investigation of $BiFeO_3/LaNiO_3$, $BiFeO_3$/Pt and $BiFeO_3/IrO_2$ thin films prepared by chemical solution deposition" Monika Tomczyk, Daniel G. Stroppa, Ian M. Reaney, Paula M Vilarinho, Electroceramics XV, June 27-29th 2016, Limoges, France – ***oral*** presentation.
3. "Electrical properties of $BiFeO_3$ thin films on different electrodes fabricated by Chemical Solution Deposition" Monika Tomczyk, P. M.Vilarinho, Materials Challenges In Alternative and Renewable Energy (MCARE2016), April 17-21st 2016, Clearwater, USA.
4. "Isosymmetric Structural Changes in $YMn_{1-x}Ti_xO_3$ – X-ray and neutron diffraction studies" Monika Tomczyk, Igor Levin, Paula M Vilarinho, Jornadas CICECO 2015 - Nanotechnology … from the lab to the industry, April 14-15th 2015, Aveiro, Portugal – ***poster*** presentation.
5. "HRTEM observation of interfaces of $BiFeO_3/LaNiO_3$ thin films prepared by chemical solution deposition" Monika Tomczyk, Daniel G. Stroppa, Paula M Vilarinho, INCOMAM'14, November 6-7th 2014, Porto Portugal – ***oral*** presentation.
6. "Activated solutions enabling low-temperature processing of functional ferroelectric oxides for flexible electronics" Iñigo Bretos, Ricardo Jiménez, M. Lourdes Calzada, Aiying Wu, Monika Tomczyk, Paula M. Vilarinho, Closing COST MP0904 SIMUFER Conference and final MC meeting, January 31th-February 1st 2014, Genoa, Italy – ***oral*** presentation.
7. "Low temperature fabrication of ferroic $BiFeO_3$ thin films by Chemical Solution Deposition" Monika Tomczyk, Paula M. Vilarinho, Armando J. Pérez Rivero, Ricardo Jiménez, Jesús Ricote, Iñigo Bretos, M. Lourdes Calzada, 13th International Meeting on Ferroelectricity, September 2-6th 2013, Kraków, Poland – ***oral*** presentation.
8. "High-Temperature Structural Transitions in $YMn_{1-x}Ti_xO_3$" Monika Tomczyk, Paula M. Vilarinho, Valentin V. Laguta Igor Levin, Joint UffC, EFTF and PFM Symposium, July 21-25th 2013, Prague, Czech Republic – ***poster*** presentation.
9. "Structural studies at high temperature of $YMn_{1-x}Ti_xO_3$", Monika Tomczyk, Paula M. Vilarinho, Igor Levin, ISAF-ECAPD-PFM 2012, July 10-13th 2012, Aveiro, Portugal – ***poster*** presentation.

Doctoral Programme

List of disciplines, and obtained final marks, of Programa Doutoral em Ciência e Engenharia de Materiais (9206, Universidade de Aveiro):

	Course	Final mark (0-20)
1	***Técnicas Avançadas de Caracterização de Materiais***	17
2	***Cinética no Processamento Avançado de Sólidos***	17
3	***Nanoquímica***	16
4	***Dispositivos e Sensores***	17
5	***Materiais 2D e 3D Nanoestruturados***	19
6	***Laboratórios de Microscopia Electrónica de Transmissão***	17
7	***Sistemas de Gestão Ambiental***	14
8	***Português Língua Estrangeira***	18

References

[1] S.B. Ogale, Thin Films and Heterostructures for Oxide Electronics, Springer US2006.
[2] N. Setter, D. Damjanovic, L. Eng, G. Fox, S. Gevorgian, S. Hong, A. Kingon, H. Kohlstedt, N.Y. Park, G.B. Stephenson, I. Stolitchnov, A.K. Taganstev, D.V. Taylor, T. Yamada, S. Streiffer, Ferroelectric Thin Films: Review of Materials, Properties, and Applications, Journal of Applied Physics 100(5) (2006) 051606-46.
[3] C.K. Kwok, S.B. Desu, Low-Temperature Perovskite Formation of Lead Zirconate Titanate Thin-Film by a Seeding Process, Journal of Materials Research 8(2) (1993) 339-344.
[4] Z. Huang, Q. Zhang, R.W. Whatmore, Low temperature crystallization of lead zirconate titanate thin films by a sol-gel method, Journal of Applied Physics 85(10) (1999) 7355-7361.
[5] H. Suzuki, T. Koizumi, Y. Kondo, S. Kaneko, Low-Temperature Processing of $Pb(Zr_{0.53}Ti_{0.47})O_3$ Thin Film from Stable Precursor Sol, Journal of the European Ceramic Society 19(6-7) (1999) 1397-1401.
[6] M. Mandeljc, M. Kosec, B. Malič, Z. Samardzija, Low Temperature Processing of Lanthanum Doped PZT Thin Films, Integrated Ferroelectrics 30(1-4) (2000) 149-156.
[7] K. Kato, Low-Temperature Synthesis of $SrBi_2Ta_2O_9$ Ferroelectric Thin Films through the Complex Alkoxide Method: Effects of Functional Group, Hydrolysis and Water Vapor Treatment, Japanese Journal of Applied Physics 37 (1998) 5178.
[8] S.S.N. Bharadwaja, T. Dechakupt, S. Trolier-McKinstry, H. Beratan, Excimer Laser Crystallized $(Pb,La)(Zr,Ti)O_3$ Thin Films, Journal of the American Ceramic Society 91(5) (2008) 1580-1585.
[9] T.P. Comyn, T. Chakraborty, R.E. Miles, S.J. Milne, Characterization of Laser-Transferred Bismuth Ferrite Lead Titanate Ferroelectric Thick Films, Applied Physics Letters 93(5) (2008) 052909-3.
[10] A. Wu, I.M.M. Salvado, P.M. Vilarinho, J.L. Baptista, Processing and Seeding Effects on Crystallisation of PZT Thin Films from Sol-Gel Method, Journal of the European Ceramic Society 17(12) (1997) 1443-1452.
[11] A. Wu, P.M. Vilarinho, I.M.M. Salvado, J.L. Baptista, C.M. de Jesus, M.F. da Silva, Characterization of Seeded Sol–Gel Lead Zirconate Titanate Thin Films, Journal of the European Ceramic Society 19(6–7) (1999) 1403-1407.
[12] A. Wu, P.M. Vilarinho, I.M. Reaney, I.M. Miranda Salvado, J.L. Baptista, Kinetic Aspects of the Formation of Seeded Lead Zirconate Titanate Thin Films, Integrated Ferroelectrics 30(1-4) (2000) 261-270.
[13] A. Wu, P.M. Vilarinho, I.M.M. Salvado, J.L. Baptista, Z. Zhou, I.M. Reaney, A.R. Ramos, M.F. da Silva, Effect of Lead Zirconate Titanate Seeds on Pt_xPb Formation during the Pyrolysis of Lead Zirconate Titanate Thin Films, Journal of the American Ceramic Society 85(3) (2002) 641-646.
[14] M.L. Calzada, A. Gonzalez, R. Poyato, L. Pardo, Photo-Sensitive Sol-Gel Solutions for the Low-Temperature UV-Assisted Processing of $PbTiO_3$ Based Ferroelectric Thin Films, J Mater Chem 13(6) (2003) 1451-1457.
[15] R.E. Van de Leest, UV Photo-Annealing of Thin Sol-Gel Films, Applied Surface Science 86(1–4) (1995) 278-285.
[16] I. Bretos, R. Jiménez, A. Wu, A.I. Kingon, P.M. Vilarinho, M.L. Calzada, Activated Solutions Enabling Low-Temperature Processing of Functional Ferroelectric Oxides for Flexible Electronics, Advanced Materials 26(9) (2014) 1405-1409.
[17] J. Rödel, K.G. Webber, R. Dittmer, W. Jo, M. Kimura, D. Damjanovic, Transferring lead-free piezoelectric ceramics into application, Journal of the European Ceramic Society 35(6) (2015) 1659-1681.
[18] G. Catalan, J.F. Scott, Physics and Applications of Bismuth Ferrite, Advanced Materials 21(24) (2009) 2463-2485.

[19] V.V. Shvartsman, D.C. Lupascu, Lead-Free Relaxor Ferroelectrics, Journal of the American Ceramic Society 95(1) (2012) 1-26.
[20] R. Safi, H. Shokrollahi, Physics, chemistry and synthesis methods of nanostructured bismuth ferrite ($BiFeO_3$) as a ferroelectro-magnetic material, Progress in Solid State Chemistry 40(1–2) (2012) 6-15.
[21] M. Arredondo, M. Saunders, A. Petraru, H. Kohlstedt, I. Vrejoiu, M. Alexe, D. Hesse, N.D. Browning, P. Munroe, V. Nagarajan, Structural defects and local chemistry across ferroelectric–electrode interfaces in epitaxial heterostructures, J Mater Sci 44(19) (2009) 5297-5306.
[22] B. Nagaraj, S. Aggarwal, R. Ramesh, Influence of contact electrodes on leakage characteristics in ferroelectric thin films, Journal of Applied Physics 90(1) (2001) 375-382.
[23] Y.W. Li, J.L. Sun, J. Chen, X.J. Meng, J.H. Chu, Preparation and characterization of $BiFeO_3$ thin films grown on $LaNiO_3$-coated $SrTiO_3$ substrate by chemical solution deposition, Journal of Crystal Growth 285(4) (2005) 595-599.
[24] Z. Liu, H. Liu, G. Du, J. Zhang, K. Yao, Electric properties of $BiFeO_3$ films deposited on $LaNiO_3$ by sol-gel process, Journal of Applied Physics 100(4) (2006) 044110.
[25] H. Liu, X. Wang, Rectangular and saturated hysteresis loops of $BiFeO_3$ film on $LaNiO_3$ bottom electrode, Journal of Alloys and Compounds 485(1–2) (2009) 769-772.
[26] Y. Wang, Z. Li, Y. Lin, C.W. Nan, Magnetic-electric behaviors in $BiFeO_3$ films grown on $LaNiO_3$-buffered Si substrate, Journal of Applied Physics 106(7) (2009) 073917.
[27] H. Zhang, X. Chen, T. Wang, F. Wang, W. Shi, Structure and electrical properties of $BiFeO_3$ thin films grown on $LaNiO_3$ electrode by chemical solution deposition, Journal of Alloys and Compounds 500(1) (2010) 46-48.
[28] P.M. Vilarinho, Functional Materials: Properties, Processing and Applications, in: P. Vilarinho, Y. Rosenwaks, A. Kingon (Eds.), Scanning Probe Microscopy: Characterization, Nanofabrication and Device Application of Functional Materials, Springer Netherlands2005, pp. 3-33.
[29] Z.L. Wang, Z.C. Kang, Introduction, Functional and Smart Materials: Structural Evolution and Structure Analysis, Springer US, Boston, MA, 1998, pp. 1-6.
[30] S. Zlotnik, A. Tkach, P.M. Vilarinho, Functional Tantalum-based Oxides: From the Structure to the Applications, in: A. Tiwari, R.A. Gerhardt, M. Szutkowska (Eds.), Advanced Ceramic Materials, John Wiley & Sons, Inc.2016, pp. 337-383.
[31] P. Boch, J.-F. Baumard, Ceramic Compounds: Ceramic Materials, Ceramic Materials, ISTE2010, pp. 1-28.
[32] A.S. Bhalla, R. Guo, R. Roy, The Perovskite Structure – A Review of its Role in Ceramic Science and Technology, Mat Res Innovat 4(1) (2000) 3-26.
[33] D. Fatih, L. Hong, G.-V. Maryline, P. Octavio, Focus on properties and applications of perovskites, Science and Technology of Advanced Materials 16(2) (2015) 020301.
[34] J.F. Scott, Applications of Modern Ferroelectrics, Science 315(5814) (2007) 954-959.
[35] J. Varghese, R.W. Whatmore, J.D. Holmes, Ferroelectric nanoparticles, wires and tubes: synthesis, characterisation and applications, Journal of Materials Chemistry C 1(15) (2013) 2618-2638.
[36] N. Nuraje, K. Su, Perovskite ferroelectric nanomaterials, Nanoscale 5(19) (2013) 8752-8780.
[37] D. Damjanovic, Chapter 4 - Hysteresis in Piezoelectric and Ferroelectric Materials A2 - Bertotti, Giorgio, in: I.D. Mayergoyz (Ed.), The Science of Hysteresis, Academic Press, Oxford, 2006, pp. 337-465.
[38] H. Han, Y. Kim, M. Alexe, D. Hesse, W. Lee, Nanostructured Ferroelectrics: Fabrication and Structure–Property Relations, Advanced Materials 23(40) (2011) 4599-4613.
[39] L.W. Martin, A.M. Rappe, Thin-film ferroelectric materials and their applications, Nature Reviews Materials 2 (2016) 16087.
[40] G.H. Haertling, Ferroelectric Ceramics: History and Technology, Journal of the American Ceramic Society 82(4) (1999) 797-818.
[41] O. Auciello, C.M. Foster, R. Ramesh, Processing Technologies for Ferroelectric Thin Films and Heterostructures, Annual Review of Materials Science 28(1) (1998) 501-531.

[42] C.J. Brinker, A.J. Hurd, P.R. Schunk, G.C. Frye, C.S. Ashley, Review of Sol-Gel Thin-Film Formation, Journal of Non-Crystalline Solids 147 (1992) 424-436.
[43] L.M. Sheppard, Advances in Processing of Ferroelectric Thin-Films, Am Ceram Soc Bull 71(1) (1992) 85-95.
[44] R.W. Schwartz, T.J. Boyle, S.J. Lockwood, M.B. Sinclair, D. Dimos, C.D. Buchheit, Sol-Gel Processing of PZT Thin-Films - a Review of the State-of-the-Art and Process Optimization Strategies, Integrated Ferroelectrics 7(1-4) (1995) 259-277.
[45] B.A. Tuttle, R.W. Schwartz, Solution Deposition of Ferroelectric Thin Films, Mrs Bull 21(6) (1996) 49-54.
[46] I.M. Reaney, D.V. Taylor, K.G. Brooks, Ferroelectric PZT Thin Films by Sol-Gel Deposition, J Sol-Gel Sci Techn 13(1-3) (1998) 813-820.
[47] P.K. Panda, Review: Environmental Friendly Lead-Free Piezoelectric Materials, J Mater Sci 44(19) (2009) 5049-5062.
[48] J. Rödel, W. Jo, K.T.P. Seifert, E.-M. Anton, T. Granzow, D. Damjanovic, Perspective on the Development of Lead-Free Piezoceramics, Journal of the American Ceramic Society 92(6) (2009) 1153-1177.
[49] D. Sando, Y. Yang, E. Bousquet, C. Carrétéro, V. Garcia, S. Fusil, D. Dolfi, A. Barthélémy, P. Ghosez, L. Bellaiche, M. Bibes, Large elasto-optic effect and reversible electrochromism in multiferroic $BiFeO_3$, Nature Communications 7 (2016) 10718.
[50] V.A. Isupov, Ferroelectric $Na_{0.5}Bi_{0.5}TiO_3$ and $K_{0.5}Bi_{0.5}TiO_3$ Perovskites and Their Solid Solutions, Ferroelectrics 315(1) (2005) 123-147.
[51] D.E. Dausch, Ferroelectric Polarization Fatigue in PZT-Based RAINBOWs and Bulk Ceramics, Journal of the American Ceramic Society 80(9) (1997) 2355-2360.
[52] M.W. Hooker, Properties of PZT-Based Piezoelectric Ceramics Between -150 and 250 C, NASA Langley Research Center, 1998, pp. 1-28.
[53] S. Kim, V. Gopalan, A. Gruverman, Coercive fields in ferroelectrics: A case study in lithium niobate and lithium tantalate, Applied Physics Letters 80(15) (2002) 2740-2742.
[54] J. Wang, J.B. Neaton, H. Zheng, V. Nagarajan, S.B. Ogale, B. Liu, D. Viehland, V. Vaithyanathan, D.G. Schlom, U.V. Waghmare, N.A. Spaldin, K.M. Rabe, M. Wuttig, R. Ramesh, Epitaxial $BiFeO_3$ Multiferroic Thin Film Heterostructures, Science 299(5613) (2003) 1719-1722.
[55] D. Lebeugle, D. Colson, A. Forget, M. Viret, Very Large Spontaneous Electric Polarization in $BiFeO_3$ Single Crystals at Room Temperature and its Evolution Under Cycling Fields, Applied Physics Letters 91(2) (2007) 022907-3.
[56] V.V. Shvartsman, W. Kleemann, R. Haumont, J. Kreisel, Large Bulk Polarization and Regular Domain Structure in Ceramic $BiFeO_3$, Applied Physics Letters 90(17) (2007) 172115-3.
[57] D. Lin, K.W. Kwok, H.L.W. Chan, Piezoelectric and ferroelectric properties of $K_xNa_{1-x}NbO_3$ lead-free ceramics with MnO_2 and CuO doping, Journal of Alloys and Compounds 461(1–2) (2008) 273-278.
[58] J. Shieh, J.H. Yeh, Y.C. Shu, J.H. Yen, Hysteresis behaviors of barium titanate single crystals based on the operation of multiple 90° switching systems, Materials Science and Engineering: B 161(1–3) (2009) 50-54.
[59] H. Uršič, A. Benčan, M. Škarabot, M. Godec, M. Kosec, Dielectric, ferroelectric, piezoelectric, and electrostrictive properties of $K_{0.5}Na_{0.5}NbO_3$ single crystals, Journal of Applied Physics 107(3) (2010) 033705.
[60] S. Gupta, S. Priya, Ferroelectric properties and dynamic scaling of (100) oriented $(K_{0.5}Na_{0.5})NbO_3$ single crystals, Applied Physics Letters 98(24) (2011) 242906.
[61] D. Kobor, M. Tine, A. Hajjaji, L. Lebrun, D. Guyomar, Mn Effect on Nonlinear and Structural Properties of <110> Oriented PZN-4.5PT Single Crystals, Journal of Modern Physics 3(5) (2012) 404-411.
[62] O. Namsar, A. Watcharapasorn, S. Jiansirisomboon, Structure–property relations of ferroelectric $BaTiO_3$ ceramics containing nano-sized Si_3N_4 particulates, Ceramics International 38, Supplement 1 (2012) S95-S99.

[63] Sonia, R.K. Patel, P. Kumar, C. Prakash, D.K. Agrawal, Low temperature synthesis and dielectric, ferroelectric and piezoelectric study of microwave sintered $BaTiO_3$ ceramics, Ceramics International 38(2) (2012) 1585-1589.
[64] P. Kumar, M. Pattanaik, Sonia, Synthesis and characterizations of KNN ferroelectric ceramics near 50/50 MPB, Ceramics International 39(1) (2013) 65-69.
[65] S. Swain, P. Kumar, D.K. Agrawal, Sonia, Dielectric and ferroelectric study of KNN modified NBT ceramics synthesized by microwave processing technique, Ceramics International 39(3) (2013) 3205-3210.
[66] Y. Yan, S. Priya, High performance textured piezoelectric ceramics and method for manufacturing same, Virginia Tech Intellectual Properties, Inc., 2013.
[67] T. Rojac, A. Bencan, B. Malic, G. Tutuncu, J.L. Jones, J.E. Daniels, D. Damjanovic, $BiFeO_3$ Ceramics: Processing, Electrical, and Electromechanical Properties, Journal of the American Ceramic Society 97(7) (2014) 1993-2011.
[68] X. Li, C. Chen, H. Deng, H. Zhang, D. Lin, X. Zhao, H. Luo, The Growth and Properties of Lead-Free Ferroelectric Single Crystals, Crystals 5(2) (2015) 172.
[69] J. Lv, J. Wu, W. Wu, Enhanced Electrical Properties of Quenched $(1 - x)Bi_{1-y}Sm_yFeO_3–xBiScO_3$ Lead-Free Ceramics, The Journal of Physical Chemistry C 119(36) (2015) 21105-21115.
[70] S.H. Song, Q.S. Zhu, L.Q. Weng, V.R. Mudinepalli, A comparative study of dielectric, ferroelectric and magnetic properties of $BiFeO_3$ multiferroic ceramics synthesized by conventional and spark plasma sintering techniques, Journal of the European Ceramic Society 35(1) (2015) 131-138.
[71] U. Lewczuk, J. Suchanicz, M. Karpierz, G. Stachowski, Dielectric and ferroelectric properties of NBT-BT systems, Phase Transitions (2016) 1-5.
[72] S. Mitra, A.R. Kulkarni, Synthesis and Electrical Properties of New Lead-free $(100−x)(Li_{0.12}Na_{0.88})NbO_3–xBaTiO_3$ $(0 \leq x \leq 40)$ Piezoelectric Ceramics, Journal of the American Ceramic Society 99(3) (2016) 888-895.
[73] K. Shalini, M. Muneeswaran, N.V. Giridharan, Structural and electrical properties of ferroelectric $Na_{0.5}(Bi_{1-x}Pr_x)_{0.5}TiO_3$ (x=0.00 and 0.10) ceramics synthesized by Sol-Gel method, AIP Conference Proceedings 1731(1) (2016) 140018.
[74] H. Schmid, Multi-ferroic magnetoelectrics, Ferroelectrics 162(1) (1994) 317-338.
[75] W. Eerenstein, N.D. Mathur, J.F. Scott, Multiferroic and magnetoelectric materials, Nature 442(7104) (2006) 759-765.
[76] L.W. Martin, R. Ramesh, Multiferroic and magnetoelectric heterostructures, Acta Materialia 60(6–7) (2012) 2449-2470.
[77] F. Gao, X.Y. Chen, K.B. Yin, S. Dong, Z.F. Ren, F. Yuan, T. Yu, Z.G. Zou, J.M. Liu, Visible-Light Photocatalytic Properties of Weak Magnetic $BiFeO_3$ Nanoparticles, Advanced Materials 19(19) (2007) 2889-2892.
[78] S.R. Basu, L.W. Martin, Y.H. Chu, M. Gajek, R. Ramesh, R.C. Rai, X. Xu, J.L. Musfeldt, Photoconductivity in $BiFeO_3$ thin films, Applied Physics Letters 92(9) (2008) 091905.
[79] T. Choi, S. Lee, Y.J. Choi, V. Kiryukhin, S.-W. Cheong, Switchable Ferroelectric Diode and Photovoltaic Effect in $BiFeO_3$, Science 324(5923) (2009) 63-66.
[80] N. Bassiri-Gharb, Y. Bastani, A. Bernal, Chemical solution growth of ferroelectric oxide thin films and nanostructures, Chemical Society Reviews 43(7) (2014) 2125-2140.
[81] F. Kubel, H. Schmid, Structure of a Ferroelectric and Ferroelastic Monodomain Crystal of the Perovskite $BiFeO_3$, Acta Crystallogr B 46 (1990) 698-702.
[82] P. Je-Geun, L. Manh Duc, J. Jaehong, L. Sanghyun, Structure and spin dynamics of multiferroic $BiFeO_3$, Journal of Physics: Condensed Matter 26(43) (2014) 433202.
[83] J. Wu, Z. Fan, D. Xiao, J. Zhu, J. Wang, Multiferroic bismuth ferrite-based materials for multifunctional applications: Ceramic bulks, thin films and nanostructures, Progress in Materials Science 84 (2016) 335-402.
[84] D. Sando, B. Xu, L. Bellaiche, V. Nagarajan, A multiferroic on the brink: Uncovering the nuances of strain-induced transitions in $BiFeO_3$, Applied Physics Reviews 3(1) (2016) 011106.

[85] P. Ravindran, R. Vidya, A. Kjekshus, H. Fjellvag, O. Eriksson, Theoretical Investigation of Magnetoelectric Behavior in $BiFeO_3$, Physical Review B 74(22) (2006).
[86] C. Michel, J.M. Moreau, R. Gerson, W.J. James, Atomic Structure in Perovskitic $BiFeO_3$, Acta Crystall a-Crys A 25 (1969) S56.
[87] P. Fischer, M. Polomska, I. Sosnowska, M. Szymanski, Temperature dependence of the crystal and magnetic structures of $BiFeO_3$, J Phys C Solid State 13(10) (1980) 1931-1940.
[88] I. Sosnowska, T.P. Neumaier, E. Steichele, Spiral magnetic ordering in bismuth ferrite, Journal of Physics C: Solid State Physics 15(23) (1982) 4835.
[89] D. Lebeugle, D. Colson, A. Forget, M. Viret, A.M. Bataille, A. Gukasov, Electric-Field-Induced Spin Flop in $BiFeO_3$ Single Crystals at Room Temperature, Physical Review Letters 100(22) (2008) 227602.
[90] C. Ederer, N.A. Spaldin, Weak ferromagnetism and magnetoelectric coupling in bismuth ferrite, Physical Review B 71(6) (2005) 060401.
[91] J.R. Teague, R. Gerson, W.J. James, Dielectric hysteresis in single crystal $BiFeO_3$, Solid State Commun 8(13) (1970) 1073-1074.
[92] W. Eerenstein, F.D. Morrison, J. Dho, M.G. Blamire, J.F. Scott, N.D. Mathur, Comment on "Epitaxial $BiFeO_3$ Multiferroic Thin Film Heterostructures", Science 307(5713) (2005) 1203-1203.
[93] J. Li, J. Wang, M. Wuttig, R. Ramesh, N. Wang, B. Ruette, A.P. Pyatakov, A.K. Zvezdin, D. Viehland, Dramatically enhanced polarization in (001), (101), and (111) $BiFeO_3$ thin films due to epitiaxial-induced transitions, Applied Physics Letters 84(25) (2004) 5261-5263.
[94] X. Qi, J. Dho, R. Tomov, M.G. Blamire, J.L. MacManus-Driscoll, Greatly reduced leakage current and conduction mechanism in aliovalent-ion-doped $BiFeO_3$, Applied Physics Letters 86(6) (2005) 062903.
[95] H. Ishiwara, Impurity substitution effects in $BiFeO_3$ thin films—From a viewpoint of FeRAM applications, Current Applied Physics 12(3) (2012) 603-611.
[96] S.K. Singh, H. Ishiwara, K. Maruyama, Room temperature ferroelectric properties of Mn-substituted $BiFeO_3$ thin films deposited on Pt electrodes using chemical solution deposition, Applied Physics Letters 88(26) (2006) 262908.
[97] D. Sando, A. Barthélémy, M. Bibes, $BiFeO_3$ epitaxial thin films and devices: past, present and future, Journal of Physics: Condensed Matter 26(47) (2014) 473201.
[98] J. Seidel, L.W. Martin, Q. He, Q. Zhan, Y.H. Chu, A. Rother, M.E. Hawkridge, P. Maksymovych, P. Yu, M. Gajek, N. Balke, S.V. Kalinin, S. Gemming, F. Wang, G. Catalan, J.F. Scott, N.A. Spaldin, J. Orenstein, R. Ramesh, Conduction at domain walls in oxide multiferroics, Nat Mater 8(3) (2009) 229-234.
[99] J. Guyonnet, I. Gaponenko, S. Gariglio, P. Paruch, Conduction at Domain Walls in Insulating $Pb(Zr_{0.2}Ti_{0.8})O_3$ Thin Films, Advanced Materials 23(45) (2011) 5377-5382.
[100] M. Schröder, A. Haußmann, A. Thiessen, E. Soergel, T. Woike, L.M. Eng, Conducting Domain Walls in Lithium Niobate Single Crystals, Advanced Functional Materials 22(18) (2012) 3936-3944.
[101] N.N. Krainik, N.P. Khuchua, V.V. Zhdanova, V.A. Evseev, Phase transition in $BiFeO_3$, Sov Phys-Sol State 8 (1966) 654-658.
[102] S.A.T. Redfern, C. Wang, J.W. Hong, G. Catalan, J.F. Scott, Elastic and electrical anomalies at low-temperature phase transitions in $BiFeO_3$, Journal of Physics: Condensed Matter 20(45) (2008) 452205.
[103] R.J. Zeches, M.D. Rossell, J.X. Zhang, A.J. Hatt, Q. He, C.-H. Yang, A. Kumar, C.H. Wang, A. Melville, C. Adamo, G. Sheng, Y.-H. Chu, J.F. Ihlefeld, R. Erni, C. Ederer, V. Gopalan, L.Q. Chen, D.G. Schlom, N.A. Spaldin, L.W. Martin, R. Ramesh, A Strain-Driven Morphotropic Phase Boundary in $BiFeO_3$, Science 326(5955) (2009) 977-980.
[104] M.H. Lee, D.J. Kim, J.S. Park, S.W. Kim, T.K. Song, M.-H. Kim, W.-J. Kim, D. Do, I.-K. Jeong, High-Performance Lead-Free Piezoceramics with High Curie Temperatures, Advanced Materials 27(43) (2015) 6976-6982.
[105] A. Kumar, R.C. Rai, N.J. Podraza, S. Denev, M. Ramirez, Y.-H. Chu, L.W. Martin, J. Ihlefeld, T. Heeg, J. Schubert, D.G. Schlom, J. Orenstein, R. Ramesh, R.W. Collins, J.L. Musfeldt, V.

Gopalan, Linear and nonlinear optical properties of $BiFeO_3$, Applied Physics Letters 92(12) (2008) 121915.
[106] S.J. Clark, J. Robertson, Band gap and Schottky barrier heights of multiferroic $BiFeO_3$, Applied Physics Letters 90(13) (2007) 132903.
[107] S.M. Sze, K.K. Ng, Physics and Properties of Semiconductors—A Review, Physics of Semiconductor Devices, John Wiley & Sons, Inc.2006, pp. 5-75.
[108] A.M. Kadomtseva, Y.F. Popov, A.P. Pyatakov, G.P. Vorob'ev, A.K. Zvezdin, D. Viehland, Phase transitions in multiferroic $BiFeO_3$ crystals, thin-layers, and ceramics: enduring potential for a single phase, room-temperature magnetoelectric 'holy grail', Phase Transitions 79(12) (2006) 1019-1042.
[109] F. Bai, J. Wang, M. Wuttig, J. Li, N. Wang, A.P. Pyatakov, A.K. Zvezdin, L.E. Cross, D. Viehland, Destruction of spin cycloid in (111)c-oriented $BiFeO_3$ thin films by epitiaxial constraint: Enhanced polarization and release of latent magnetization, Applied Physics Letters 86(3) (2005) 032511.
[110] T.-J. Park, G.C. Papaefthymiou, A.J. Viescas, A.R. Moodenbaugh, S.S. Wong, Size-Dependent Magnetic Properties of Single-Crystalline Multiferroic $BiFeO_3$ Nanoparticles, Nano Letters 7(3) (2007) 766-772.
[111] A.F. Popkov, M.D. Davydova, K.A. Zvezdin, S.V. Solov'yov, A.K. Zvezdin, Origin of the giant linear magnetoelectric effect in perovskitelike multiferroic $BiFeO_3$, Physical Review B 93(9) (2016) 094435.
[112] C. Tabares-Muñoz, J.P. Rivera, A. Bezinges, A. Monnier, H. Schmid, Measurement of the Quadratic Magnetoelectric Effect on Single Crystalline $BiFeO_3$, Japanese Journal of Applied Physics 24(S2) (1985) 1051.
[113] M. Lorenz, G. Wagner, V. Lazenka, P. Schwinkendorf, H. Modarresi, M.J. Van Bael, A. Vantomme, K. Temst, O. Oeckler, M. Grundmann, Correlation of magnetoelectric coupling in multiferroic $BaTiO_3$-$BiFeO_3$ superlattices with oxygen vacancies and antiphase octahedral rotations, Applied Physics Letters 106(1) (2015) 012905.
[114] F.M.A. Inc., Press Release. 2 August 2006. http://www.fujitsu.com/ca/en/news/pr/fma_20060802.html, 2006 (accessed 18.09.2013.).
[115] K. Maruyama, M. Kondo, S.K. Singh, H. Ishiwara, New Ferroelectric Material for Embedded FRAM LSIs, Fujitsu Scientific and Technical Journal 43(4) (2007) 502-507.
[116] M. Bibes, A. Barthelemy, Multiferroics: Towards a magnetoelectric memory, Nat Mater 7(6) (2008) 425-426.
[117] A. Roy, R. Gupta, A. Garg, Multiferroic Memories, Advances in Condensed Matter Physics 2012 (2012) 12.
[118] R. Guo, L. You, Y. Zhou, Z. Shiuh Lim, X. Zou, L. Chen, R. Ramesh, J. Wang, Non-volatile memory based on the ferroelectric photovoltaic effect, Nat Commun 4 (2013).
[119] A. Steiner, C. Tabares Munoz, H. Schmid, Nachweis und Eigenschaften ferroelektrischer 180°-Domaenen in $BiFeO_3$-Einkristalen, Helvetica Physica Acta 60(2) (1987) 294-300.
[120] F. Kubel, H. Schmid, Growth, twinning and etch figures of ferroelectric/ferroelastic dendritic $BiFeO_3$ single domain crystals, Journal of Crystal Growth 129(3) (1993) 515-524.
[121] R. Palai, R.S. Katiyar, H. Schmid, P. Tissot, S.J. Clark, J. Robertson, S.A.T. Redfern, G. Catalan, J.F. Scott, β phase and γ−β metal-insulator transition in multiferroic $BiFeO_3$, Physical Review B 77(1) (2008) 014110.
[122] D. Lebeugle, D. Colson, A. Forget, M. Viret, P. Bonville, J.F. Marucco, S. Fusil, Room-temperature coexistence of large electric polarization and magnetic order in $BiFeO_3$ single crystals, Physical Review B 76(2) (2007) 024116.
[123] Z.V. Gabbasova, M.D. Kuz'min, A.K. Zvezdin, I.S. Dubenko, V.A. Murashov, D.N. Rakov, I.B. Krynetsky, $Bi_{1-x}R_xFeO_3$ (R=rare earth): a family of novel magnetoelectrics, Physics Letters A 158(9) (1991) 491-498.

[124] T. Ito, T. Ushiyama, Y. Yanagisawa, R. Kumai, Y. Tomioka, Growth of Highly Insulating Bulk Single Crystals of Multiferroic $BiFeO_3$ and Their Inherent Internal Strains in the Domain-Switching Process, Crystal Growth & Design 11(11) (2011) 5139-5143.
[125] A. Maître, M. François, J.C. Gachon, Experimental study of the Bi_2O_3-Fe_2O_3 pseudo-binary system, Journal of Phase Equilibria and Diffusion 25(1) (2004) 59-67.
[126] S.M. Selbach, M.-A. Einarsrud, T. Grande, On the Thermodynamic Stability of $BiFeO_3$, Chemistry of Materials 21(1) (2009) 169-173.
[127] M.S. Bernardo, T. Jardiel, M. Peiteado, A.C. Caballero, M. Villegas, Reaction pathways in the solid state synthesis of multiferroic $BiFeO_3$, Journal of the European Ceramic Society 31(16) (2011) 3047-3053.
[128] S.T. Zhang, M.H. Lu, D. Wu, Y.F. Chen, N.B. Ming, Larger polarization and weak ferromagnetism in quenched $BiFeO_3$ ceramics with a distorted rhombohedral crystal structure, Applied Physics Letters 87(26) (2005) 262907.
[129] G.L. Yuan, S.W. Or, Y.P. Wang, Z.G. Liu, J.M. Liu, Preparation and multi-properties of insulated single-phase $BiFeO_3$ ceramics, Solid State Commun 138(2) (2006) 76-81.
[130] K.D. Sung, T.K. Le, Y.A. Park, N. Hur, J.H. Jung, Photo-carrier control of exchange bias in $BiFeO_3$/$La_{2/3}Sr_{1/3}MnO_3$ thin films, Applied Physics Letters 104 (2014).
[131] R.R. Das, D.M. Kim, S.H. Baek, C.B. Eom, F. Zavaliche, S.Y. Yang, R. Ramesh, Y.B. Chen, X.Q. Pan, X. Ke, M.S. Rzchowski, S.K. Streiffer, Synthesis and ferroelectric properties of epitaxial $BiFeO_3$ thin films grown by sputtering, Applied Physics Letters 88(24) (2006) 242904.
[132] Z.-W. Peng, B.-T. Liu, Abnormal capacitance–voltage and switchable photovoltaic effect of epitaxial Mn-doped $BiFeO_3$ thin film capacitor, Functional Materials Letters 08(05) (2015) 1550057.
[133] R. Ueno, S. Okaura, H. Funakubo, K. Saito, Crystal Structure and Electrical Properties of Epitaxial $BiFeO_3$ Thin Films Grown by Metal Organic Chemical Vapor Deposition, Japanese Journal of Applied Physics 44(9L) (2005) L1231.
[134] S.K. Singh, Y.K. Kim, H. Funakubo, H. Ishiwara, Epitaxial $BiFeO_3$ thin films fabricated by chemical solution deposition, Applied Physics Letters 88(16) (2006) 162904.
[135] J.X. Zhang, Q. He, M. Trassin, W. Luo, D. Yi, M.D. Rossell, P. Yu, L. You, C.H. Wang, C.Y. Kuo, J.T. Heron, Z. Hu, R.J. Zeches, H.J. Lin, A. Tanaka, C.T. Chen, L.H. Tjeng, Y.H. Chu, R. Ramesh, Microscopic Origin of the Giant Ferroelectric Polarization in Tetragonal-like $BiFeO_3$, Physical Review Letters 107(14) (2011) 147602.
[136] J.X. Zhang, XiangB, HeQ, SeidelJ, R.J. Zeches, YuP, S.Y. Yang, C.H. Wang, Y.H. Chu, L.W. Martin, A.M. Minor, RameshR, Large field-induced strains in a lead-free piezoelectric material, Nat Nano 6(2) (2011) 98-102.
[137] Y. Yang, I.C. Infante, B. Dkhil, L. Bellaiche, Strain effects on multiferroic $BiFeO_3$ films, Comptes Rendus Physique 16(2) (2015) 193-203.
[138] R.W. Schwartz, T. Schneller, R. Waser, Chemical solution deposition of electronic oxide films, Comptes Rendus Chimie 7(5) (2004) 433-461.
[139] G. Teowee, K. McCarthy, F. McCarthy, T.J. Bukowski, T.P. Alexander, D.R. Uhlmann, Dielectric and Ferroelectric Properties of Sol-Gel Derived $BiFeO_3$ Films, Integrated Ferroelectrics 18(1-4) (1997) 329-337.
[140] A.Z. Simões, C.S. Riccardi, M.L. Dos Santos, F.G. Garcia, E. Longo, J.A. Varela, Effect of annealing atmosphere on phase formation and electrical characteristics of bismuth ferrite thin films, Materials Research Bulletin 44(8) (2009) 1747-1752.
[141] Y. Nakamura, K.Y. Yun, S. Nakashima, M. Okuyama, Sol-Gel Preparation and Characterization of Multiferroic $BiFeO_3$ Thin Films with Various Bi/Fe Ratio, Integrated Ferroelectrics 95 (2007) 226-233.
[142] Y. Nakamura, S. Nakashima, M. Okuyama, $BiFeO_3$ Thin Films Prepared by Chemical Solution Deposition with Approaches for Improvement of Ferroelectricity, Ferroelectrics - Material Aspects, in: M. Lallart (Ed.), Ferroelectrics - Material Aspects, InTech2011.

[143] F. Tyholdt, S. Jørgensen, H. Fjellvåg, A.E. Gunnæs, Synthesis of Oriented $BiFeO_3$ Thin Films by Chemical Solution Deposition: Phase, Texture, and Microstructural Development, Journal of Materials Research 20(08) (2005) 2127-2139.
[144] S. Habouti, C.-H. Solterbeck, M. Es-Souni, UV assisted pyrolysis of solution deposited $BiFeO_3$ multiferroic thin films. Effects on microstructure and functional properties, J Sol-Gel Sci Techn 42(3) (2007) 257-263.
[145] C. Gutiérrez-Lázaro, I. Bretos, R. Jiménez, J. Ricote, H.E. Hosiny, D. Pérez-Mezcua, R.J. Jiménez Rioboó, M. García-Hernández, M.L. Calzada, Solution Synthesis of $BiFeO_3$ Thin Films onto Silicon Substrates with Ferroelectric, Magnetic, and Optical Functionalities, Journal of the American Ceramic Society 96(10) (2013) 3061-3069.
[146] L. Jin, X. Tang, D. Song, R. Wei, J. Yang, J. Dai, W. Song, X. Zhu, Y. Sun, Annealing temperature effects on (111)-oriented $BiFeO_3$ thin films deposited on $Pt/Ti/SiO_2/Si$ by chemical solution deposition, Journal of Materials Chemistry C 3(41) (2015) 10742-10747.
[147] K.Y. Yun, M. Noda, M. Okuyama, Effects of Annealing Atmosphere on Crystallization and Electrical Properties in $BiFeO_3$ Thin Films by Chemacal Solution Deposition (CSD), Journal of the Korean Physical Society 42(SUPPL.) (2003) S1153-S1156.
[148] X. Tang, X. Zhu, J. Dai, Y. Sun, Self-limited grain growth, dielectric, leakage and ferroelectric properties of nanocrystalline $BiFeO_3$ thin films by chemical solution deposition, Acta Materialia 61(5) (2013) 1739-1747.
[149] Q. Zhang, N. Valanoor, O. Standard, Epitaxial (001) $BiFeO_3$ thin-films with excellent ferroelectric properties by chemical solution deposition-the role of gelation, Journal of Materials Chemistry C 3(3) (2015) 582-595.
[150] S.Y. Yang, F. Zavaliche, L. Mohaddes-Ardabili, V. Vaithyanathan, D.G. Schlom, Y.J. Lee, Y.H. Chu, M.P. Cruz, Q. Zhan, T. Zhao, R. Ramesh, Metalorganic chemical vapor deposition of lead-free ferroelectric $BiFeO_3$ films for memory applications, Applied Physics Letters 87(10) (2005) 102903.
[151] J.F. Li, J.L. Wang, M. Wuttig, R. Ramesh, N. Wang, B. Ruette, A.P. Pyatakov, A.K. Zvezdin, D. Viehland, Dramatically Enhanced Polarization in (001), (101), and (111) $BiFeO_3$ Thin Films Due to Epitiaxial-Induced Transitions, Applied Physics Letters 84(25) (2004) 5261-5263.
[152] Y. Nakamura, S. Nakashima, M. Okuyama, Influences of Surface Texture and Bi/Fe Ratio on Electric Properties of $BiFeO_3$ Thin Films Prepared by Chemical Solution Deposition, Japanese Journal of Applied Physics 47(9R) (2008) 7250.
[153] Y. Wang, Y. Lin, C.-W. Nan, Thickness dependent size effect of $BiFeO_3$ films grown on $LaNiO_3$-buffered Si substrates, Journal of Applied Physics 104(12) (2008) 123912.
[154] S. Singh, K., R. Ueno, H. Funakubo, H. Uchida, S. Koda, H. Ishiwara, Dependence of Ferroelectric Properties on Thickness of $BiFeO_3$ Thin Films Fabricated by Chemical Solution Deposition, Japanese Journal of Applied Physics 44(12R) (2005) 8525.
[155] A.Z. Simões, A.H.M. Gonzalez, L.S. Cavalcante, C.S. Riccardi, E. Longo, J.A. Varela, Ferroelectric characteristics of $BiFeO_3$ thin films prepared via a simple chemical solution deposition, Journal of Applied Physics 101(7) (2007) 074108.
[156] G.A. Smolenskii, V.A. Isupov, A.I. Agranovskaya, N.N. Krainik, New Ferroelectrics of Complex Composition, Sov Phys-Sol State 2(11) (1961) 2651-2654.
[157] J. Suchanicz, K. Roleder, A. Kania, J. Handerek, Electrostrictive Strain and Pyroeffect in the Region of Phase Coexistence in $Na_{0.5}Bi_{0.5}TiO_3$, Ferroelectrics 77 (1988) 107-110.
[158] K. Roleder, J. Suchanicz, A. Kania, Time-Dependence of Electric Permittivity in $Na_{0.5}Bi_{0.5}TiO_3$ Single Crystals, Ferroelectrics 89 (1989) 1-5.
[159] J. Suchanicz, Investigations of the Phase Transitions in $Na_{0.5}Bi_{0.5}TiO_3$, Ferroelectrics 172(1) (1995) 455-458.
[160] G.O. Jones, P.A. Thomas, Investigation of the Structure and Phase Transitions in the Novel A-site Substituted Distorted Perovskite Compound $Na_{0.5}Bi_{0.5}TiO_3$, Acta Crystallogr B 58 (2002) 168-178.

[161] L.E. Cross, Relaxor Ferroelectrics, Piezoelectricity: Evolution and Future of a Technology, Springer Berlin Heidelberg, Berlin, Heidelberg, 2008, pp. 131-155.
[162] K. Sakata, Y. Masuda, Ferroelectric and Antiferroelectric Properties of $(Na_{0.5}Bi_{0.5})TiO_3$-$SrTiO_3$ Solid Solution Ceramics, Ferroelectrics 7(1) (1974) 347-349.
[163] V. Dorcet, G. Trolliard, P. Boullay, Reinvestigation of Phase Transitions in $Na_{0.5}Bi_{0.5}TiO_3$ by TEM. Part I: First Order Rhombohedral to Orthorhombic Phase Transition, Chemistry of Materials 20(15) (2008) 5061-5073.
[164] G. Trolliard, V. Dorcet, Reinvestigation of Phase Transitions in $Na_{0.5}Bi_{0.5}TiO_3$ by TEM. Part II: Second Order Orthorhombic to Tetragonal Phase Transition, Chemistry of Materials 20(15) (2008) 5074-5082.
[165] S. Gorfman, P.A. Thomas, Evidence for a non-rhombohedral average structure in the lead-free piezoelectric material $Na_{0.5}Bi_{0.5}TiO_3$, Journal of Applied Crystallography 43(6) (2010) 1409-1414.
[166] V. Dorcet, G. Trolliard, A transmission electron microscopy study of the A-site disordered perovskite $Na_{0.5}Bi_{0.5}TiO_3$, Acta Materialia 56(8) (2008) 1753-1761.
[167] I. Levin, I.M. Reaney, Nano- and Mesoscale Structure of $Na_{1\backslash2}Bi_{1\backslash2}TiO_3$: A TEM Perspective, Advanced Functional Materials 22(16) (2012) 3445-3452.
[168] K. Reichmann, A. Feteira, M. Li, Bismuth Sodium Titanate Based Materials for Piezoelectric Actuators, Materials 8(12) (2015) 5469.
[169] B.N. Rao, R. Datta, S.S. Chandrashekaran, D.K. Mishra, V. Sathe, A. Senyshyn, R. Ranjan, Local structural disorder and its influence on the average global structure and polar properties in $Na_{0.5}Bi_{0.5}TiO_3$, Physical Review B 88(22) (2013) 224103.
[170] H. Nagata, T. Shinya, Y. Hiruma, T. Takenaka, I. Sakaguchi, H. Haneda, Piezoelectric Properties of Bismuth Sodium Titanate Ceramics, Developments in Dielectric Materials and Electronic Devices, John Wiley & Sons, Inc.2006, pp. 213-221.
[171] Y.S. Sung, J.M. Kim, J.H. Cho, T.K. Song, M.H. Kim, H.H. Chong, T.G. Park, D. Do, S.S. Kim, Effects of Na nonstoichiometry in $(Bi_{0.5}Na_{0.5+x})TiO_3$ ceramics, Applied Physics Letters 96(2) (2010) 022901.
[172] Y.S. Sung, J.M. Kim, J.H. Cho, T.K. Song, M.H. Kim, T.G. Park, Effects of Bi nonstoichiometry in $(Bi_{0.5+x}Na)TiO_3$ ceramics, Applied Physics Letters 98(1) (2011) 012902.
[173] M. Li, M.J. Pietrowski, R.A. De Souza, H. Zhang, I.M. Reaney, S.N. Cook, J.A. Kilner, D.C. Sinclair, A family of oxide ion conductors based on the ferroelectric perovskite $Na_{0.5}Bi_{0.5}TiO_3$, Nat Mater 13(1) (2014) 31-35.
[174] M. Li, H. Zhang, S.N. Cook, L. Li, J.A. Kilner, I.M. Reaney, D.C. Sinclair, Dramatic Influence of A-Site Nonstoichiometry on the Electrical Conductivity and Conduction Mechanisms in the Perovskite Oxide $Na_{0.5}Bi_{0.5}TiO_3$, Chemistry of Materials 27(2) (2015) 629-634.
[175] Y.-M. Chiang, G.W. Farrey, A.N. Soukhojak, Lead-free high-strain single-crystal piezoelectrics in the alkaline–bismuth–titanate perovskite family, Applied Physics Letters 73(25) (1998) 3683-3685.
[176] H. Yasuharu, H. Kouichi, Y. Yohachi, Crystal Growth and Electrical Properties of Lead-Free Piezoelectric Material $(Na_{1/2}Bi_{1/2})TiO_3$–$BaTiO_3$, Japanese Journal of Applied Physics 40(9S) (2001) 5722.
[177] K. Aravinth, G. Anandha Babu, P. Ramasamy, Flux growth and characterization of lead-free Sodium Bismuth Titanate–Barium Titanate single crystals, Journal of Crystal Growth 401 (2014) 787-790.
[178] I.P. Pronin, P.P. Syrnikov, V.A. Isupov, V.M. Egorov, N.V. Zaitseva, Peculiarities of phase transitions in sodium-bismuth titanate, Ferroelectrics 25(1) (1980) 395-397.
[179] J.A. Zvirgzds, P.P. Kapostin, J.V. Zvirgzde, T.V. Kruzina, X-ray study of phase transitions in ferroelectric $Na_{0.5}Bi_{0.5}TiO_3$, Ferroelectrics 40(1) (1982) 75-77.
[180] S.-E. Park, S.-J. Chung, I.-T. Kim, K.S. Hong, Nonstoichiometry and the Long-Range Cation Ordering in Crystals of $(Na_{1/2}Bi_{1/2})TiO_3$, Journal of the American Ceramic Society 77(10) (1994) 2641-2647.

[181] S.-E. Park, S.-J. Chung, I.-T. Kim, Ferroic Phase Transitions in $(Na_{1/2}Bi_{1/2})TiO_3$ Crystals, Journal of the American Ceramic Society 79(5) (1996) 1290-1296.
[182] T.V. Kruzina, V.M. Duda, J. Suchanicz, Peculiarities of optical behaviour of $Na_{0.5}Bi_{0.5}TiO_3$ single crystals, Materials Science and Engineering: B 87(1) (2001) 48-52.
[183] G. Xu, Z. Duan, X. Wang, D. Yang, Growth and some electrical properties of lead-free piezoelectric crystals $(Na_{1/2}Bi_{1/2})TiO_3$ and $(Na_{1/2}Bi_{1/2})TiO_3$–$BaTiO_3$ prepared by a Bridgman method, Journal of Crystal Growth 275(1–2) (2005) 113-119.
[184] M. Naderer, T. Kainz, D. Schütz, K. Reichmann, The influence of Ti-nonstoichiometry in $Bi_{0.5}Na_{0.5}TiO_3$, Journal of the European Ceramic Society 34(3) (2014) 663-667.
[185] Y. Liu, Y. Lu, S. Dai, Hydrothermal synthesis of monosized $Bi_{0.5}Na_{0.5}TiO_3$ spherical particles under low alkaline solution concentration, Journal of Alloys and Compounds 484(1–2) (2009) 801-805.
[186] B. Li, M.-S. Cao, J. Liu, D.-W. Wang, Domain Structure and Enhanced Electrical Properties in Sodium Bismuth Titanate Ceramics Sintered from Crystals with Different Morphologies, Journal of the American Ceramic Society (2016) n/a-n/a.
[187] L. Ju, C. Shi, L. Sun, Y. Zhang, H. Qin, J. Hu, Room-temperature magnetoelectric coupling in nanocrystalline $Na_{0.5}Bi_{0.5}TiO_3$, Journal of Applied Physics 116(8) (2014) 083909.
[188] V.R. Mudinepalli, F. Leng, M.P. Reddy, W.C. Lin, B.S. Murty, Structural, dielectric and ferroelectric properties of lead-free $Na_{0.5}Bi_{0.5}TiO_3$ ceramics prepared by spark plasma sintering technique, Indian Journal of Physics 90(2) (2016) 131-138.
[189] C.Y. Kim, T. Sekino, Y. Yamamoto, K. Niihara, The synthesis of lead-free ferroelectric $Bi_{1/2}Na_{1/2}TiO_3$ thin film by solution-sol-gel method, J Sol-Gel Sci Techn 33(3) (2005) 307-314.
[190] T. Yu, K.W. Kwok, H.L.W. Chan, The Synthesis of Lead-Free Ferroelectric $Bi_{0.5}Na_{0.5}TiO_3$-$Bi_{0.5}K_{0.5}TiO_3$ Thin Films by Sol-Gel Method, Mater Lett 61(10) (2007) 2117-2120.
[191] Z.H. Zhou, J.M. Xue, W.Z. Li, J. Wang, H. Zhu, J.M. Miao, Ferroelectric and electrical behavior of $(Na_{0.5}Bi_{0.5})TiO_3$ thin films, Applied Physics Letters 85(5) (2004) 804-806.
[192] M. Bousquet, J.R. Duclere, B. Gautier, A. Boulle, A. Wu, S. Deputier, D. Fasquelle, F. Remondiere, D. Albertini, C. Champeaux, P. Marchet, M. Guilloux-Viry, P. Vilarinho, Electrical Properties of (110) Epitaxial Lead-Free Ferroelectric $Na_{0.5}Bi_{0.5}TiO_3$ Thin Films Grown by Pulsed Laser Deposition: Macroscopic and Nanoscale Data, Journal of Applied Physics 111(10) (2012).
[193] X.G. Tang, J. Wang, X.X. Wang, H.L.W. Chan, Preparation and Electrical Properties of Highly (111)-oriented $(Na_{0.5}Bi_{0.5})TiO_3$ Thin Films by a Sol-Gel Process, Chemistry of Materials 16(25) (2004) 5293-5296.
[194] T. Yu, K.W. Kwok, H.L.W. Chan, Preparation and Properties of Sol-Gel-derived $Bi_{0.5}Na_{0.5}TiO_3$ Lead-Free Ferroelectric Thin Film, Thin Solid Films 515(7-8) (2007) 3563-3566.
[195] X.-G. Tang, J. Wang, X.-X. Wang, H.L.-W. Chan, Preparation and Electrical Properties of Highly (111)-Oriented $(Na_{0.5}Bi_{0.5})TiO_3$ Thin Films by a Sol−Gel Process, Chemistry of Materials 16(25) (2004) 5293-5296.
[196] M.B. González, A. Wu, P.M. Vilarinho, Influence of Solvents on the Microstructure and Dielectric Properties of $Ba_{0.5}Sr_{0.5}TiO_3$ Thin Films Prepared by a Diol-Based Sol−Gel Process, Chemistry of Materials 18(7) (2006) 1737-1744.
[197] N. Izyumskaya, Y.I. Alivov, S.J. Cho, H. Morkoç, H. Lee, Y.S. Kang, Processing, Structure, Properties, and Applications of PZT Thin Films, Critical Reviews in Solid State and Materials Sciences 32(3-4) (2007) 111-202.
[198] Q. Yu, J.-F. Li, Y. Chen, L.-Q. Cheng, W. Sun, Z. Zhou, Z. Wang, Effect of Pyrolysis Temperature on Sol–Gel Synthesis of Lead-free Piezoelectric $(K,Na)NbO_3$ Films on $Nb:SrTiO_3$ Substrates, Journal of the American Ceramic Society 97(1) (2014) 107-113.
[199] U. Hasenkox, S. Hoffmann, R. Waser, Influence of Precursor Chemistry on the Formation of $MTiO_3$ (M = Ba, Sr) Ceramic Thin Films, J Sol-Gel Sci Techn 12(2) (1998) 67-79.
[200] S. Halder, T. Schneller, R. Waser, Crystallization Temperature Limit of $(Ba,Sr)TiO_3$ Thin Films Prepared by a Non Oxocarbonate Phase Forming CSD Route, J Sol-Gel Sci Techn 33(3) (2005) 299-306.

[201] A. Wu, P.M. Vilarinho, I. Reaney, I.M. Miranda Salvado, Early Stages of Crystallization of Sol−Gel-Derived Lead Zirconate Titanate Thin Films, Chemistry of Materials 15(5) (2003) 1147-1155.
[202] Z. Huang, Q. Zhang, R.W. Whatmore, The Role of an Intermetallic Phase on the Crystallization of Lead Zirconate Titanate in Sol-Gel Process, J. Mater. Sci. Lett. 17(14) (1998) 1157-1159.
[203] T. Kijima, H. Ishiwara, Si-substituted Ultrathin Ferroelectric Films, Jpn J Appl Phys 2 41(6B) (2002) L716-L719.
[204] W. Zhiqiang, Y. Kaoru, O. Masanori, Preparation of $Pb(Zr_{0.52}TiO_{0.48})O_3$ Thin Films at Low-Temperature of Less than 400°C by Hydrothermal Treatment Following Sol-Gel Deposition, Japanese Journal of Applied Physics 40(9S) (2001) 5539.
[205] J. Xu, J. Zhai, X. Yao, Structure and dielectric properties of barium titanate thin films grown by sol-gel-hydrothermal process, Applied Physics Letters 89(25) (2006) 252902.
[206] R.Z. Hou, A. Wu, P.M. Vilarinho, Low-Temperature Hydrothermal Deposition of $(Ba_xSr_{1-x})TiO_3$ Thin Films on Flexible Polymeric Substrates for Embedded Applications, Chemistry of Materials 21(7) (2009) 1214-1220.
[207] I. Bretos, R. Jiménez, D. Pérez-Mezcua, N. Salazar, J. Ricote, M.L. Calzada, Low-Temperature Liquid Precursors of Crystalline Metal Oxides Assisted by Heterogeneous Photocatalysis, Advanced Materials 27(16) (2015) 2608-2613.
[208] C.K. Barlingay, S.K. Dey, Rapid Thermal Processing and Properties of Sol-Gel Derived Ferroelectric Thin-Films for Non-Volatile Memories, MRS Proceedings 224 (1991).
[209] Z. Wu, R. Pascual, C.V.R. Vasant Kumar, D. Amd, M. Sayer, Rapid Thermal Processing of Ferroelectric Thin Films, MRS Proceedings 224 (1991).
[210] E.K.F. Dang, R.J. Gooding, Theory of the Effects of Rapid Thermal Annealing on Thin-Film Crystallization, Physical Review Letters 74(19) (1995) 3848-3851.
[211] G. González-Aguilar, I.M. Miranda Salvado, M.E. Costa, Rapid thermal annealing and conventional furnace effect on $SrBi_2Ta_2O_9$ thin films crystallization, Thin Solid Films 517(19) (2009) 5728-5733.
[212] E.B. Araújo, J.A. Eiras, Effects of crystallization conditions on dielectric and ferroelectric properties of PZT thin films, Journal of Physics D: Applied Physics 36(16) (2003) 2010.
[213] S.D. Russell, D.A. Sexton, Method of Laser Processing Ferroelectric Materials The United Stated of America as represented by the Secretary of the Navy (Washington, DC) USA, 1994.
[214] Z.J. Wang, H. Kokawa, H. Takizawa, M. Ichiki, R. Maeda, Low-temperature growth of high-quality lead zirconate titanate thin films by 28 GHz microwave irradiation, Applied Physics Letters 86(21) (2005) 212903.
[215] Y.-H. Lee, J.-M. Wu, Y.-L. Chueh, L.-J. Chou, Low-temperature growth and interface characterization of $BiFeO_3$ thin films with reduced leakage current, Applied Physics Letters 87(17) (2005) 172901.
[216] S. Maekawa, T. Ohishi, Evaluation of SiO_2 Thin Films Prepared by Sol-Gel Method Using Photoirradiation, Journal of Non-Crystalline Solids 169(1-2) (1994) 207-209.
[217] J.J. Yu, Formation of High-Quality Advanced High-k Oxide Layers at Low Temperature by Excimer UV Lamp-Assisted Photo-CVD and Sol-Gel Processing, Chemical Research in Chinese Universities 20(4) (2004) 396-402.
[218] Y. Nakao, T. Nakamura, A. Kamisawa, H. Takasu, N. Soyama, G. Sasaki, T. Atsuki, T. Yonezawa, K. Ogi, Electrical Properties of PZT Thin Films Derived from Sol-Gel Solution Containing Photo-Sensitive Water-Generater, Applications of Ferroelectrics, 1994.ISAF '94., Proceedings of the Ninth IEEE International Symposium on, 1994, pp. 450-453.
[219] H. Uchida, N. Soyama, K. Kageyama, K. Ogi, M.G. Scott, J.D. Cuchiaro, L.D. McMillan, C.A. Paz De Araujo, Characterization of Self-Patterned SBT/SBNT Thin Films from Photo-Sensitive Solutions, Integrated Ferroelectrics 18(1-4) (1998) 249-261.
[220] M. Azuma, L.D. McMillan, C.A. Paz De Araujo, M.C. Scott, UV Radiation Process for Making Electronic Devices having Low-Leakage-Current and Low-Polarization Fatigue, EP 0489519A2, US, 1999.

[221] H. Uchida, N. Soyama, K. Kageyama, K. Ogi, M.C. Scott, L.D. McMillan, C.A. Paz de Araujo, Shelf-Stable Liquid Metal Arylketone Alcoholate Solutions and Use Thereof in Photoinitiated Patterning of Thin Films, US 4880770, US, 1999.
[222] M.L. Calzada, I. Bretos, R. Jiménez, H. Guillon, L. Pardo, Low-Temperature Processing of Ferroelectric Thin Films Compatible with Silicon Integrated Circuit Technology, Advanced Materials 16(18) (2004) 1620-1624.
[223] Y. Zhang, R.H. Terrill, P.W. Bohn, Ultraviolet Photochemistry and ex Situ Ozonolysis of Alkanethiol Self-Assembled Monolayers on Gold, Chemistry of Materials 11(8) (1999) 2191-2198.
[224] I.W. Boyd, J.-Y. Zhang, Photo-induced growth of dielectrics with excimer lamps, Solid-State Electronics 45(8) (2001) 1413-1431.
[225] L. Pardo, R. Poyato, A. González, M.L. Calzada, E. Lynch, S. O'Brien, P.V. Kelly, I. Stolichnov, H. Guillon, Ca and La-Modified Lead Titanate Sol-Gel Thin Films by UV-Assisted Processing for Piezoelectric Sensors, Ferroelectrics 267(1) (2002) 335-340.
[226] M.L. Calzada, I. Bretos, R. Jiménez, H. Guillon, J. Ricote, L. Pardo, Low-Temperature Ultraviolet Sol-Gel Photoannealing Processing of Multifunctional Lead-Titanate-Based Thin Films, Journal of Materials Research 22(07) (2007) 1824-1833.
[227] I. Bretos, R. Jiménez, E. Rodriguez-Castellón, J. García-López, M.L. Calzada, Heterostructure and Compositional Depth Profile of Low-Temperature Processed Lead Titanate-Based Ferroelectric Thin Films Prepared by Photochemical Solution Deposition, Chemistry of Materials 20(4) (2008) 1443-1450.
[228] I.i. Bretos, R. Jiménez, J. Garcïa-López, L. Pardo, M.L. Calzada, Photochemical Solution Deposition of Lead-Based Ferroelectric Films: Avoiding the PbO-Excess Addition at Last, Chemistry of Materials 20(18) (2008) 5731-5733.
[229] A. Wu, G. Gonzalez-Aguilar, P.M. Vilarinho, I.M. Miranda Salvado, M.E.V. Costa, Comparing macroscopic and microscopic properties of seeded ferroelectric thin films, J Electroceram 21(1-4) (2008) 193-197.
[230] T. Schneller, R. Waser, M. Kosec, D. Payne, Chemical Solution Deposition of Functional Oxide Thin Films, Springer Vienna2014.
[231] M. Yoshimura, H. Suda, Hydrothermal processing of hydroxyapatite: past, present, and future, in: P.W. Brown, B. Constantz (Eds.), Hydroxyapatite and Related Materials, CRC Press, Inc., Boca Raton, FL, 1994, pp. 45-72.
[232] K. Byrappa, M. Yoshimura, Handbook of Hydrothermal Technology, Elsevier Science2008.
[233] Y. Wang, G. Xu, Z. Ren, X. Wei, W. Weng, P. Du, G. Shen, G. Han, Low temperature polymer assisted hydrothermal synthesis of bismuth ferrite nanoparticles, Ceramics International 34(6) (2008) 1569-1571.
[234] B. Malič, A. Kupec, M. Kosec†, Thermal Analysis, in: T. Schneller, R. Waser, M. Kosec, D. Payne (Eds.), Chemical Solution Deposition of Functional Oxide Thin Films, Springer Vienna2013, pp. 163-179.
[235] P.N. Gibson, Grazing Incidence X-Ray Methods for Near-Surface Structural Studies, Surface and Thin Film Analysis, Wiley-VCH Verlag GmbH & Co. KGaA2011, pp. 311-327.
[236] U. Welzel, J. Ligot, P. Lamparter, A.C. Vermeulen, E.J. Mittemeijer, Stress analysis of polycrystalline thin films and surface regions by X-ray diffraction, Journal of Applied Crystallography 38(1) (2005) 1-29.
[237] J. Liu, High-Resolution Scanning Electron Microscopy, in: N. Yao, Z. Wang (Eds.), Handbook of Microscopy for Nanotechnology, Springer US2005, pp. 325-359.
[238] D.B. Williams, C.B. Carter, The Transmission Electron Microscope, in: D.B. Williams, C.B. Carter (Eds.), Transmission Electron Microscopy, Springer US2009, pp. 3-22.
[239] B. Fultz, J.M. Howe, The TEM and its Optics, in: B. Fultz, J.M. Howe (Eds.), Transmission Electron Microscopy and Diffractometry of Materials, Springer Berlin Heidelberg2008, pp. 61-118.
[240] D.B. Williams, C.B. Carter, Transmission Electron Microscopy: A Textbook for Materials Science, Springer2009.

[241] D.G. Stroppa, L.F. Zagonel, L.A. Montoro, E.R. Leite, A.J. Ramirez, High-Resolution Scanning Transmission Electron Microscopy (HRSTEM) Techniques: High-Resolution Imaging and Spectroscopy Side by Side, ChemPhysChem 13(2) (2012) 437-443.
[242] S. Hillyard, J. Silcox, Detector geometry, thermal diffuse scattering and strain effects in ADF STEM imaging, Ultramicroscopy 58(1) (1995) 6-17.
[243] D.B. Williams, C.B. Carter, Specimen Preparation, Transmission Electron Microscopy, Springer US2009, pp. 173-193.
[244] R.F. Egerton, TEM Specimens and Images, in: R.F. Egerton (Ed.), Physical Principles of Electron Microscopy, Springer US2005, pp. 93-124.
[245] J. Ayache, L. Beaunier, J. Boumendil, G. Ehret, D. Laub, Thinning Preparation Techniques, Sample Preparation Handbook for Transmission Electron Microscopy, Springer New York2010, pp. 107-152.
[246] E. Smith, G. Dent, Introduction, Basic Theory and Principles, Modern Raman Spectroscopy – A Practical Approach, John Wiley & Sons, Ltd2005, pp. 1-21.
[247] E. Smith, G. Dent, The Raman Experiment – Raman Instrumentation, Sample Presentation, Data Handling and Practical Aspects of Interpretation, Modern Raman Spectroscopy – A Practical Approach, John Wiley & Sons, Ltd2005, pp. 23-70.
[248] T. Owen, Fundamentals of modern UV-visible spectroscopy Agilent Technologies, Germany, 2000.
[249] N. Balke, I. Bdikin, S.V. Kalinin, A.L. Kholkin, Electromechanical Imaging and Spectroscopy of Ferroelectric and Piezoelectric Materials: State of the Art and Prospects for the Future, Journal of the American Ceramic Society 92(8) (2009) 1629-1647.
[250] A.L. Kholkin, S.V. Kalinin, A. Roelofs, A. Gruverman, Review of Ferroelectric Domain Imaging by Piezoresponse Force Microscopy, in: S. Kalinin, A. Gruverman (Eds.), Scanning Probe Microscopy: Electrical and Electromechanical Phenomena at the Nanoscale, Springer New York, New York, NY, 2007, pp. 173-214.
[251] D. Denning, J. Guyonnet, B.J. Rodriguez, Applications of piezoresponse force microscopy in materials research: from inorganic ferroelectrics to biopiezoelectrics and beyond, International Materials Reviews 61(1) (2016) 46-70.
[252] E. Soergel, Piezoresponse force microscopy (PFM), Journal of Physics D: Applied Physics 44(46) (2011) 464003.
[253] Utilization Manual, Coulter, 1997.
[254] S. Foner, Versatile and Sensitive Vibrating-Sample Magnetometer, Review of Scientific Instruments 30(7) (1959) 548-557.
[255] H. Zhang, P. Xu, E. Patterson, J. Zang, S. Jiang, J. Rödel, Preparation and enhanced electrical properties of grain-oriented $(Bi_{1/2}Na_{1/2})TiO_3$-based lead-free incipient piezoceramics, Journal of the European Ceramic Society 35(9) (2015) 2501-2512.
[256] G.O. Jones, P.A. Thomas, The tetragonal phase of $Na_{0.5}Bi_{0.5}TiO_3$ - A new variant of the perovskite structure, Acta Crystallographica Section B: Structural Science 56(3) (2000) 426-430.
[257] G.O. Jones, P.A. Thomas, Investigation of the structure and phase transitions in the novel A-site substituted distorted perovskite compound $Na_{0.5}Bi_{0.5}TiO_3$, Acta Crystallographica Section B 58(2) (2002) 168-178.
[258] K. Roleder, I. Franke, A.M. Glazer, P.A. Thomas, S. Miga, J. Suchanicz, The piezoelectric effect in $Na_{0.5}Bi_{0.5}TiO_3$ ceramics, Journal of Physics Condensed Matter 14(21) (2002) 5399-5406.
[259] J. Suchanicz, I.P. Mercurio, P. Marchet, T.V. Kruzina, Axial pressure influence on dielectric and ferroelectric properties of $Na_{0.5}Bi_{0.5}TiO_3$ ceramic, Physica Status Solidi (B) Basic Research 225(2) (2001) 459-466.
[260] C.H. Yang, Z. Wang, Q.X. Li, J.H. Wang, Y.G. Yang, S.L. Gu, D.M. Yang, J.R. Han, Properties of $Na_{0.5}Bi_{0.5}TiO_3$ ferroelectric films prepared by chemical solution decomposition, Journal of Crystal Growth 284(1–2) (2005) 136-141.
[261] Z.H. Zhou, J.M. Xue, W.Z. Li, J. Wang, H. Zhu, J.M. Miao, Leakage current and charge carriers in $(Na_{0.5}Bi_{0.5})TiO_3$ thin film, Journal of Physics D: Applied Physics 38(4) (2005) 642.

[262] M. Bousquet, J.-R. Duclère, C. Champeaux, A. Boulle, P. Marchet, A. Catherinot, A. Wu, P.M. Vilarinho, S. Députier, M. Guilloux-Viry, A. Crunteanu, B. Gautier, D. Albertini, C. Bachelet, Macroscopic and nanoscale electrical properties of pulsed laser deposited (100) epitaxial lead-free $Na_{0.5}Bi_{0.5}TiO_3$ thin films, Journal of Applied Physics 107(3) (2010) 034102.
[263] M. Bousquet, J.-R. Duclère, B. Gautier, A. Boulle, A. Wu, S. Députier, D. Fasquelle, F. Rémondière, D. Albertini, C. Champeaux, P. Marchet, M. Guilloux-Viry, P. Vilarinho, Electrical properties of (110) epitaxial lead-free ferroelectric $Na_{0.5}Bi_{0.5}TiO_3$ thin films grown by pulsed laser deposition: Macroscopic and nanoscale data, Journal of Applied Physics 111(10) (2012) 104106.
[264] F. Rémondière, A. Wu, P.M. Vilarinho, J.P. Mercurio, Piezoforce microscopy study of lead-free perovskite $Na_{0.5}Bi_{0.5}TiO_3$ thin films, Applied Physics Letters 90(15) (2007) 152905.
[265] F. Rémondière, B. Malič, M. Kosec, J.-P. Mercurio, Synthesis and crystallization pathway of $Na_{0.5}Bi_{0.5}TiO_3$ thin film obtained by a modified sol–gel route, Journal of the European Ceramic Society 27(13–15) (2007) 4363-4366.
[266] S. Kumar, G.L. Messing, W.B. White, Metal Organic Resin Derived Barium Titanate: I, Formation of Barium Titanium Oxycarbonate Intermediate, Journal of the American Ceramic Society 76(3) (1993) 617-624.
[267] A. Li, D. Wu, H. Ling, T. Yu, M. Wang, X. Yin, Z. Liu, N. Ming, Effects of processing on the characteristics of $SrBi_2Ta_2O_9$ films prepared by metalorganic decomposition, Journal of Applied Physics 88(2) (2000) 1035-1041.
[268] S. Gorfman, D.S. Keeble, A. Bombardi, P.A. Thomas, Topology and temperature dependence of the diffuse X-ray scattering in $Na_{0.5}Bi_{0.5}TiO_3$ ferroelectric single crystals, Journal of Applied Crystallography 48(5) (2015) 1543-1550.
[269] S.K. Singh, H. Ishiwara, K. Maruyama, Enhanced polarization and reduced leakage current in $BiFeO_3$ thin films fabricated by chemical solution deposition, Journal of Applied Physics 100(6) (2006) 064102.
[270] M. Beihai, L. Shanshan, T. Sheng, N. Manoj, E.K. Rachel, H. Zhongqiang, B. Uthamalingam, Residual stress of $(Pb_{0.92}La_{0.08})(Zr_{0.52}Ti_{0.48})O_3$ films grown by a sol–gel process, Smart Materials and Structures 22(5) (2013) 055019.
[271] L. Pardo, E. Mercadelli, A. Garcia, K. Brebol, C. Galassi, Field-induced phase transition and relaxor character in submicrometer-structured lead-free $(Bi_{0.5}Na_{0.5})_{0.94}Ba_{0.06}TiO_3$ piezoceramics at the morphotropic phase boundary, IEEE Transactions on Ultrasonics, Ferroelectrics, and Frequency Control 58(9) (2011) 1893-1904.
[272] Y. Xu, J.D. Mackenzie, Ferroelectric thin films prepared by sol-gel processing, Integrated Ferroelectrics 1(1) (1992) 17-42.
[273] L. Jin, F. Li, S. Zhang, Decoding the Fingerprint of Ferroelectric Loops: Comprehension of the Material Properties and Structures, Journal of the American Ceramic Society 97(1) (2014) 1-27.
[274] A.S. Daryapurkar, J.T. Kolte, P.R. Apte, P. Gopalan, Structural and electrical properties of sodium bismuth titanate ($Na_{0.5}Bi_{0.5}TiO_3$) thin films optimized using the Taguchi approach, Ceramics International 40(1, Part B) (2014) 2441-2450.
[275] J. Xu, Y. Liu, R.L. Withers, F. Brink, H. Yang, M. Wang, Ferroelectric and non-linear dielectric characteristics of $Bi_{0.5}Na_{0.5}TiO_3$ thin films deposited via a metallorganic decomposition process, Journal of Applied Physics 104(11) (2008) 116101.
[276] T. Yu, K.W. Kwok, H.L.W. Chan, Preparation and properties of sol–gel-derived $Bi_{0.5}Na_{0.5}TiO_3$ lead-free ferroelectric thin film, Thin Solid Films 515(7–8) (2007) 3563-3566.
[277] R. Ramesh, N.A. Spaldin, Multiferroics: progress and prospects in thin films, Nat Mater 6(1) (2007) 21-29.
[278] B.C. Jeon, D. Lee, M.H. Lee, S.M. Yang, S.C. Chae, T.K. Song, S.D. Bu, J.-S. Chung, J.-G. Yoon, T.W. Noh, Flexoelectric Effect in the Reversal of Self-Polarization and Associated Changes in the Electronic Functional Properties of $BiFeO_3$ Thin Films, Advanced Materials 25(39) (2013) 5643-5649.

[279] S. Iakovlev, C.-H. Solterbeck, M. Kuhnke, M. Es-Souni, Multiferroic $BiFeO_3$ thin films processed via chemical solution deposition: Structural and electrical characterization, Journal of Applied Physics 97(9) (2005) 094901.
[280] J. Mendiola, M.L. Calzada, P. Ramos, M.J. Martin, F. Agulló-Rueda, On the effects of stresses in ferroelectric (Pb,Ca)TiO_3 thin films, Thin Solid Films 315(1–2) (1998) 195-201.
[281] A. Lahmar, K. Zhao, S. Habouti, M. Dietze, C.H. Solterbeck, M. Es-Souni, Off-stoichiometry effects on $BiFeO_3$ thin films, Solid State Ionics 202(1) (2011) 1-5.
[282] D. Khomskii, Classifying multiferroics: Mechanisms and effects, Physics 2 (2009) 20.
[283] G.D. Achenbach, W.J. James, R. Gerson, Preparation of Single-Phase Polycrystalline $BiFeO_3$, Journal of the American Ceramic Society 50(8) (1967) 437-437.
[284] M. Murakami, S. Fujino, S.-H. Lim, L.G. Salamanca-Riba, M. Wuttig, I. Takeuchi, B. Varughese, H. Sugaya, T. Hasegawa, S.E. Lofland, Microstructure and phase control in Bi–Fe–O multiferroic nanocomposite thin films, Applied Physics Letters 88(11) (2006) 112505.
[285] H. Zhang, I.M. Reaney, D.M. Marincel, S. Trolier-McKinstry, Q.M. Ramasse, I. MacLaren, S.D. Findlay, R.D. Fraleigh, I.M. Ross, S. Hu, W. Ren, W. Mark Rainforth, Stabilisation of Fe_2O_3-rich Perovskite Nanophase in Epitaxial Rare-earth Doped $BiFeO_3$ Films, Scientific Reports 5 (2015) 13066.
[286] F. Tyholdt, H. Fjellvåg, A.E. Gunnæs, A. Olsen, Synthesis of epitaxial $BiFeO_3$ films by chemical solution deposition on Pt(100), Journal of Applied Physics 102(7) (2007) 074108.
[287] C.U. Pinnow, I. Kasko, N. Nagel, T. Mikolajick, C. Dehm, F. Jahnel, M. Seibt, U. Geyer, K. Samwer, Oxygen tracer diffusion in IrO_2 barrier films, Journal of Applied Physics 91(3) (2002) 1707-1709.
[288] A.K. Tagantsev, I. Stolichnov, E.L. Colla, N. Setter, Polarization fatigue in ferroelectric films: Basic experimental findings, phenomenological scenarios, and microscopic features, Journal of Applied Physics 90(3) (2001) 1387-1402.
[289] J. Xiao, A. Wu, P.M. Vilarinho, A.R. Ramos, E. Alves, Electrical properties of sol-gel derived MPB 0.37$BiScO_3$-0.63$PbTiO_3$ thin films deposited on iridium oxide electrodes, J Mater Chem 19(31) (2009) 5572-5579.
[290] K.H. Yoon, J.-H. Sohn, B.D. Lee, D.H. Kang, Effect of $LaNiO_3$ interlayer on dielectric properties of $(Ba_{0.5}Sr_{0.5})TiO_3$ thin films deposited on differently oriented Pt electrodes, Applied Physics Letters 81(26) (2002) 5012-5014.
[291] Z.X. Cheng, X.L. Wang, H. Kimura, K. Ozawa, S.X. Dou, La and Nb codoped $BiFeO_3$ multiferroic thin films on $LaNiO_3$/Si and IrO_2/Si substrates, Applied Physics Letters 92(9) (2008) 092902.
[292] A.H.M. Gonzalez, A.Z. Simões, L.S. Cavalcante, E. Longo, J.A. Varela, C.S. Riccardi, Soft Chemical Deposition of $BiFeO_3$ Multiferroic Thin Films, Applied Physics Letters 90(5) (2007).
[293] T. Sun, H. Hu, Z. Pan, X. Li, J. Wang, V.P. Dravid, In situ real-time investigation of kinetics of nucleation and growth of sol-gel-derived functional oxide thin films, Physical Review B 77(20) (2008) 205414.
[294] P. Muralt, Texture control and seeded nucleation of nanosize structures of ferroelectric thin films, Journal of Applied Physics 100(5) (2006) 051605.
[295] R.W. Schwartz, P.G. Clem, J.A. Voigt, E.R. Byhoff, M. Van Stry, T.J. Headley, N.A. Missert, Control of Microstructure and Orientation in Solution-Deposited $BaTiO_3$ and $SrTiO_3$ Thin Films, Journal of the American Ceramic Society 82(9) (1999) 2359-2367.
[296] Y. Bastani, N. Bassiri-Gharb, Processing Optimization of Lead Magnesium Niobate-Lead Titanate Thin Films for Piezoelectric MEMS Application, Journal of the American Ceramic Society 95(4) (2012) 1269-1275.
[297] S. Yakovlev, J. Zekonyte, C.H. Solterbeck, M. Es-Souni, Interfacial effects on the electrical properties of multiferroic $BiFeO_3$/Pt/Si thin film heterostructures, Thin Solid Films 493(1–2) (2005) 24-29.

[298] Y.P. Zhao, G.C. Wang, T.M. Lu, G. Palasantzas, J.T.M. De Hosson, Surface-roughness effect on capacitance and leakage current of an insulating film, Physical Review B 60(12) (1999) 9157-9164.
[299] K.K. Maurya, S.K. Halder, S. Sen, A. Bose, S. Bysakh, High resolution X-ray and electron microscopy characterization of PZT thin films prepared by RF magnetron sputtering, Applied Surface Science 313 (2014) 196-206.
[300] F. Spaepen, Interfaces and stresses in thin films, Acta Materialia 48(1) (2000) 31-42.
[301] S. Lu, C. Zuo, H. Zeng, W. Huang, H. Ji, Residual stress and structure characteristics in PZT ferroelectric thin films annealed at different ramp rates, Mater Lett 60(2) (2006) 255-260.
[302] G. Bayer, H.G. Wiedemann, Formation, dissociation and expansion behavior of platinum group metal oxides (PdO, RuO_2, IrO_2), Thermochimica Acta 11(1) (1975) 79-88.
[303] B.H. Kim, J.H. An, K.S. Hwang, Surface observation of $LaNiO_3$/MgO (100) structure, J Mater Sci 41(7) (2006) 2165-2166.
[304] S.R. Das, P. Bhattacharya, R.N.P. Choudhary, R.S. Katiyar, Effect of La substitution on structural and electrical properties of $BiFeO_3$ thin film, Journal of Applied Physics 99(6) (2006) 066107.
[305] S.K. Singh, H. Ishiwara, K. Sato, K. Maruyama, Microstructure and frequency dependent electrical properties of Mn-substituted $BiFeO_3$ thin films, Journal of Applied Physics 102(9) (2007) 094109.
[306] N.M. Murari, A. Kumar, R. Thomas, R.S. Katiyar, Reduced leakage current in chemical solution deposited multiferroic $BiFeO_3/Ba_{0.25}Sr_{0.75}TiO_3$ heterostructured thin films on platinized silicon substrates, Applied Physics Letters 92(13) (2008) 132904.
[307] N.M. Murari, R. Thomas, R.E. Melgarejo, S.P. Pavunny, R.S. Katiyar, Structural, electrical, and magnetic properties of chemical solution deposited $BiFe_{1-x}Ti_xO_3$ and $BiFe_{0.9}Ti_{0.05}Co_{0.05}O_3$ thin films, Journal of Applied Physics 106(1) (2009) 014103.
[308] N.M. Murari, R. Thomas, S.P. Pavunny, J.R. Calzada, R.S. Katiyar, $DyScO_3$ buffer layer for a performing metal-ferroelectric-insulator-semiconductor structure with multiferroic $BiFeO_3$ thin film, Applied Physics Letters 94(14) (2009) 142907.
[309] N.M. Murari, R. Thomas, A. Winterman, R.E. Melgarejo, S.P. Pavunny, R.S. Katiyar, Structural, electrical, and magnetic properties of chemical solution deposited $Bi(Fe_{0.95}Cr_{0.05})O_3$ thin films on platinized silicon substrates, Journal of Applied Physics 105(8) (2009) 084110.
[310] T. Reji, J.F. Scott, N.B. Dwarka, S.K. Ram, Multiferroic thin-film integration onto semiconductor devices, Journal of Physics: Condensed Matter 22(42) (2010) 423201.
[311] J. Wu, J. Wang, D. Xiao, J. Zhu, Ferroelectric Behavior in Bismuth Ferrite Thin Films of Different Thickness, ACS Applied Materials & Interfaces 3(9) (2011) 3261-3263.
[312] W. Liu, G. Tan, G. Dong, X. Yan, W. Ye, H. Ren, A. Xia, Structure transition and multiferroic properties of Mn-doped $BiFeO_3$ thin films, Journal of Materials Science: Materials in Electronics 25(2) (2014) 723-729.
[313] H. Liu, Y. Sun, Substantially enhanced ferroelectricity in Ti doped $BiFeO_3$ films, Journal of Physics D: Applied Physics 40(23) (2007) 7530.
[314] F. Huang, X. Lu, W. Lin, Y. Kan, J. Zhang, Q. Chen, Z. Wang, L. Li, J. Zhu, Thickness-dependent structural and magnetic properties of $BiFeO_3$ films prepared by metal organic decomposition method, Applied Physics Letters 97(22) (2010) 222901.
[315] X. Tang, J. Dai, X. Zhu, J. Lin, Q. Chang, D. Wu, W. Song, Y. Sun, Thickness-Dependent Dielectric, Ferroelectric, and Magnetodielectric Properties of $BiFeO_3$ Thin Films Derived by Chemical Solution Deposition, Journal of the American Ceramic Society 95(2) (2012) 538-544.
[316] K. Jeong Hwan, F. Hiroshi, I. Hiroshi, Comparison of Ferroelectric and Insulating Properties of Mn-Doped $BiFeO_3$ Films Formed on Pt, $SrRuO_3$/Pt, and $LaNiO_3$/Pt Bottom Electrodes by Radio-Frequency Sputtering, Japanese Journal of Applied Physics 50(5R) (2011) 051501.
[317] M. Tomczyk, D.G. Stroppa, I.M. Reaney, P.M. Vilarinho, The role of electrodes in the growth of $BiFeO_3$ thin films by chemical solution deposition, Physical Chemistry Chemical Physics (accepted April 2017) (2017).

[318] L. Jin, X. Tang, R. Wei, B. Yang, J. Yang, W. Song, J. Dai, X. Zhu, Y. Sun, $BiFeO_3$(00l)/$LaNiO_3$/Si thin films with enhanced polarization: an all-solution approach, RSC Advances 6(82) (2016) 78629-78635.
[319] A. Perez-Rivero, M. Tomczyk, R. Jimenez, I. Bretos, J. Ricote, P. Vilarinho, M.L. Calzada, Polarization switching at room temperature of undoped $BiFeO_3$ thin films crystallized at temperatures between $400 \leq T \leq 500°C$, Journal of Materials Science: Matererials in Electronics 26 (2015) 9373-9386.
[320] M.K. Singh, H.M. Jang, S. Ryu, M.-H. Jo, Polarized Raman scattering of multiferroic $BiFeO_3$ epitaxial films with rhombohedral R3c symmetry, Applied Physics Letters 88(4) (2006) 042907.
[321] H. Fukumura, S. Matsui, H. Harima, T. Takahashi, T. Itoh, K. Kisoda, M. Tamada, Y. Noguchi, M. Miyayama, Observation of phonons in multiferroic $BiFeO_3$ single crystals by Raman scattering, Journal of Physics: Condensed Matter 19(36) (2007) 365224.
[322] Y. Yang, J.Y. Sun, K. Zhu, Y.L. Liu, L. Wan, Structure properties of $BiFeO_3$ films studied by micro-Raman scattering, Journal of Applied Physics 103(9) (2008).
[323] S.K. Streiffer, C. Basceri, C.B. Parker, S.E. Lash, A.I. Kingon, Ferroelectricity in thin films: The dielectric response of fiber-textured $(Ba_xSr_{1-x})Ti_{1+y}O_{3+z}$ thin films grown by chemical vapor deposition, Journal of Applied Physics 86(8) (1999) 4565-4575.
[324] S. Dutta, A. Pandey, O.P. Thakur, R. Pal, R. Chatterjee, Estimation of residual stress in $Pb(Zr_{0.52}Ti_{0.48})O_3/BiFeO_3$ multilayers deposited on silicon, Journal of Applied Physics 114(17) (2013) 174103.
[325] M.K. Singh, W. Prellier, M.P. Singh, R.S. Katiyar, J.F. Scott, Spin-glass transition in single-crystal $BiFeO_3$, Physical Review B 77(14) (2008) 144403.
[326] C.-S. Park, J.-W. Lee, G.-T. Park, H.-E. Kim, J.-J. Choi, Microstructural evolution and piezoelectric properties of thick $Pb(Zr,Ti)O_3$ films deposited by multi-sputtering method: Part I. Microstructural evolution, Journal of Materials Research 22(5) (2007) 1367-1372.
[327] J.B. Neaton, C. Ederer, U.V. Waghmare, N.A. Spaldin, K.M. Rabe, First-principles study of spontaneous polarization in multiferroic $BiFeO_3$, Physical Review B 71(1) (2005) 014113.
[328] M. Dawber, K.M. Rabe, J.F. Scott, Physics of thin-film ferroelectric oxides, Reviews of Modern Physics 77(4) (2005) 1083-1130.
[329] Masruroh, M. Toda, Asymmetric Hysteresis Loops, Leakage Current and Capacitance Voltage Behaviors in Ferroelectric PZT Films Deposited on a $Pt/Al_2O_3/SiO_2/Si$ Substrate by MOCVD method with a vapor-deposited Gold Top Electrode, International Journal of Applied Physics and Mathematics 1(2) (2011) 144-148.
[330] F. Yan, I. Sterianou, S. Miao, I.M. Reaney, M.O. Lai, L. Lu, Multiferroic properties of $Bi(Fe_{0.5}Sc_{0.5})O_3$ –$PbTiO_3$ thin films, Physica Scripta 2010(T139) (2010) 014003.
[331] J.M. Bernhard, Work Function Study of Iridium Oxide and Molybdenum Using UPS and Simultaneous Fowler-Nordheim I-V Plots with Field Emission Energy Distributions, University of North Texas, Denton, Texas, 1999.
[332] S. Hussain, S.K. Hasanain, G. Hassnain Jaffari, S. Ismat Shah, Thickness dependent magnetic and ferroelectric properties of $LaNiO_3$ buffered $BiFeO_3$ thin films, Current Applied Physics 15(3) (2015) 194-200.
[333] D.P. Vijay, S.B. Desu, Electrodes for $PbZr_xTi_{1-x}O_3$ Ferroelectric Thin Films, Journal of The Electrochemical Society 140(9) (1993) 2640-2645.
[334] X. Wang, B. Yan, Z. Dai, M. Liu, S. Xu, W. Li, H. Liu, Effect of annealing temperature on the ferroelectric properties of $BiFeO_3$ thin films prepared by sol-gel process, Journal of Wuhan University of Technology-Mater. Sci. Ed. 25(3) (2010) 384-387.
[335] P.M. Vilarinho, A. Wu, M.L. Calzada, R. Jimenez Rioboo, I. Bretos, Method for the preparation at low temperatures of ferroelectric thin films, the ferroelectric thin films thus obtained and their applications, 2013.
[336] A. Nathan, A. Ahnood, M.T. Cole, S. Lee, Y. Suzuki, P. Hiralal, F. Bonaccorso, T. Hasan, L. Garcia-Gancedo, A. Dyadyusha, S. Haque, P. Andrew, S. Hofmann, J. Moultrie, D. Chu, A.J. Flewitt, A.C. Ferrari, M.J. Kelly, J. Robertson, G.A.J. Amaratunga, W.I. Milne, Flexible Electronics: The

Next Ubiquitous Platform, Proceedings of the IEEE 100(Special Centennial Issue) (2012) 1486-1517.
[337] C.R. Bowen, H.A. Kim, P.M. Weaver, S. Dunn, Piezoelectric and ferroelectric materials and structures for energy harvesting applications, Energy & Environmental Science 7(1) (2014) 25-44.
[338] Y. Yuan, Z. Xiao, B. Yang, J. Huang, Arising applications of ferroelectric materials in photovoltaic devices, Journal of Materials Chemistry A 2(17) (2014) 6027-6041.
[339] M.L. Calzada, Sol–Gel Electroceramic Thin Films, The Sol-Gel Handbook, Wiley-VCH Verlag GmbH & Co. KGaA2015, pp. 841-882.
[340] Y. Qi, N.T. Jafferis, K. Lyons, C.M. Lee, H. Ahmad, M.C. McAlpine, Piezoelectric Ribbons Printed onto Rubber for Flexible Energy Conversion, Nano Letters 10(2) (2010) 524-528.
[341] J. Rho, S.J. Kim, W. Heo, N.E. Lee, H.S. Lee, J.H. Ahn, $PbZr_xTi_{1-x}O_3$ Ferroelectric Thin-Film Capacitors for Flexible Nonvolatile Memory Applications, Ieee Electr Device L 31(9) (2010) 1017-1019.
[342] Y.H. Do, W.S. Jung, M.G. Kang, C.Y. Kang, S.J. Yoon, Preparation on transparent flexible piezoelectric energy harvester based on PZT films by laser lift-off process, Sensors and Actuators A: Physical 200 (2013) 51-55.
[343] T. Nakajima, K. Shinoda, T. Tsuchiya, UV-assisted nucleation and growth of oxide films from chemical solutions, Chemical Society Reviews 43(7) (2014) 2027-2041.
[344] K. Yin, M. Li, Y. Liu, C. He, F. Zhuge, B. Chen, W. Lu, X. Pan, R.-W. Li, Resistance switching in polycrystalline $BiFeO_3$ thin films, Applied Physics Letters 97(4) (2010) 042101.
[345] A.K. Zvezdin, A.M. Kadomtseva, S.S. Krotov, A.P. Pyatakov, Y.F. Popov, G.P. Vorob'ev, Magnetoelectric interaction and magnetic field control of electric polarization in multiferroics, Journal of Magnetism and Magnetic Materials 300(1) (2006) 224-228.
[346] C.-C. Lee, J.-M. Wu, Effect of film thickness on interface and electric properties of $BiFeO_3$ thin films, Applied Surface Science 253(17) (2007) 7069-7073.
[347] Q. Zhang, N. Valanoor, O. Standard, Chemical solution deposition derived (001)-oriented epitaxial $BiFeO_3$ thin films with robust ferroelectric properties using stoichiometric precursors (invited), Journal of Applied Physics 116(6) (2014) 066810.
[348] X. Tang, L. Hu, J. Yang, L. Chen, J. Dai, W. Song, Z. Yang, X. Zhu, Y. Sun, $BiFeO_3$ thin films prepared on metallic Ni tapes by chemical solution deposition: effects of annealing temperature and a $La_{0.5}Sr_{0.5}TiO_3$ buffer layer on the dielectric, ferroelectric and leakage properties, RSC Advances 4 (2014) 32738–32743.
[349] M. Coll, J. Gazquez, I. Fina, Z. Khayat, A. Quindeau, M. Alexe, M. Varela, S. Trolier-McKinstry, X. Obradors, T. Puig, Nanocrystalline Ferroelectric $BiFeO_3$ Thin Films by Low-Temperature Atomic Layer Deposition, Chemistry of Materials 27(18) (2015) 6322-6328.
[350] J.-K. Chung, W.-J. Kim, J.K. Kim, S.S. Kim, T.K. Song, The characteristics of $BiFeO_3$ multiferroic thin films grown by pulsed laser deposition Integrated Ferroelectrics 87(1) (2007) 25-32.
[351] Y.-T. Liu, C.-S. Ku, S.-J. Chiu, H.-Y. Lee, S.-Y. Chen, Ultrathin Oriented $BiFeO_3$ Films from Deposition of Atomic Layers with Greatly Improved Leakage and Ferroelectric Properties, ACS Applied Materials & Interfaces 6(1) (2014) 443-449.
[352] D. Rivero, L. Pardo, R. Jiménez, Instalación para medir el lazo de histéresis y las corrientes de conmutación en láminas delgadas de materiales ferroeléctricos, Revista Cubana de Física 26(2A) (2009) 169-173.
[353] S. Farhadi, N. Rashidi, Perovskite-type ferromagnetic $BiFeO_3$ nanopowder: a new magnetically recoverable heterogeneous nanocatalyst for efficient and selective transfer hydrogenation of aromatic nitro compounds into aromatic amines under microwave heating, Journal of the Iranian Chemical Society 9(6) (2012) 1021-1031.
[354] I. Bretos, R. Jiménez, M. Tomczyk, E. Rodríguez-Castellón, P.M. Vilarinho, M.L. Calzada, Active layers of high-performance lead zirconate titanate at temperatures compatible with silicon nano- and microelectronic devices, Scientific Reports 6 (2016) 20143.

[355] J.A. Voigt, B.A. Tuitle, T.J. Headley, M.O. Eatough, D.L. Lamppa, D. Goodnow, Oriented Lead Zirconate Titanate thin Films: Characterization of Film Crystallization, MRS Proceedings 310 (1993).
[356] H. Yan, F. Inam, G. Viola, H. Ning, H. Zhang, Q. Jiang, T. Zeng, Z. Gao, M. Reece, The contribution of electrical conductivity, dielectric permittivity and domain wsitching in ferroelectric hysteresis loops Journal of Advanced Dielectrics 01(01) (2011) 107-118.
[357] T.M. Shaw, S. Trolier-McKinstry, P.C. McIntyre, The Properties of Ferroelectric Films at Small Dimensions, Annual Review of Materials Science 30(1) (2000) 263-298.
[358] H. Imai, Ultraviolet (UV) Irradiation, in: S. Sakka (Ed.), Handbook of Sol-Gel Science and Technology: Processing, Characterisation and Applications Kluwer Academic Publishers, Boston, 2005, pp. 639–650.
[359] C. De Dobbelaere, A. Hardy, M.K. Van Bael, I. Bretos, R. Jiménez, M.L. Calzada, Low-Temperature Photochemical Solution Deposition of Ferroelectric and Multiferroic Thin Films, Nanoscale Ferroelectrics and Multiferroics, John Wiley & Sons, Ltd2016, pp. 163-199.
[360] B. Marchand, P. Jalkanen, V. Tuboltsev, M. Vehkamäki, M. Puttaswamy, M. Kemell, K. Mizohata, T. Hatanpää, A. Savin, J. Räisänen, M. Ritala, M. Leskelä, Electric and Magnetic Properties of ALD-Grown $BiFeO_3$ Films, The Journal of Physical Chemistry C 120(13) (2016) 7313-7322.